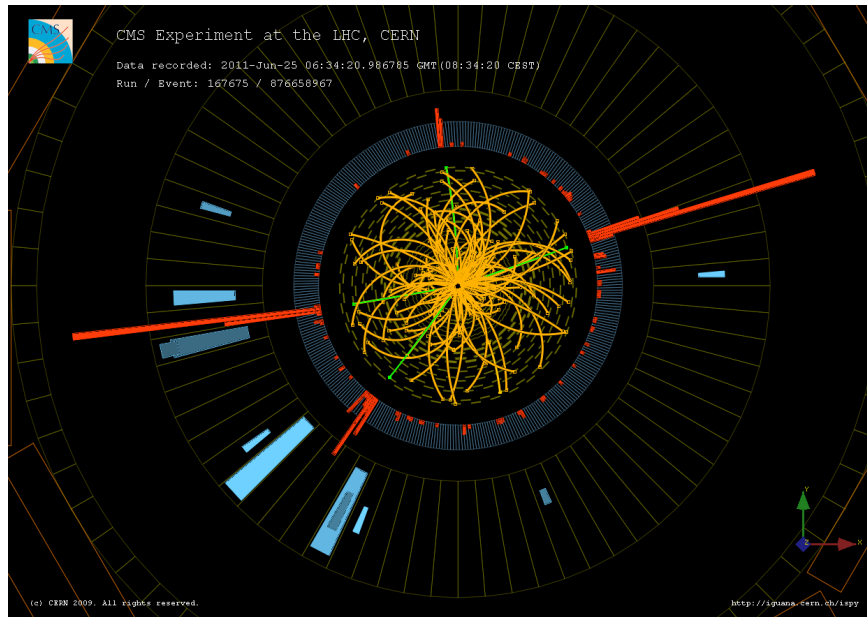


Phenomenology of Particle Physics I

ETH Zurich and University of Zurich

HS 2009



Prof. Dr. Vincenzo Chiochia [UNIVERSITY OF ZURICH]

Prof. Dr. Günther Dissertori [ETH ZURICH]

Prof. Dr. Thomas Gehrmann [UNIVERSITY OF ZURICH]

Typeset by Julián Cancino and Julian Schrenk

June 13, 2014

This script is based on the lecture given originally by Prof. Dr. Chiochia (University of Zurich), Prof. Dr. Günther Dissertori (ETH Zurich) and Prof. Dr. Thomas Gehrmann (University of Zurich) in the fall semester 2009 (PPP1) and the spring semester 2010 (PPP2).

Please feel free to send feedback to julian.cancino@gmail.com and kenjschrenk@gmail.com.

We would like to thank the lecturers who used the script in the later semesters, as well as in particular Romain Müller and Murad Tovmasyan for making valuable suggestions and pointing out numerous typos.

Contents

| | | |
|----------|--|-----------|
| 1 | Introduction | 1 |
| 1.1 | Units | 2 |
| 1.2 | Elementary interactions | 4 |
| 2 | Relativistic kinematics | 7 |
| 2.1 | Particle decay | 8 |
| 2.2 | Two-particle scattering | 9 |
| 2.2.1 | Scattering angle | 12 |
| 2.2.2 | Elastic scattering | 12 |
| 2.2.3 | Angular distribution | 13 |
| 2.2.4 | Relative velocity | 13 |
| 2.2.5 | Center of mass and laboratory systems | 13 |
| 2.3 | Crossing symmetry | 14 |
| 2.3.1 | Interpretation of antiparticle-states | 15 |
| 3 | Lorentz invariant scattering cross section | 19 |
| 3.1 | \mathcal{S} -operator | 20 |
| 3.2 | Fermi's golden rule | 21 |
| 3.2.1 | Total decay rate | 22 |
| 3.2.2 | Scattering cross section | 23 |
| 3.2.3 | Invariant phase space for n_f -particles | 23 |
| 3.2.4 | Differential cross section | 24 |
| 3.3 | $2 \rightarrow 2$ scattering cross section | 24 |
| 3.3.1 | Phase space | 24 |
| 3.3.2 | Differential cross section | 26 |
| 3.4 | Unitarity of the \mathcal{S} -operator | 26 |

| | | |
|----------|--|-----------|
| 4 | Accelerators and collider experiments | 29 |
| 4.1 | Particle accelerators: motivations | 29 |
| 4.1.1 | Center of mass energy | 32 |
| 4.2 | Acceleration methods | 33 |
| 4.2.1 | Cyclotron | 34 |
| 4.2.2 | Synchrotron | 37 |
| 4.3 | Particle physics experiments | 38 |
| 4.3.1 | Cross section | 40 |
| 4.3.2 | Luminosity | 40 |
| 4.3.3 | Particle detectors | 43 |
| 4.4 | Kinematics and data analysis methods | 46 |
| 4.4.1 | Pseudorapidity and transverse momentum | 46 |
| 4.4.2 | Momentum conservation in particle jets | 47 |
| 4.4.3 | Missing mass method | 49 |
| 4.4.4 | Invariant mass method | 50 |
| 5 | Elements of quantum electrodynamics | 55 |
| 5.1 | Quantum mechanical equations of motion | 55 |
| 5.2 | Solutions of the Dirac equation | 59 |
| 5.2.1 | Free particle at rest | 60 |
| 5.2.2 | Free particle | 60 |
| 5.2.3 | Explicit form of u and v | 60 |
| 5.2.4 | Operators on spinor spaces | 61 |
| 5.3 | Field operator of the Dirac field | 65 |
| 5.4 | Dirac propagator | 68 |
| 5.4.1 | Feynman propagator | 69 |
| 5.5 | Photon field operator | 72 |
| 5.6 | Interaction representation | 74 |
| 5.6.1 | Time evolution operator | 75 |
| 5.6.2 | Time ordering | 75 |
| 5.7 | Scattering matrix | 78 |
| 5.8 | Feynman rules of quantum electrodynamics | 80 |
| 5.9 | Trace techniques for γ -matrices | 90 |

| | | |
|----------|--|------------|
| 5.10 | Annihilation process : $e^+e^- \rightarrow \mu^+\mu^-$ | 92 |
| 5.11 | Compton scattering | 94 |
| 5.12 | QED as a gauge theory | 98 |
| 6 | Tests of QED | 101 |
| 6.1 | Measurement of the electron anomalous magnetic moment | 101 |
| 6.1.1 | Electron magnetic moment | 101 |
| 6.1.2 | QED: higher order corrections | 102 |
| 6.1.3 | $g/2$ measurements | 103 |
| 6.1.3.1 | Experiment | 103 |
| 6.1.3.2 | Theoretical predictions | 106 |
| 6.2 | High energy tests | 108 |
| 6.2.1 | e^+e^- colliders | 108 |
| 6.2.2 | Detector elements | 110 |
| 6.2.3 | Cross section measurement | 112 |
| 6.2.4 | Bhabha scattering | 113 |
| 6.2.5 | Lepton pair production | 116 |
| 6.2.6 | Hadronic processes | 121 |
| 6.2.7 | Limits of QED | 122 |
| 7 | Unitary symmetries and QCD as a gauge theory | 125 |
| 7.1 | Isospin $SU(2)$ | 125 |
| 7.1.1 | Isospin invariant interactions | 129 |
| 7.2 | Quark model of hadrons | 130 |
| 7.3 | Hadron spectroscopy | 131 |
| 7.3.1 | Quarks and leptons | 131 |
| 7.3.2 | Strangeness | 133 |
| 7.3.3 | Strong vs. weak decays | 135 |
| 7.3.4 | Mesons | 136 |
| 7.3.5 | Gell-Mann-Nishijima formula | 136 |
| 7.4 | Quantum chromodynamics and color $SU(3)$ | 138 |
| 7.4.1 | Strength of QCD interaction | 145 |
| 7.4.2 | QCD coupling constant | 148 |

| | | |
|----------|--|------------|
| 8 | QCD in e^+e^- annihilations | 153 |
| 8.1 | The basic process: $e^+e^- \rightarrow q\bar{q}$ | 155 |
| 8.1.1 | Singularities | 156 |
| 8.2 | Jets and other observables | 159 |
| 8.2.1 | Jet algorithms | 160 |
| 8.2.1.1 | Examples of jet algorithms | 162 |
| 8.2.2 | Event shape variables | 166 |
| 8.2.3 | Applications | 172 |
| 8.3 | Measurements of the strong coupling constant | 179 |
| 8.4 | Measurements of the QCD color factors | 190 |
| 8.5 | Hadronization | 191 |

Chapter 1

Introduction

Literature:

- Halzen/Martin [1]
- Aitchison/Hey [2] (rigorous)
- Seiden [3] (experimental, up to date)
- Nachtmann [4] (difficult to purchase)

Elementary particles are the smallest constituents of matter. Therefore the notion “elementary” changes with scientific progress (cf. Tab. 1.1).

We can define “elementary” as “having no resolvable inner structure”. This also means that there can be no excited states. Elementary particles interact in a well-defined way through fundamental interactions. These are

- gravity,
- electromagnetic interaction,
- weak interaction, and
- strong interaction,

where only the last three are relevant, at the elementary particle level, at energies currently available. Range of phenomena:

- structure of matter
- stability of matter

| | | | |
|------|------------------------------|-------------------------------|---------------------------|
| 1869 | Mendeleev/Meyer | periodic system | atom |
| 1890 | J. Thomson | electron | |
| 1910 | Bequerel/Curie | radioactivity | atomic nucleus & electron |
| | Rutherford | scattering | |
| 1932 | Chadwick | neutron | proton, neutron, electron |
| | Anderson | positron | & their antiparticles |
| 1947 | Blackett/Powell | pion, muon | “particle zoo” |
| 1956 | Cowan/Reines | neutrino | |
| 1967 | Glashow/Weinberg/Salam | electroweak theory | |
| 1968 | SLAC | deep inelastic scattering | quarks & leptons |
| 1972 | Fritzsch/Gell-Mann/Leutwyler | quantum chromodynamics | |
| 1974 | SLAC/BNL | c quark, τ lepton | |
| 1979 | DESY | gluon | |
| 1977 | Fermilab | b quark | |
| 1983 | CERN | W , Z bosons | |
| 1995 | Fermilab | t quark, ν_τ | |

Table 1.1: Historical outline of the concept of “elementarity”

- instability of matter, radioactivity: decay of elementary particles
- scattering of elementary particles
- production of new particles
- indirect implications
 - early history of the universe
 - fuel cycle in stars
 - astrophysical phenomena: supernovae, very high energy cosmic rays

1.1 Units

The Planck constant

$$\hbar = \frac{h}{2\pi} = 1.0546 \cdot 10^{-34} \text{ Js} \quad (1.1)$$

has dimension of action and angular momentum. Another important physical constant is the speed of light

$$c = 2.998 \cdot 10^8 \frac{\text{m}}{\text{s}}. \quad (1.2)$$

Because we are dealing with constants, Eq. (1.1) and (1.2) establish a relationship among the units for energy, time, and length. Using so-called natural units, i. e. setting $\hbar = c = 1$, we find

$$[c] = [\text{length}] \cdot [\text{time}]^{-1} = [L][T]^{-1} \Rightarrow [L] = [T] \quad (1.3)$$

$$[\hbar] = [\text{energy}] \cdot [\text{time}] = [M][L]^2[T]^{-1} \Rightarrow [M] = [L]^{-1} \quad (1.4)$$

$$\Rightarrow [M] = [L]^{-1} = [T]^{-1} \text{ and } [E] = [M]. \quad (1.5)$$

This raises the question of a suitable fundamental unit for energy. One electron volt is the energy acquired by an electron passing a potential difference of 1 V :

$$1 \text{ eV} = 1.602 \cdot 10^{-19} \text{ J}$$

$$\text{keV} = 10^3 \text{ eV}$$

$$\text{MeV} = 10^6 \text{ eV}$$

$$\text{GeV} = 10^9 \text{ eV}$$

$$\text{TeV} = 10^{12} \text{ eV}.$$

Examples of some orders of magnitude are

$$m_e = 511 \text{ keV}$$

$$m_p = 938 \text{ MeV}$$

$$m_n = 939 \text{ MeV}$$

$$E_e(\text{LEP}) = 104.5 \text{ GeV}$$

$$E_p(\text{Tevatron}) = 980 \text{ GeV}$$

$$E_p(\text{LHC}) = 7 \text{ TeV}.$$

Converting the units for energy, time, and length into each other yields, in agreement with Eq. (1.5),

$$\hbar = 6.58 \cdot 10^{-25} \text{ GeV} \cdot \text{s} \stackrel{!}{=} 1 \Rightarrow \boxed{1 \text{ GeV}^{-1} \simeq 6.58 \cdot 10^{-25} \text{ s}}, \quad (1.6)$$

(recall lifetime $\tau = \frac{1}{\Gamma}$ with Γ the resonance width), and

$$c = 2.998 \cdot 10^8 \frac{\text{m}}{\text{s}} \stackrel{!}{=} 1 \Rightarrow \boxed{1 \text{ fm} = 10^{-15} \text{ m} \simeq \frac{1}{200 \text{ MeV}}}. \quad (1.7)$$

Cross sections have dimensions of area:

$$[\sigma] = [L]^2 = [M]^{-2} = \frac{1}{(\text{eV})^2}. \quad (1.8)$$

As unit we choose

$$\frac{1}{(1 \text{ GeV})^2} = 389379 \text{ nb} = 389379 \cdot 10^{-9} \text{ b}$$

with $1 \text{ b} : 1 \text{ barn} = 10^{-24} \text{ cm}^2$ the typical scale of nuclear absorption.

The unit of electrical charge can be defined in different ways. The dimensionless fine structure constant α is accordingly expressed differently in terms of e in different systems of units,

$$\begin{aligned}\alpha &= \left. \frac{e^2}{4\pi\epsilon_0\hbar c} \right|_{\text{SI}} = 7.2972 \cdot 10^{-3} \simeq \frac{1}{137} \\ &= \left. \frac{e^2}{\hbar c} \right|_{\text{CGS}} \\ &= \left. \frac{e^2}{4\pi\hbar c} \right|_{\text{Heaviside-Lorentz}},\end{aligned}$$

and determines the strength of the electromagnetic interaction. Therefore, in Heaviside-Lorentz units, the electron charge is fixed to be

$$e = \sqrt{4\pi\alpha} \Big|_{\text{HL}}. \quad (1.9)$$

1.2 Elementary interactions

Gravitation. Since

$$Gm_p^2 \approx 10^{-39}$$

and because of the fact that gravity's range is infinite, it is relevant for macroscopic systems (and can be neglected here).

Electromagnetic interaction. Recall that $\alpha \simeq \frac{1}{137}$. The range of the electromagnetic interaction is infinite and typical lifetimes of particles decaying through electromagnetic interactions range from $\tau_{\Sigma^0 \rightarrow \Lambda^0 \gamma} = 10^{-20} \text{ s}$ to $\tau_{\pi^0 \rightarrow \gamma\gamma} = 10^{-16} \text{ s}$. Typical cross sections are of order $\sigma_{ep \rightarrow ep} = 1 \mu\text{b}$. QED's (quantum electrodynamics') predictions have been tested to high theoretical and experimental precision. Consider for example the anomalous magnetic moment of the electron:

$$\begin{aligned}\mu_e^{\text{QED}} &= \frac{e}{2m_e} \frac{g}{2} = \frac{e}{2m_e} \left\{ \underbrace{1}_{\text{Dirac}} + \underbrace{\frac{1}{2} \frac{\alpha}{\pi}}_{\text{Schwinger}} - \underbrace{0.388 \frac{\alpha^2}{\pi^2}}_{\text{Petermann}} + \underbrace{1.18 \frac{\alpha^3}{\pi^3}}_{\text{Laporta/Remiddi}} \right\} \\ &= \frac{e}{2m_e} \{1.0011596521465(270)\} \\ \mu_e^{\text{exp.}} &= \frac{e}{2m_e} \{1.0011596521883(42)\},\end{aligned}$$

where the experimental value was obtained by Van Dyck, Schwinberg and Dehmelt.

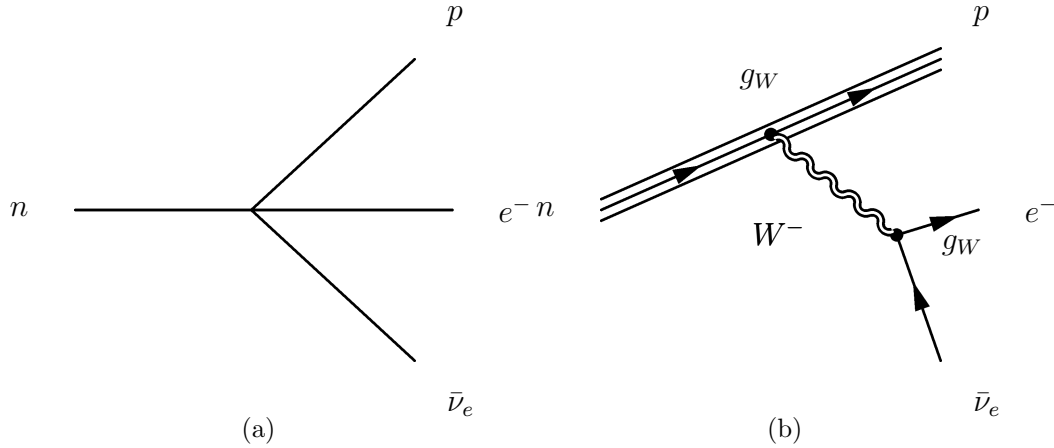


Figure 1.1: *Beta decay of neutron*. Depicted as a point like process, as described by Fermi's constant (a) and via W^- boson exchange (b).

Weak interaction. As an example for weak interactions consider β decay: $n \rightarrow pe\bar{\nu}_e$: see Fig. 1.1(a). The range is about 1 fm and for the coupling we have

$$G_F m_p^2 \approx 10^{-5}.$$

The lifetimes go from 10^{-10} s to 10^3 s and cross sections are of order $\sigma \approx 1$ fb. Theoretically, the process is explained by W^- boson exchange, see Fig. 1.1(b), which yields for Fermi's constant $G_F = \frac{g_w^2}{8M_W^2}$.

Strong interaction. At the nuclear level, the Yukawa theory of pion exchange (see figures 1.2(a) and 1.2(b)) is still used. It explains the bonding of protons and neutrons by exchange of massive pions: $m_\pi = 130$ MeV \Rightarrow range $\simeq \frac{1}{m_\pi} = \frac{1}{130 \text{ MeV}} \simeq 1.4$ fm. QCD (quantum chromodynamics) states that particles like p , n , and π consist of quarks which interact through gluons. Gluons (in contrast to photons) carry themselves the charges they are coupling to which influences the strong interaction's potential, see fig.1.3. The QCD coupling constant is approximately given by $\alpha_s \simeq 0.12$.

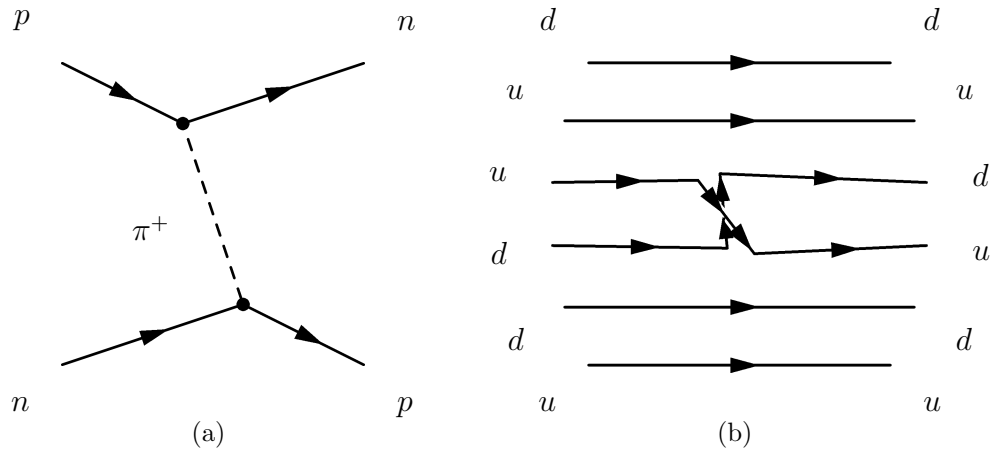


Figure 1.2: *Yukawa theory*. Interaction by pion exchange (a) and exchange of quark and anti-quark (b).

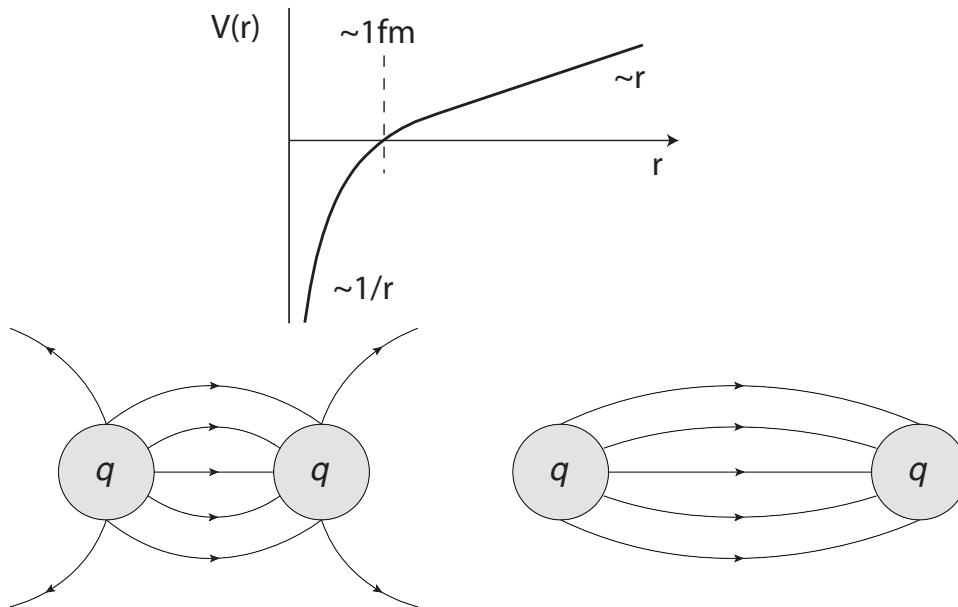


Figure 1.3: *Potential of the strong interaction*.

Chapter 2

Relativistic kinematics

Literature:

- Nachtmann [4]
- Hagedorn [5]
- Byckling/Kajantie [6]

We state some notation concerning special relativity:

$$x^\mu = (x^0 = t, x^1, x^2, x^3) = (t, \vec{x}) \quad \text{contravariant four-vector} \quad (2.1)$$

$$x_\mu = (t, -\vec{x}) \quad \text{covariant four-vector} \quad (2.2)$$

$$g^{\mu\nu} = g_{\mu\nu} = \begin{pmatrix} 1 & & & \\ & -1 & & \\ & & -1 & \\ & & & -1 \end{pmatrix} \quad \text{metric tensor} \quad (2.3)$$

$$\tau^2 = t^2 - \vec{x}^2 = g_{\mu\nu} x^\mu x^\nu = x^\mu x_\mu = x^2 \quad \text{Lorentz invariant} \quad (2.4)$$

$$d\tau = dt \sqrt{1 - \left(\frac{d\vec{x}}{dt}\right)^2} = \frac{dt}{\gamma} \quad \text{proper time.} \quad (2.5)$$

Combining Eq. (2.1) and (2.5) we arrive at the four-velocity

$$u^\mu = \frac{dx^\mu}{d\tau} = \frac{dx^\mu}{dt} \frac{dt}{d\tau} = \gamma(1, \vec{v}).$$

Since

$$u^2 = \gamma^2(1 - \vec{v}^2) = 1 > 0,$$

u is a time-like four-vector. The four-momentum is then defined as

$$p^\mu = mu^\mu = m\gamma(1, \vec{v}) = (p^0 = E, \vec{p}).$$

By calculating the corresponding Lorentz invariant,

$$p^2 = m^2 u^2 = m^2 = E^2 - \vec{p}^2,$$

we find the energy-momentum relation

$$E = \sqrt{m^2 + \vec{p}^2}. \quad (2.6)$$

A particle is said to be relativistic if $\vec{p}^2 \not\ll m^2$. Conversely, for a non-relativistic particle, $\vec{p}^2 \ll m^2$, and therefore

$$E = \sqrt{m^2 + \vec{p}^2} = m \left(1 + \frac{1}{2} \frac{\vec{p}^2}{m^2} + \dots \right) = m + \frac{1}{2} \frac{\vec{p}^2}{m} + \dots$$

so that we recover the expression for $|\vec{v}| \ll 1$ of Newtonian mechanics.

2.1 Particle decay

The decaying particle's four-momentum is, in the rest frame, given by $p = (M, 0, 0, 0)$, see Fig. 2.1. The decay time (lifetime) is

$$d\tau^2 = dt^2(1 - \vec{v}^2)$$

where dt^2 is the lifetime in the laboratory frame:

$$dt = \gamma d\tau > d\tau. \quad (2.7)$$

The result stated in equation (2.7) has been verified experimentally:

$$\begin{aligned} \tau_{\pi^+ \rightarrow \mu^+ \nu_\mu} &= 2.6 \cdot 10^{-8} \text{ s} \\ E_\pi &= 20 \text{ GeV}, \quad \gamma = \frac{E_\pi}{m_\pi} = 143 \Leftrightarrow v = 0.9999 \\ \Rightarrow \frac{t'_\pi}{t_\pi} &= 143. \end{aligned}$$

Constraints are (i) conservation of energy and momentum, $p = p_1 + p_2$ (4 equations), and (ii) the mass-shell condition, $p_i^2 = m_i^2$:

$$\begin{array}{lll} p^2 = M^2 & p_1^2 = m_1^2 & p_2^2 = m_2^2 \\ p = (M, \vec{0}) & p_1 = (E_1, \vec{p}_1) & p_2 = (E_2, \vec{p}_2). \end{array}$$

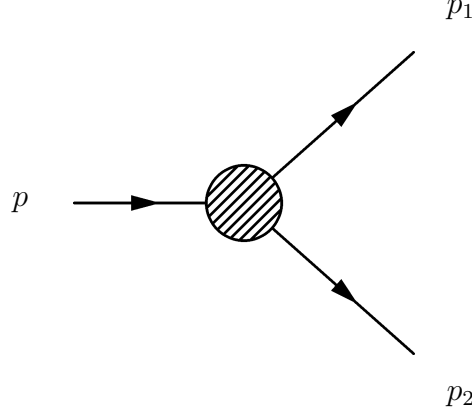


Figure 2.1: *Particle decay*. Dynamics will be discussed later on; at the moment we are dealing with kinematics.

It therefore follows that

$$p \cdot p_i = ME_i \Rightarrow E_i = \frac{1}{M} p \cdot p_i = \frac{1}{M} (p_1 \cdot p_i + p_2 \cdot p_i).$$

And, by using $p_1 \cdot p_2 = \frac{1}{2}[(p_1 + p_2)^2 - p_1^2 - p_2^2] = \frac{1}{2}[M^2 - m_1^2 - m_2^2]$, we find

$$\begin{aligned} E_1 &= \frac{1}{M} (p_1^2 + p_1 \cdot p_2) = \frac{1}{2M} (M^2 + m_1^2 - m_2^2) \\ E_2 &= \frac{1}{2M} (M^2 - m_1^2 + m_2^2). \end{aligned}$$

By using equation (2.6) and $\vec{p}_1 + \vec{p}_2 = 0$, the absolute value of the three-momenta,

$$\vec{p}_1^2 = E_1^2 - m_1^2 = \frac{1}{4M^2} \left(M^4 - 2M^2(m_1^2 + m_2^2) + (m_1^2 - m_2^2)^2 \right) = \vec{p}_2^2,$$

is also fixed. This means that only the directions of \vec{p}_1 and \vec{p}_2 remain unknown, while the energies and the absolute values of the momenta can be calculated directly.

2.2 Two-particle scattering

For a visualisation of the process see Fig. 2.2(a). Once again, the constraints are

$$\begin{aligned} p_i^2 &= m_i^2 \quad (i = 1, \dots, 4) \\ p_1 + p_2 &= p_3 + p_4. \end{aligned}$$

We talk of elastic scattering if $m_1 = m_3$ and $m_2 = m_4$. Consider the Lorentz invariants

$$p_i^2 = m_i^2 \text{ and } \underbrace{p_1 \cdot p_2, p_1 \cdot p_3, p_1 \cdot p_4, p_2 \cdot p_3, p_2 \cdot p_4, p_3 \cdot p_4}_{\substack{6 \text{ invariants, 2 linearly independent, 4 linearly dependent}}}.$$

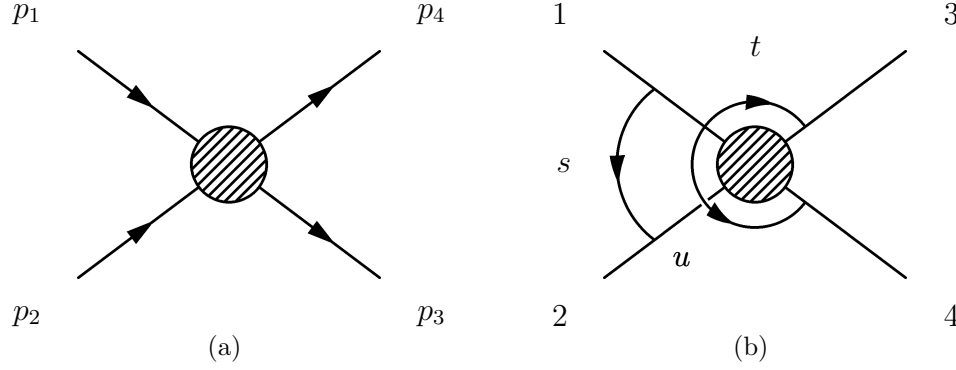


Figure 2.2: *Two-particle scattering*. The kinematical constraints are energy-momentum conservation and the mass shell condition (a). Visualization of Mandelstam variables (b).

Four of them have to be linearly dependent, since there are only two degrees of freedom in the system (center of mass energy and scattering angle).

We now define the Mandelstam variables (see Fig. 2.2(b))

$$\begin{aligned} s &= (p_1 + p_2)^2 \\ t &= (p_1 - p_3)^2 \\ u &= (p_1 - p_4)^2, \end{aligned}$$

where s denotes total center of mass energy squared (positive) and t is the four-momentum transfer squared (negative). Note also that $s + t + u = \sum_{i=1}^4 m_i^2$.

The center of mass frame is defined by

$$\vec{p}_1 + \vec{p}_2 = 0 = \vec{p}_3 + \vec{p}_4. \quad (2.8)$$

One usually denote variables in this frame with an asterisk: (cm., $p_i = p_i^*$). The laboratory frame is defined by $\vec{p}_2 = 0$ (fixed target) and variables are labelled with an L : (lab., $p_i = p_i^L$). In deep inelastic scattering the Breit system ($p_i = p_i^B$) is used, which is defined by $\vec{p}_1 + \vec{p}_3 = 0$.

In the following we take a closer look at the center of mass frame, see Fig. 2.3. Equation (2.8) leads to

$$\begin{aligned} \vec{p}_1^* &= -\vec{p}_2^* = \vec{p} \\ \vec{p}_3^* &= -\vec{p}_4^* = \vec{p}' \\ p_1 &= \left(E_1^* = \sqrt{\vec{p}^2 + m_1^2}, \vec{p} \right) \\ p_2 &= \left(E_2^* = \sqrt{\vec{p}^2 + m_2^2}, -\vec{p} \right) \\ p_3 &= (E_3^*, \vec{p}') \\ p_4 &= (E_4^*, -\vec{p}'). \end{aligned}$$

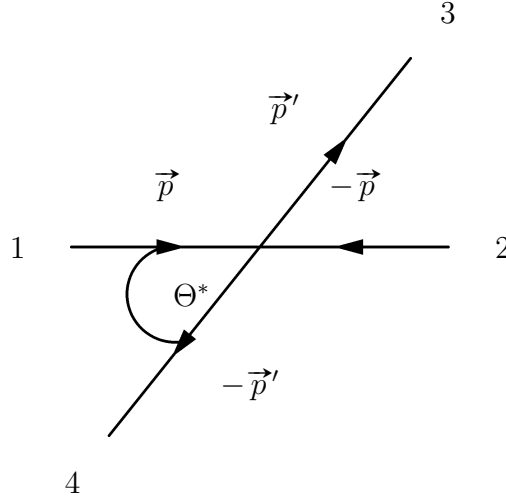


Figure 2.3: *Two-particle scattering in center of mass frame.* For the constraints on the scattering angle Θ^* see section 2.2.1.

The sum

$$p_1 + p_2 = (\underbrace{E_1^* + E_2^*}_{\sqrt{s}}, \vec{0})$$

is no Lorentz invariant, whereas

$$s = (p_1 + p_2)^2 = (E_1^* + E_2^*)^2$$

is one. Now we can express E_i^* , $|\vec{p}|$, and $|\vec{p}'|$ in terms of s (see exercise sheet 1):

$$E_{1,3}^* = \frac{1}{2\sqrt{s}}(s + m_{1,3}^2 - m_{2,4}^2) \quad (2.9)$$

$$\vec{p}^2 = (E_1^*)^2 - m_1^2 = \frac{1}{4s}\lambda(s, m_1^2, m_2^2), \quad (2.10)$$

where we have used the Källén function (triangle function) which is defined by

$$\begin{aligned} \lambda(a, b, c) &= a^2 + b^2 + c^2 - 2ab - 2ac - 2bc \\ &= \left[a - (\sqrt{b} + \sqrt{c})^2 \right] \left[a - (\sqrt{b} - \sqrt{c})^2 \right] \\ &= a^2 - 2a(b + c) + (b - c)^2. \end{aligned}$$

We can see that the Källén function has the following properties:

- symmetric under $a \leftrightarrow b \leftrightarrow c$ and
- asymptotic behavior: $a \gg b, c : \lambda(a, b, c,) \rightarrow a^2$.

This enables us to determine some properties of scattering processes. From $\vec{p}^2, \vec{p}'^2 > 0$ it follows that

$$s_{\min} = \max \left\{ (m_1 + m_2)^2, (m_3 + m_4)^2 \right\} \geq 0$$

is the threshold of the process in the s -channel. In the high energy limit ($s \gg m_i^2$) Eq. (2.9) and (2.10) simplify because of the asymptotic behavior of λ and one obtains:

$$E_1^* = E_2^* = E_3^* = E_4^* = |\vec{p}| = |\vec{p}'| = \frac{\sqrt{s}}{2}.$$

2.2.1 Scattering angle

In the center of mass frame, the scattering angle Θ^* is defined by

$$\vec{p} \cdot \vec{p}' = |\vec{p}| \cdot |\vec{p}'| \cos \Theta^*.$$

We also know that

$$\begin{aligned} p_1 \cdot p_3 &= E_1^* E_3^* - |\vec{p}_1^*| |\vec{p}_3^*| \cos \Theta^* \\ t &= (p_1 - p_3)^2 = m_1^2 + m_3^2 - 2p_1 p_3 = (p_2 - p_4)^2 \end{aligned}$$

and can derive $\cos \Theta^* = \text{function}(s, t, m_i^2)$:

$$\cos \Theta^* = \frac{s(t - u) + (m_1^2 - m_2^2)(m_3^2 - m_4^2)}{\sqrt{\lambda(s, m_1^2, m_2^2)} \sqrt{\lambda(s, m_3^2, m_4^2)}}.$$

This means that $2 \rightarrow 2$ scattering is described by two independent variables:

$$\sqrt{s} \text{ and } \Theta^* \quad \quad \quad \text{or} \quad \quad \quad \sqrt{s} \text{ and } t.$$

2.2.2 Elastic scattering

We now consider the case of elastic scattering. This means that $m_1 = m_3$ and $m_2 = m_4$ (e. g. $ep \rightarrow ep$). Therefore Eq. (2.9) and (2.10) simplify:

$$\begin{aligned} E_1^* &= E_3^*, \quad E_2^* = E_4^* \\ |\vec{p}|^2 &= |\vec{p}'|^2 = \frac{1}{4s} \left(s - (m_1 + m_2)^2 \right) \left(s - (m_1 - m_2)^2 \right) \end{aligned}$$

and we find for the scattering angle (in the case of elastic scattering)

$$\begin{aligned} t &= (p_1 - p_3)^2 = -(\vec{p}_1 - \vec{p}_3)^2 = -2\vec{p}^2(1 - \cos \Theta^*) \\ \Rightarrow \quad &\boxed{\cos \Theta^* = 1 + \frac{t}{2|\vec{p}|^2}}. \end{aligned}$$

Restriction to the physically valid region yields

$$\left. \begin{aligned} -1 &\leq \cos \Theta^* \leq 1 \\ \vec{p}^2 &\geq 0 \end{aligned} \right\} \Leftrightarrow \left\{ \begin{aligned} -4|\vec{p}|^2 &\leq t \leq 0 \\ s &\geq (m_1 + m_2)^2 \end{aligned} \right. .$$

2.2.3 Angular distribution

Finally, we find for the angular distribution (bearing in mind that the distribution is rotationally invariant with respect to the “ \vec{p} -axis” such that $\int d\phi = 2\pi$)

$$\begin{aligned} d\Omega^* &= 2\pi d\cos\Theta^* \\ \frac{d\Omega^*}{dt} &= \frac{4\pi s}{\sqrt{\lambda(s, m_1^2, m_2^2)}\sqrt{\lambda(s, m_3^2, m_4^2)}} = \frac{\pi}{|\vec{p}||\vec{p}'|}. \end{aligned} \quad (2.11)$$

2.2.4 Relative velocity

At this point, we introduce the relative velocity, which we will see to be of relevance in defining the particle flux and hence the collider construction,

$$v_{12} = |\vec{v}_1 - \vec{v}_2| = \left| \frac{\vec{p}_1}{E_1} - \frac{\vec{p}_2}{E_2} \right| = \left| \frac{\vec{p}_1^*}{E_1^*} - \frac{\vec{p}_2^*}{E_2^*} \right| = \frac{|\vec{p}_1^*|}{E_1^* E_2^*} \underbrace{(E_1^* + E_2^*)}_{\sqrt{s}}, \quad (2.12)$$

from which we get,

$$\begin{aligned} v_{12} E_1^* E_2^* &= \sqrt{s} |\vec{p}_1^*| = \sqrt{s} \sqrt{E_1^{*2} - m_1^2} \\ &= \sqrt{s} \sqrt{\frac{1}{4s} (s + m_1^2 - m_2^2)^2 - m_1^2} \\ &= \sqrt{(p_1 \cdot p_2)^2 - m_1^2 m_2^2}, \end{aligned} \quad (2.13)$$

the so called Møller flux factor. In going from the first line to the second, we used the definition of the Källén function and in going to the third the fact that $s = m_1^2 + m_2^2 + 2p_1 \cdot p_2$.

We stress here that $v_{12} E_1^* E_2^*$ is a frame independent quantity. It appears in the definition of the incoming particle flux, and thus in the cross section. It also plays an important role in the normalization issues, since the classical volume element is not Lorentz invariant.

2.2.5 Center of mass and laboratory systems

For the center of mass and the laboratory systems respectively, we have,

$$\begin{aligned} CM : s &= (E_1^* + E_2^*)^2 = (\text{total energy})^2 \\ L : s &= m_1^2 + m_2^2 + 2m_2 E_1^L \xrightarrow{E_1^L \gg m_1, m_2} 2m_2 E_1^L. \end{aligned}$$

As an example for the difference, we look at the two operating modes of the Tevatron at Fermilab (Figure 2.4). The energy of the beam particles is $E_{\text{beam}} = 980 \text{ GeV}$.

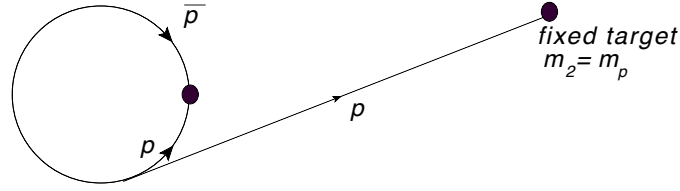
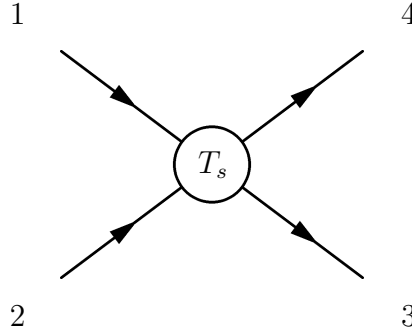


Figure 2.4: Sketch of the Tevatron accelerator at Fermilab.

Figure 2.5: s -channel.

Used in the $p\bar{p}$ -mode, the collision is head on and we are allowed to consider the problem in the center of mass frame and,

$$\sqrt{s_{p\bar{p}}}(\text{Collider}) = 1960 \text{ GeV},$$

which is ideal for discovering new phenomena with the highest possible energy.

If on the other hand, the pN -mode is chosen (N is a nucleus in the target), we need to consider the laboratory frame and we get

$$\sqrt{s_{pN}}(\text{Fixed target}) = 42.7 \text{ GeV} < m_W.$$

Although this mode is less energetic, it is then possible to create a secondary beam. With this method, the existence of ν_τ could be proven.

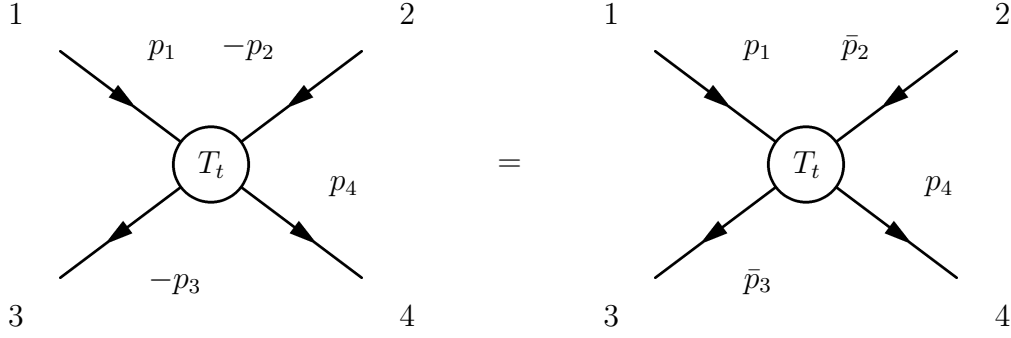
2.3 Crossing symmetry

The $2 \rightarrow 2$ scattering process has some underlying symmetries, which we shall explore now.

Example When we exchange p_3 and p_4 , s is not affected but t and u interchange their roles.

We take now a look at the reaction (Figure 2.5), $1 + 2 \rightarrow 3 + 4$, for which the 4-momentum is conserved :

$$p_1 + p_2 = p_3 + p_4.$$

Figure 2.6: *t*-channel.

It is called “*s*-channel” reaction, because the only positive Mandelstam variable is s . T_s describes the scattering dynamics of the process and will be treated later. It depends on the three Mandelstam variables and is predicted by theoretically (QED, QCD, EW, SUSY,...),

$$T_s(s, t, u) = T(s, t, u)|_{s>0, t\leq 0, u\leq 0}. \quad (2.14)$$

T can then be extended analytically to the whole range $s, t, u \in \mathbb{R}$. Depending on the region, it can then describe different **crossed reactions**.

For instance, suppose we exchange p_2 and p_3 , we then get naively (Figure 2.6),

$$p_1 + (-p_3) = (-p_2) + p_4.$$

We now make the interpretation

$$-p_n = p_{\bar{n}},$$

in which \bar{n} stands for the antiparticle of the particle n , leading to the expression (Figure 2.6),

$$p_1 + p_{\bar{3}} = p_{\bar{2}} + p_4.$$

Since 1 and $\bar{3}$ are the incoming particles, we speak of the “*t*-channel” process. One has

$$T_t(s, t, u) = T(s, t, u)|_{s\leq 0, t>0, u\leq 0}. \quad (2.15)$$

2.3.1 Interpretation of antiparticle-states

As stated above, we interpret particles with 4-momentum $-p$ to be antiparticles with 4-momentum p . The reason for that becomes clear when we look at the 4-current,

$$j^\mu \stackrel{ED}{=} \left(\frac{\rho}{\vec{j}} \right) \stackrel{QM}{=} \underbrace{\underbrace{-e}_{\text{electron charge}} \underbrace{i(\varphi^* \partial^\mu \varphi - \varphi \partial^\mu \varphi^*)}_{\text{probability density}}}_{\text{charge density}}. \quad (2.16)$$

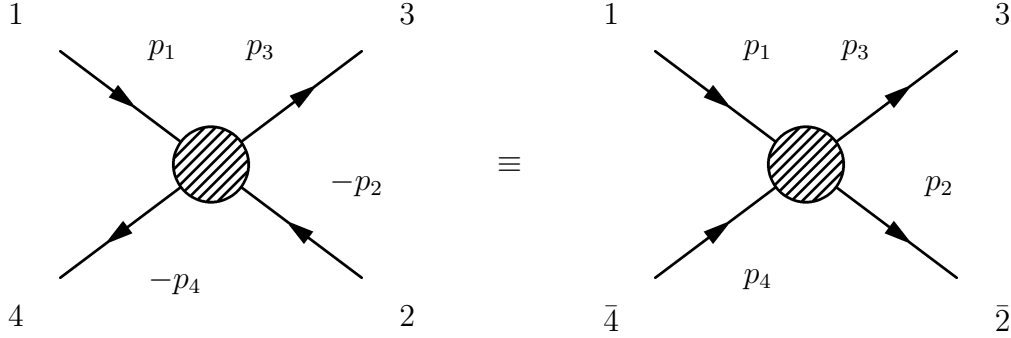


Figure 2.7: *Emission of a positron and absorption of an electron.* The emission of a positron with energy $+E$ is equivalent to the absorption of an electron with energy $-E$.

Inserting the wave function of the free electron,

$$\varphi = Ne^{-ip \cdot x}, \quad (2.17)$$

in the definition of the 4-current Eq. (2.16), one gets

$$\begin{aligned} e^- \text{ with 4-momentum } +p^\mu : j^\mu(e^-) &= -2e|N|^2 p^\mu = -2e|N|^2 \begin{pmatrix} +E \\ +\vec{p} \end{pmatrix}, \\ e^+ \text{ with 4-momentum } +p^\mu : j^\mu(e^+) &= +2e|N|^2 p^\mu = -2e|N|^2 (-p)^\mu, \\ e^- \text{ with 4-momentum } -p^\mu : j^\mu(e^-) &= -2e|N|^2 (-p)^\mu = -2e|N|^2 \begin{pmatrix} -E \\ -\vec{p} \end{pmatrix}, \end{aligned}$$

and hence the rule,

$$\boxed{j^\mu(e^+) = j^\mu(e^-) \text{ with the substitution } p^\mu \rightarrow -p^\mu}. \quad (2.18)$$

We stress here the fact that the *whole* 4-vector p^μ takes a minus sign, and not only the spatial part \vec{p} .

What we effectively used here is the fact that in the phase of Eq. (2.17) we can flip the signs of both p^μ and x^μ without changing the wave function. There is no place here for particle travelling backwards in time!

A particle with 4-momentum $-p^\mu$ is a *representation* for the corresponding *antiparticle* with 4-momentum p^μ . Alternatively, one can say that the emission of a positron with energy $+E$ corresponds to the absorption of an electron with energy $-E$. Figure 2.7 restates the last sentence as a Feynman diagram.

The three reactions (s -, t - and u -channels) are described by a single function $T(s, t, u)$ evaluated in the relevant kinematical region ($s \geq 0$ or $t \geq 0$ or $u \geq 0$).

In order to represent the situation, one usually refers to the **Dalitz plot**¹ (Figure 2.8).

¹or equilateral coordinates

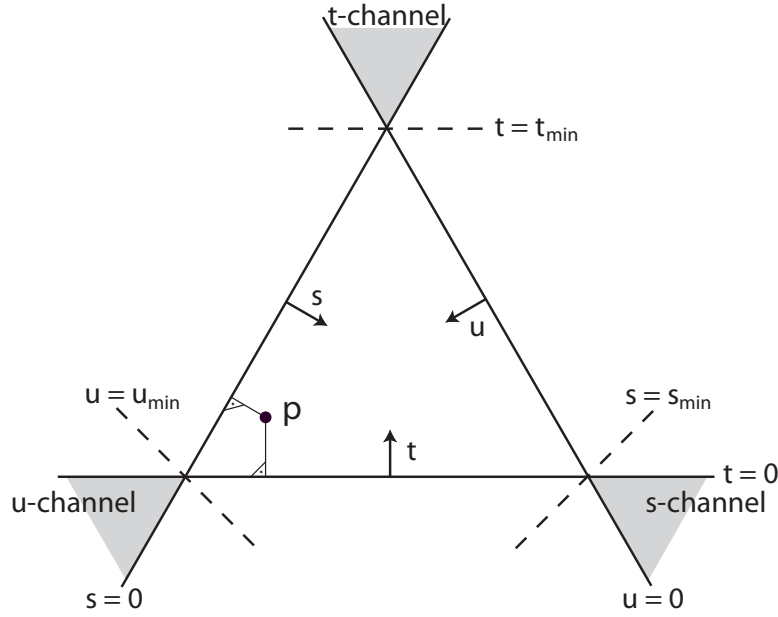
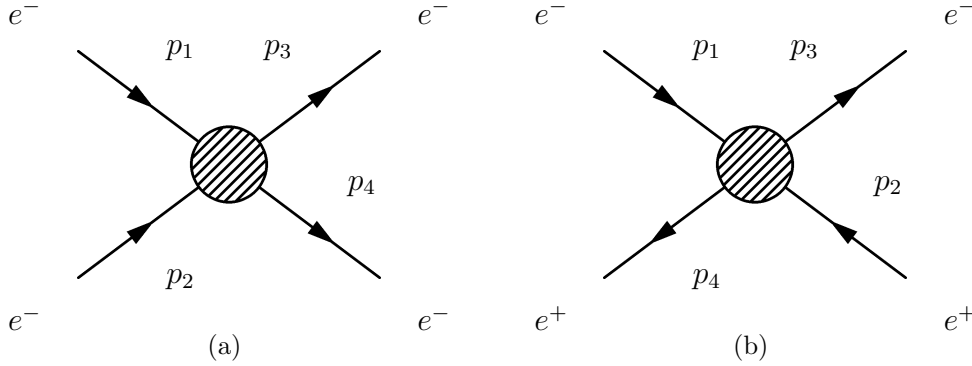
Figure 2.8: Dalitz plot of s -, t -, and u -channels.

Figure 2.9: Møller scattering (a) and Bhabha scattering (b).

Example We take a look at the **Møller scattering**,

$$e^-e^- \rightarrow e^-e^-,$$

which is the s -channel of the reaction depicted on Figure 2.9(a). By crossing, we get as u -channel reaction the **Bhabha scattering**,

$$e^+e^- \rightarrow e^+e^-,$$

which is the reaction depicted on Figure 2.9(b).

The considerations of this chapter enable us to derive *constraints* on the possible dynamics but are not sufficient to *decide* on the dynamics. To “get” the dynamics we must calculate and compare to experiments decay rates and scattering cross-sections.

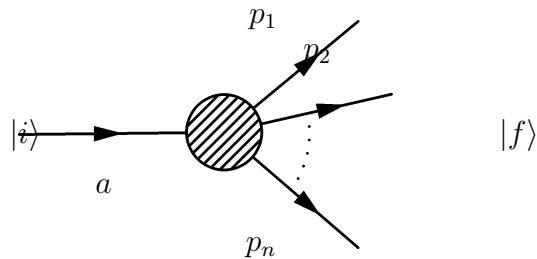
Chapter 3

Lorentz invariant scattering cross section and phase space

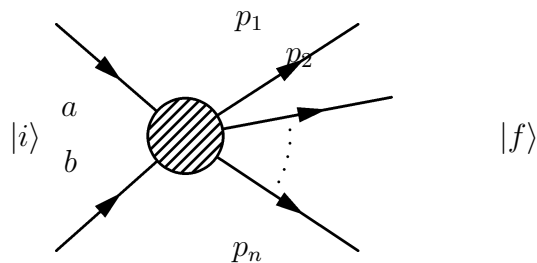
In particle physics, there are basically two observable quantities :

- Decay rates,
- Scattering cross-sections.

Decay:



Scattering:



3.1 \mathcal{S} -operator

In both cases $|i\rangle$ denotes the initial state, $|f\rangle$ denotes a multiparticle final state in a Fock space and the box represents the dynamics/interactions and is called the **\mathcal{S} -operator**. The last is predicted by the theory describing the interaction.

Example In QM I/II, $\mathcal{S} \propto H'(t) \propto V(t)$ in the first order perturbation theory of the Schrödinger equation.

\mathcal{S} is usually a very complicated object : it contains the information about *all* possible transitions $|i\rangle \rightarrow |f\rangle$. Another way to state this is to remark that \mathcal{S} contains all the dynamics of the process.

In experiments one does not get/need/want the full \mathcal{S} -operator. Instead, one restricts oneself to specific $|i\rangle$ and $|f\rangle$ e.g. by choosing the beam particles (muon beam,...) for the first and looking only at specific outcomes (3-jets events,...) for the latter.

One represents the \mathcal{S} -operator by looking at its matrix elements,

$$\underbrace{\sum_{f'} |f'\rangle \langle f'|}_{\mathbb{1}} \mathcal{S} |i\rangle = \sum_{f'} |f'\rangle \mathcal{S}_{f'i} \quad (3.1)$$

where

$$\mathcal{S}_{f'i} = \langle f' | \mathcal{S} | i \rangle \quad (3.2)$$

To isolate a specific outcome $|f\rangle$, one multiplies Eq. (3.1) by $\langle f|$, and gets,

$$\langle f | \sum_{f'} |f'\rangle \mathcal{S}_{f'i} = \sum_{f'} \underbrace{\langle f | f' \rangle}_{=\delta_{ff'}} \mathcal{S}_{f'i} = \mathcal{S}_{fi}. \quad (3.3)$$

Hence, the probability for the process $|i\rangle \rightarrow |f\rangle$ is,

$$P(|i\rangle \rightarrow |f\rangle) = |\mathcal{S}_{fi}|^2 \quad (3.4)$$

In general we can write,

$$\mathcal{S}_{fi} = \underbrace{\delta_{fi}}_{\text{no int.}} + \underbrace{i(2\pi)^4 \delta^{(4)}(p_f - p_i)}_{\text{4-momentum cons.}} \cdot \underbrace{\mathcal{T}_{fi}}_{\text{scat. amplitude}}, \quad (3.5)$$

or using a shorthand notation

$$\mathcal{S} = \mathbb{1} + i\mathcal{T},$$

in Feynman diagrams:



In the discussion of particle physics, a frequently used quantity is the transition probability per unit time,

$$w_{fi} = \frac{|\mathcal{S}_{fi}|^2}{T}. \quad (3.6)$$

3.2 Fermi's golden rule

From Eqs. (3.4) and (3.5), we see that we must address the issue of defining the value of a squared Dirac δ -function. To do this we use the rather pragmatic approach due to Fermi:

$$\begin{aligned} [2\pi\delta(p_f^0 - p_i^0)]^2 &= \int dt e^{i(p_f^0 - p_i^0)t} \cdot 2\pi\delta(p_f^0 - p_i^0) \\ &= T \cdot 2\pi\delta(p_f^0 - p_i^0) \end{aligned} \quad (3.7)$$

$$\begin{aligned} [(2\pi)^3\delta^{(3)}(\vec{p}_f - \vec{p}_i)]^2 &= \iiint d^3x e^{i(\vec{p}_f - \vec{p}_i) \cdot \vec{x}} \cdot (2\pi)^3\delta^{(3)}(\vec{p}_f - \vec{p}_i) \\ &= V \cdot (2\pi)^3\delta^{(3)}(\vec{p}_f - \vec{p}_i) \end{aligned} \quad (3.8)$$

$$\Rightarrow w_{fi} = \frac{|\mathcal{S}_{fi}|^2}{T} = V \cdot (2\pi)^4\delta^{(4)}(p_f - p_i) \cdot |\mathcal{T}_{fi}|^2 \quad (3.9)$$

To talk about the transition rate, we look at a Fock-space with a fixed number of particles. Experimentally, the angle and energy-momentum is only accessible up to a given accuracy. We therefore use differential cross-sections in angle $d\Omega$ and energy-momentum dp near Ω, p respectively.

Motivating example In a cubic box of volume $V = L^3$ with infinitely high potential wells, the authorized momentum-values are discretely distributed.

$$p = \frac{2\pi}{L}n \Rightarrow dn = \frac{L}{2\pi}dp \Rightarrow d^3n = \left(\frac{L}{2\pi}\right)^3 d^3p,$$

and hence,

$$dw_{fi} = V \cdot (2\pi)^4\delta^{(4)}(p_f - p_i) \cdot |\mathcal{T}_{fi}|^2 \cdot \prod_{f=1}^{n_f} \frac{V}{(2\pi)^3} d^3p_f, \quad (3.10)$$

where n_f stands for the number of particles in the final state.

In order to get rid of normalization factors, we define a new matrix element \mathcal{M}_{fi} by,

$$\mathcal{T}_{fi} \stackrel{!}{=} \left(\prod_{i=1}^{n_i} \frac{1}{\sqrt{2E_i V}} \right) \left(\prod_{f=1}^{n_f} \frac{1}{\sqrt{2E_f V}} \right) \mathcal{M}_{fi}. \quad (3.11)$$

At first sight, the apparation of the energies of both the initial and final states might be surprising. It is however needed in order to compensate the noninvariance of the volume, so that EV is a Lorentz invariant quantity. From now on we will always normalize our states to $2E$ (instead of 1 as is usually the case in nonrelativistic quantum mechanics).

We now substitute the definition (3.11) in Eq. (3.10) to get the fundamentally important expression,

$$dw_{fi} = \frac{V^{1-n_i}}{(2\pi)^{3n_f-4}} \delta^{(4)}(p_f - p_i) \cdot |\mathcal{M}_{fi}|^2 \cdot \prod_{i=1}^{n_i} \frac{1}{2E_i} \prod_{f=1}^{n_f} \frac{d^3 p_f}{2E_f}. \quad (3.12)$$

We can then specify this result for the two cases of interest, as we do in the following subsections.

3.2.1 Total decay rate

In the case where $n_i = 1$, we view w_{fi} as a **decay rate** for the reaction,

$$a \rightarrow 1 + 2 + \cdots + n_f.$$

We have

$$\Gamma_{a \rightarrow \{n_f\}} = w_{\{f\}a} \quad (\text{decay width}), \quad (3.13)$$

$$\tau_{a \rightarrow \{n_f\}} = \frac{1}{\Gamma_{a \rightarrow \{n_f\}}} \quad (\text{lifetime}), \quad (3.14)$$

where $\{n_f\}$ stands for the n_f -particle final state $1 + 2 + \cdots + n_f$.

The next step is the definition of the **total decay width**,

$$\Gamma_a = \sum_{\{n_f\}} \Gamma_{a \rightarrow \{n_f\}} = \frac{1}{2E_a} \frac{1}{(2\pi)^{3n_f-4}} \cdot \int \frac{d^3 p_1}{2E_1} \cdots \frac{d^3 p_{n_f}}{2E_{n_f}} \delta^{(4)}(p_f - p_i) |\mathcal{M}_{fi}|^2, \quad (3.15)$$

and the lifetime

$$\tau_a = \frac{1}{\Gamma_a} \quad (3.16)$$

We remark that since E_a is not a Lorentz invariant quantity, Γ_a also depends on the reference frame. The quantity stated under the name “lifetime” in particle physics listings is always the lifetime as measured in the rest frame of the particle and is hence always the shortest one.

Example Without relativistic time dilation, one would expect the μ leptons generated by cosmic rays in the high atmosphere and traveling almost at the speed of light to be able to travel $c\tau_\mu \approx 600$ m before decaying, making their detection on the earth surface almost impossible. When one takes time dilation into account, the distance becomes $c\tau_\mu \approx 10$ km, which is in accordance with the observed μ leptons number reaching the earth. This was actually for long the only available test of special relativity.

3.2.2 Scattering cross section

We now analyze the case of $n_i = 2$, i.e. the case of two particles interacting via the reaction,

$$a + b \rightarrow 1 + 2 + \cdots + n_f,$$

thus getting the **scattering cross section** $\sigma(a + b \rightarrow 1 + 2 + \cdots n_f)$ defined by,

$$\sigma = \frac{\# \text{ of transitions } a + b \rightarrow 1 + 2 + \cdots n_f \text{ per unit time}}{\# \text{ of incoming particles per unit surface and time}} = \frac{w_{fi}}{\text{incoming flux}}. \quad (3.17)$$

The denominator can also be stated as,

$$\text{incoming flux} = (\text{number density}) \cdot (\text{relative velocity}) = \frac{v_{ab}}{V}.$$

Using Eqs. (2.12) and (3.17) we then find,

$$\sigma_{i \rightarrow \{n_f\}} = \frac{1}{4F} \frac{1}{(2\pi)^{3n_f-4}} \int \left(\prod_{f=1}^{n_f} \frac{d^3 p_f}{2E_f} \right) \delta^{(4)} \left(\sum_{f=1}^{n_f} p_f - p_a - p_b \right) |\mathcal{M}_{fi}|^2, \quad (3.18)$$

in which we see once more the Lorentz invariant Møller flux factor,

$$\begin{aligned} F &= E_a E_b v_{ab} = \sqrt{(p_a \cdot p_b)^2 - m_a^2 m_b^2} \\ &= \frac{1}{2} \sqrt{(s - (m_a + m_b)^2)(s - (m_a - m_b)^2)} \xrightarrow{s \gg m_a^2, m_b^2} \frac{s}{2}. \end{aligned} \quad (3.19)$$

From the form of (3.18), we see that the total cross section is manifestly a Lorentz invariant quantity, since it only depends on Lorentz invariants.

3.2.3 Invariant phase space for n_f -particles

We have already seen that the scattering angle is related to the Mandelstam t -variable (Section 2.2.2).

In order to make the same statement for multiparticle final states, we define the n_f -particles phase space,

$$R_{n_f} = \int dR_{n_f} = \int \frac{d^3 p_1}{2E_1} \dots \frac{d^3 p_{n_f}}{2E_{n_f}} \delta^{(4)} \left(\sum_{f=1}^{n_f} p_f - \sum_{i=1}^{n_i} p_i \right). \quad (3.20)$$

We now prove that R_n is a Lorentz invariant quantity.

$$\frac{d^3 p_i}{2E_i} = \int_0^\infty dE_i \delta(p_i^2 - m_i^2) d^3 p_i \quad (3.21)$$

$$= \int_{-\infty}^\infty \underbrace{d^4 p_i}_{\text{L.I.}} \underbrace{\delta(p_i^2 - m_i^2)}_{\text{L.I.}} \underbrace{\theta(E_i)}_{E_i > 0 \text{ is L.I.}}. \quad (3.22)$$

3.2.4 Differential cross section

In order to get the differential cross section, we define,

$$t_{jk} := (p_j - p_k)^2 = f(\angle(\vec{p}_j, \vec{p}_k)), \quad (3.23)$$

and write

$$\frac{d\sigma}{dt_{jk}} = \frac{1}{4F} \frac{1}{(2\pi)^{3n_f-4}} \int dR_{n_f} |\mathcal{M}_{fi}|^2 \delta(t_{jk} - (p_j - p_k)^2). \quad (3.24)$$

Starting from this expression, one can deduce differential distributions in all other kinematical variables (energies, angles) by expressing those through the t_{jk} 's.

3.3 $2 \rightarrow 2$ scattering cross section

Next we turn our attention towards the very important special case of $2 \rightarrow 2$ scattering, $n_i = n_f = 2$:

$$a + b \rightarrow 1 + 2.$$

3.3.1 Phase space

First, we take a look at the phase space R_2 , we see that there are 6 integration variables and 4 constraints, i.e. we are left with only 2 free parameters. The goal of the next steps

will be to get rid of the δ -functions.

$$\begin{aligned}
R_2 &= \int \frac{d^3 \vec{p}_1}{2\tilde{E}_1} \frac{d^3 \vec{p}_2}{2\tilde{E}_2} \delta^{(4)}(p_1 + p_2 - p_a - p_b) \\
&\stackrel{(3.26)}{=} \int d^4 p_1 \delta(p_1^2 - m_1^2) d^4 p_2 \delta(p_2^2 - m_2^2) \theta(E_1) \theta(E_2) \delta^{(4)}(p_1 + p_2 - p_a - p_b) \\
&\stackrel{(3.27)}{=} \int d^4 p_1 \delta(p_1^2 - m_1^2) \delta((p_a + p_b - p_1)^2 - m_2^2) \theta(E_1) \theta(E_a + E_b - E_1) \\
&= \int_0^{E_a + E_b} dE_1 \int_0^\infty |\vec{p}_1|^2 d|\vec{p}_1| d\Omega \delta(E_1^2 - \vec{p}_1^2 - m_1^2) \delta((p_a + p_b - p_1)^2 - m_2^2) \\
&\stackrel{(3.28)}{=} \int_0^{E_a + E_b} dE_1 d\Omega \underbrace{\frac{\sqrt{E_1^2 - m_1^2}}{2}}_{\int_0^\infty |\vec{p}_1|^2 \delta(E_1^2 - \vec{p}_1^2 - m_1^2) d|\vec{p}_1|} \delta(s - 2(p_a + p_b) \cdot p_1 + m_1^2 - m_2^2) \quad (3.25)
\end{aligned}$$

where we have used,

$$\frac{1}{2\tilde{E}_1} = \int dE_1 \delta(E_1^2 - \vec{p}_1^2 - m_1^2) \theta(E_1), \quad \tilde{E}_1 = \sqrt{m_1^2 + \vec{p}_1^2} \quad (3.26)$$

$$1 = \int d^4 p_2 \delta^{(4)}(p_1 + p_2 - p_a - p_b), \quad (3.27)$$

$$\delta(E_1^2 - \vec{p}_1^2 - m_1^2) = \frac{1}{2|\vec{p}_1|} \left(\delta\left(|\vec{p}_1| - \sqrt{E_1^2 - m_1^2}\right) + \underbrace{\delta\left(|\vec{p}_1| + \sqrt{E_1^2 - m_1^2}\right)}_{=0, \text{ since } |\vec{p}_1| \geq 0} \right). \quad (3.28)$$

We did not make any assumption about the reference frame up to this point. We now specify our calculation for the center of mass frame,

$$\vec{p}_a + \vec{p}_b = 0 \Rightarrow E_a + E_b = \sqrt{s},$$

bringing Eq. (3.25) into,

$$\begin{aligned}
R_2 &= \int_0^{\sqrt{s}} dE_1^* d\Omega^* \frac{|\vec{p}_1^*|}{2} \delta(s - 2\sqrt{s}E_1^* + m_1^2 - m_2^2) \\
&= \int d\Omega^* \frac{|\vec{p}_1^*|}{4\sqrt{s}} \\
&\Rightarrow dR_2 = \frac{1}{8s} \sqrt{\lambda(s, m_1^2, m_2^2)} d\Omega^*. \quad (3.29)
\end{aligned}$$

For the last steps we used Eq. (2.10) and the fact that,

$$\delta(s - 2\sqrt{s}E_1^* + m_1^2 - m_2^2) = \frac{1}{2\sqrt{s}} \delta\left(E_1^* - \frac{1}{2\sqrt{s}}(s + m_1^2 - m_2^2)\right).$$

A last step of the calculation can be made if the integrand has *no* angular dependency: since we are in the center of mass frame, we then have manifestly a 4π -symmetry and the scattering angle can take any value, the only restriction being that the two scattered particles are flying back-to-back in the center of mass frame. Therefore R_2 is then simply the integrand multiplied with the volume of the unit sphere, i.e.

$$R_2 = \int dR_2 = \frac{\pi}{2s} \sqrt{\lambda(s, m_1^2, m_2^2)}. \quad (3.30)$$

This simplification always applies for a $1 \rightarrow 2$ decay, but usually not for a $2 \rightarrow 2$ scattering reaction, where the incoming beam direction breaks the 4π -symmetry.

3.3.2 Differential cross section

Using Eq. (2.11) and (3.24) for $n_f = 2$, we get,

$$\frac{d\sigma}{d\Omega^*} = \frac{d\sigma}{dt} \frac{dt}{d\Omega^*} = \frac{|\vec{p}_1^*|}{64\pi^2 F \sqrt{s}} |\mathcal{M}_{fi}|^2, \quad (3.31)$$

resulting in the **differential cross section**,

$$\boxed{\frac{d\sigma}{d\Omega^*} = \frac{1}{64\pi^2 s} \frac{|\vec{p}_1^*|}{|\vec{p}_a^*|} |\mathcal{M}_{fi}|^2}, \quad (3.32)$$

since from Eq. (2.12) $F = \sqrt{s} |\vec{p}_a^*|$.

For the special case of elastic scattering $|\vec{p}_1^*| = |\vec{p}_a^*|$, we get,

$$\boxed{\frac{d\sigma^{el.}}{d\Omega^*} = \frac{1}{64\pi^2 s} |\mathcal{M}_{fi}|^2}. \quad (3.33)$$

Finally, we write here the invariant differential cross section of $a + b \rightarrow 1 + 2$ in terms of invariants for future references,

$$\boxed{\frac{d\sigma}{dt} = \frac{1}{16\pi \lambda(s, m_a^2, m_b^2)} |\mathcal{M}_{fi}|^2} \xrightarrow{s \gg m_1^2, m_2^2} \frac{1}{16\pi s^2} |\mathcal{M}_{fi}|^2. \quad (3.34)$$

3.4 Unitarity of the \mathcal{S} -operator

We can compute the transition probability from the matrix elements for the transition $|i\rangle \rightarrow |f\rangle$,

$$|\mathcal{S}_{fi}|^2 = |\langle f | \mathcal{S} | i \rangle|^2, \quad (3.35)$$

$$\sum_f |\mathcal{S}_{fi}|^2 = 1, \quad (3.36)$$

where \sum_f stands for

$$\sum_{\text{spins, particle types, quantum numbers}} \int \prod_f \left(\frac{V}{(2\pi)^3} d^3 p_f \right).$$

Developing and using the completeness relation,

$$\sum_f |f\rangle \langle f| = \mathbb{1},$$

we obtain

$$\begin{aligned} 1 &= \sum_f \langle i | \mathcal{S}^\dagger | f \rangle \langle f | \mathcal{S} | i \rangle = \langle i | \mathcal{S}^\dagger \mathcal{S} | i \rangle \quad \forall |i\rangle \\ &\Rightarrow \boxed{\mathcal{S}^\dagger \mathcal{S} = \mathbb{1}}, \end{aligned} \tag{3.37}$$

in other words \mathcal{S} is a unitary operator.

This important fact has profound implications. We state here two of them.

First, for two orthogonal states $|i\rangle$ and $|j\rangle$, we have,

$$\langle j | \mathcal{S}^\dagger \mathcal{S} | i \rangle = \langle j | i \rangle = \delta_{ij}.$$

The other implication concerns the expression introduced in Eq. (3.5),

$$\mathcal{S}_{fi} = \delta_{fi} + i(2\pi)^4 \delta^{(4)}(p_f - p_i) \cdot \mathcal{T}_{fi}. \tag{3.38}$$

For a free theory, $\mathcal{T}_{fi} = 0$ and hence $\mathcal{S}_{fi} = \delta_{fi}$. On the other hand, for an interacting theory $\text{Im } \mathcal{S}_{fi} \neq 0$.

An obvious comparison of the real and imaginary parts of \mathcal{S}_{fi} , tells us that,

$$\begin{aligned} \text{Re } \mathcal{T}_{fi} &\leadsto \text{Im } \mathcal{S}_{fi} && \text{(virtual contribution),} \\ \text{Im } \mathcal{T}_{fi} &\leadsto \text{Re } \mathcal{S}_{fi} && \text{(absorptive contribution).} \end{aligned}$$

Taking a closer look at the absorptive contribution, we get,

$$2i \text{Im } \mathcal{T}_{fi} = \mathcal{T}_{fi} - \mathcal{T}_{fi}^* = i(2\pi)^4 \delta^{(4)}(p_f - p_i) \sum_n \mathcal{T}_{fn} \mathcal{T}_{in}^*,$$

where n denotes an intermediate state.

The special case of elastic forward scattering ($|f\rangle = |i\rangle, \Theta^* = 0$) yields the surprising **optical theorem**,

$$\boxed{\text{Im } \mathcal{M}_{ii} = \sqrt{\lambda(s, m_a^2, m_b^2)} \sigma_{tot}}, \tag{3.39}$$

relating a very specific element of \mathcal{S}_{fi} with the total cross section for the transition $|i\rangle \rightarrow |f\rangle$, which is a measure for the probability for this transition to occur at all.

We can rewrite it symbolically with Feynman diagrams:

$$\text{Im} \left[\begin{array}{c} a \\ \swarrow \searrow \\ \bullet \\ \nearrow \nwarrow \\ b \end{array} \right]_{\Theta=0} = \sum_f \left[\begin{array}{c} a \\ \swarrow \searrow \nearrow \nwarrow \rightarrow \rightarrow \rightarrow \rightarrow \\ \bullet \\ \nearrow \nwarrow \rightarrow \rightarrow \rightarrow \rightarrow \\ b \end{array} \right]^2_f$$

The computation of the matrix elements \mathcal{M}_{fi} will be treated from Chapter 5 on.

Chapter 4

Accelerators and collider experiments

This chapter gives an introduction to particle accelerators and detectors as well as to data analysis tools relevant in this context. This involves the definition and application of concepts based on the kinematics developed in Chap. 2. Basic principles of particle accelerators are discussed as well as fixed target and beam collider experiments. The concepts of center of mass energy, luminosity, cross section, and event rates are introduced, followed by the basic building blocks of particle physics experiments. In order to be able to analyze the data gathered with collider experiments, we will introduce the concepts of rapidity, transverse and missing momentum (applications of momentum conservation) and invariant mass.

Modern techniques in experimental particle physics can be classified according to their use of accelerators. Non-accelerator-based experiments (e. g. the setup in Fig. 4.1) include measurements based on cosmic rays, solar and atmospheric neutrinos, and searches for dark matter. The latter, together with dark energy, could account for 95% of the universe. In the case of cosmic rays we can study high energy particles without having to accelerate them. Advances in neutrino physics have been achieved using large targets of (heavy) water surrounded by photomultipliers (e. g. Super-Kamiokande: neutrino oscillations). Accelerator-based experiments, on the other hand, include fixed target experiments and particle colliders, which are the topic of this chapter. As an example for particle colliders, the Large Hadron Collider (LHC) is shown in Fig. 4.2 with its four collision sites.

4.1 Particle accelerators: motivations

Particle accelerators are a fundamental tool for research in physics. Their importance and fields of use can be understood when one considers their main parameter, the beam energy. If we intend to use accelerators as large “microscopes”, the spatial resolution increases with beam energy. According to the de Broglie equation, the relation between



Figure 4.1: *Example of a non-accelerator-based experiment.* Heavy water targets can be protected from radiation background by installing them in deep-underground facilities. The target is surrounded by photomultipliers.



Figure 4.2: *The Large Hadron Collider at CERN with its four experiments CMS, ATLAS, LHCb, and ALICE.*

momentum $|\vec{p}|$ and wavelength λ of a wave packet is given by

$$\lambda = \frac{h}{|\vec{p}|}. \quad (4.1)$$

Therefore, larger momenta correspond to shorter wavelengths and access to smaller structures. In addition, it is possible to use accelerators to produce new particles. As we have seen in Chap. 2, this requires the more energy the heavier the particles are. Because beams are circulated for several hours accelerators are based on beams of stable particles and antiparticles, such as e^+, e^- or p, \bar{p} or e, p (Deutsches Elektronen-Synchrotron, DESY). There are two possibilities as to what to collide a beam of accelerated particles with:

1. collision with another beam;
2. collision with a fixed target.

In both cases one can study the resulting interactions with particle detectors. By using a fixed target, one can furthermore produce a beam of secondary particles that may be stable, unstable, charged or neutral, solving the impossibility of accelerating unstable or neutral particles directly.

In the search for new sub-structures, Eq. (4.1) is the fundamental relation. It tells us that the resolution increases as we go to higher energies. For instance the resolution of 1 GeV/c and 10^3 GeV/c are:

$$\begin{aligned} |\vec{p}| = 1 \frac{\text{GeV}}{c} &\rightarrow \lambda = 1.24 \cdot 10^{-15} \text{ m} \simeq \text{size of a proton} \\ |\vec{p}| = 10^3 \frac{\text{GeV}}{c} &\rightarrow \lambda = 1.24 \cdot 10^{-18} \text{ m} \simeq \text{size of proton substructures, e.g. quarks.} \end{aligned}$$

Consider now the second scenario mentioned above, namely the search for new particles with high mass. For a collision of a particle with mass m_1 and momentum \vec{p}_1 with another particle m_2, \vec{p}_2 the energy in the laboratory frame is given by¹

$$\begin{aligned} E_L &= \sqrt{\vec{p}_1^2 c^2 + m_1^2 c^4} + \sqrt{\vec{p}_2^2 c^2 + m_2^2 c^4} \\ |\vec{p}_L| &= |\vec{p}_1 + \vec{p}_2| \\ E_L^2 - \vec{p}_L^2 c^2 &= E^{*2} - \underbrace{\vec{p}^{*2}}_{=0} c^2 \\ \Rightarrow E^* &= \sqrt{E_L^2 - \vec{p}_L^2 c^2}. \end{aligned}$$

The production energy threshold for particles produced at rest is therefore:

$$E^* = \sum_i m_i c^2, \text{ while } E_{\text{kin}} = 0$$

¹Recall that we asterisk quantities given in the center of mass frame. See Sect. 2.2 for labeling conventions.

where m_i is the mass of the i -th particle of the final state. We can conclude that, since the center of mass energy E^* grows with the energy in the laboratory frame E_L , we can produce higher masses if we have higher energies at our disposal. This allows to produce particles not contained in ordinary matter.

Example: As an example, consider inelastic proton collisions. Imagine we want to produce three protons and one antiproton by colliding a proton beam against a proton target (e.g. a hydrogen target). The corresponding reaction is

$$pp \rightarrow \bar{p}ppp$$

where conservation of the baryon number requires the presence of one antiproton in the final state. What is the minimum momentum of the proton beam for the reaction to take place? Since particles and antiparticles have the same mass and the target is at rest in the laboratory frame, we find

$$\begin{aligned} m_1 = m_2 = m &= 0.9383 \frac{\text{GeV}}{c^2} \\ |\vec{p}_L| &= |\vec{p}_1|, \quad |\vec{p}_2| = 0 \\ \text{at threshold: } E^* &= 4mc^2 = 3.7532 \text{ GeV} \\ \Rightarrow |\vec{p}_1| &= 6.5 \frac{\text{GeV}}{c}. \end{aligned}$$

4.1.1 Center of mass energy

As we have seen, the center of mass energy E^* is the energy available in collision experiments. We therefore want to compare fixed target and colliding beam experiments concerning their available energy. In the case of beam-target collision, E^* is determined by (with m the mass of both the beam and target particles)

$$\begin{aligned} E_L &= \sqrt{\vec{p}_L^2 c^2 + m^2 c^4} + mc^2 \\ E^{*2} &= M^2 c^4 = E_L^2 - \vec{p}_L^2 c^2 = 2m^2 c^4 + 2mc^2 \sqrt{\vec{p}_L^2 c^2 + m^2 c^4}. \end{aligned}$$

Setting $|\vec{p}_L| = p_{\text{inc}}$ and neglecting the mass of the target we get:

$$E^* = \sqrt{2mc^2 p_{\text{inc}} c} = 1.37 \sqrt{\text{GeV}} \sqrt{p_{\text{inc}} c} = 1.37 \sqrt{\text{GeV}} \sqrt{E_{\text{inc}}}.$$

This means that, in the case of a fixed target experiment, the center of mass energy grows only with square root of E_{inc} (see Fig. 4.3).

However, in beam-beam collisions, we find $E^* = E_{\text{CM}} = 2E_{\text{inc}}$. Therefore, it is much more efficient to use two beams in opposite directions, as the following examples demonstrate

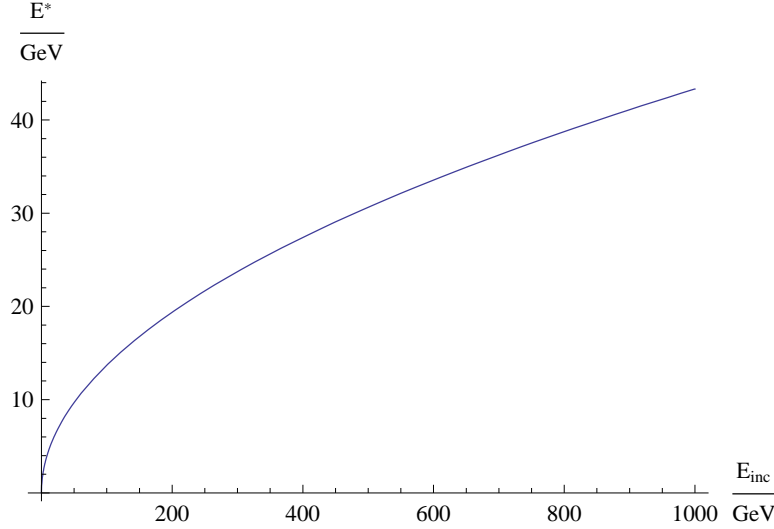


Figure 4.3: *Center of mass energy of the colliding beam for a fixed target experiment.* The energy increases with the square root of the beam energy.

(target is for instance hydrogen):

$$\begin{aligned} \overrightarrow{22 \text{ GeV}} + \overleftarrow{22 \text{ GeV}} &\text{ has the same } E_{\text{CM}} \text{ as } \overrightarrow{1 \text{ TeV}} + m_{\text{target}}; \\ \overrightarrow{1 \text{ TeV}} + \overleftarrow{1 \text{ TeV}} &\text{ has the same } E_{\text{CM}} \text{ as } \overrightarrow{10^3 \text{ TeV}} + m_{\text{target}}. \end{aligned}$$

The concept of colliding beams naturally leads to large circular accelerators. But for them to work properly some technical problems have to be solved. For instance, the particle density in a beam is much lower than in a solid or liquid target (see also the concept of luminosity in Sect. 4.3.2). Therefore, one tries to cross the beams many times and maximize the beam intensities (number of particle bunches per beam). As mentioned before, this approach only works with stable particles or antiparticles. Furthermore, in order to avoid beam-gas interactions (unintended fixed target collisions), a high vacuum is needed in the beam-pipe (about 10^{-9} Pa). Two beam lines are needed in the particle-particle case, whereas in the particle-antiparticle case one beam line is sufficient, with the two beams circulating in opposite directions. Finally, electronics represent another crucial part of the setup. At a rate of about $40 \cdot 10^6$ collisions per second a fast electronic system is necessary to decide what collisions to select.

4.2 Acceleration methods

Bearing in mind that an electric field \vec{E} produces an accelerating force \vec{F} on a charge q ,

$$\vec{F} = q\vec{E},$$

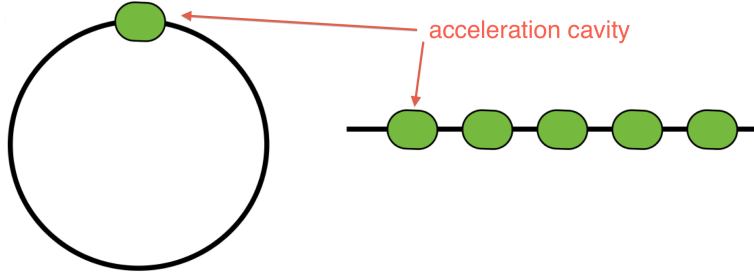


Figure 4.4: *Sketch of a circular (left) and linear (right) accelerator.* A circular machine needs to have one acceleration cavity, while a linear machine needs several cavities in series in order to reach high energies.

one could use an electrostatic field to accelerate charged particles. Since the maximal available potential difference (cf. Van de Graaff accelerator) is about 10 MV, one can accelerate particles up to 10 MeV. However, the fact that the electrostatic field is conservative ($\oint \vec{E} \cdot d\vec{l} = 0$) implies that the energy transfer only depends on the potential difference and not on the path. Therefore, circulating the beam in an electrostatic field does not lead to an increasing acceleration. The problem is solved by using several times a small but variable potential difference. This can be done using circular or linear machines. In a circular accelerator, one can use several times the same acceleration cavity (see Fig. 4.4, left), whereas in a linear accelerator several cavities in series are needed to reach high energies (see Fig. 4.4, right). In the case of a circular accelerator, the particles will receive a certain amount of energy at every turn, provided they are in phase with the accelerating potential. Because of the inertia principle, one further needs a magnetic field providing the centripetal force to keep particles on a circular path. An outline of historical developments in particle accelerators is given in Tab. 4.1. In the following sections, we will take a more detailed look at two types of accelerators: cyclotrons and synchrotrons.

4.2.1 Cyclotron

The sketch of a cyclotron is shown in Fig. 4.5. Particles are injected in the center and accelerated with a variable potential while a magnetic field \vec{B} keeps them on spiral trajectories. Finally, particles are extracted and used in experiments. Cyclotrons are rather compact, as one can also see in Fig. 4.6. The maximal energy is of order 20 MeV for cyclotrons and up to 600 MeV for synchro-cyclotrons. For a particle moving in the cyclotron the centripetal and Lorentz forces are balanced:

$$m \frac{v^2}{\rho} = qvB \quad (4.2)$$

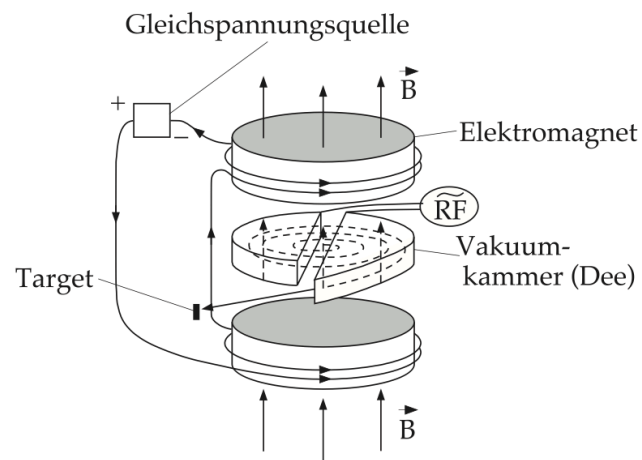


Figure 4.5: *Sketch of a cyclotron accelerator.* Source: [8, p. 108].

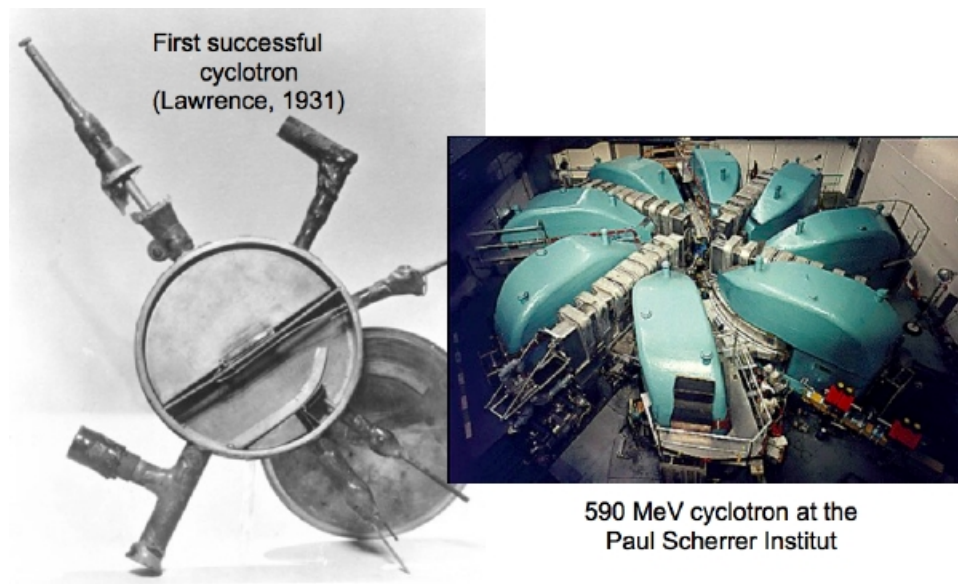


Figure 4.6: *A first prototype of a cyclotron (by Lawrence) and the 590 MeV isochronous cyclotron at PSI.*

| Year | Accelerator | Beam energy |
|-----------|--|-----------------|
| 1921 | “Kaskadengenerator” (Greinacher) | |
| 1924–1928 | Concept and first prototype of linear accelerator (Ising / Wideröe) | |
| 1932 | First nuclear reaction induced by cascade particle accelerator, $p^7\text{Li} \rightarrow 2\alpha$ (Cockroft / Walton) | 400 keV protons |
| 1930 | First Van de Graaff accelerator | 1.5 MV |
| 1930–1932 | First cyclotron (concept: Lawrence) | 1.5 MeV |
| | Upgraded cyclotrons (Synchrocyclotron) | 300 – 700 MeV |
| 1953 | First synchrotron at Brookhaven lab—Cosmotron (concept: Oliphant / Veksler / McMillan) | 3 GeV |
| 1958 | Proton Synchrotron (CERN) | 28 GeV |
| 1983 | Tevatron (Fermilab) | 1000 GeV |
| 1990 | HERA (DESY): first and only electron-proton collider | |
| 2008 | Large Hadron Collider (CERN) | up to 7000 GeV |

Table 4.1: Evolution timeline in particle accelerators (q. v. [7, pp. 9]).

where v is the velocity of the particle, m the mass, q the charge, and ρ the trajectory radius. This yields for the cyclotron frequency ω

$$v = \omega \rho \quad (4.3)$$

$$\Rightarrow \omega = \frac{qB}{m}. \quad (4.4)$$

The alternating high voltage used to accelerate the particles (see Fig. 4.5) matches the cyclotron frequency, such that the particles are accelerated when passing the capacitor between the two half disks, also called as “D’s”. We can also conclude that the radius of the particle trajectory grows linearly with its momentum. For relativistic particles, Eq. (4.4) has to be modified:

$$\omega' = \frac{qB}{\gamma m}$$

where $\gamma = 1/\sqrt{1 - v^2/c^2}$. This modification has, for example, the following effect on the revolution frequency:

$$\begin{aligned} \frac{v}{c} = 50\% &\Rightarrow \gamma = 1.155 \Rightarrow \omega' = 0.86\omega \\ \frac{v}{c} = 99\% &\Rightarrow \gamma = 7.1 \Rightarrow \omega' = 0.14\omega. \end{aligned}$$

Isochronous cyclotrons compensate for the variation in frequency by increasing the magnetic field (rather than changing the frequency) with the radius.

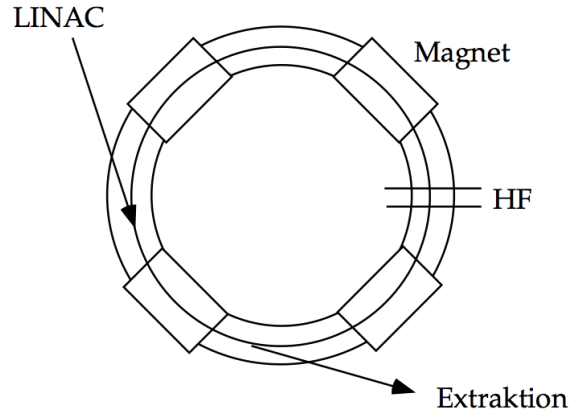


Figure 4.7: *Sketch of a synchrotron accelerator.* High frequency cavities are used to accelerate the particles. Dipole magnets keep them on circular trajectories. Linear accelerators are used for pre-acceleration and injection. Source: [8, p. 110].

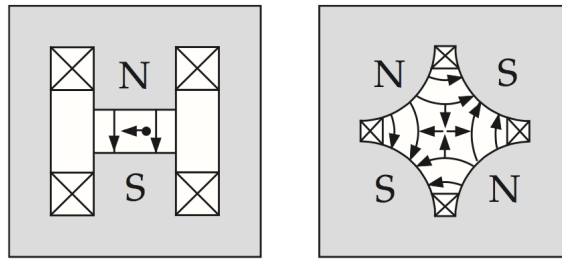


Figure 4.8: *Magnets used in synchrotrons.* Dipole magnets (left) keep the beam on a circular path, while quadrupole magnets (right) focus particles in the vertical or horizontal plane. Source: [8, p. 111].

4.2.2 Synchrotron

In the case of the synchrotron, the trajectory radius is kept constant. This is achieved by dipole magnets (see Fig. 4.8), while high frequency cavities are used to accelerate the particles (see Fig. 4.7). The problem of reducing the cross section to increase the particle density is solved by using quadrupole magnets (see Fig. 4.8). Their focussing and defocussing properties can be combined in a way as to lead to an overall focussing of the beam. Starting from Eq. (4.2), we have for the radius ρ

$$\rho = \frac{p}{qB}.$$

This yields, setting $q = ze$ (with e the unit charge),

$$cp[\text{eV}] = czB\rho = 3 \cdot 10^8 \frac{\text{m}}{\text{s}} zB[\text{T}]\rho[\text{m}] \quad (4.5)$$

$$\Rightarrow p \left[\frac{\text{GeV}}{c} \right] = 0.3zB[\text{T}]\rho[\text{m}] \quad (4.6)$$

for the momentum.

Example: As an example, we consider the LHC at CERN: With a circumference of 27 km, yielding a radius of 4.3 km, an average magnetic field of 5.4 T is needed to keep protons with momentum 7 TeV/c on circular trajectories. Magnetic fields of this magnitude require very large currents and therefore superconductors which only work at low temperatures (about 2° K). The superconducting cables are therefore cooled with liquid helium.

Particle beams are injected into the vacuum pipe at relatively low energy with the magnetic field at its minimal value. Because the particles traverse acceleration cavities at every turn, the momentum grows accordingly. Since the beam has to be kept on the same radius, the magnetic field also has to grow. On the other hand, rising velocity means changing revolution frequency and the frequency of the potential differences must be kept in phase with the particles. When maximum momentum is reached the accelerating cavities are switched off and the beam can be extracted to be used in experimental areas (see Fig. 4.9) or to be injected in larger synchrotrons (see Fig. 4.10). If the beam remains in the synchrotron ring it can be steered to cross other beams in collision points.

Another possible application of synchrotrons is to use the synchrotron radiation emitted by circulating beams. For this purpose one uses electrons, since they produce more synchrotron radiation than hadrons because of their smaller mass. The highly energetic photons emitted are used for measurements in solid state physics and protein research. An example is the Swiss Light Source at the Paul Scherrer Institute (Villigen, Switzerland), where electrons are pre-accelerated by a 100 MeV linear accelerator, injected into a synchrotron of 288 m circumference, kept on track by 36 dipole magnets with 1.4 T field, focussed by 177 quadrupole magnets, for a total beam energy of 2.8 GeV.

4.3 Particle physics experiments

In the following sections we introduce or recapitulate some basic concepts in particle physics experiments.

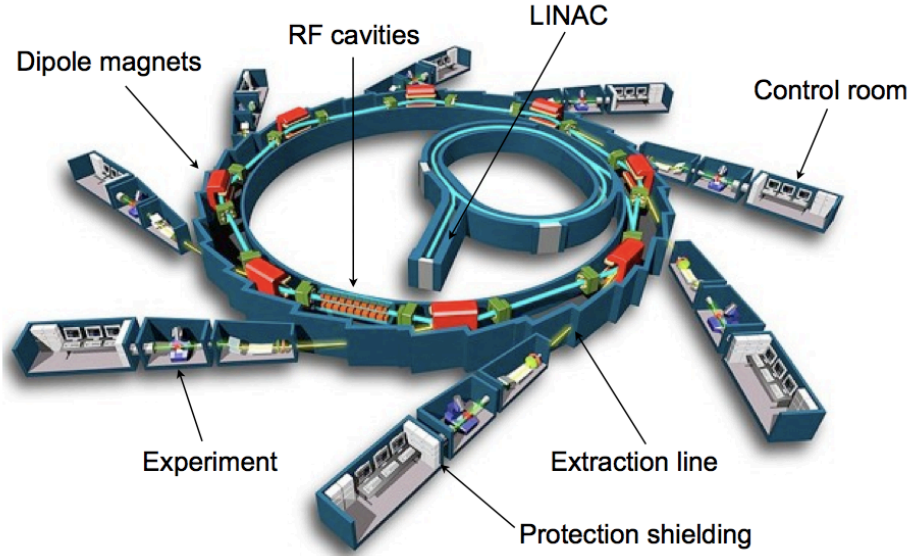


Figure 4.9: *Schematic view of a synchrotron.* Beams can be extracted and used in several experimental areas.

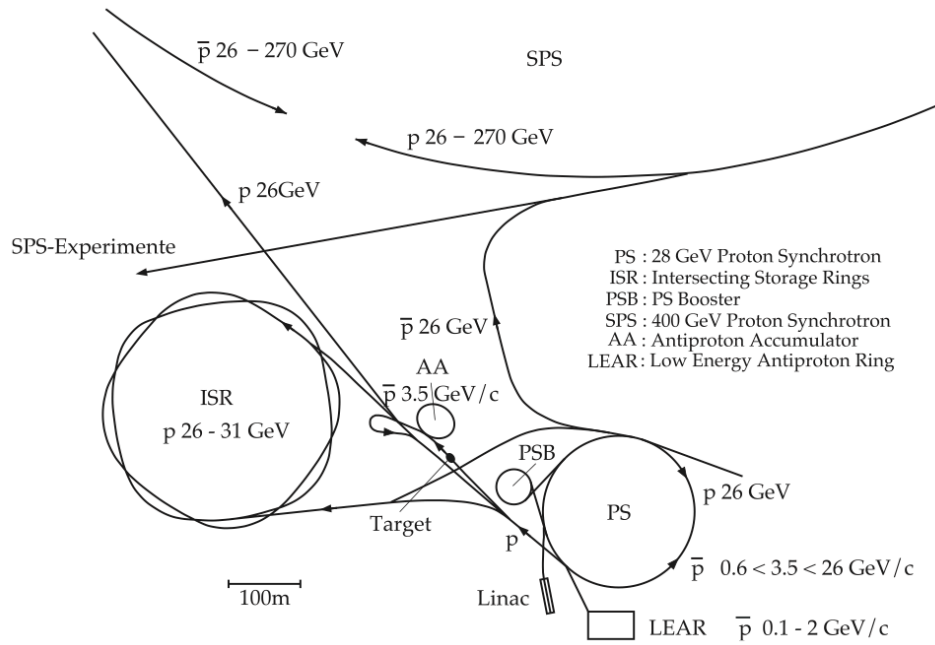


Figure 4.10: *Accelerator system at CERN.* Beams accelerated in linear machines and small synchrotrons are injected into larger synchrotron rings. Source: [8, p. 113].

4.3.1 Cross section

For a detailed introduction to the concept of cross section see Sect. 3.2.2. We recall that cross sections have dimension of area (cm^2). The common unit is barn, defined as

$$1 \text{ b} = 10^{-24} \text{ cm}^2.$$

Until now, we have used the total cross section σ . This is a sum of contributions by many final states:

$$\sigma_{\text{tot}} = \sum_i \sigma_i.$$

Example: Results of total cross section measurements for pp and $p\bar{p}$ collisions are shown in Fig. 4.11.

4.3.2 Luminosity

While cross sections characterize the scattering process, the luminosity characterizes an accelerators performance. With cross section σ and number of events per second R , the luminosity L is given by

$$R = L\sigma. \quad (4.7)$$

Because the dimension of the cross section is a surface, the units of luminosity are $\text{cm}^{-2}\text{s}^{-1}$.

The meaning of luminosity can be illustrated considering e.g. an e^+e^- accelerator with N particles per beam, revolving f times per second. We assume a Gaussian shaped beam with dimensions s_x and s_y , which yields a transverse size of $4\pi s_x s_y$. In one turn, one electron crosses $N/(4\pi s_x s_y)$ positrons. Because there are N particles revolving in each beam f times per second the number of collisions per second is

$$L = \frac{fN^2}{4\pi s_x s_y}. \quad (4.8)$$

From Eq. 4.7, the number of events per second is

$$R = \frac{\sigma f N^2}{4\pi s_x s_y}. \quad (4.9)$$

From Eq.(4.8) we notice that the luminosity can be increased by reducing the cross section of the beam, by increasing the number of particles in the beam or by increasing the revolution frequency.

In general, the luminosity of an accelerator gradually increases over time, while accelerator physicists learn how to operate the machine and to squeeze the beam size at the

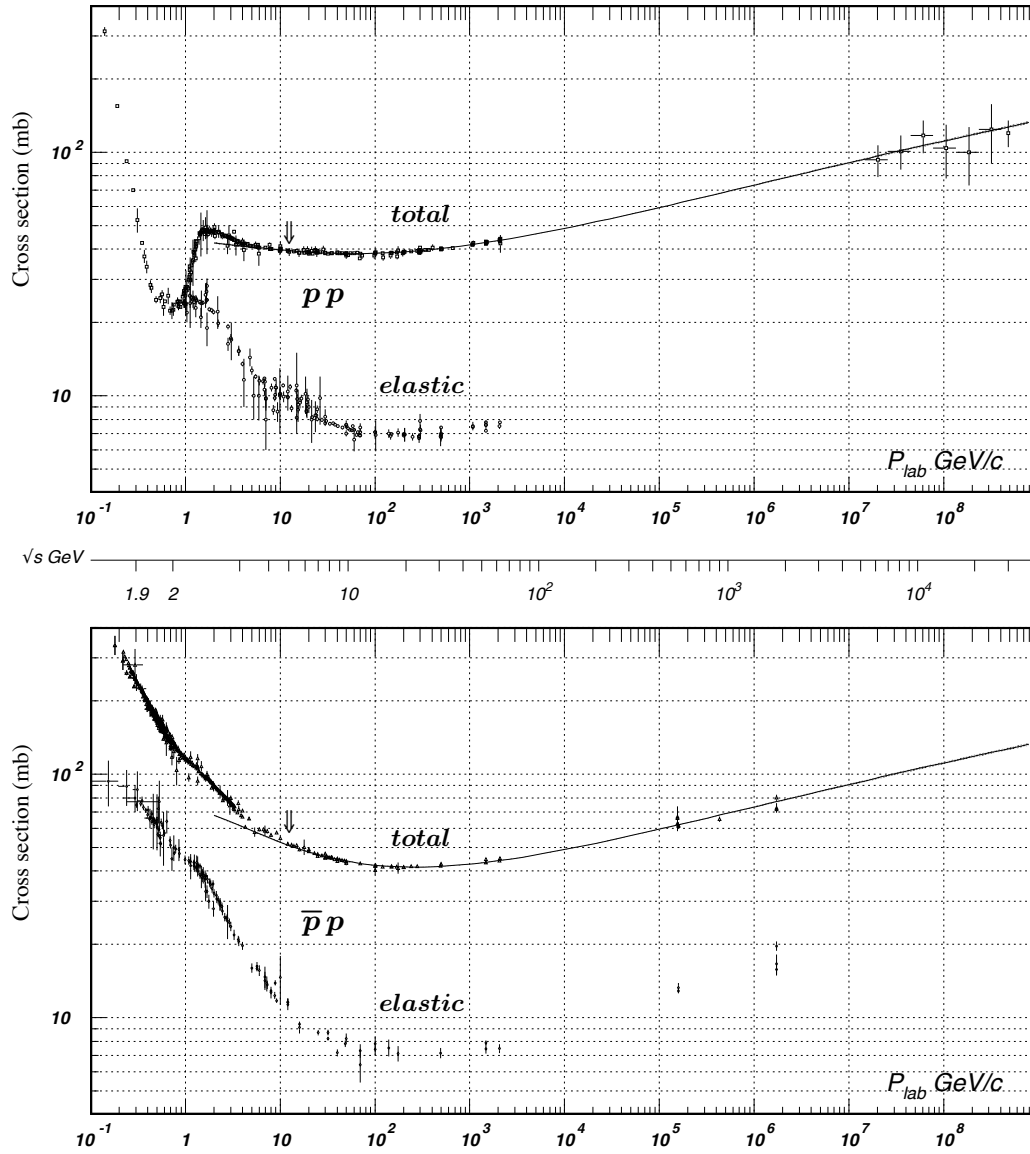


Figure 4.11: Total and elastic cross sections for pp and $\bar{p}p$ collisions as a function of laboratory beam momentum and total center of mass energy. Source: [9].

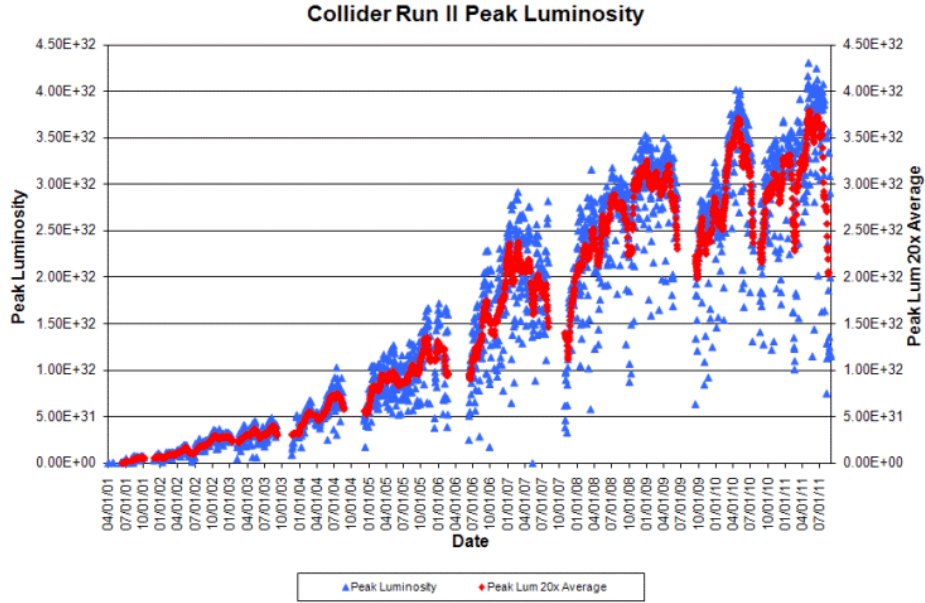


Figure 4.12: *Instantaneous luminosity at Tevatron as a function of time (2001 – 2009).* Note that the target luminosity for LHC is $10^{34} \text{ cm}^{-2}\text{s}^{-1}$.

intersection point. For example, the evolution of instantaneous luminosity over time at Tevatron is shown in Fig. 4.12.

The integral of the delivered luminosity over time is called integrated luminosity and is a measure of the collected data size. The integrated luminosity delivered by Tevatron until early 2009 is shown in Fig. 4.13.

Example: Consider an accelerator ring with the following properties:

- Ring length = 100 m;
- Revolution frequency = $3 \cdot 10^6 \text{ Hz} = 3 \text{ MHz}$;
- $N = 10^{10}$ particles;
- $s_x = 0.1 \text{ cm}$, $s_z = 0.01 \text{ cm}$.

Using Eq. (4.9), we can calculate $L = 10^{29} \text{ cm}^{-2}\text{s}^{-1}$. If we are interested in a rare process, for example $e^+e^- \rightarrow p\bar{p}$ (the cross section is $\sigma = 1 \text{ nb} = 10^{-33} \text{ cm}^2$) and have $E_{\text{CM}} \sim 2 - 3 \text{ GeV}$ we only expect $R = 10^{-4}$ events per second or about 0.35 events per hour.

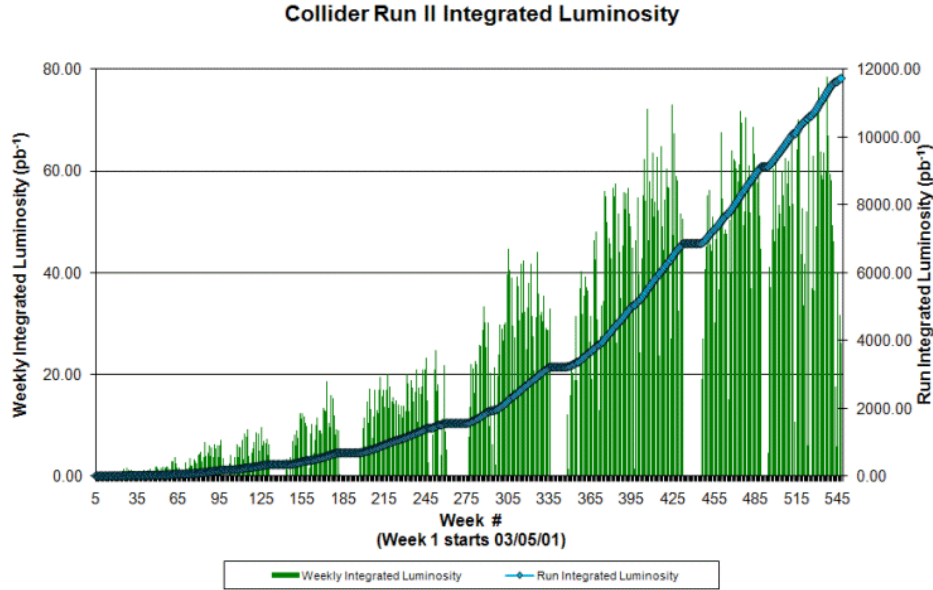


Figure 4.13: *Integrated luminosity at Tevatron as function of time.*

4.3.3 Particle detectors

To gather data from experiments carried out at accelerators, we need particle detectors. They are disposed around the interaction region and detect (directly or indirectly) the reaction products. Typically, the following measurements are performed on final state particles:

- Spatial coordinates and timing of final state;
- Momentum;
- Energy;
- Type of particle (particle ID).

Because of kinematical constraints, for fixed target experiments the production of final states is mainly in the forward direction. Therefore, the detector has to cover only a small solid angle (see Fig. 4.14). In colliding beam experiments, on the other hand, cylindrically symmetric detectors with hermeticity down to small angles are preferred (see Fig. 4.15). A collider physics experiment has in general tracking detectors in a solenoidal field surrounded by calorimeters and particle ID detectors (e. g. muon ID). To allow the momentum measurements, a solenoidal magnetic field is applied parallel to the colliding beams. The particles trajectories in the magnetic field are measured in the inner layers by silicon pixel and silicon strip tracking devices. They are surrounded by calorimeters measuring the particles' energy. The general structure of such a detector, shown in Fig. 4.15,

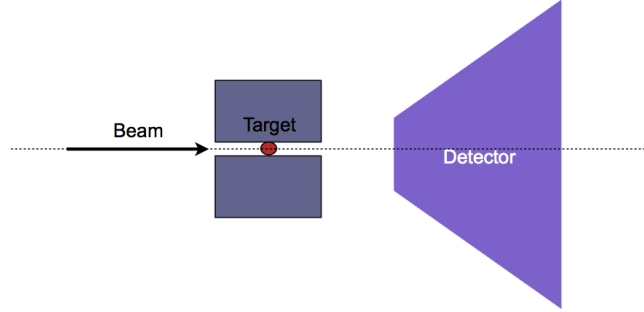


Figure 4.14: *Schematic view of an experimental setup for a fixed target experiment.*

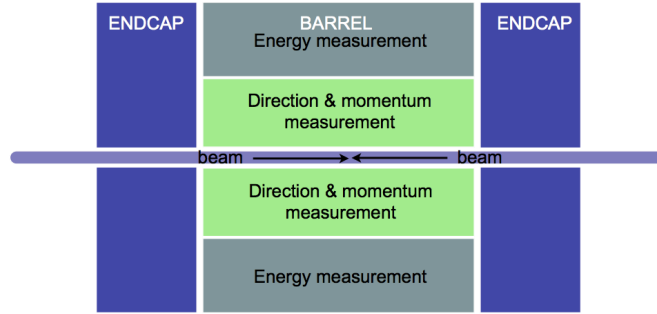


Figure 4.15: *Schematic view of a detector for colliding beam experiments.*

is also visible in the Compact Muon Solenoid (CMS) experiment at LHC. A sketch of the CMS experiment is given in Fig. 4.16.

In high energy experiments the momentum measurement is based on the deflection of charged particles in a magnetic field. Consider a simple case involving a dipole magnet (Fig. 4.17(a)). One can measure the track direction before and after the bending influence of the magnetic field to obtain the angle θ . The momentum is derived from Eq. (4.6):

$$\begin{aligned}
 p &= 0.3BR \\
 \text{length} = l &= 2R \sin\left(\frac{\theta}{2}\right) \sim R\theta \\
 \Rightarrow \theta &= \frac{\text{length}}{R} = \frac{0.3Bl}{p} \\
 \Rightarrow p &= \frac{0.3Bl}{\theta}.
 \end{aligned}$$

In collider experiments the B field is parallel to the beams, which means that curvature only happens in the transverse plane (Fig. 4.17(b)). The momentum resolution is given by

$$\frac{\sigma(p_T)}{p_T} = \frac{\sigma_{r\phi} p_T}{0.3Bl_R^2} \left[\frac{720}{n+4} \right]^{-\frac{1}{2}}$$

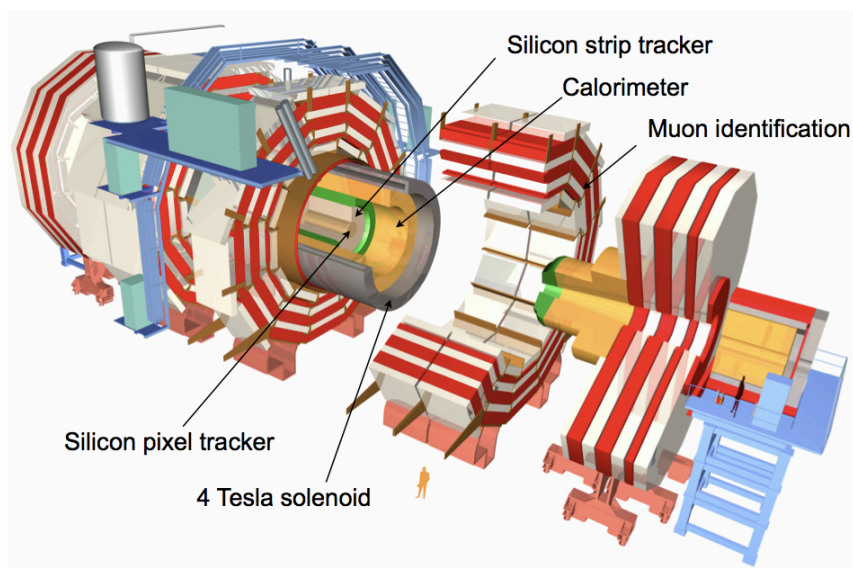


Figure 4.16: *The CMS experiment at the LHC.*

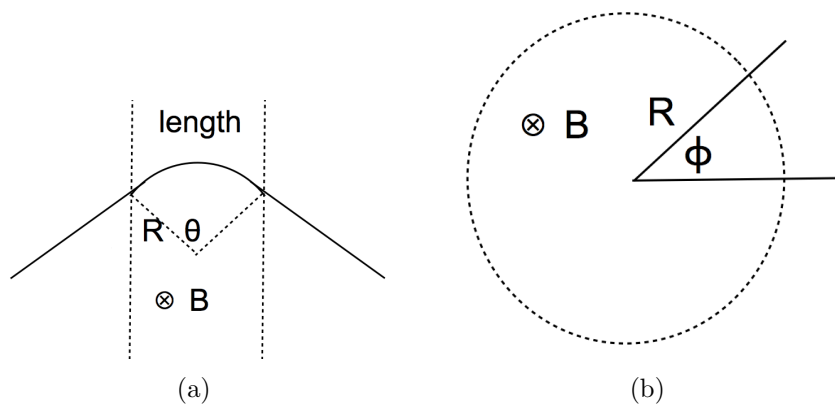


Figure 4.17: *Momentum measurement in collider experiments using a magnetic field. The magnetic field is parallel to the beams (orthogonal to the page).*

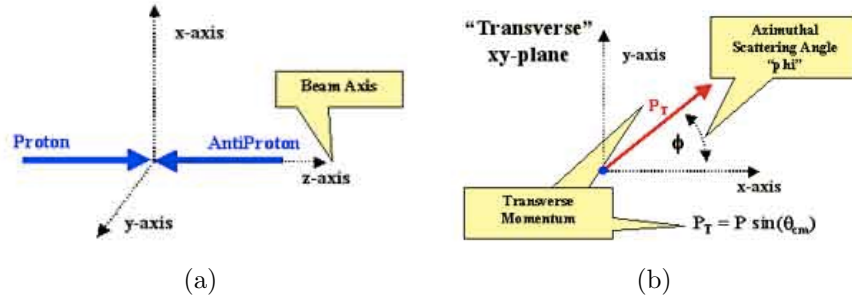


Figure 4.18: *Axes labelling conventions (a) and definition of transverse momentum (b).* Source: [10].

where $\sigma_{r\phi}$ is the error on each measurement point, l_R the radial length of the track, and n the number of equidistant points.

4.4 Kinematics and data analysis methods

In this section we describe the data analysis tools used in collider particle physics experiments discussed in Sect. 4.3. We introduce variables in the laboratory frame and methods based on momentum conservation and invariant mass. Momentum conservation leads to the concepts of transverse momentum and missing mass. As examples, we discuss two- and three-jet events as well as the W boson discovery.

4.4.1 Pseudorapidity and transverse momentum

Consider the collision of two beams in the laboratory frame. The axes labelling conventions are given in Fig. 4.18(a) ($p\bar{p}$ scattering). The momentum of each particle produced in a collision can be decomposed in a component parallel to the beams (longitudinal, along the z direction) and one perpendicular to the beams (transverse, in the xy plane) as shown in Fig. 4.18(b). The transverse component of the momentum is given by ($\Theta^* \equiv \theta_{CM}$)

$$p_T = p \sin(\theta_{CM})$$

and spans an angle ϕ with the x axis. To measure the longitudinal angle of the emerging particle jet one usually uses a variable called pseudorapidity η . It is defined by

$$\eta = -\ln \left[\tan \left(\frac{\theta_{CM}}{2} \right) \right]$$

and is Lorentz invariant under longitudinal boosts (see Fig. 4.19(a)). Momenta in the transverse plane are also invariant under longitudinal relativistic transformations. Therefore, the distance between single particles or jets of particles is usually measured in the $\eta\phi$ plane, as shown in Fig. 4.19(b).

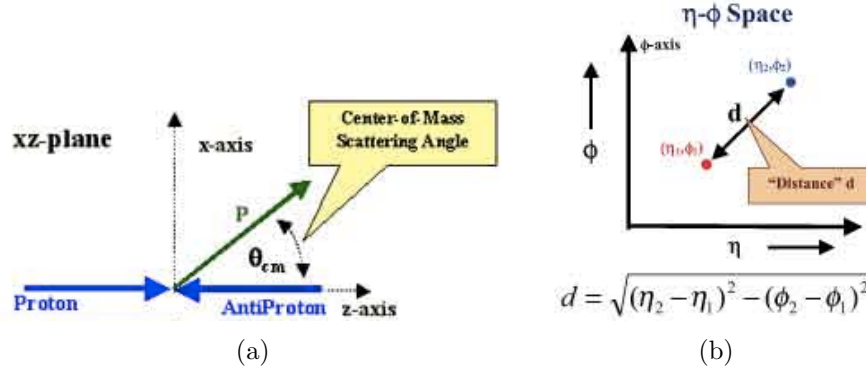


Figure 4.19: Definition of the longitudinal scattering angle θ_{CM} (a) and definition of particle distance in the η - ϕ plane (b). Source: [10].

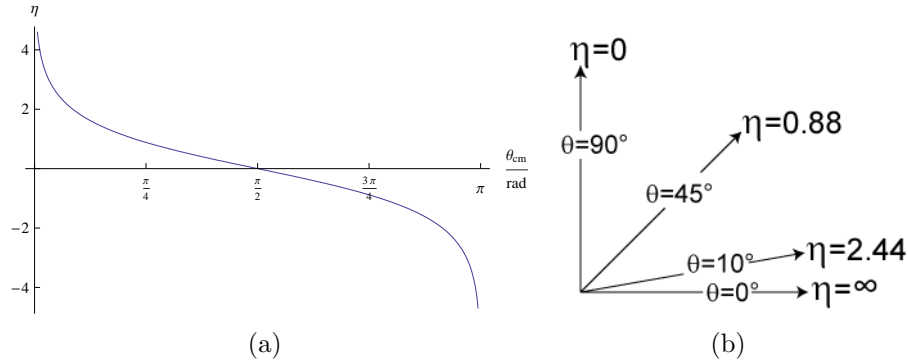


Figure 4.20: Pseudorapidity as a function of θ_{CM} (a) and pseudorapidity for various values of θ_{CM} (b). Source (b): [11].

Particles produced at $\theta_{CM} = 90^\circ$ have zero pseudorapidity. As visualized by Fig. 4.20(a) and 4.20(b), high $|\eta|$ values are equivalent to very shallow scattering angles. Typical coverage of central detectors extends to $|\eta| \sim 3$. Coverage of high rapidities ($\theta_{CM} < 5^\circ$) can be achieved with detectors placed at large z positions.

4.4.2 Momentum conservation in particle jets

Experiments in hadron colliders usually deal with particles at high transverse momentum. This is because the incoming particles collide head-on and have no transverse momentum before scattering and therefore, the final state particles must have zero *total* transverse momentum. Processes involving large momentum transfer produce particles in the center of the detector (small pseudorapidity). An example of such a process is given in Fig. 4.21. The experimental signature of a two jet event is shown in Fig. 4.22. The calorimeter measures the deposited energy in cells of the η - ϕ plane. Both charged and neutral particles are detected. The histogram shows the energy measured in each cell. Note that the main signals are symmetric in azimuth and at about zero pseudorapidity. The momentum of

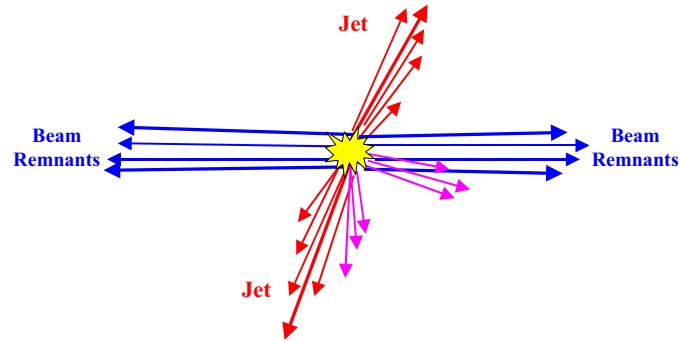


Figure 4.21: *Two jet event production at hadron colliders.* Source: [12].

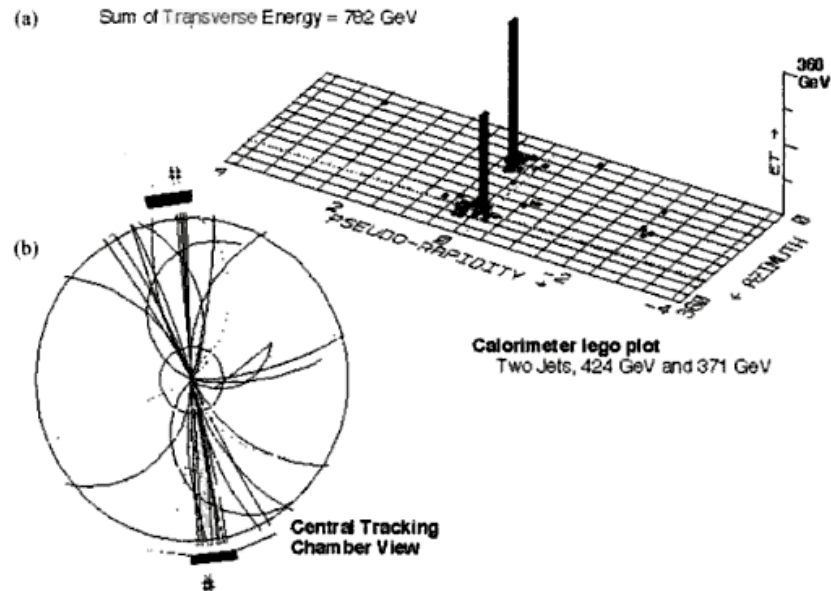


Figure 4.22: *Two jet event, reconstructed in the tracking chamber (b) and calorimeter signals (a) of the DØ experiment.*

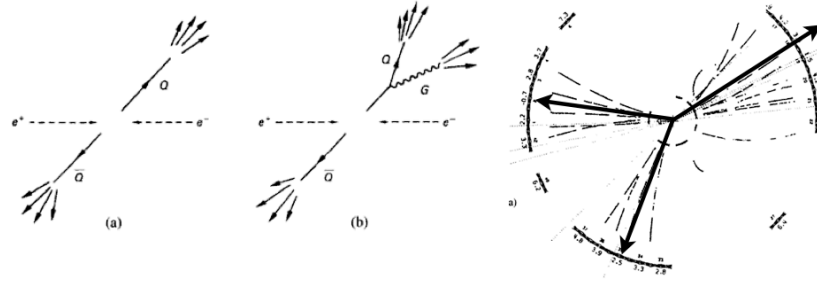


Figure 4.23: *Two- and three-jet events in e^+e^- collisions.* The rightmost sketch shows the tracks reconstructed in the central tracking detector.

each *charged* particle in a jet is measured by the central tracking chamber. Low momentum components yield smaller bending radii and the total transverse momentum has to be zero.

Electron-positron pairs can annihilate producing quark pairs (see Fig. 4.23(a)). This was studied for example at the Large Electron-Positron Collider (LEP). In some cases, a gluon can be radiated from one of the outgoing quarks (see Fig. 4.23(b)). In the latter case one observes three particle jets in the final state: two quark jets and one gluon jet. If no particle escapes the detector the three jets must have total transverse energy equal to zero. In the next section we discuss the case of particles escaping the experiment undetected. This topic is discussed more thoroughly in Chap. 8.

4.4.3 Missing mass method

A collision is characterized by an initial total energy and momentum ($E_{\text{in}}, \vec{p}_{\text{in}}$). In the final state we have n particles with total energy and momentum given by:

$$E = \sum_i^n E_i, \quad (4.10)$$

$$\vec{p} = \sum_i^n \vec{p}_i. \quad (4.11)$$

Sometimes an experiment may measure $E < E_{\text{in}}$ and $\vec{p} \neq \vec{p}_{\text{in}}$. In this case one or more particles have not been detected. Typically this happens with neutral particles, most often neutrinos, but also with neutrons, π^0 , or K_L^0 . The latter have a long lifetime and may decay outside the sensitive volume. To quantify this process, we introduce the concept of missing mass:

$$\text{missing mass} \times c^2 = \sqrt{(E_{\text{in}} - E)^2 - (\vec{p}_{\text{in}} - \vec{p})^2 c^2}. \quad (4.12)$$

The missing mass is measured for every collision and its spectrum is plotted. If the spectrum has a well-defined peak one particle has escaped our detector.

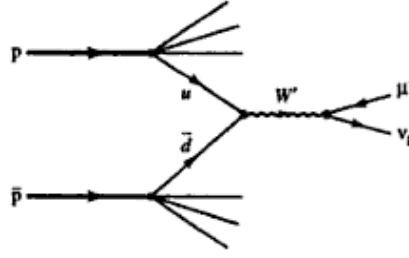


Figure 4.24: *Production and decay of a W^+ boson in a $p\bar{p}$ collision.*

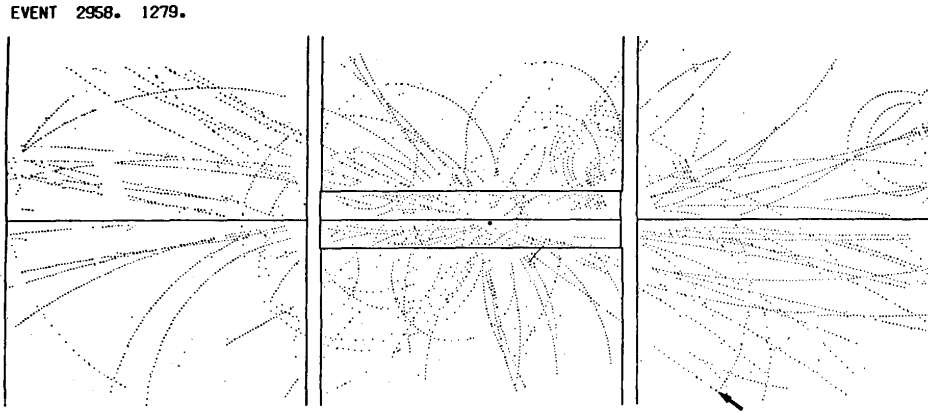


Figure 4.25: *Event with a W boson decay candidate via $W^+ \rightarrow e^+ + \nu_e$. The event was recorded by the UA1 experiment (CERN). Source: [13, p. 112].*

Example: Consider the decay of W bosons. They can be produced in proton-anti-proton collisions mainly via the process shown in Fig. 4.24; a u quark collides with an anti- d quark producing a W^+ boson. The W^+ then decays into a neutrino-lepton pair. The muon is detected and its momentum can be measured. The neutrino escapes the detector undetected. The total sum of the transverse momenta is therefore not zero! In other words, the experimental signature of the neutrino in the experiment is the *missing transverse momentum*. One of the first events [13, p. 112] attributed to production and decay of a W^+ boson is shown in Fig. 4.25. The arrow shows the lepton (e^+) and the missing momentum is compatible with the e^+ transverse momentum.

4.4.4 Invariant mass method

The invariant mass is a characteristic of the total energy and momentum of an object or a system of objects that is the same in all frames of reference. When the system as a whole is at rest, the invariant mass is equal to the total energy of the system divided by c^2 . If

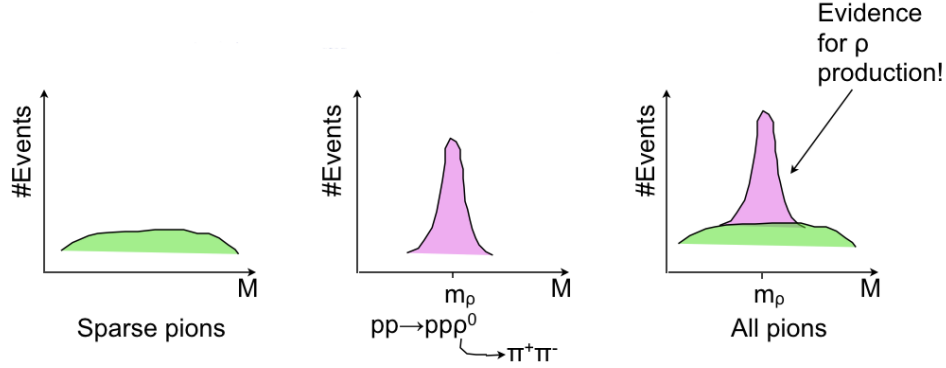


Figure 4.26: Event distribution for invariant mass of the pion pair in the process $pp \rightarrow pp\pi^+\pi^-$. The sparse pions' (left) distribution is broad and can be predicted using simulation techniques. The invariant mass of the pion pairs stemming from ρ^0 decay (center) is peaked around m_ρ . All pions contribute to the recorded events (right).

the system is one particle, the invariant mass may also be called the rest mass:

$$m^2c^4 = E^2 - \vec{p}^2c^2.$$

For a system of N particles we have

$$W^2c^4 = \left(\sum_i^N E_i \right)^2 - \left(\sum_i^N \vec{p}_i c \right)^2 \quad (4.13)$$

where W is the invariant mass of the decaying particle. For a particle of Mass M decaying into two particles, $M \rightarrow 1 + 2$, Eq. 4.13 becomes:

$$M^2c^4 = (E_1 + E_2)^2 - (\vec{p}_1 + \vec{p}_2)^2c^2 = m_1^2c^4 + m_2^2c^4 + 2(E_1E_2 - \vec{p}_1 \cdot \vec{p}_2c^2) = (p_1 + p_2)^2.$$

Example: Particles like ρ, ω, ϕ have average lifetime of $10^{-22} - 10^{-23}$ s. How do we know of their existence if they live so shortly? Consider, for example, the reaction $pp \rightarrow pp\pi^+\pi^-$. We identify all four particles in the final state and measure their momentum. Let's focus on the pion pair, the total energy and momentum of the pair are:

$$\begin{aligned} E &= E_+ + E_- \\ \vec{p} &= \vec{p}_+ + \vec{p}_-. \end{aligned}$$

The corresponding invariant mass is

$$Mc^2 = \sqrt{E^2 - \vec{p}^2c^2}.$$

The event distribution for the variable M will look like the plot in Fig. 4.26. The peak in the event rate at m_ρ is evidence for ρ production.

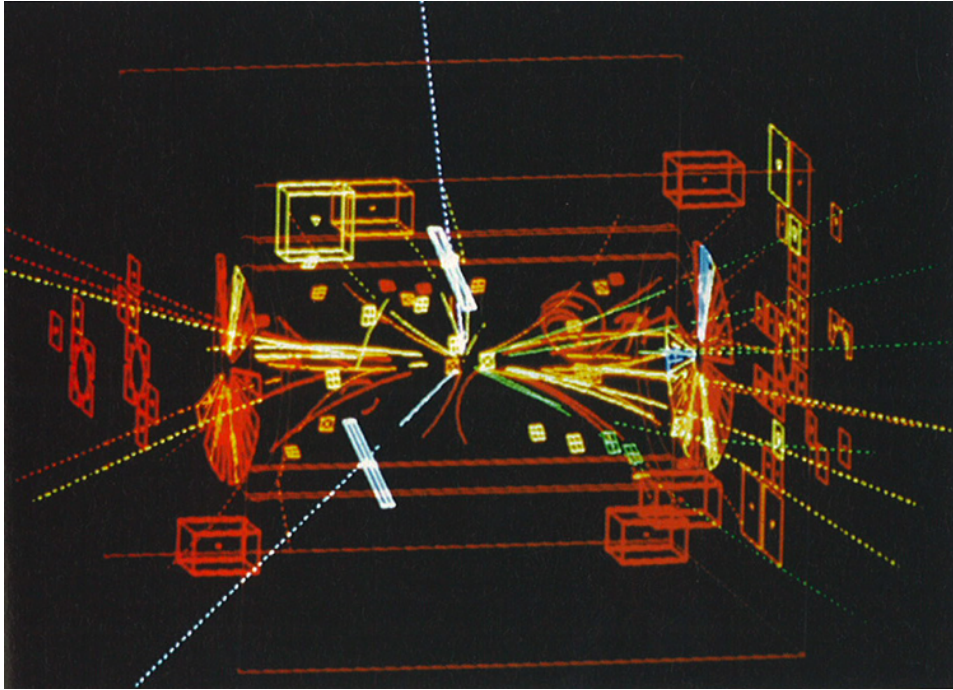


Figure 4.27: Z^0 boson discovery at the UA1 experiment (CERN). The Z^0 boson decays into a e^+e^- pair, shown as white dashed lines.

Example: Another example illustrating this point is the Z discovery in 1984. Fig. 4.27 shows an event where the Z boson, after production by proton-proton collision decays into an e^+e^- pair (white dashed lines). The invariant mass of the pair is about 92 GeV.

Example: Consider now the π^0 reconstruction. Neutral pions decay in photon pairs in about 99% of the cases. By measuring the angle and energy of the emitted photons (see Fig. 4.28) one can reconstruct the mass of the decaying pion (see Fig. 4.29).

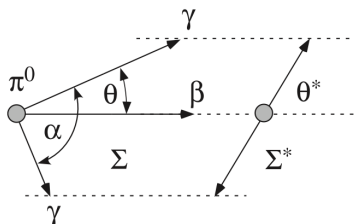


Figure 4.28: π^0 decay in two photons. Σ denotes the laboratory frame (left) and Σ^* denotes the pion rest frame (right). Source [8, p. 95].

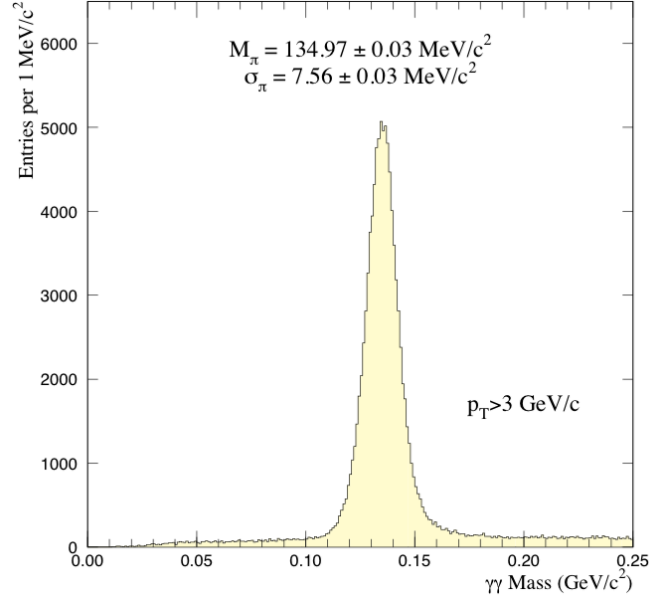


Figure 4.29: *Invariant mass spectrum for photon pairs.* The π^0 appears as a peak at the pion mass.

Example: In case of three body decays, $R \rightarrow 1 + 2 + 3$, one can define three invariant masses:

$$\begin{aligned} m_{12}^2 c^4 &\equiv (p_1 + p_2)^2 \\ m_{13}^2 c^4 &\equiv (p_1 + p_3)^2 \\ m_{23}^2 c^4 &\equiv (p_2 + p_3)^2. \end{aligned}$$

This yields

$$\begin{aligned} m_{12}^2 + m_{13}^2 + m_{23}^2 &= m_1^2 + m_2^2 + m_3^2 + (p_1 + p_2 + p_3)^2 \frac{1}{c^4} \\ &= m_1^2 + m_2^2 + m_3^2 + M^2. \end{aligned}$$

This means that there are only two independent invariant masses.

As an example, let's study the reaction:

$$K^- p \rightarrow \Lambda \pi^+ \pi^- \quad (\Lambda \rightarrow \pi^- p).$$

We can measure two invariant masses:

$$m_{12} \equiv m(\Lambda \pi^-) \text{ and } m_{13} \equiv m(\Lambda \pi^+).$$

The so-called “Dalitz plot” given in Fig. 4.30 shows the relation between m_{13}^2 and m_{12}^2 . The Σ^\pm resonances appear as two bands in the Dalitz plot around 1.4 GeV.

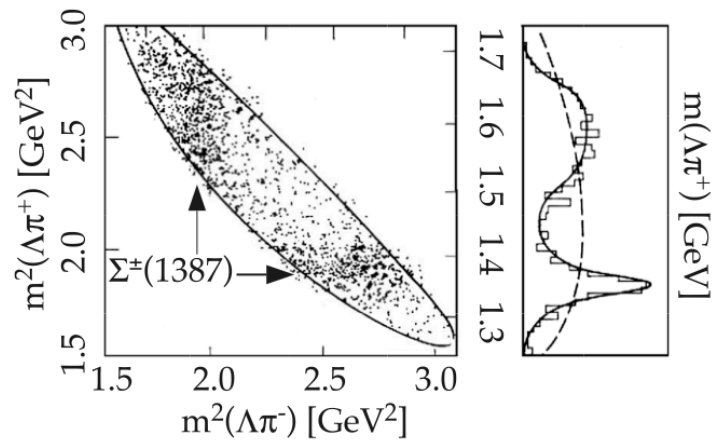


Figure 4.30: *Dalitz plot for $K^- p \rightarrow \pi^+ \pi^- \Lambda$ ($\Lambda \rightarrow \pi^- p$).* Source: [8, p. 200].

Chapter 5

Elements of quantum electrodynamics

5.1 Quantum mechanical equations of motion

In quantum mechanics I & II, the correspondence principle played a central role. It is in a sense the recipe to quantize a system whose Hamiltonian is known. It consists in the following two substitution rules :

$$\vec{p} \longmapsto -i\nabla \quad \text{(momentum),} \quad (5.1)$$

$$E \longmapsto i\partial_t \quad \text{(energy).} \quad (5.2)$$

For nonrelativistic quantum mechanics we get the celebrated **Schrödinger equation**,

$$i\partial_t\psi = H\psi, \quad \text{with } H = -\frac{1}{2m}\Delta + V(\vec{x}), \quad (5.3)$$

whose free solution ($V(\vec{x}) \equiv 0$) is,

$$\psi(\vec{x}, t) = Ce^{-i(Et - \vec{p} \cdot \vec{x})} \quad \text{with } E = \frac{\vec{p}^2}{2m}.$$

The relativistic version of the energy-momentum relationship is however,

$$E^2 = \vec{p}^2 + m^2, \quad (5.4)$$

from which we get, using again the correspondence principle Eq. (5.1),

$$-\partial_t^2\psi = (-\Delta + m^2)\psi. \quad (5.5)$$

At this point we define some important symbols which will follow us throughout the rest of this lecture,

$$\partial_\mu := (\partial_t, \nabla), \quad (5.6)$$

$$\partial^\mu := g^{\mu\nu} \partial_\nu = (\partial_t, -\nabla), \quad (5.7)$$

$$\square := \partial_\mu \partial^\mu = \partial_t^2 - \Delta. \quad (5.8)$$

With this notation we can then reformulate Eq. (5.5) to get the **Klein-Gordon equation**,

$$\boxed{(\square + m^2) \psi = 0}, \quad (5.9)$$

with solutions,

$$\psi(\vec{x}, t) = C e^{-i(Et - \vec{p} \cdot \vec{x})} \quad \text{with } E = \pm \sqrt{\vec{p}^2 + m^2}.$$

We see that in this case it is possible to have negative energy eigenvalues, a fact not arising with the nonrelativistic case.

As in the case of the Schrödinger equation (5.3) we can formulate a continuity equation. To do so we multiply the Klein-Gordon equation (5.9) by the left with ψ^* and its conjugate, $(\square + m^2) \psi^* = 0$, by ψ and then subtract both equations to get,

$$\begin{aligned} 0 &= \psi^* \partial^\mu \partial_\mu \psi - \psi \partial^\mu \partial_\mu \psi^* \\ &= \partial^\mu (\psi^* \partial_\mu \psi - \psi \partial_\mu \psi^*) \\ &\Rightarrow \partial_t (\psi^* \partial_t \psi - \psi \partial_t \psi^*) + \nabla \cdot (\psi^* \nabla \psi - \psi \nabla \psi^*) = 0. \end{aligned} \quad (5.10)$$

We would like to interpret $\psi^* \partial_t \psi - \psi \partial_t \psi^*$ in Eq. (5.10) as a probability density, or more exactly,

$$\rho = i(\psi^* \partial_t \psi - \psi \partial_t \psi^*),$$

which is *not* a positive definite quantity (as we can convince ourselves by computing ρ for the plane wave solution), and hence cannot be interpreted as a probability density as it was the case in QM.

When computing the continuity equation for the Schrödinger equation, where such a problem does not arise, we see that the problem lies essentially in the presence of a *second* order time derivative in the Klein-Gordon equation.

We now make a big step, by imposing that our equation of motion only contains a *first* order time derivative. Since we want a Lorentz invariant equation of motion, we conclude that only a *linear* dependence on ∇ is allowed. Following Dirac's intuition, we make the ansatz,

$$(i\gamma^\mu \partial_\mu - m)\psi = (i\gamma^0 \partial_t + i\vec{\gamma} \cdot \nabla - m)\psi = 0. \quad (5.11)$$

Turning back to the correspondence principle we remark that,

$$\begin{aligned} (\gamma^0 E - \vec{\gamma} \cdot \vec{p} - m)\psi &= 0 \\ \Rightarrow (\gamma^0 E - \vec{\gamma} \cdot \vec{p} - m)^2 \psi &= 0, \end{aligned} \quad (5.12)$$

which must stay compatible with the mass-shell relation, $E^2 = \vec{p}^2 + m^2$.

This implies that the γ^μ 's cannot be numbers since it would then be impossible to satisfy,

$$(\vec{\gamma} \cdot \vec{p})^2 = \left(\sum_{i=1}^3 \gamma^i p_i \right)^2 \stackrel{!}{\propto} \vec{p}^2,$$

so we let them be $n \times n$ matrices, for an n which is still to be determined.

We now derive relations that the γ^μ 's must fullfill, so that the mass-shell relation remains true. From Eq. (5.12), and again with the correspondence principle, we must have,

$$\begin{aligned} \underbrace{i\partial_t}_E &= (\gamma^0)^{-1} \vec{\gamma} \cdot \underbrace{(-i\nabla)}_{\vec{p}} + (\gamma^0)^{-1} m \\ \Rightarrow \underbrace{-\partial_t^2}_{E^2} &= - \sum_{i,j=1}^3 \frac{1}{2} \left((\gamma^0)^{-1} \gamma^i (\gamma^0)^{-1} \gamma^j + (\gamma^0)^{-1} \gamma^j (\gamma^0)^{-1} \gamma^i \right) \partial_i \partial_j \end{aligned} \quad (5.13)$$

$$- i \cdot m \sum_{i=1}^3 \left((\gamma^0)^{-1} \gamma^i (\gamma^0)^{-1} + (\gamma^0)^{-1} (\gamma^0)^{-1} \gamma^i \right) \partial_i \quad (5.14)$$

$$+ m^2 (\gamma^0)^{-1} (\gamma^0)^{-1} \quad (5.15)$$

$$\begin{aligned} &\stackrel{!}{=} (\partial_i \partial_i + m^2) \\ &= \underbrace{(-\Delta)}_{\vec{p}^2} + m^2. \end{aligned} \quad (5.16)$$

Comparing Eqs. (5.16) and (5.15) we conclude that,

$$(\gamma^0)^{-1} (\gamma^0)^{-1} \stackrel{!}{=} \mathbb{1} \Rightarrow (\gamma^0)^{-1} = \gamma^0. \quad (5.17)$$

Defining $\{a, b\} := ab + ba$ and comparing Eq. (5.16) and Eq. (5.14) we get

$$\gamma^0 \gamma^i (\gamma^0)^{-1} \stackrel{!}{=} 0 \Rightarrow \{\gamma^i, \gamma^0\} = 0. \quad (5.18)$$

Finally, comparing Eq. (5.16) and Eq. (5.13), we have,

$$-\frac{1}{2} \left((\gamma^0)^{-1} \gamma^i (\gamma^0)^{-1} \gamma^j + (\gamma^0)^{-1} \gamma^j (\gamma^0)^{-1} \gamma^i \right) \stackrel{!}{=} \delta_{ij} \Rightarrow \{\gamma^i, \gamma^j\} = -2\delta_{ij}. \quad (5.19)$$

We can summarize Eqs. (5.17), (5.18) and (5.19) in the **Clifford algebra of the γ -matrices**,

$$\boxed{\{\gamma^\mu, \gamma^\nu\} = 2g^{\mu\nu} \mathbb{1}}, \quad (5.20)$$

where $g^{00} = 1$, $g^{ii} = -1$ and all the other elements vanish.

Important facts : The eigenvalues of γ^0 can only be ± 1 and those of $\gamma^i \pm i$ and the γ -matrices have vanishing trace :

$$\begin{aligned} \text{Tr } \gamma^i &= \text{Tr } (\gamma^0 \gamma^0 \gamma^i) = -\text{Tr } (\gamma^0 \gamma^i \gamma^0) = -\text{Tr } \gamma^i \Rightarrow \text{Tr } \gamma^i = 0, \\ \text{Tr } \gamma^0 &= \text{Tr } (\gamma^0 \gamma^i (\gamma^i)^{-1}) = -\text{Tr } (\gamma^i \gamma^0 (\gamma^i)^{-1}) = -\text{Tr } (\gamma^0) \Rightarrow \text{Tr } \gamma^0 = 0. \end{aligned}$$

The eigenvalue property of γ^0 implies with the last equation that the dimension n of the γ -matrices must be even.

For $n = 2$ there are no matrices satisfying Eq. (5.20), as can be checked by direct computation.

For $n = 4$ there are many possibilities. The most common choice in textbooks is the Dirac-Pauli representation :

$$\gamma^0 = \mathbb{1} \otimes \sigma^3 = \begin{pmatrix} \mathbb{1} & 0 \\ 0 & -\mathbb{1} \end{pmatrix}, \quad \gamma^i = \sigma^i \otimes (i\sigma^2) = \begin{pmatrix} 0 & \sigma^i \\ -\sigma^i & 0 \end{pmatrix}, \quad (5.21)$$

with the Pauli matrices,

$$\sigma^0 = \mathbb{1} = \begin{pmatrix} 1 & 0 \\ 0 & 1 \end{pmatrix}, \quad \sigma^1 = \begin{pmatrix} 0 & 1 \\ 1 & 0 \end{pmatrix}, \quad \sigma^2 = \begin{pmatrix} 0 & -i \\ i & 0 \end{pmatrix}, \quad \sigma^3 = \begin{pmatrix} 1 & 0 \\ 0 & -1 \end{pmatrix},$$

and the Kronecker product of 2×2 -matrices,

$$A \otimes B = \begin{pmatrix} b_{11}A & b_{12}A \\ b_{21}A & b_{22}A \end{pmatrix}.$$

Looking at the **Dirac equation**

$$\boxed{(i\gamma^\mu \partial_\mu - m)\psi = 0} \quad (5.22)$$

we see that ψ is no longer a function but a vector, called **(4-)spinor**,

$$\psi = \begin{pmatrix} \psi_1 \\ \psi_2 \\ \psi_3 \\ \psi_4 \end{pmatrix}.$$

For 4-spinors, there are two types of adjoints, namely,

- the hermitian adjoint $\psi^\dagger = (\psi_1^*, \psi_2^*, \psi_3^*, \psi_4^*)$, and
- the Dirac adjoint $\bar{\psi} := \psi^\dagger \gamma^0 = (\psi_1^*, \psi_2^*, -\psi_3^*, -\psi_4^*)$.

Note that $\bar{\psi}$ satisfies a dirac equation of its own,

$$i\partial_\mu \bar{\psi} \gamma^\mu + m\bar{\psi} = 0. \quad (5.23)$$

We now focus our attention on the continuity equation for the Dirac field. From Eqs. (5.22) and (5.23),

$$i\psi^\dagger(\partial_t \psi) = (-i\psi^\dagger \gamma^0 \gamma^i \partial_i + \psi^\dagger \gamma^0 m) \psi,$$

and its hermitian conjugate,

$$-i(\partial_t \psi^\dagger) \psi = (i(\partial_i \psi^\dagger) \gamma^0 \gamma^i + \psi^\dagger \gamma^0 m) \psi,$$

we get the difference,

$$\begin{aligned} \partial_t(\psi^\dagger \psi) &= -[(\partial_i \psi^\dagger) \gamma^0 \gamma^i \psi + \psi^\dagger \gamma^0 \gamma^i i(\partial_i \psi)], \\ \partial_t(\bar{\psi} \gamma^0 \psi) &= -\partial_i(\bar{\psi} \gamma^i \psi). \end{aligned} \quad (5.24)$$

We identify the components as,

$$\rho = \bar{\psi} \gamma^0 \psi, \quad \vec{j} = \bar{\psi} \vec{\gamma} \psi,$$

or interpreting them as components of a 4-vector as in classical electrodynamics,

$$j^\mu = \bar{\psi} \gamma^\mu \psi, \quad (5.25)$$

we see that Eq. (5.24) can be reexpressed in the manifestly covariant form,

$$\boxed{\partial_\mu j^\mu = 0}. \quad (5.26)$$

5.2 Solutions of the Dirac equation

Before we look at the solutions of the free Dirac equation, we introduce the slash notation for contraction with the γ -matrices : $\not{a} := \gamma^\mu a_\mu$. The Dirac equation then reads $(i\not{\partial} - m)\psi = 0$.

5.2.1 Free particle at rest

In the rest frame of a particle, the Dirac equation reduces to,

$$i\gamma^0\partial_t\psi = m\psi,$$

for which we find four linearly independent solutions, namely,

$$\begin{aligned} \psi_1 &= e^{-imt} \begin{pmatrix} 1 \\ 0 \\ 0 \\ 0 \end{pmatrix}, & \psi_2 &= e^{-imt} \begin{pmatrix} 0 \\ 1 \\ 0 \\ 0 \end{pmatrix}, & E &= m & (\text{particles}) \\ \psi_3 &= e^{+imt} \begin{pmatrix} 0 \\ 0 \\ 1 \\ 0 \end{pmatrix}, & \psi_4 &= e^{+imt} \begin{pmatrix} 0 \\ 0 \\ 0 \\ 1 \end{pmatrix}, & E &= -m & (\text{antiparticles}). \end{aligned}$$

5.2.2 Free particle

In order to preserve the Lorentz invariance of a solution, it must only depend on Lorentz scalars – quantities which are invariant under Lorentz transformations – like $p \cdot x = p_\mu x^\mu$. We make the ansatz,

$$\begin{aligned} \psi_{1,2} &= e^{-ip \cdot x} u_\pm(p), & p^0 &> 0 \\ \psi_{3,4} &= e^{+ip \cdot x} v_\mp(-p), & p^0 &< 0. \end{aligned}$$

Plugging those ansatz in the Dirac equation, we get,

$$(\not{p} - m)u_\pm(p) = \bar{u}_\pm(\not{p} - m) = 0, \quad (5.27)$$

$$(\not{p} + m)v_\pm(p) = \bar{v}_\mp(\not{p} + m) = 0, \quad (5.28)$$

where we replaced $-p \mapsto p$ in the second equation, having thus $p^0 > 0$ in both cases now.

5.2.3 Explicit form of u and v

As checked in the exercices, the explicit form for the u and v functions are,

$$u_\pm(p) = \sqrt{p^0 + m} \begin{pmatrix} \chi_\pm \\ \frac{\vec{\sigma} \cdot \vec{p}}{p^0 + m} \chi_\pm \end{pmatrix}, \quad (5.29)$$

$$v_\pm(p) = \sqrt{p^0 + m} \begin{pmatrix} \frac{\vec{\sigma} \cdot \vec{p}}{p^0 + m} \chi_\mp \\ \chi_\mp \end{pmatrix}, \quad (5.30)$$

where $\chi_+ = \begin{pmatrix} 1 \\ 0 \end{pmatrix}$ corresponds to a “spin up” state and $\chi_- = \begin{pmatrix} 0 \\ 1 \end{pmatrix}$ to a “spin down” state.

We note on the way that the application,

$$\vec{p} \mapsto \vec{\sigma} \cdot \vec{p} = \sigma^i p_i = \begin{pmatrix} p_3 & p_1 - ip_2 \\ p_1 + ip_2 & -p_3 \end{pmatrix},$$

defines an isomorphism between the vector spaces of 3-vectors and hermitian 2×2 -matrices.

5.2.4 Operators on spinor spaces

Hamiltonian The Hamiltonian is defined by $i\partial_t\psi = H\psi$. Isolating the time derivative in the Dirac equation, Eq. (5.22), we read out,

$$H = -i\gamma^0\gamma^i\partial_i + \gamma^0m = \begin{pmatrix} m\mathbb{1} & \vec{\sigma} \cdot \vec{p} \\ \vec{\sigma} \cdot \vec{p} & -m\mathbb{1} \end{pmatrix}. \quad (5.31)$$

Helicity The helicity is the component of the spin in the direction of motion $\hat{p} := \frac{\vec{p}}{|\vec{p}|}$, and is defined by,

$$h = \frac{1}{2}\vec{\sigma} \cdot \hat{p} \otimes \mathbb{1} = \frac{1}{2} \begin{pmatrix} \vec{\sigma} \cdot \hat{p} & 0 \\ 0 & \vec{\sigma} \cdot \hat{p} \end{pmatrix}. \quad (5.32)$$

By direct computation, one can check that $[H, h] = 0$, and thus there exist a set of eigenfunctions diagonalizing H and h simultaneously. The eigenvalues of h are then constants of the motion and hence good quantum numbers to label the corresponding states.

This quantum number λ can take two values,

$$\lambda = \begin{cases} +\frac{1}{2} & \text{positive helicity} \iff \vec{s} \uparrow \parallel \vec{p}, \\ -\frac{1}{2} & \text{negative helicity} \iff \vec{s} \uparrow \downarrow \vec{p}. \end{cases} \quad (5.33)$$

We stress here that helicity/handedness is *not* a Lorentz invariant quantity for massive particles.

Consider \vec{p} in the z -direction, then,

$$\frac{1}{2}\vec{\sigma} \cdot \hat{p}\chi_{\pm} = \frac{1}{2}\sigma^3\chi_{\pm} = \pm\frac{1}{2}\chi_{\pm}.$$

From the last argumentative steps, we are not surprised with the statement that the Dirac equation describes spin- $\frac{1}{2}$ particles.

Chirality Consider the Dirac equation for the case of massless particles. This is a good approximation for $E \gg m$, which is often the case in accelerator experiments. Setting $m = 0$ simplifies Eq. (5.22) leading to

$$i\gamma^\mu \partial_\mu \psi = 0.$$

Eq. (5.29) and (5.30) change accordingly. We consider for now the particle solutions u_\pm :

$$u_\pm(p) = \sqrt{|\vec{p}|} \begin{pmatrix} \chi_\pm \\ \frac{\vec{\sigma} \cdot \vec{p}}{|\vec{p}|} \chi_\pm \end{pmatrix} = \sqrt{|\vec{p}|} \begin{pmatrix} \chi_\pm \\ \pm \chi_\pm \end{pmatrix}. \quad (5.34)$$

It is convenient to define the so-called chirality matrix γ_5 :

$$\gamma_5 = i\gamma^0\gamma^1\gamma^2\gamma^3$$

which in the Dirac-Pauli representation reads

$$\gamma_5 = \begin{pmatrix} 0 & \mathbb{1} \\ \mathbb{1} & 0 \end{pmatrix}.$$

Using that the γ -matrices fulfill $\{\gamma^\mu, \gamma^\nu\} = 2g^{\mu\nu}$ (see Eq. (5.20)), one can show that

$$\{\gamma_5, \gamma^\mu\} = 0 \text{ and} \quad (5.35)$$

$$\gamma_5^2 = \mathbb{1}. \quad (5.36)$$

These properties of γ_5 imply that if ψ is a solution of the Dirac equation then so is $\gamma_5\psi$. Furthermore, since $\gamma_5^2 = \mathbb{1}$ the eigenvalues of the chirality matrix are ± 1 :

$$\gamma_5\psi_\pm = \pm\psi_\pm$$

which defines the chirality basis ψ_\pm .

Let us apply the γ_5 matrix to the spinor part of particle solutions of the free Dirac equation given in Eq. (5.34):

$$\gamma_5 u_\pm(p) = \begin{pmatrix} 0 & \mathbb{1} \\ \mathbb{1} & 0 \end{pmatrix} \sqrt{|\vec{p}|} \begin{pmatrix} \chi_\pm \\ \pm \chi_\pm \end{pmatrix} = \sqrt{|\vec{p}|} \begin{pmatrix} \pm \chi_\pm \\ \chi_\pm \end{pmatrix} \quad (5.37)$$

$$= \pm \sqrt{|\vec{p}|} \begin{pmatrix} \chi_\pm \\ \pm \chi_\pm \end{pmatrix} = \pm u_\pm(p). \quad (5.38)$$

A similar calculation shows that for the antiparticle solutions

$$\gamma_5 v_\pm(p) = \mp v_\pm(p). \quad (5.39)$$

Therefore, the helicity eigenstates for $m = 0$ are equivalent to the chirality eigenstates. Results (5.38) and (5.39) lead to the notion of handedness (which is borrowed from chemistry):

- u_+ describes a right handed particle: $\overrightarrow{\text{spin}} \uparrow \uparrow \vec{p}_{e-}$ and
- v_+ describes a left handed antiparticle: $\overleftarrow{\text{spin}} \downarrow \uparrow \vec{p}_{e+}$

where the converse holds for u_- and v_- .

Exploiting the eigenvalue equations (5.38) and (5.39), one can define the projectors

$$P_R = \frac{1}{2}(\mathbb{1} \pm \gamma_5). \quad (5.40)$$

They project to u_\pm, v_\pm for arbitrary spinors. For example we have

$$P_L u_\pm = \frac{1}{2}(\mathbb{1} - \gamma_5)u_\pm = \frac{1}{2}(\mathbb{1} \mp \mathbb{1})u_\pm = \begin{cases} 0 \\ \mathbb{1}u_- \end{cases}.$$

To show that Eq. (5.40) indeed defines projectors, we check (using Eq. 5.36) for idempotence,

$$P_R^2 = \frac{1}{4}(\mathbb{1} \pm \gamma_5)(\mathbb{1} \pm \gamma_5) = \frac{1}{4}(\mathbb{1} \pm 2\gamma_5 + \gamma_5^2) = \frac{1}{2}(\mathbb{1} \pm \gamma_5) = P_R,$$

orthogonality,

$$P_R P_L = \frac{1}{4}(\mathbb{1} + \gamma_5)(\mathbb{1} - \gamma_5) = \frac{1}{4}(\mathbb{1} - \gamma_5^2) = 0,$$

and completeness,

$$P_R + P_L = \mathbb{1}.$$

Note that the projectors P_L and P_R are often used to indicate the chirality basis:

$$\begin{aligned} u_{L,R} &= P_{L,R}u \\ v_{L,R} &= P_{L,R}v. \end{aligned}$$

What has been derived so far rests on the assumption that the mass be zero. In this case, chirality is equivalent to helicity which is also Lorentz invariant. If, on the other hand $m \neq 0$, chirality and helicity are not equivalent: In this case chirality, while Lorentz invariant, is not a constant of the motion,

$$[\gamma_5, H_{\text{Dirac}}] \neq 0,$$

and therefore not a good quantum number. Helicity though is a constant of the motion, but, since spin is unaffected by boosts, it is not Lorentz invariant for non-vanishing mass: For every possible momentum \vec{p} in one frame of reference there is another frame in

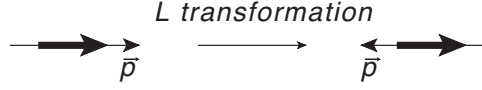


Figure 5.1: Helicity for the case of non-vanishing mass.

| | | Chirality $\gamma_5 = i\gamma^0\gamma^1\gamma^2\gamma^3$ | Helicity $h(\vec{p}) = \frac{1}{2}\vec{\sigma} \cdot \vec{p} \otimes \mathbb{1}$ |
|------------|--------------------|---|---|
| $m = 0$ | Constant of motion | ✓ | ✓ |
| | Lorentz invariant | ✓ | ✓ |
| $m \neq 0$ | Constant of motion | ✗ | ✓ |
| | Lorentz invariant | ✓ | ✗ |

Table 5.1: Chirality and helicity.

which the particle moves in direction $-\vec{p}/|\vec{p}|$ (see Fig. 5.1). A comparison of chirality and helicity is given in Tab. 5.1.

Although chirality is not a constant of the motion for $m \neq 0$, it is still a useful concept (and becomes important when one considers weak interactions). A solution of the Dirac equation ψ can be decomposed:

$$\psi = \psi_L + \psi_R$$

where ψ_L and ψ_R are not solutions of the Dirac equation. The W vector boson of the weak interaction only couples to ψ_L .

As for the normalization of the orthogonal spinors (5.29) and (5.30), the most convenient choice is:

$$\begin{aligned}\bar{u}_s(p)u_{s'}(p) &= 2m\delta_{ss'} \\ \bar{v}_s(p)v_{s'}(p) &= -2m\delta_{ss'}\end{aligned}$$

where $s, s' = \pm$.

Using $\bar{\psi} = \psi^\dagger \gamma^0$, one can show that the following completeness relations (or polarization sum rules) hold:

$$\sum_{s=\pm} u_s(p)\bar{u}_s(p) = \not{p} + m \quad (5.41)$$

$$\sum_{s=\pm} v_s(p)\bar{v}_s(p) = \not{p} - m. \quad (5.42)$$

Comparing these polarization sums with, for instance, the Dirac equation for u , Eq. (5.27), one sees that $\not{p} + m$ projects on the subspace of particle solutions.

5.3 Field operator of the Dirac field

The spinors

$$\begin{aligned} u_s(p)e^{-ip \cdot x}, \text{ eigenvalues } E_p = +\sqrt{|\vec{p}|^2 + m^2}, \text{ and} \\ v_s(-p)e^{ip \cdot x}, \text{ eigenvalues } E_p = -\sqrt{|\vec{p}|^2 + m^2}, \end{aligned}$$

are eigenfunctions of the Dirac Hamiltonian and therefore solutions of the Dirac equation. From these solutions we can deduce the field operator of the Dirac field (which fulfills the Dirac equation)¹:

$$\psi(x) = \int \frac{d^3p}{(2\pi)^3} \frac{1}{\sqrt{2p^0}} \sum_{s=\pm} \left\{ a_s(\vec{p}) u_s(p) e^{-ip \cdot x} + b_s^\dagger(\vec{p}) v_s(p) e^{ip \cdot x} \right\} \quad (5.43)$$

$$\bar{\psi}(x) = \int \frac{d^3p}{(2\pi)^3} \frac{1}{\sqrt{2p^0}} \sum_{s=\pm} \left\{ a_s^\dagger(\vec{p}) \bar{u}_s(p) e^{ip \cdot x} + b_s(\vec{p}) \bar{v}_s(p) e^{-ip \cdot x} \right\} \quad (5.44)$$

where

$$\begin{aligned} a_s^\dagger(\vec{p}) &: \text{creation operator of particle with momentum } \vec{p} \\ b_s^\dagger(\vec{p}) &: \text{creation operator of antiparticle with momentum } \vec{p} \\ a_s(\vec{p}) &: \text{annihilation operator of particle with momentum } \vec{p} \\ b_s(\vec{p}) &: \text{annihilation operator of antiparticle with momentum } \vec{p}. \end{aligned}$$

In advanced quantum mechanics we have seen that field operators create or annihilate position eigenstates. The field operator in Eq. (5.44) does the same thing while furthermore consistently combining the equivalent possibilities for particle creation and antiparticle annihilation: $a_s^\dagger(\vec{p})$ creates individual particle momentum eigenstates from which a weighted superposition is formed, the integral over $b_s(\vec{p})$ on the other hand, annihilates a weighted superposition of antiparticles. Since the creation of a particle at position x is equivalent to the annihilation of its antiparticle at position x , both terms have to appear in the field operator $\bar{\psi}(x)$. Because we have to consider particles and antiparticles, here the energy spectrum is more complicated than in the pure particle case. The creation terms come with a positive-sign plane wave factor $e^{ip \cdot x}$ while the annihilation terms contribute $e^{-ip \cdot x}$. The equivalence of particle creation and antiparticle annihilation is to be understood in the sense that they lead to the same change in a given field configuration.

The Dirac field is a spin-1/2 field. Therefore, the Pauli exclusion principle must hold, imposing anti-commutation relations on the field operators:

$$\begin{aligned} \{\psi(\vec{x}, t), \psi(\vec{x}', t)\} &= \{\bar{\psi}(\vec{x}, t), \bar{\psi}(\vec{x}', t)\} = 0 \\ \{\psi(\vec{x}, t), \bar{\psi}(\vec{x}', t)\} &= \gamma^0 \delta^3(\vec{x} - \vec{x}'). \end{aligned}$$

¹The normalization is chosen to avoid an explicit factor $2p^0$ in the anticommutators of the fields and of the creation and annihilation operators.

Because of Eq. (5.43) and (5.44), this implies for the creation and annihilation operators

$$\begin{aligned}\{a_r^\dagger(\vec{p}), a_s^\dagger(\vec{p}')\} &= \{a_r(\vec{p}), a_s(\vec{p}')\} = 0 \\ \{b_r^\dagger(\vec{p}), b_s^\dagger(\vec{p}')\} &= \{b_r(\vec{p}), b_s(\vec{p}')\} = 0 \\ \{a_r(\vec{p}), a_s^\dagger(\vec{p}')\} &= \delta_{rs}(2\pi)^3 \delta^3(\vec{p} - \vec{p}') \\ \{b_r(\vec{p}), b_s^\dagger(\vec{p}')\} &= \delta_{rs}(2\pi)^3 \delta^3(\vec{p} - \vec{p}').\end{aligned}$$

As an example for the relation of field operator and ladder operator anti-commutation relations, we calculate $\{\psi(\vec{x}, t), \bar{\psi}(\vec{x}', t)\}$, assuming anti-commutation relations for the creation and annihilation operators:

$$\begin{aligned}\{\psi(\vec{x}, t), \bar{\psi}(\vec{y}, t)\} &= \int \frac{d^3p d^3\vec{q}}{(2\pi)^6} \frac{1}{\sqrt{2p^0 2q^0}} \sum_{r,s} \left[e^{ip \cdot x} e^{-iqy} v_r(p) \bar{v}_s(q) \{b_r^\dagger(\vec{p}), b_s(\vec{q})\} \right. \\ &\quad \left. + e^{-ip \cdot x} e^{iqy} u_r(p) \bar{u}_s(q) \{a_r(\vec{p}), a_s^\dagger(\vec{q})\} \right] \\ &= \int \frac{d^3p}{(2\pi)^3} \frac{1}{2p^0} \left[e^{-i\vec{p}(\vec{x}-\vec{y})} \sum_s v_s(p) \bar{v}_s(p) + e^{i\vec{p}(\vec{x}-\vec{y})} \sum_s u_s(p) \bar{u}_s(p) \right]\end{aligned}$$

which, using the completeness relations, Eq. (5.41) and (5.42),

$$\begin{aligned}&= \int \frac{d^3p}{(2\pi)^3} \frac{1}{2p^0} \left[e^{-i\vec{p}(\vec{x}-\vec{y})} \underbrace{(p^0 \gamma^0)}_{\text{even}} - \underbrace{\vec{p} \cdot \vec{\gamma}}_{\text{odd}} - m + e^{i\vec{p}(\vec{x}-\vec{y})} \underbrace{(p^0 \gamma^0)}_{\text{even}} - \underbrace{\vec{p} \cdot \vec{\gamma}}_{\text{odd}} + m \right] \\ &= \gamma^0 \int \frac{d^3p}{(2\pi^3)} e^{i\vec{p}(\vec{x}-\vec{y})} = \gamma^0 \delta^3(\vec{x} - \vec{y}).\end{aligned}$$

However, in the laboratory one prepares in general (to a first approximation) momentum eigenstates, rather than position eigenstates. Therefore, we give the expression² for the momentum operator:

$$P^\mu = \int \frac{d^3k}{(2\pi)^3} k^\mu \sum_s \left(a_s^\dagger(\vec{k}) a_s(\vec{k}) + b_s^\dagger(\vec{k}) b_s(\vec{k}) \right)$$

which is just the momentum weighted with the number operator $N = a^\dagger a + b^\dagger b$. Using the anti-commutation relations for the ladder operators, one can show that the momentum operator fulfills the following useful commutation relations:

$$\begin{aligned}[P^\mu, a_s^\dagger(\vec{p})] &= p^\mu a_s^\dagger(\vec{p}) \\ [P^\mu, b_s^\dagger(\vec{p})] &= p^\mu b_s^\dagger(\vec{p}) \\ [P^\mu, a_s(\vec{p})] &= -p^\mu a_s(\vec{p}) \\ [P^\mu, b_s(\vec{p})] &= -p^\mu b_s(\vec{p}).\end{aligned}$$

²This expression is obtained from Noether's theorem using the technique of normal ordering. These topics are discussed in text books on quantum field theory, e.g. by Peskin/Schroeder [14].

Vacuum state The vacuum state is denoted by $|0\rangle$ and has the property³,

$$P^\mu |0\rangle = 0, \quad (5.45)$$

i.e. the vacuum has no momentum.

Using the commutation relations stated above and the property (5.45), we conclude that,

$$P^\mu a_s^\dagger(\vec{p}) |0\rangle = p^\mu a_s^\dagger(\vec{p}) |0\rangle, \quad (5.46)$$

in other words, the state $a_s^\dagger(\vec{p}) |0\rangle$ is an eigenstate of P^μ with momentum p^μ .

With this fact in mind, we define the following states,

$$|e^-(p, s)\rangle = \sqrt{2E_{\vec{p}}} a_s^\dagger(\vec{p}) |0\rangle, \quad (5.47)$$

$$|e^+(p, s)\rangle = \sqrt{2E_{\vec{p}}} b_s^\dagger(\vec{p}) |0\rangle, \quad (5.48)$$

of a particle respectively antiparticle with momentum eigenstate p and spin s .

The factor $\sqrt{2E_{\vec{p}}}$ is there in order to ensure a Lorentz invariant normalization,

$$\begin{aligned} \langle e^-(q, r) | e^-(p, s) \rangle &= 2\sqrt{E_{\vec{q}}E_{\vec{p}}} \langle 0 | a_r(\vec{q}) a_s^\dagger(\vec{p}) | 0 \rangle \\ &= 2\sqrt{E_{\vec{q}}E_{\vec{p}}} \langle 0 | \{a_r(\vec{q}), a_s^\dagger(\vec{p})\} - a_s^\dagger(\vec{p}) \underbrace{a_r(\vec{q}) | 0 \rangle}_{=0} \\ &= \delta_{rs} 2E_{\vec{p}} (2\pi)^3 \delta^{(3)}(\vec{q} - \vec{p}). \end{aligned}$$

The definition of states (5.47) and (5.48) corresponds to a continuum normalization in infinite volume. From the above equation, it can be seen that the dimensionality of the one-particle norm $\langle e^-(p, s) | e^-(p, s) \rangle$ is,

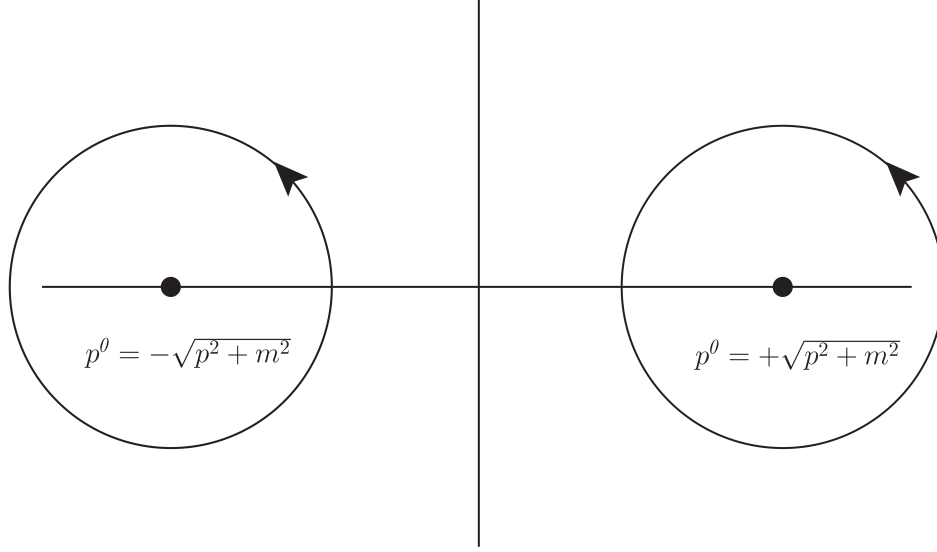
$$\frac{(\text{energy})}{(\text{momentum})^3} = (\text{energy}) \cdot (\text{volume}),$$

meaning that we have a constant particle density of $2E$ particles per unit volume. To obtain single particle states in a given volume V , one must therefore multiply $|e^-(p, s)\rangle$ with a normalization factor $1/\sqrt{2EV}$:

$$|e^-(p, s)\rangle_{\text{single-particle}} = \frac{1}{\sqrt{2EV}} |e^-(p, s)\rangle \quad (5.49)$$

$$|e^+(p, s)\rangle_{\text{single-particle}} = \frac{1}{\sqrt{2EV}} |e^+(p, s)\rangle \quad (5.50)$$

³After applying the nontrivial concept of normal ordering, here only motivated by the number interpretation in the operator P^μ .

Figure 5.2: *Integration paths for Dirac propagator.*

5.4 Dirac propagator

In order to solve general Dirac equations, we want to apply a formalism similar to the one used in classical electrodynamics, namely Green's functions.

We introduce the scalar propagator,

$$\begin{aligned}\Delta^\pm(x) &= \pm \frac{1}{i} \int \frac{d^3p}{(2\pi)^3 2p^0} e^{\mp i p \cdot x} \\ &= \pm \frac{1}{i} \int \frac{d^4p}{(2\pi)^3} \delta(p^2 - m^2) e^{\mp i p \cdot x},\end{aligned}\tag{5.51}$$

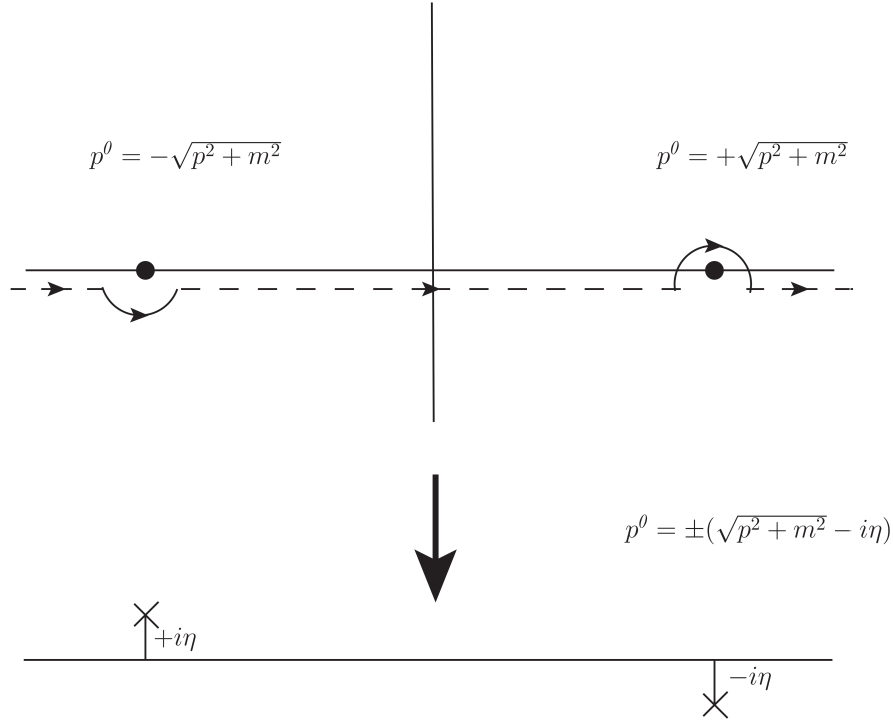
which satisfies the Klein-Gordon equation,

$$(\square + m^2)\Delta^\pm(x) = 0.$$

Representation as a contour integral

$$\Delta^\pm(x) = - \int_{C^\pm} \frac{d^4p}{(2\pi)^4} \frac{e^{-i p \cdot x}}{p^2 - m^2},\tag{5.52}$$

where the paths C^\pm are depicted in Fig. 5.2.

Figure 5.3: *Deformed integration paths and $+i\varepsilon$ convention.*

5.4.1 Feynman propagator

To get a “true” Green’s function for the operator $\square + m^2$, we need to introduce a discontinuity, and define the Feynman propagator

$$\Delta_F(x) = \theta(t)\Delta^+(x) - \theta(-t)\Delta^-(x), \quad (5.53)$$

where we deform the paths of Fig. 5.3 according to the sign of $t = x^0$ to get convergent integrals over the real line (details can be found in a complex analysis book, see e.g. Freitag & Busam [15]) :

- $x^0 > 0, \text{Im } p^0 < 0 \Rightarrow e^{-ip^0 x^0} \xrightarrow{R \rightarrow \infty} 0 : C^+,$
- $x^0 < 0, \text{Im } p^0 > 0 \Rightarrow e^{-ip^0 x^0} \xrightarrow{R \rightarrow \infty} 0 : C^-.$

$+i\varepsilon$ convention Instead of deforming the integration path, one can also shift the two poles and integrate over the whole real p^0 -axis, without having to worry about the poles,

$$p^0 = \pm\sqrt{\vec{p}^2 + m^2} \longrightarrow \pm(\sqrt{\vec{p}^2 + m^2} - i\eta),$$

yielding

$$\Delta_F(x) = \lim_{\varepsilon \rightarrow 0^+} \int \frac{d^4 p}{(2\pi)^4} \frac{e^{-ip \cdot x}}{p^2 - m^2 + i\varepsilon}, \quad (5.54)$$

the Green's function of the Klein-Gordon equation,

$$(\square + m^2)\Delta_F(x) = \int \frac{d^4 p}{(2\pi)^4} e^{-ip \cdot x} \frac{-p^2 + m^2}{p^2 - m^2} = -\delta^{(4)}(x). \quad (5.55)$$

Propagator A propagator is the transition amplitude of a particle between creation at x^μ and annihilation at x'^μ (or vice-versa). It is a fundamental tool of quantum field theory.

After getting the Feynman propagator for the Klein-Gordon field (spin 0), we want to focus on the propagator for fermions (spin 1/2).

We compute the anticommutation relations for the field in this case getting,

$$\begin{aligned} \{\psi(x), \bar{\psi}(x')\} &= \int \frac{d^3 p d^3 p'}{(2\pi)^6 \sqrt{2p^0} \sqrt{2p'^0}} \sum_{r,s} \left[e^{i(p \cdot x - p' \cdot x')} v_r(p) \bar{v}_s(p') \{b_r^\dagger(p), b_s(p')\} \right. \\ &\quad \left. e^{-i(p \cdot x - p' \cdot x')} u_r(p) \bar{u}_s(p') \{a_r(p), a_s^\dagger(p')\} \right] \\ &= \int \frac{d^3 p}{(2\pi)^3 2p^0} \left[e^{ip \cdot (x - x')} (\not{p} - m) + e^{-ip \cdot (x - x')} (\not{p} + m) \right] \\ &= (i\not{\partial} + m) \int \frac{d^3 p}{(2\pi)^3 2p^0} \left(e^{-ip \cdot (x - x')} - e^{ip \cdot (x - x')} \right), \end{aligned} \quad (5.56)$$

where we made use of the completeness relations (5.41) and (5.42) in going from the first to the second line.

We now define the **Feynman fermion propagator**,

$$iS(x - x') \equiv (i\not{\partial} + m)(\Delta^+(x - x') + \Delta^-(x - x')). \quad (5.57)$$

Splitting ψ and $\bar{\psi}$ in their creation $\psi^-, \bar{\psi}^-$ and annihilation $\psi^+, \bar{\psi}^+$ parts (looking only at the operators a_s^\dagger, b_s^\dagger and a_s, b_s respectively), we get the comutation relations,

$$\{\psi^+(x), \bar{\psi}^-(x')\} = (i\not{\partial} + m)\Delta^+(x - x') = iS^+(x - x'), \quad (5.58)$$

$$\{\psi^-(x), \bar{\psi}^+(x')\} = (i\not{\partial} + m)\Delta^-(x - x') = iS^-(x - x'). \quad (5.59)$$

$S^\pm(x - x')$ can as well be represented as contour integrals,

$$S^\pm(x) = \int_{C^\pm} \frac{d^4 p}{(2\pi)^4} e^{-ip \cdot x} \frac{\not{p} + m}{p^2 - m^2} = \int_{C^\pm} \frac{d^4 p}{(2\pi)^4} e^{-ip \cdot x} \frac{1}{\not{p} - m}, \quad (5.60)$$

which is well defined because $(\not{p} + m)(\not{p} - m) = (p^2 - m^2)\mathbb{1}$.

We take a look at the time ordered product of fermion operators,

$$\begin{aligned} T(\psi(x)\bar{\psi}(x')) &= \begin{cases} \psi(x)\bar{\psi}(x'), & t > t' \\ -\bar{\psi}(x')\psi(x), & t' > t \end{cases} \\ &= \theta(t - t')\psi(x)\bar{\psi}(x') - \theta(t' - t)\bar{\psi}(x')\psi(x). \end{aligned}$$

The Feynman fermion propagator is then the vacuum expectation value of this time ordered product,

$$iS_F(x - x') = \langle 0 | T(\psi(x)\bar{\psi}(x')) | 0 \rangle. \quad (5.61)$$

Remembering the destroying effect of annihilation operators on the vacuum, we can skip some trivial steps of the calculation. We look separately at both time ordering cases, getting,

$$\begin{aligned} \langle 0 | \psi(x)\bar{\psi}(x') | 0 \rangle &= \langle 0 | \psi^+(x)\bar{\psi}^-(x') | 0 \rangle = \langle 0 | \{\psi^+(x), \bar{\psi}^-(x')\} | 0 \rangle = iS^+(x - x'), \\ \langle 0 | \bar{\psi}(x')\psi(x) | 0 \rangle &= \langle 0 | \bar{\psi}^+(x')\psi^-(x) | 0 \rangle = \langle 0 | \{\bar{\psi}^+(x'), \psi^-(x)\} | 0 \rangle = iS^-(x - x'), \end{aligned}$$

yielding,

$$S_F(x) = \theta(t)S^+(x) - \theta(-t)S^-(x) = (i\not{\partial} + m)\Delta_F(x), \quad (5.62)$$

or, as a contour integral,

$$S_F(x) = \int_{C_F} \frac{d^4p}{(2\pi)^4} e^{-ip \cdot x} \frac{1}{\not{p} - m} = \lim_{\varepsilon \rightarrow 0^+} \int \frac{d^4p}{(2\pi)^4} e^{-ip \cdot x} \frac{\not{p} + m}{p^2 - m^2 + i\varepsilon}. \quad (5.63)$$

We then see that the fermion propagator is nothing else than the Green's function of the Dirac equation,

$$(i\not{\partial} - m)S_F(x) = \int \frac{d^4p}{(2\pi)^4} e^{-ip \cdot x} \frac{(\not{p} - m)(\not{p} + m)}{p^2 - m^2} = \delta^{(4)}(x)\mathbb{1}. \quad (5.64)$$

The interpretation of S_F is then similar to the one of the Green's function in classical electrodynamics:

$$x' \text{ creation} \quad t > t' \qquad t' > t \quad x' \text{ annihilation}$$



x annihilation x creation

We can ask ourselves why the time ordering procedure is important. In scattering processes both orderings are not distinguishable (see Fig. 5.4) in experiments, so that we can understand as a sum over both time ordering possibilities.

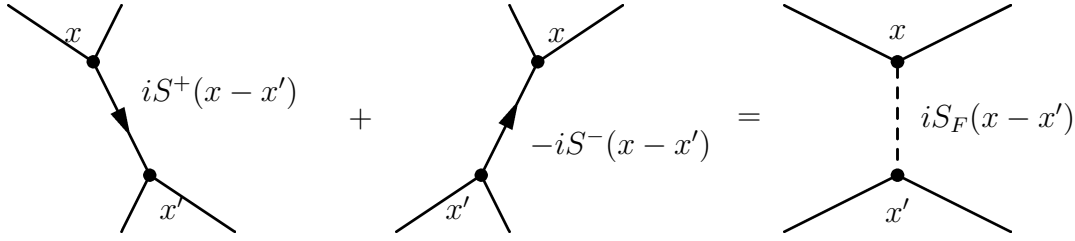


Figure 5.4: Sum of both time orderings

5.5 Photon field operator

After being able to describe free scalar fields (Klein-Gordon, spin 0) and free fermion fields (Dirac, spin 1/2), we go on to vector fields (spin 1) like the one describing the photon. The photon field will be shown to have a fundamental importance in QED since it is the interaction field between fermions.

To start, we recall the photon field operator of advanced quantum mechanics, which reads in Coulomb gauge,

$$\vec{A}(x) = \sum_{\alpha=1,2} \int \frac{d^3k}{(2\pi)^3} \frac{1}{\sqrt{2\omega_k}} \left(a_{\alpha}(\vec{k}) \vec{\varepsilon}_{\alpha}(\vec{k}) e^{-ik \cdot x} + a_{\alpha}^{\dagger}(\vec{k}) \vec{\varepsilon}_{\alpha}^*(\vec{k}) e^{ik \cdot x} \right). \quad (5.65)$$

In Eq. (5.65), $a_{\alpha}^{\dagger}(\vec{k})$ creates a photon of momentum \vec{k} and polarization α , and $a_{\alpha}(\vec{k})$ destroys the same.

Since we are dealing with a bosonic field, we impose the commutation relations,

$$[a_{\alpha}(\vec{k}), a_{\beta}^{\dagger}(\vec{k}')] = -g_{\alpha\beta} (2\pi)^3 \delta^{(3)}(\vec{k} - \vec{k}'), \quad (5.66)$$

$$[a_{\alpha}(\vec{k}), a_{\beta}(\vec{k}')] = [a_{\alpha}^{\dagger}(\vec{k}), a_{\beta}^{\dagger}(\vec{k}')] = 0. \quad (5.67)$$

Supposing that the photon propagates in the z -direction ($k^{\mu} = (k, 0, 0, k)^{\top}$), we have the following possibilities for the polarization vectors :

- linear : $\varepsilon_1^{\mu} = (0, 1, 0, 0)^{\top}$, $\varepsilon_2^{\mu} = (0, 0, 1, 0)^{\top}$,
- circular : $\varepsilon_+^{\mu} = \frac{1}{\sqrt{2}}(\varepsilon_1^{\mu} + i\varepsilon_2^{\mu}) = \frac{1}{\sqrt{2}}(0, 1, i, 0)^{\top}$, $\varepsilon_-^{\mu} = \frac{1}{\sqrt{2}}(\varepsilon_1^{\mu} - i\varepsilon_2^{\mu}) = \frac{1}{\sqrt{2}}(0, 1, -i, 0)^{\top}$.

These vector sets satisfy the completeness relation,

$$\Pi^{\mu\nu} = \sum_{\substack{\lambda = \pm \\ (\text{or } \lambda = 1, 2)}} \varepsilon_{\lambda}^{*\mu} \varepsilon_{\lambda}^{\nu} = \begin{pmatrix} 0 & & & \\ & 1 & & \\ & & 1 & \\ & & & 0 \end{pmatrix}. \quad (5.68)$$

By applying a well chosen boost to $\Pi^{\mu\nu}$ we can easily check that it is in general not Lorentz invariant. We have to choose a specific gauge depending on the reference frame, parametrized by a real number n .

To do so we define a auxiliary vector $n^\mu = n(1, 0, 0, -1)^\top$ satisfying $n_\sigma k^\sigma = 2kn$ and get the “axial gauge”,

$$\Pi^{\mu\nu} = -g^{\mu\nu} + \frac{n^\mu k^\nu + k^\mu n^\nu}{n_\sigma k^\sigma}. \quad (5.69)$$

For $n = 1$, we recover the Coulomb gauge,

$$\Pi^{\mu\nu} = \begin{pmatrix} -1 & & & \\ & 1 & & \\ & & 1 & \\ & & & 1 \end{pmatrix} + \begin{pmatrix} 1 & & & \\ & 0 & & \\ & & 0 & \\ & & & -1 \end{pmatrix} = \begin{pmatrix} 0 & & & \\ & 1 & & \\ & & 1 & \\ & & & 0 \end{pmatrix}.$$

In physical processes, the photon field couples to an external current,

$$j^\mu(x) = j^\mu(k)e^{ik \cdot x},$$

and we have the current conservation,

$$\partial_\mu j^\mu = 0,$$

which yields in Fourier space,

$$k_\mu j^\mu = 0,$$

and thus,

$$j_\mu \Pi^{\mu\nu} = j_\nu \Pi^{\mu\nu} = 0,$$

i.e. the $n^\mu k^\nu + k^\mu n^\nu$ term vanishes when contracted with external currents, such that we are left with an effective polarization sum,

$$p_{\text{eff}}^{\mu\nu} = -g^{\mu\nu}. \quad (5.70)$$

We now look at the time ordered product of photon field operators,

$$T(A_\mu(x)A_\nu(x')) = \begin{cases} A_\mu(x)A_\nu(x'), & t > t' \\ A_\nu(x')A_\mu(x), & t' > t \end{cases}. \quad (5.71)$$

Repeating the same steps as in the fermion case, we get the **photon propagator**,

$$iD_{F,\mu\nu}(x - x') = \langle 0 | T(A_\mu(x)A_\nu(x')) | 0 \rangle \quad (5.72)$$

$$= -ig_{\mu\nu}\Delta_F(x - x') \quad (5.73)$$

$$= -ig_{\mu\nu} \lim_{\varepsilon \rightarrow 0+} \int \frac{d^4 k}{(2\pi)^4} \frac{e^{-ik \cdot x}}{k^2 + i\varepsilon}. \quad (5.74)$$

Finally, we see that the photon propagator is the Green’s function of the wave equation,

$$\square D_{F,\mu\nu}(x) = g_{\mu\nu}\delta^{(4)}(x). \quad (5.75)$$

5.6 Interaction representation

In the previous sections, we have gained an understanding of the free fields occurring in QED. The next step is to introduce a way to handle interactions between those fields.

Idea: decompose the Hamiltonian in the Schrödinger representation,

$$H_S = H_{0,S} + H'_S,$$

and define states and operators in the free Heisenberg representation,

$$\begin{aligned}\psi_I &= e^{iH_0, st} \psi_S \\ O_I &= e^{iH_0, st} O_S e^{-iH_0, st},\end{aligned}$$

and you get the **interaction representation** (also called **Dirac representation**).

We have, in particular,

$$H_{0,I} = H_{0,S} = H_0, \tag{5.76}$$

and the time evolution of ψ_I respectively O_I becomes,

$$i\partial_t \psi_I = H'_I \psi_I, \tag{5.77}$$

$$i\partial_t O_I = -H_0 O_I + O_I H_0 = [O_I, H_0], \tag{5.78}$$

i.e. ψ_I is influenced only by the “true” interaction part; the “trivial” time evolution (free part) has been absorbed in the operators O_I .

Comparison The Schrödinger, Heisenberg, and interaction representations differ in the way they describe time evolution:

- Schrödinger representation: states contain time evolution, operators are time independent;
- Heisenberg representation: states are time independent, operators contain time evolution;
- Interaction representation: time dependence of states only due to interactions, free (also called “trivial”) time evolution for operators.

This comparison shows that the interaction representation is a mixture of both other representations.

5.6.1 Time evolution operator

In preparation for time-dependent perturbation theory, we consider the time evolution operator $U(t, t_0)$ in the interaction representation:

$$\psi_I(t) = U(t, t_0)\psi_I(t_0). \quad (5.79)$$

The time evolution operator in Eq. (5.79) can be written in terms of the free and interaction Hamiltonians, Eq. (5.76), in the Schrödinger representation by using the time evolution properties:

$$\psi_I(t) = e^{iH_0 t}\psi_S(t) = e^{iH_0 t}e^{-iH_S(t-t_0)}\psi_S(t_0) = e^{iH_0 t}e^{-iH_S(t-t_0)}e^{-iH_0 t_0}\psi_I(t_0).$$

Comparing this result with Eq. (5.79) yields

$$U(t, t_0) = e^{iH_0 t}e^{-iH_S(t-t_0)}e^{-iH_0 t_0}. \quad (5.80)$$

An interaction picture operator is related by

$$O_H(t) = U^\dagger(t, t_0)O_I U(t, t_0)$$

to its Heisenberg picture equivalent.

Because of Eq. (5.80) the time evolution operator has the following properties:

- $U(t_0, t_0) = \mathbb{1}$,
- $U(t_2, t_1)U(t_1, t_0) = U(t_2, t_0)$,
- $U^{-1}(t_0, t_1) = U(t_1, t_0)$, and
- $U^\dagger(t_1, t_0) = U^{-1}(t_1, t_0) = U(t_0, t_1)$.

5.6.2 Time ordering

To find the time evolution operator, the time evolution (Schrödinger) equation

$$i\frac{\partial}{\partial t}U(t, t_0) = H'_I U(t, t_0) \quad (5.81)$$

has to be solved. This is equivalent to the integral equation

$$U(t, t_0) = \mathbb{1} + (-i) \int_{t_0}^t dt_1 H'_I(t_1)U(t_1, t_0)$$

which can be iterated to give the Neumann series

$$U(t, t_0) = \mathbb{1} + (-i) \int_{t_0}^t dt_1 H'_I(t_1) \quad (5.82)$$

$$+ (-i)^2 \int_{t_0}^t dt_1 \int_{t_0}^{t_1} dt_2 H'_I(t_1) H'_I(t_2) \quad (5.83)$$

$$+ \dots \quad (5.84)$$

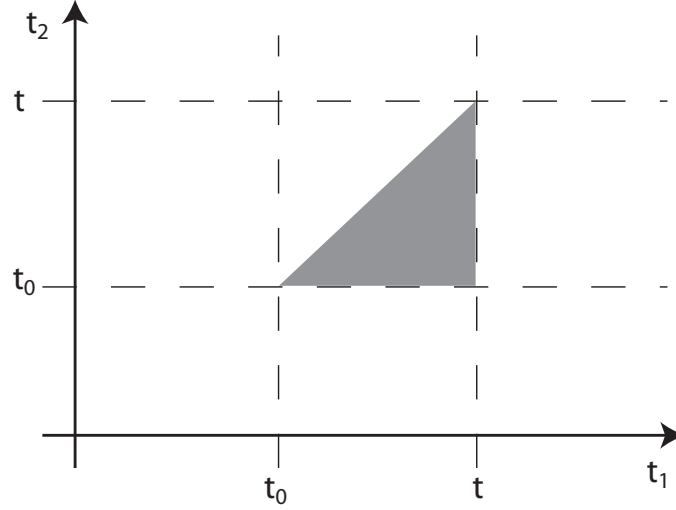
$$+ (-i)^n \int_{t_0}^t dt_1 \int_{t_0}^{t_1} dt_2 \dots \int_{t_0}^{t_{n-1}} dt_n H'_I(t_1) \dots H'_I(t_n). \quad (5.85)$$

This is not yet satisfactory since the boundary of every integral but the first depends on the foregoing integration. To solve this problem, one uses time ordering. Let us first consider the following identities:

$$\begin{aligned} \int_{t_0}^t dt_1 \int_{t_0}^{t_1} dt_2 H'_I(t_1) H'_I(t_2) &= \int_{t_0}^t dt_2 \int_{t_2}^t dt_1 H'_I(t_1) H'_I(t_2) \\ &= \int_{t_0}^t dt_1 \int_{t_1}^t dt_2 H'_I(t_2) H'_I(t_1) \end{aligned}$$

where in the first line the integration domains are identical (see Fig. 5.5) and in going to the second line the variable labels are exchanged. We can combine these terms in a more compact expression:

$$\begin{aligned} &2 \int_{t_0}^t dt_1 \int_{t_0}^{t_1} dt_2 H'_I(t_1) H'_I(t_2) \\ &= \int_{t_0}^t dt_2 \int_{t_2}^t dt_1 H'_I(t_1) H'_I(t_2) + \int_{t_0}^t dt_1 \int_{t_1}^t dt_2 H'_I(t_2) H'_I(t_1) \\ &= \int_{t_0}^t dt_1 \int_{t_0}^t dt_2 \left(H'_I(t_1) H'_I(t_2) \theta(t_1 - t_2) + H'_I(t_2) H'_I(t_1) \theta(t_2 - t_1) \right) \\ &= \int_{t_0}^t dt_1 \int_{t_0}^t dt_2 T \left(H'_I(t_1) H'_I(t_2) \right). \end{aligned}$$

Figure 5.5: *Identical integration domains.*

All terms of the Neumann series can be rewritten in this way. For the n -th term in Eq. (5.85) we have

$$\begin{aligned} n! \int_{t_0}^t dt_1 \dots \int_{t_0}^{t_{n-1}} dt_n H'_I(t_1) \dots H'_I(t_n) \\ = \int_{t_0}^t dt_1 \dots \int_{t_0}^t dt_n T\left(H'_I(t_1) \dots H'_I(t_n)\right). \end{aligned}$$

We therefore obtain the following perturbation series⁴ for the time evolution operator:

$$U(t, t_0) = \sum_{n=0}^{\infty} \frac{1}{n!} (-i)^n \int_{t_0}^t dt_1 \dots \int_{t_0}^t dt_n T\left(H'(t_1) \dots H'(t_n)\right). \quad (5.86)$$

Defining the time ordered exponential, Eq. (5.86) can be written as

$$\boxed{U(t, t_0) = T \exp \left(-i \int_{t_0}^t dt' H'(t') \right)}. \quad (5.87)$$

⁴We are working in the interaction picture and drop the index I for simplicity.

We check that this result indeed solves the time evolution equation (5.81):

$$\begin{aligned}
 i \frac{\partial}{\partial t} U(t, t_0) &= i \sum_{n=1}^{\infty} \frac{1}{n!} (-i)^n n \int_{t_0}^t dt_1 \dots \int_{t_0}^t dt_{n-1} \\
 &\quad T \left(H'(t_0) \dots H'(t_{n-1}) H'(t) \right) \\
 &= H'(t) \sum_{n=1}^{\infty} \frac{1}{(n-1)!} (-i)^{n-1} \int_{t_0}^t dt_1 \dots \int_{t_0}^t dt_{n-1} \\
 &\quad T \left(H'(t_0) \dots H'(t_{n-1}) \right) \\
 &= H'(t) U(t, t_0).
 \end{aligned}$$

5.7 Scattering matrix

Our overall aim is to develop a formalism to compute scattering matrix elements which describe the transition from initial states defined at $t \rightarrow -\infty$ to final states observed at $t \rightarrow +\infty$. To this end, we split up the Hamiltonian into a solvable free part which determines the operators' time evolution and an interaction part responsible for the time evolution of the states. Now we investigate how the time ordered exponential that is the time evolution operator, see Eq. (5.87), relates to the \mathcal{S} -matrix.

The scattering matrix element $\langle f | \mathcal{S} | i \rangle$ is the transition amplitude for $|i\rangle \rightarrow |f\rangle$ caused by interactions. The state of the system is described by the time dependent state vector $|\psi(t)\rangle$. The above statement about asymptotically large times can now be recast in a more explicit form: The initial state is given by

$$\lim_{t \rightarrow -\infty} |\psi(t)\rangle = |\phi_i\rangle$$

where $|\phi_i\rangle$ is an eigenstate of the free Hamilton operator and $t \rightarrow -\infty$ is justified since the interaction timescale is about 10^{-15} s. The scattering matrix element \mathcal{S}_{fi} is given by the projection of the state vector $|\psi(t)\rangle$ onto a final state $|\phi_f\rangle$:

$$\mathcal{S}_{fi} = \lim_{t \rightarrow +\infty} \langle \phi_f | \psi(t) \rangle = \langle \phi_f | \mathcal{S} | \phi_i \rangle.$$

Using the time evolution operator (and its action on a state, see Eq. (5.79)), this can be expressed as

$$\mathcal{S}_{fi} = \lim_{t_2 \rightarrow +\infty} \lim_{t_1 \rightarrow -\infty} \langle \phi_f | U(t_2, t_1) | \phi_i \rangle.$$

We can therefore conclude that

$$\boxed{\mathcal{S} = U(+\infty, -\infty)} = \sum_{n=0}^{\infty} \frac{1}{n!} (-i)^n \int_{-\infty}^{\infty} dt_1 \dots \int_{-\infty}^{\infty} dt_n T \left(H'(t_1) \dots H'(t_n) \right). \quad (5.88)$$

As an instructive example, we consider $2 \rightarrow 2$ scattering:

$$k_1 + k_2 \rightarrow k_3 + k_4.$$

The scattering matrix element is given by

$$\mathcal{S}_{fi} = \langle f | \mathcal{S} | i \rangle = \underbrace{\langle 0 | a(k_4) a(k_3)}_{\langle \phi_f |} | \mathcal{S} | \underbrace{a^\dagger(k_1) a^\dagger(k_2) | 0 \rangle}_{| \phi_i \rangle}.$$

The \mathcal{S} -operator itself consists of further creation and annihilation operators belonging to further quantum fields. By evaluation of the creators and annihilators in \mathcal{S} (using commutation or anticommutation relations), it follows that there is only one single non-vanishing contribution to \mathcal{S}_{fi} being of the (“normally ordered”) form

$$f(k_1, k_2, k_3, k_4) a^\dagger(k_3) a^\dagger(k_4) a(k_2) a(k_1).$$

Note that in the above expression, the annihilation operators stand on the right hand side, while the creation operators are on the left. Such expressions are said to be in normal order and are denoted by colons, $: ABC :$. Since the aim is to find the non-vanishing contributions, a way has to be found how time ordered products can be related to products in normal order. For instance, consider the time ordered product of two Boson field operators (where A^+ , B^+ are annihilators and A^- , B^- creators)⁵

$$\begin{aligned} T\left(A(x_1)B(x_2)\right)\Big|_{t_1 > t_2} &= A(x_1)B(x_2) \\ &= A^+(x_1)B^+(x_2) + A^-(x_1)B^+(x_2) \\ &\quad + \underbrace{A^+(x_1)B^-(x_2)}_{\text{not in normal order}} + A^-(x_1)B^-(x_2). \end{aligned}$$

⁵The \pm sign is motivated by the decomposition of field operators in positive and negative frequency parts:

$$\phi(x) = \phi^+(x) + \phi^-(x).$$

Consider for example the Klein-Gordon field where

$$\phi(x) = \int \frac{d^3p}{(2\pi)^3} \frac{1}{\sqrt{2p^0}} \left(a(p) e^{+i\vec{p}\cdot\vec{x}} + a^\dagger(p) e^{-i\vec{p}\cdot\vec{x}} \right)$$

and therefore

$$\begin{aligned} \phi^+(x) &= \int \frac{d^3p}{(2\pi)^3} \frac{1}{\sqrt{2p^0}} a(p) e^{+i\vec{p}\cdot\vec{x}} \\ \phi^-(x) &= \int \frac{d^3p}{(2\pi)^3} \frac{1}{\sqrt{2p^0}} a^\dagger(p) e^{-i\vec{p}\cdot\vec{x}}. \end{aligned}$$

One can observe that only one of the above terms is not in normal order while the other three would vanish upon evaluation in $\langle 0 | \cdot | 0 \rangle$. Using

$$\underbrace{A^+(x_1)B^-(x_2)}_{\text{not in normal order}} = \underbrace{B^-(x_2)A^+(x_1)}_{\text{in normal order}} + \underbrace{[A^+(x_1), B^-(x_2)]}_{\text{c-number}},$$

we rewrite

$$\begin{aligned} [A^+(x_1), B^-(x_2)] &= \langle 0 | [A^+(x_1), B^-(x_2)] | 0 \rangle \\ &= \langle 0 | A^+(x_1)B^-(x_2) | 0 \rangle \\ &= \langle 0 | T(A(x_1)B(x_2)) | 0 \rangle. \end{aligned}$$

Since the same holds for $t_1 < t_2$, we draw the conclusion

$$T\left(A(x_1)B(x_2)\right) = :A(x_1)B(x_2): + \langle 0 | T(A(x_1)B(x_2)) | 0 \rangle.$$

An analogous calculation for fermion operators yields the same result.

The next step towards Feynman diagrams is to formalize this connection between time and normal ordered products. We first define the following shorthand

$$\underbrace{\phi_A(x_1)\phi_B(x_2)} = \langle 0 | T(\phi_A(x_1)\phi_B(x_2)) | 0 \rangle$$

which is called contraction of operators. This allows to state the following in compact notation.

Wick's theorem: The time ordered product of a set of operators can be decomposed into the sum of all corresponding contracted products in normal order. All combinatorially allowed contributions appear:

$$\begin{aligned} T(ABC \dots XYZ) &= :ABC \dots XYZ: \\ &+ :\underbrace{AB}C \dots XYZ: + \dots + :\underbrace{ABC \dots XYZ}: + \dots + :ABC \dots \underbrace{XY}Z: \\ &+ :\underbrace{AB} \underbrace{CD} \dots XYZ: + :\underbrace{ABCD} \dots XYZ: + \dots \\ &+ :\text{threefold contractions}: + \dots \end{aligned}$$

5.8 Feynman rules of quantum electrodynamics

The Lagrangian density of QED is given by

$$\mathcal{L} = \mathcal{L}_0^{\text{Dirac}} + \mathcal{L}_0^{\text{photon}} + \mathcal{L}'$$

where the subscript 0 denotes the free Lagrangian densities and ' denotes the interaction part. In particular, we have

$$\mathcal{L}_0^{\text{Dirac}} = \bar{\psi}(i\cancel{D} - m)\psi \quad (5.89)$$

$$\mathcal{L}_0^{\text{photon}} = -\frac{1}{4}F_{\mu\nu}F^{\mu\nu} \quad (5.90)$$

$$\mathcal{L}' = -e\bar{\psi}\gamma_\mu\psi A^\mu = -j_\mu A^\mu \quad (5.91)$$

where $F^{\mu\nu} = \partial^\mu A^\nu - \partial^\nu A^\mu$. Note that from $\mathcal{L}_0^{\text{photon}}$ the free Maxwell's equations can be derived using the Euler-Lagrange equations. Using $\mathcal{L}_0^{\text{photon}} + \mathcal{L}'$ yields Maxwell's equations in the presence of sources and $\mathcal{L}_0^{\text{Dirac}} + \mathcal{L}'$ does the same for the Dirac equation. The interaction term \mathcal{L}' describes current-field interactions and therefore couples the fermions described by the Dirac equation to photons described by Maxwell's equations.

Using Eq. (5.91), one finds the quantized interaction Hamiltonian density

$$\mathcal{H}' = -\mathcal{L}' = e\bar{\psi}\gamma_\mu\psi A^\mu.$$

Integrating the interaction Hamiltonian density over all space yields the interaction Hamiltonian,

$$H' = \int d^3\vec{x} \mathcal{H}',$$

and, in the integral representation of \mathcal{S} given in Eq. (5.88), this leads to integrations over space-time:

$$\mathcal{S} = \sum_{n=0}^{\infty} \frac{1}{n!} (-ie)^n \int d^4x_1 \dots d^4x_n T\left(\bar{\psi}(x_1)\gamma_{\mu_1}\psi(x_1)A^{\mu_1} \dots \bar{\psi}(x_n)\gamma_{\mu_n}\psi(x_n)A^{\mu_n}\right). \quad (5.92)$$

Since $e = \sqrt{4\pi\alpha}$ (see Eq. (1.9)), the coupling constant appears in the interaction term and n -th order terms are suppressed with e^n . This means that we found an expansion of \mathcal{S} in the small parameter e which is the starting point for perturbation theory. The structure of the n -th term in the perturbation series in Eq. (5.92) is

$$\mathcal{S}^{(n)} = \frac{1}{n!} \int d^4x_1 \dots d^4x_n \mathcal{S}_n \quad (5.93)$$

where

$$\mathcal{S}_n = \sum_{\text{contractions}} K(x_1, \dots, x_n) : \dots \bar{\psi}(x_i) \dots \psi(x_j) \dots A(x_n) :. \quad (5.94)$$

For a specific scattering process, the relevant matrix element is

$$\mathcal{S}_{fi} = \underbrace{\langle f |}_{\sim a} \mathcal{S} \underbrace{| i \rangle}_{\sim a^\dagger}$$

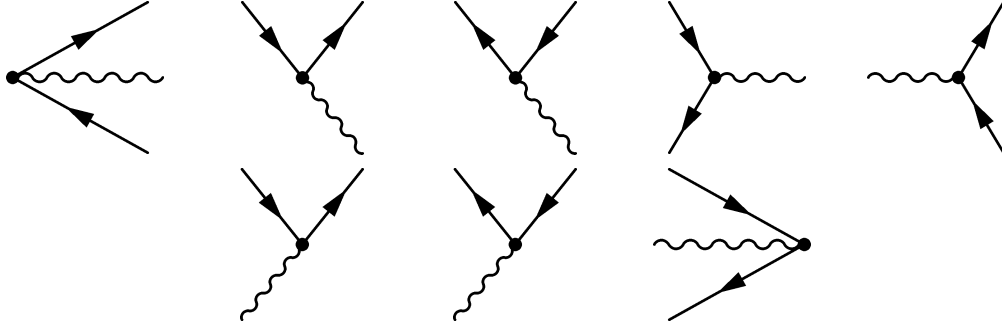


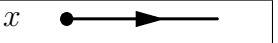
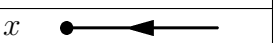
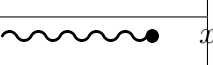
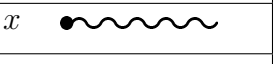
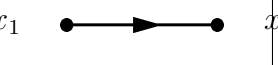
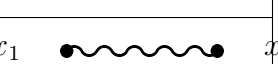
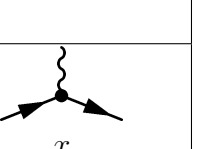


Figure 5.6: *First order contributions* $\mathcal{S}^{(1)}$. These processes violate energy-momentum conservation and are therefore unphysical.

which means that only terms in \mathcal{S} matching $\langle f | \cdot | i \rangle$ yield contributions to the transition amplitude. The following field operators, which constitute the Feynman rules in position space, are contained in $\mathcal{S}(\overrightarrow{\text{time}})$.

| | | |
|--|-------------------------------|---|
| $\psi^+(x)$ | absorption of electron at x |  |
| $\bar{\psi}^+(x)$ | absorption of positron at x |  |
| $\bar{\psi}^-(x)$ | emission of electron at x |  |
| $\psi^-(x)$ | emission of positron at x |  |
| $A^+(x)$ | absorption of photon at x |  |
| $A^-(x)$ | emission of photon at x |  |
| $\underbrace{\psi(x_2)\bar{\psi}(x_1)}_{= iS_F(x_2 - x_1)}$ | Fermion propagator |  |
| $\underbrace{A^\mu(x_2)A^\nu(x_1)}_{= iD_F^{\mu\nu}(x_2 - x_1)}$ | photon propagator |  |
| $-ie\bar{\psi}(x)\gamma_\mu\psi(x)A^\mu(x)$ $= -ie\gamma_\mu \cdot \text{vertex at } x$ | vertex at x |  |

The \mathcal{S} -operator at order n is examined using Wick's theorem. At first order, this yields (remembering Eq. (5.92) while ignoring disconnected contributions from Wick's theorem) the following $2^3 = 8$ contributions:

$$\mathcal{S}^{(1)} = -ie \int d^4x T(\bar{\psi}(x)\gamma_\mu\psi(x)A^\mu(x)) = -ie \int d^4x : \bar{\psi}(x)\gamma_\mu\psi(x)A^\mu(x) :.$$

There is a total of 8 possible combinations, since A^μ creates or annihilates a photon, $\bar{\psi}$ creates an electron or annihilates a positron, and ψ creates a positron or annihilates an electron. Fig. 5.6 shows the corresponding Feynman diagrams.

However, all these processes are unphysical because they violate energy-momentum con-

servation:

$$\pm p_{e^+} \pm p_{e^-} \pm p_\gamma \neq 0$$

which is because free particles fulfill

$$p_{e^+}^2 = m_e^2 \qquad p_{e^-}^2 = m_e^2 \qquad p_\gamma^2 = 0.$$

To find physical contributions to the interaction Hamiltonian, we turn to the second order contributions to \mathcal{S} (see Eq. (5.92)):

$$\mathcal{S}^{(2)} = \frac{1}{2!} (-ie)^2 \int d^4x_1 d^4x_2 T \left(\bar{\psi}(x_1) \gamma_{\mu_1} \psi(x_1) A^{\mu_1}(x_1) \bar{\psi}(x_2) \gamma_{\mu_2} \psi(x_2) A^{\mu_2}(x_2) \right).$$

Application of Wick's theorem yields contraction terms. We first note that contractions of the form

$$\underbrace{\psi(x_1) \psi(x_2)} \qquad \underbrace{\bar{\psi}(x_1) \bar{\psi}(x_2)}$$

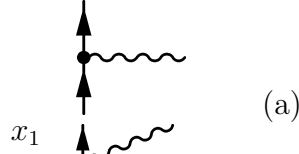
vanish because they contain creators and annihilators, respectively, for different particles and thus

$$\langle 0 | T(\psi(x_1) \psi(x_2)) | 0 \rangle = 0.$$

The remaining terms read, using shorthands like $\bar{\psi}(x_1) = \bar{\psi}_1$,

$$\mathcal{S}^{(2)} = \frac{(-ie)^2}{2!} \int d^4x_1 d^4x_2 \{$$

$$:\bar{\psi}_1 \gamma_{\mu_1} \psi_1 \bar{\psi}_2 \gamma_{\mu_2} \psi_2 A_1^{\mu_1} A_2^{\mu_2} :$$



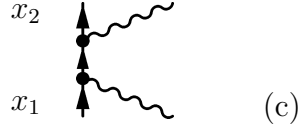
(a)

$$+ :\bar{\psi}_1 \gamma_{\mu_1} \psi_1 \bar{\psi}_2 \gamma_{\mu_2} \psi_2 A_1^{\mu_1} A_2^{\mu_2} :$$



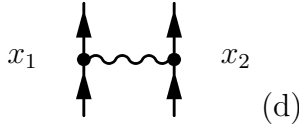
(b)

$$+ :\bar{\psi}_1 \gamma_{\mu_1} \psi_1 \bar{\psi}_2 \gamma_{\mu_2} \psi_2 A_1^{\mu_1} A_2^{\mu_2} :$$



(c)

$$+ :\bar{\psi}_1 \gamma_{\mu_1} \psi_1 \bar{\psi}_2 \gamma_{\mu_2} \psi_2 A_1^{\mu_1} A_2^{\mu_2} :$$



(d)

$$+ :\bar{\psi}_1 \gamma_{\mu_1} \psi_1 \bar{\psi}_2 \gamma_{\mu_2} \psi_2 A_1^{\mu_1} A_2^{\mu_2} :$$



(e)

$$+ :\bar{\psi}_1 \gamma_{\mu_1} \psi_1 \bar{\psi}_2 \gamma_{\mu_2} \psi_2 A_1^{\mu_1} A_2^{\mu_2} :$$



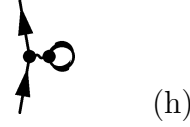
(f)

$$+ :\bar{\psi}_1 \gamma_{\mu_1} \psi_1 \bar{\psi}_2 \gamma_{\mu_2} \psi_2 A_1^{\mu_1} A_2^{\mu_2} :$$



(g)

$$+ :\bar{\psi}_1 \gamma_{\mu_1} \psi_1 \bar{\psi}_2 \gamma_{\mu_2} \psi_2 A_1^{\mu_1} A_2^{\mu_2} :$$



(h)

$$+ :\bar{\psi}_1 \gamma_{\mu_1} \psi_1 \bar{\psi}_2 \gamma_{\mu_2} \psi_2 A_1^{\mu_1} A_2^{\mu_2} :$$



(i)

$$+ :\bar{\psi}_1 \gamma_{\mu_1} \psi_1 \bar{\psi}_2 \gamma_{\mu_2} \psi_2 A_1^{\mu_1} A_2^{\mu_2} :$$



(j)

$$+ :\bar{\psi}_1 \gamma_{\mu_1} \psi_1 \bar{\psi}_2 \gamma_{\mu_2} \psi_2 A_1^{\mu_1} A_2^{\mu_2} : \}.$$



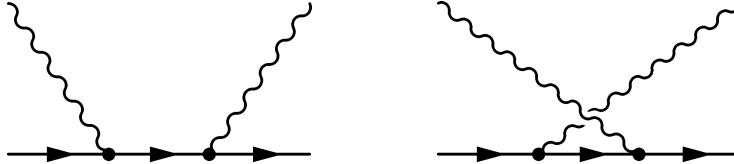
(k)

It follows a discussion of the contributions (a) through (k).

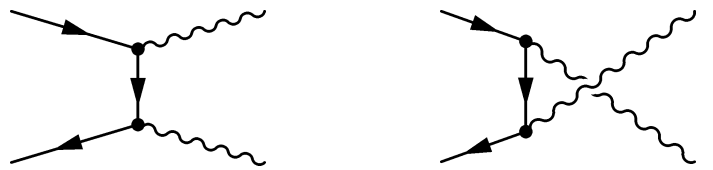
(a) *Independent emission or absorption.* These diagrams violate energy-momentum conservation.

(b)&(c) *Processes involving two electrons or positrons and two photons.*

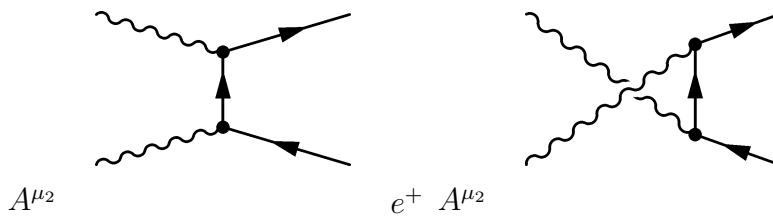
1. Compton scattering: $\gamma e^- \rightarrow \gamma e^-$, $\gamma e^+ \rightarrow \gamma e^+$



2. Electron-positron pair annihilation: $e^+ e^- \rightarrow \gamma \gamma$

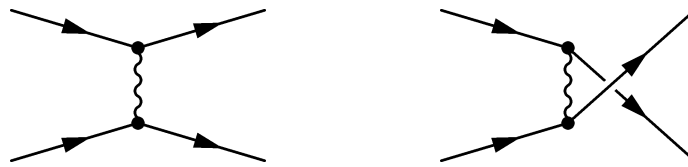


3. Electron-positron pair creation: $\gamma \gamma \rightarrow e^+ e^-$

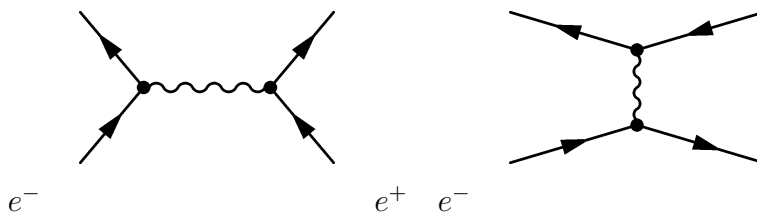


(d) *Processes involving four electrons or positrons.*

1. Møller scattering: $e^- e^- \rightarrow e^- e^-$, $e^+ e^+ \rightarrow e^+ e^+$



2. Bhabha scattering: $e^+ e^- \rightarrow e^+ e^-$



- (e)&(f) *No interaction between external particles.* No scattering takes place, these terms are corrections to the fermion propagator.
- (g) *Correction to photon propagator.*
- (h)&(i) *Corrections to fermion propagator, vanishing.*
- (j)&(k) *Vacuum \rightarrow vacuum transitions, disconnected graphs.*

This constitutes a list of all known processes (for practical purposes) in $\mathcal{S}^{(2)}$; in general, we can find all processes by examining all orders of the scattering matrix operator \mathcal{S} .

The \mathcal{S} -matrix elements are defined as matrix elements between single-particle states. Consequently, we need to apply the norm (5.49) respectively (5.50) to external states. The invariant amplitudes \mathcal{M}_{fi} , which are derived from the \mathcal{S} -matrix elements according to Eq. (3.11) properly account for this normalization factor, and are evaluated for continuum states as defined in Eq. (5.47) and Eq. (5.48).

The contractions of the field operators (see Eq. (5.43) and (5.44)) with external momentum eigenstates (as given in Eq. (5.49) and (5.50)) are for electrons

$$\begin{aligned}\psi(x) |e^-(p, s)\rangle_{\text{single-particle}} &= \frac{1}{\sqrt{2E_p V}} \int \frac{d^3k}{(2\pi)^3} \frac{1}{\sqrt{2E_k}} \sum_r a_r(k) u_r(k) e^{-ik \cdot x} \sqrt{2E_p} a_s^\dagger(p) |0\rangle \\ &= \frac{1}{\sqrt{2E_p V}} e^{-ip \cdot x} u_s(p) |0\rangle \\ \langle e^-(p, s) |_{\text{single-particle}} \bar{\psi}(x) &= \frac{1}{\sqrt{2E_p V}} e^{+ip \cdot x} \langle 0 | \bar{u}_s(p),\end{aligned}$$

for positrons

$$\begin{aligned}\bar{\psi}(x) |e^+(p, s)\rangle_{\text{single-particle}} &= \frac{1}{\sqrt{2E_p V}} e^{-ip \cdot x} \bar{v}_s(p) |0\rangle \\ \langle e^+(p, s) |_{\text{single-particle}} \psi(x) &= \frac{1}{\sqrt{2E_p V}} e^{+ip \cdot x} \langle 0 | v_s(p),\end{aligned}$$

and for photons

$$\begin{aligned}A_\mu(x) |\gamma(k, \lambda)\rangle &= \frac{1}{\sqrt{2E_k V}} e^{-ik \cdot x} \varepsilon_\mu^\lambda(k) \\ \langle \gamma(k, \lambda) | A_\mu(x) &= \frac{1}{\sqrt{2E_k V}} e^{+ik \cdot x} \varepsilon_\mu^{*\lambda}(k).\end{aligned}$$

Example We treat the case of Møller scattering $e^-e^- \rightarrow e^-e^-$ as a typical example for the application of the Feynman rules.

We first define our initial and final states,

$$|i\rangle = |e^-(p_1, s_1)\rangle_{\text{single-particle}} \otimes |e^-(p_2, s_2)\rangle_{\text{single-particle}} = \sqrt{2E_1 2E_2} \frac{1}{\sqrt{2E_1 V 2E_2 V}} a_{s_1}^\dagger(p_1) a_{s_2}^\dagger(p_2) |0\rangle,$$

$$\langle f| = \langle e^-(p_3, s_3)|_{\text{single-particle}} \otimes \langle e^-(p_4, s_4)|_{\text{single-particle}} = \sqrt{2E_3 2E_4} \frac{1}{\sqrt{2E_3 V 2E_4 V}} \langle 0| a_{s_4}(p_4) a_{s_3}(p_3).$$

The transition matrix element \mathcal{S}_{fi} is then,

$$\begin{aligned} \mathcal{S}_{fi} = \langle f| \mathcal{S} |i\rangle &= \frac{(-ie)^2}{2!} \int d^4x_1 d^4x_2 \sqrt{16E_1 E_2 E_3 E_4} \langle 0| \underbrace{a_{s_4}(p_4)}_E \underbrace{a_{s_3}(p_3)}_D \\ &\quad : \underbrace{\bar{\psi}(x_1)}_D \gamma_\mu \underbrace{\psi(x_1)}_C \underbrace{\bar{\psi}(x_2)}_E \gamma_\nu \underbrace{\psi(x_2)}_A : \underbrace{A^\mu(x_1) A^\nu(x_2)}_B \underbrace{a_{s_1}^\dagger(p_1)}_A \underbrace{a_{s_2}^\dagger(p_2)}_C |0\rangle, \end{aligned} \quad (5.95)$$

$\underbrace{\quad\quad\quad}_B = -\bar{\psi}(x_2)\psi(x_1)$

yielding $2 \times 2 = 4$ Feynman graphs in position space (of which $2!$ are topologically identical). In Fig. 5.7, we labeled the last Feynman graph according to Eq. (5.95).

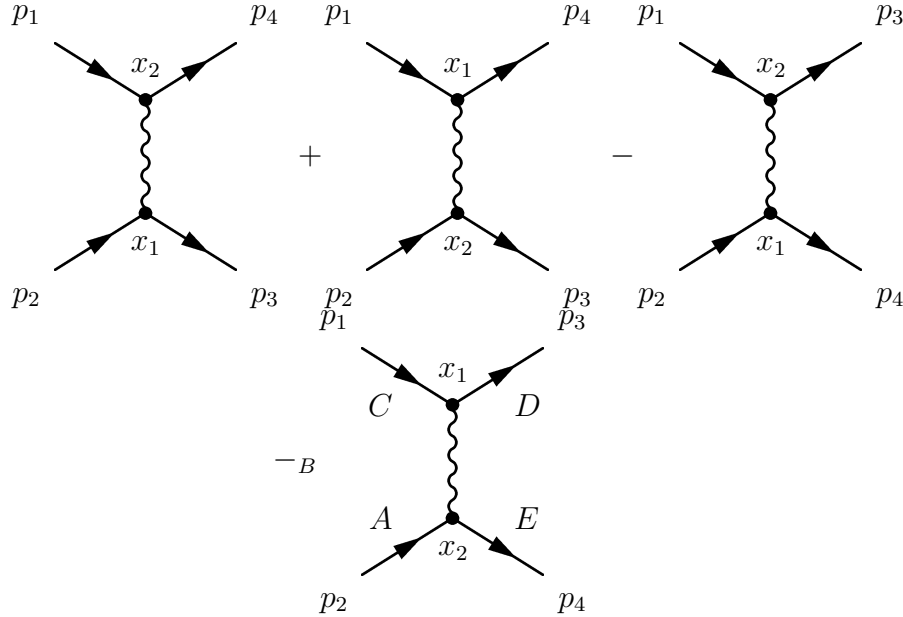


Figure 5.7: Feynman graphs associated with the Møller scattering.

We recall that each ordering of ψ , $\bar{\psi}$ corresponds to a Feynman diagram. The anticommutation relations are responsible for the relative sign changes.

With the photon propagator in momentum space,

$$iD_F^{\mu\nu}(q) = -\frac{ig^{\mu\nu}}{q^2}, \quad (5.96)$$

we get,



$$\begin{aligned} \mathcal{S}_{fi} = & (-ie)^2 (2\pi)^4 \delta^{(4)}(p_3 + p_4 - p_1 - p_2) \frac{1}{\sqrt{16E_1 E_2 E_3 E_4 V^2}} \\ & \left[\bar{u}_{s_4}(p_4) \gamma_\mu u_{s_2}(p_2) iD_F^{\mu\nu}(p_3 - p_1) \bar{u}_{s_3}(p_3) \gamma_\nu u_{s_1}(p_1) \right. \\ & \left. - \bar{u}_{s_4}(p_4) \gamma_\mu u_{s_1}(p_1) iD_F^{\mu\nu}(p_3 - p_2) \bar{u}_{s_3}(p_3) \gamma_\nu u_{s_2}(p_2) \right]. \end{aligned} \quad (5.97)$$

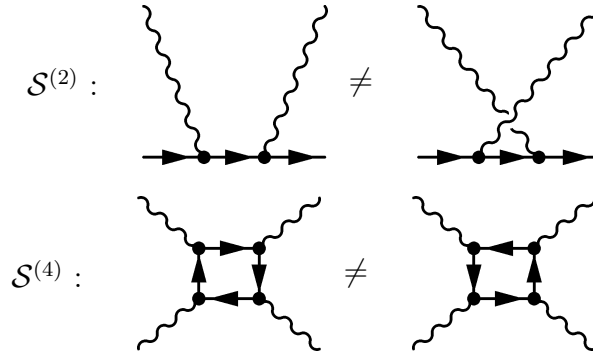
We now define the **invariant amplitude** \mathcal{M}_{fi} (see Eq. (3.11)) via,

$$\mathcal{S}_{fi} = \delta_{fi} + i(2\pi)^4 \delta^{(4)}(p_3 + p_4 - p_1 - p_2) \frac{1}{\sqrt{16E_1 E_2 E_3 E_4 V^2}} \mathcal{M}_{fi}. \quad (5.98)$$

\mathcal{M}_{fi} can then be computed using the Feynman rules in momentum space.

Application of the Feynman rules

- Momentum conservation at each vertex
- Fermion number conservation at each vertex (indicated by the direction of the arrows)
- All topologically allowed graphs contribute
- Exchange factor (-1) when interchanging two external fermions with each other
- Each closed fermion loop yields a factor (-1) , e.g.  coming from the contraction: $\bar{\psi}(x_1) \psi(x_1) \bar{\psi}(x_2) \psi(x_2)$:

- graphs in which the ordering of the vertices along a fermion line is different are not topologically equivalent, and must be summed, eg.



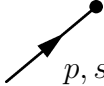

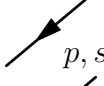
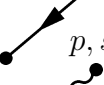

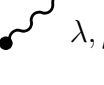
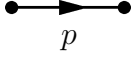
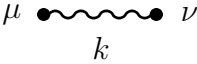

| External states | | |
|--------------------------|---|---|
| incoming electron |  | $u_s(p)$ |
| outgoing electron |  | $\bar{u}_s(p)$ |
| incoming positron |  | $\bar{v}_s(p)$ |
| outgoing positron |  | $v_s(p)$ |
| incoming photon |  | $(\varepsilon_\lambda)^\mu(p)$ |
| outgoing photon |  | $(\varepsilon_\lambda^*)^\mu(p)$ |
| Propagators | | |
| electron |  | $\frac{i(\not{p}+m)}{p^2-m^2+i\varepsilon}$ |
| photon |  | $\frac{-ig^{\mu\nu}}{k^2+i\varepsilon}$ |
| Vertex | | |
| electron-photon-electron |  | $-ieq_e\gamma^\mu$ |

Table 5.2: Feynman rules in momentum space.

5.9 Trace techniques for γ -matrices

Cross sections are proportional to $|\mathcal{M}_{fi}|^2 \propto |\bar{u}_{sf}(p_f)\Gamma u_{si}(p_i)|^2$, where Γ denotes an arbitrary product of γ -matrices.

In many experiments – but not all! –, the spin states of the initial and final states are not observed. This is for example the case at the CMS and ATLAS experiments of LHC. We then need to follow the following procedure :

- If the spin state of the final state particles cannot be measured, one must sum over the final state spins : $\sum_{s_f} |\dots|^2$,
- If the initial states particles are unpolarized, one must average over the initial state spins : $\frac{1}{2} \sum_{s_i} |\dots|^2$.

Then, remembering that $\bar{u} = u^\dagger \gamma^0$, we can write,

$$\begin{aligned}
 \frac{1}{2} \sum_{s_i, s_f} |\bar{u}_{sf}(p_f)\Gamma u_{si}(p_i)|^2 &= \frac{1}{2} \sum_{s_i, s_f} \bar{u}_{sf}(p_f)\Gamma u_{si}(p_i) u_{si}^\dagger(p_i) \gamma^0 \gamma^0 \Gamma^\dagger \gamma^0 u_{sf}(p_f) \\
 &= \frac{1}{2} \sum_{s_i, s_f} \bar{u}_{sf}(p_f)\Gamma u_{si}(p_i) \bar{u}_{si}(p_i) \bar{\Gamma} u_{sf}(p_f) \\
 &= \frac{1}{2} \sum_{s_i, s_f} (\bar{u}_{sf}(p_f))_\alpha \Gamma_{\alpha\beta} (u_{si}(p_i))_\beta (\bar{u}_{si}(p_i))_\gamma \bar{\Gamma}_{\gamma\delta} (u_{sf}(p_f))_\delta \\
 &\stackrel{(5.41)}{=} \frac{1}{2} \Gamma_{\alpha\beta} (\not{p}_i + m)_{\beta\gamma} \bar{\Gamma}_{\gamma\delta} (\not{p}_f + m)_{\delta\alpha} \\
 &= \frac{1}{2} \left(\Gamma(\not{p}_i + m) \bar{\Gamma}(\not{p}_f + m) \right)_{\alpha\alpha} \\
 &= \frac{1}{2} \text{Tr} \left(\Gamma(\not{p}_i + m) \bar{\Gamma}(\not{p}_f + m) \right),
 \end{aligned}$$

where the indices α, β, γ and δ label the matrix element, and $\bar{\Gamma} := \gamma^0 \Gamma^\dagger \gamma^0$.

We thus get the important result,

$$\boxed{\frac{1}{2} \sum_{s_i, s_f} |\bar{u}_{sf}(p_f)\Gamma u_{si}(p_i)|^2 = \frac{1}{2} \text{Tr} \left(\Gamma(\not{p}_i + m) \bar{\Gamma}(\not{p}_f + m) \right)}, \quad (5.99)$$

and its analogon for antiparticles,

$$\boxed{\frac{1}{2} \sum_{s_i, s_f} |\bar{v}_{sf}(p_f)\Gamma v_{si}(p_i)|^2 = \frac{1}{2} \text{Tr} \left(\Gamma(\not{p}_i - m) \bar{\Gamma}(\not{p}_f - m) \right)}, \quad (5.100)$$

i.e. the Clifford algebra of γ -matrices is taking care of the spin summation for us.

We now compute $\bar{\Gamma}$ for an arbitrary number of γ -matrices.

- For $\Gamma = \gamma^\mu$, $(\gamma^0)^\dagger = \gamma^0$, $(\gamma^i)^\dagger = -\gamma_i$ hence $(\gamma^\mu)^\dagger = \gamma^0 \gamma^\mu \gamma^0 \Rightarrow \bar{\gamma}^\mu = \gamma^\mu$. For later use, note that $\bar{\gamma}^5 = -\gamma^5$.
- For $\Gamma = \gamma^{\mu_1} \dots \gamma^{\mu_n}$, $\Gamma^\dagger = (\gamma^{\mu_1} \dots \gamma^{\mu_n})^\dagger = \gamma^0 \gamma^{\mu_n} \dots \gamma^{\mu_1} \gamma^0 \Rightarrow \bar{\Gamma} = \gamma^{\mu_n} \dots \gamma^{\mu_1}$. In other words, to get $\bar{\Gamma}$, we just need to read Γ in the inverse ordering.

We finally want to compute some traces for products of γ -matrices, since they appear explicitly $(\Gamma, \bar{\Gamma})$ and implicitly $(\not{p} = \gamma^\mu p_\mu)$ in the formulas (5.99) and (5.100). In doing this, one should remember that the trace is cyclic ($\text{Tr}(ABC) = \text{Tr}(BCA)$) and the Clifford algebra of γ -matrices.

- **0 γ -matrix** : $\text{Tr } \mathbb{1} = 4$.
- **1 γ -matrix** : $\text{Tr } \gamma^\mu = 0$, $\text{Tr } \gamma^5 = 0$. The last one is shown using the fact that $\{\gamma^5, \gamma^\mu\} = 0$.
- **2 γ -matrices** : $\text{Tr}(\gamma^\mu \gamma^\nu) = \frac{1}{2} \text{Tr}(\gamma^\mu \gamma^\nu + \gamma^\nu \gamma^\mu) = 4g^{\mu\nu} \Rightarrow \text{Tr}(\not{a} \not{b}) = 4a \cdot b$, where \cdot is the scalar product of 4-vectors.
- **4 γ -matrices** :

$$\begin{aligned}
\text{Tr}(\gamma^\mu \gamma^\nu \gamma^\rho \gamma^\sigma) &= \text{Tr}(\gamma^\nu \gamma^\rho \gamma^\sigma \gamma^\mu) = -\text{Tr}(\gamma^\nu \gamma^\rho \gamma^\mu \gamma^\sigma) + 2g^{\mu\sigma} \text{Tr}(\gamma^\nu \gamma^\rho) \\
&= \text{Tr}(\gamma^\nu \gamma^\mu \gamma^\rho \gamma^\sigma) + 8g^{\mu\sigma} g^{\nu\rho} - 8g^{\mu\rho} g^{\nu\sigma} \\
&= -\text{Tr}(\gamma^\mu \gamma^\nu \gamma^\rho \gamma^\sigma) + 8g^{\mu\sigma} g^{\nu\rho} - 8g^{\mu\rho} g^{\nu\sigma} + 8g^{\mu\nu} g^{\rho\sigma} \\
\Rightarrow \text{Tr}(\gamma^\mu \gamma^\nu \gamma^\rho \gamma^\sigma) &= 4(g^{\mu\nu} g^{\rho\sigma} + g^{\mu\sigma} g^{\nu\rho} - g^{\mu\rho} g^{\nu\sigma}) \\
\Rightarrow \text{Tr}(\not{a}_1 \not{a}_2 \not{a}_3 \not{a}_4) &= 4[(a_1 \cdot a_2)(a_3 \cdot a_4) + (a_1 \cdot a_4)(a_2 \cdot a_3) - (a_1 \cdot a_3)(a_2 \cdot a_4)].
\end{aligned}$$

and in general,

$$\begin{aligned}
\text{Tr}(\not{a}_1 \dots \not{a}_n) &= (a_1 \cdot a_2) \text{Tr}(\not{a}_3 \dots \not{a}_n) - (a_1 \cdot a_3) \text{Tr}(\not{a}_2 \not{a}_4 \dots \not{a}_n) \\
&\quad + \dots \pm (a_1 \cdot a_n) \text{Tr}(\not{a}_2 \dots \not{a}_{n-1}),
\end{aligned}$$

which implies inductively that the trace of a string of γ -matrices is a real number.

- **n γ -matrices (n odd)** :

$$\begin{aligned}
\text{Tr}(\gamma^{\mu_1} \dots \gamma^{\mu_n}) &= \text{Tr}(\gamma^{\mu_1} \dots \gamma^{\mu_n} \underbrace{\gamma^5 \gamma^5}_{=1}) = \text{Tr}(\gamma^5 \gamma^{\mu_1} \dots \gamma^{\mu_n} \gamma^5) \\
&= (-1)^n \text{Tr}(\gamma^{\mu_1} \dots \gamma^{\mu_n}) \Rightarrow \text{Tr}(\gamma^{\mu_1} \dots \gamma^{\mu_n}) = 0.
\end{aligned}$$

- **n γ -matrices (n even)** :

$$\text{Tr}(\gamma^{\mu_1} \dots \gamma^{\mu_n}) = \text{Tr}((\gamma^{\mu_1} \dots \gamma^{\mu_n})^\dagger) = \text{Tr}(\gamma^0 \gamma^{\mu_n} \dots \gamma^{\mu_1} \gamma^0) = \text{Tr}(\gamma^{\mu_n} \dots \gamma^{\mu_1}).$$

- **γ^5 and 2 γ -matrices** : $\text{Tr}(\gamma^5 \gamma^\mu \gamma^\nu) = 0$. To show this identity, we remark that $\gamma^5 \gamma^\mu \gamma^\nu$ is a rank-2 tensor, which does not depend on any 4-momenta. Therefore, $\text{Tr}(\gamma^5 \gamma^\mu \gamma^\nu) = c g^{\mu\nu}$. We contract with $g_{\mu\nu}$ to get $\text{Tr}(\gamma^5 \gamma^\mu \gamma_\mu) = c g^{\mu\nu} g_{\mu\nu} = 4c$, but since $\gamma^\mu \gamma_\mu = 4\mathbb{1}$ we get $c = \text{Tr} \gamma^5 = 0$.
- **γ^5 and 4 γ -matrices** : $\text{Tr}(\gamma^5 \gamma^\mu \gamma^\nu \gamma^\rho \gamma^\sigma) = -4i\varepsilon^{\mu\nu\rho\sigma}$.
- **Contractions** :

$$\gamma^\mu \gamma_\mu = 4\mathbb{1} \quad (5.101)$$

$$\gamma^\mu \not{a} \gamma_\mu = -2\not{a} \quad (5.102)$$

$$\gamma^\mu \not{a} \not{b} \gamma_\mu = 4(a \cdot b)\mathbb{1} \quad (5.103)$$

$$\gamma^\mu \not{a} \not{b} \not{c} \gamma_\mu = -2\not{c} \not{b} \not{a} \quad (5.104)$$

5.10 Annihilation process : $e^+e^- \rightarrow \mu^+\mu^-$

In this section, we compute the differential cross section of the simplest of all QED process, the reaction

$$e^-(p_1)e^+(p_2) \rightarrow \mu^-(p_3)\mu^+(p_4),$$

illustrated on Fig. 5.8. The simplicity arises from the fact that $e^- \neq \mu^-$, and hence only one diagram contributes (the e^+e^- -pair *must* be annihilated).

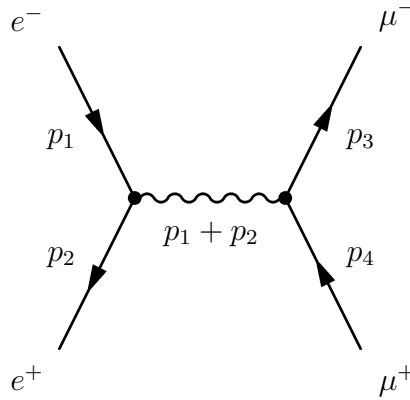


Figure 5.8: Annihilation process $e^+e^- \rightarrow \mu^+\mu^-$

We recall the Mandelstam variables for this process,

$$\begin{aligned} s &= (p_1 + p_2)^2 \\ t &= (p_1 - p_3)^2 \\ u &= (p_1 - p_4)^2. \end{aligned}$$

We make the following assumptions (very common for QED processes),

- Unpolarized leptons : $\frac{1}{2} \sum_{s_i, s_f}$,
- High energy limit : $m_e, m_\mu = 0 \Leftrightarrow \sqrt{s} \gg m_e, m_\mu$.

Using the Feynman rules of Table 5.2 for the diagram depicted in Fig. 5.8, we get,

$$\begin{aligned}
 -i\mathcal{M}_{fi} &= \bar{u}_{s_3}(p_3)ie\gamma^\mu v_{s_4}(p_4) \frac{-ig_{\mu\nu}}{(p_1 + p_2)^2} \bar{v}_{s_2}(p_2)ie\gamma^\nu u_{s_1}(p_1) \\
 \overline{|\mathcal{M}_{fi}|^2} &= \frac{1}{2} \sum_{s_1} \frac{1}{2} \sum_{s_2} \sum_{s_3} \sum_{s_4} |\mathcal{M}_{fi}|^2 \\
 &= \frac{1}{4} \frac{e^4}{s^2} \text{Tr}(\gamma^\mu \not{p}_4 \gamma^\nu \not{p}_3) \text{Tr}(\gamma_\mu \not{p}_1 \gamma_\nu \not{p}_2) \\
 &= \frac{1}{4} \frac{e^4}{s^2} 16 [2(p_1 \cdot p_3)(p_2 \cdot p_4) + 2(p_1 \cdot p_4)(p_2 \cdot p_3)].
 \end{aligned}$$

Since we are working in the high energy limit, we have $p_i^2 = 0$ and hence $t = -2p_1 \cdot p_3 = -2p_2 \cdot p_4$ and $u = -2p_1 \cdot p_4 = -2p_2 \cdot p_3$. Using the identity $s + t + u = 2m_e^2 + 2m_\mu^2 = 0$ to get rid of the Mandelstam u -variable and with $\alpha = \frac{e^2}{4\pi}$ we have,

$$\overline{|\mathcal{M}_{fi}|^2} = 32\pi^2 \alpha^2 \frac{t^2 + (s+t)^2}{s^2}. \quad (5.105)$$

Considering the center of mass frame, we have $s = 4(E^*)^2$, $t = -\frac{s}{2}(1 - \cos \Theta^*)$ and with the help of Eq. (3.34), this yields,

$$\frac{d\sigma}{dt} = \frac{1}{16\pi s^2} \overline{|\mathcal{M}_{fi}|^2} = \frac{\pi\alpha^2}{s^2} (1 + \cos^2 \Theta^*), \quad (5.106)$$

or using,

$$\frac{d\sigma}{dt} = \frac{d\Omega^*}{dt} \frac{d\sigma}{d\Omega^*} = \frac{4\pi}{s} \frac{d\sigma}{d\Omega^*},$$

we get the differential cross section for $e^+e^- \rightarrow \mu^+\mu^-$ in the center of mass frame,

$$\boxed{\frac{d\sigma^{e^+e^- \rightarrow \mu^+\mu^-}}{d\Omega^*} = \frac{\alpha^2}{4s} (1 + \cos^2 \Theta^*)}. \quad (5.107)$$

This differential cross section (see Fig. 5.9) has been very well measured and is one of the best tests of QED at high energies.

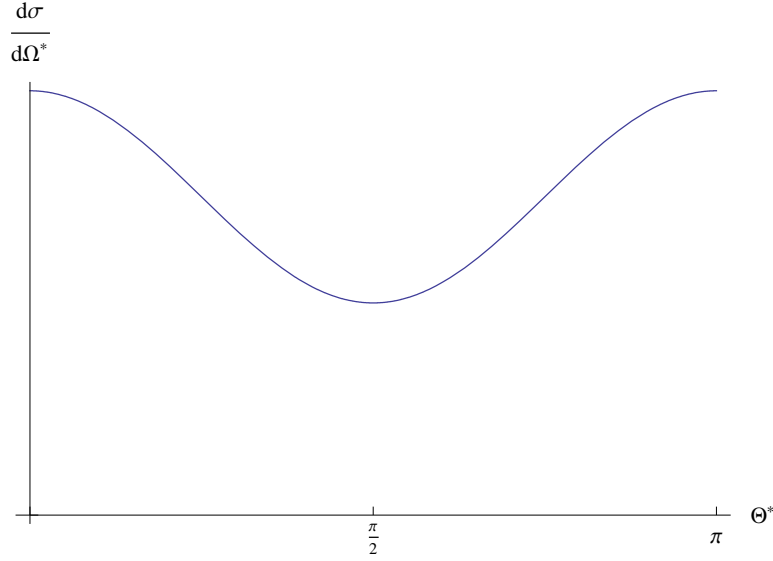


Figure 5.9: Differential cross section for $e^+e^- \rightarrow \mu^+\mu^-$ in the center of mass frame.

Using this result, we can calculate the total cross-section by integration over the solid angle:

$$\sigma = \int \frac{d\sigma}{d\Omega^*} d\Omega^* = \frac{\alpha^2}{4s} \int_0^\pi (1 + \cos^2 \Theta^*) \underbrace{\sin \Theta^* d\Theta^*}_{d \cos \Theta^*} \underbrace{\int_0^{2\pi} d\phi}_{2\pi} \quad (5.108)$$

$$= \frac{\alpha^2}{4s} 2\pi \frac{8}{3} \quad (5.109)$$

$$\Rightarrow \boxed{\sigma^{e^+e^- \rightarrow \mu^+\mu^-} = \frac{4\pi\alpha^2}{3s}} = \frac{86.9 \text{ nb}}{s [\text{GeV}^2]} \quad (5.110)$$

where $1 \text{ nb} = 10^{-33} \text{ cm}^2$. If one considers non-asymptotic energies, $s \simeq m_\mu^2$ (but $s \gg m_e^2$), one finds a result which reduces to Eq. (5.110) for $m_\mu^2 = 0$:

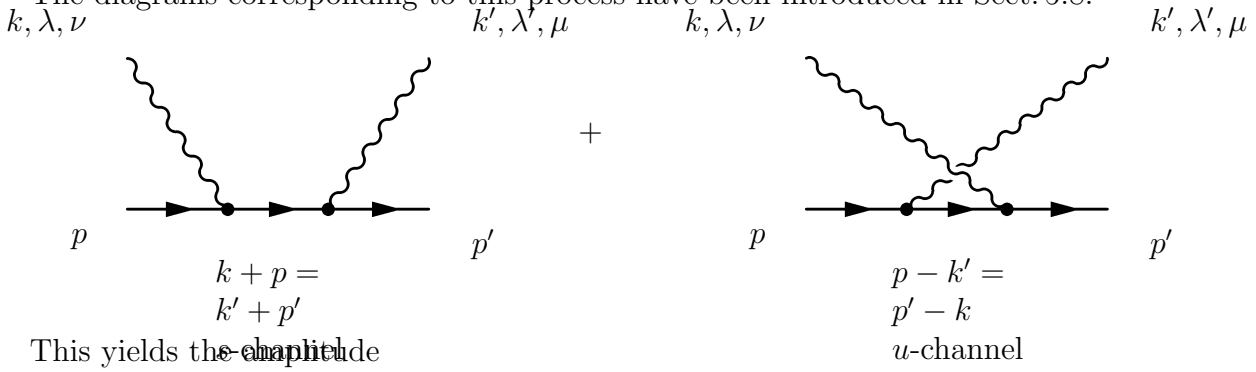
$$\sigma^{e^+e^- \rightarrow \mu^+\mu^-} = \frac{4\pi\alpha^2}{3s} \left(1 + 2\frac{m_\mu^2}{s} \right) \sqrt{1 - \frac{4m_\mu^2}{s}}.$$

5.11 Compton scattering

Let us now consider Compton scattering:

$$\gamma(k) + e^-(p) \rightarrow \gamma(k') + e^-(p').$$

The diagrams corresponding to this process have been introduced in Sect. 5.8.



This yields the amplitude

$$-i\mathcal{M}_{fi} = \varepsilon_\mu^*(k', \lambda') \varepsilon_\nu(k, \lambda) \bar{u}(p') \left[\underbrace{ie\gamma^\mu \frac{i}{\not{p} + \not{k} - m} ie\gamma^\nu}_{\text{LHS diagram}} + \underbrace{ie\gamma^\nu \frac{i}{\not{p} - \not{k}' - m} ie\gamma^\mu}_{\text{RHS diagram}} \right] u(p)$$

where the on-shell conditions read

$$k^2 = k'^2 = 0$$

$$p^2 = p'^2 = m^2$$

and the photons are transversal:

$$k \cdot \varepsilon(k) = k' \cdot \varepsilon(k') = 0.$$

It is instructive to check that the invariant amplitude is indeed also gauge invariant. Consider the gauge transformation

$$A_\nu(x) \rightarrow A_\nu(x) + \partial_\nu \Lambda(x)$$

which leaves Maxwell's equations unaltered. In the photon field operator this can be implemented by

$$\varepsilon_\nu(k, \lambda) \rightarrow \varepsilon_\nu(k, \lambda) + \beta k_\nu, \quad \beta \in \mathbb{R} \text{ arbitrary.}$$

We observe the change of the matrix element for transformation of one of the photons:

$$-i\mathcal{M}_{fi}(\varepsilon_\nu \rightarrow k_\nu) = -ie^2 \varepsilon_\mu^*(k', \lambda') \bar{u}(p') \left[\gamma^\mu \frac{1}{\not{p} + \not{k} - m} \not{k} + \not{k} \frac{1}{\not{p} - \not{k}' - m} \gamma^\mu \right] u(p).$$

In simplifying this expression, we use

$$\frac{1}{\not{p} + \not{k} - m} \not{k} u(p) = \frac{1}{\not{p} + \not{k} - m} (\not{k} + \not{p} - m) u(p) = \mathbb{1} u(p)$$

where we added a zero since $(\not{p} - m)u(p) = 0$ and analogously

$$\bar{u}(p')\not{k}\frac{1}{\not{p} - \not{k}' - m} = \bar{u}(p')(\not{k} - \not{p}' + m)\frac{1}{\not{p}' - \not{k} - m} = -\bar{u}(p')\mathbb{1}.$$

Putting the terms together, we therefore find

$$-i\mathcal{M}_{fi}(\varepsilon_\nu \rightarrow k_\nu) = -ie^2\varepsilon_\mu^*(k', \lambda')\bar{u}(p')(\gamma^\mu\mathbb{1} - \mathbb{1}\gamma^\mu)u(p) = 0.$$

The result is the same for the transformation $\varepsilon_\mu^* \rightarrow \varepsilon_\mu^* + \beta k'_\mu$.

It is generally true that only the sum of the contributing diagrams is gauge invariant. Individual diagrams are not gauge invariant and thus without physical meaning.

Recall that the aim is to find the differential cross section and therefore the squared matrix element. Since there are two contributing diagrams, one has to watch out for interference terms. Applying the trace technology developed in Sect. 5.9 yields

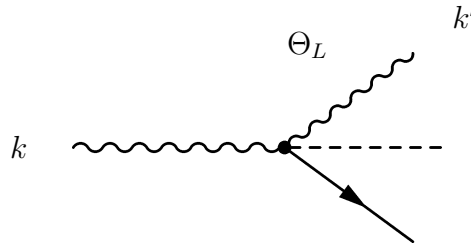
$$\begin{aligned} \overline{|\mathcal{M}_{fi}|^2} &= \frac{1}{2} \sum_\lambda \frac{1}{2} \sum_s \sum_{\lambda'} \sum_{s'} |\mathcal{M}_{fi}|^2 \\ &= 2e^4 \left[\frac{m^2 - u}{s - m^2} + \frac{m^2 - s}{u - m^2} + 4 \left(\frac{m^2}{s - m^2} + \frac{m^2}{u - m^2} \right) + 4 \left(\frac{m^2}{s - m^2} + \frac{m^2}{u - m^2} \right)^2 \right]. \end{aligned} \quad (5.111)$$

Bearing in mind that $s + t + u = 2m^2$, this yields the unpolarized Compton cross-section

$$\frac{d\sigma}{dt} = \frac{1}{16\pi(s - m^2)^2} \overline{|\mathcal{M}_{fi}|^2} \quad (5.112)$$

which is a frame independent statement.

Head-on electron-photon collision is rather uncommon; usually photons are hitting on a target. Therefore it is useful to consider the electron's rest frame (laboratory frame):



With $\omega = |\vec{k}| = E_\gamma^L$, $\omega' = |\vec{k}'| = E_\gamma'^L$, and $p = (m, \vec{0})^T$ one finds

$$s - m^2 = 2m\omega \quad (5.113)$$

$$u - m^2 = -2p \cdot k' = -2m\omega' \quad (5.114)$$

$$t = -2\omega\omega'(1 - \cos \Theta_L). \quad (5.115)$$

One of the three variables can be eliminated using $s + t + u = 2m^2$:

$$\omega' = \frac{1}{2m}(s + t - m^2) = \omega - \frac{\omega\omega'}{m}(1 - \cos \Theta_L) \quad (5.116)$$

$$\Rightarrow \frac{1}{\omega'} - \frac{1}{\omega} = \frac{1}{m}(1 - \cos \Theta_L) \quad (5.117)$$

$$\Rightarrow \omega' = \frac{\omega}{1 + \frac{\omega}{m}(1 - \cos \Theta_L)}. \quad (5.118)$$

We continue calculating the differential cross-section. Eq. (5.115) yields

$$dt = \frac{\omega'^2}{\pi} 2\pi d \cos \Theta_L = \frac{\omega'^2}{\pi} d\Omega_L.$$

Furthermore, we can use Eq. (5.117) to simplify Eq. (5.111):

$$\frac{m^2}{s - m^2} + \frac{m^2}{u - m^2} = \frac{m^2}{2m\omega} + \frac{m^2}{-2m\omega'} = \frac{m}{2} \left(\frac{1}{\omega} - \frac{1}{\omega'} \right) = -\frac{1}{2}(1 - \cos \Theta_L).$$

Using these results and remembering Eq. (5.112), we obtain

$$\frac{d\sigma^{\gamma e \rightarrow \gamma e}}{d\Omega_L} = \frac{dt}{d\Omega_L} \frac{d\sigma}{dt} = \frac{\omega'^2}{\pi} \frac{1}{16\pi(2m\omega)^2} 2e^2 \left[\frac{2m\omega'}{2m\omega} + \frac{-2m\omega}{-2m\omega'} - \sin^2 \Theta_L \right] \quad (5.119)$$

$$= \frac{\omega'^2}{\pi} \frac{2 \cdot 16\pi^2 \alpha^2}{16\pi 4m^2 \omega^2} \left[\frac{\omega'}{\omega} + \frac{\omega}{\omega'} - \sin^2 \Theta_L \right] \quad (5.120)$$

$$\Rightarrow \boxed{\frac{d\sigma^{\gamma e \rightarrow \gamma e}}{d\Omega_L} = \frac{\alpha^2}{2m^2} \left(\frac{\omega'}{\omega} \right)^2 \left[\frac{\omega'}{\omega} + \frac{\omega}{\omega'} - \sin^2 \Theta_L \right]} \quad (5.121)$$

which is called the Klein-Nishima formula.

It follows a discussion of important limiting cases.

- *Classical limit:* $\omega \ll m \Rightarrow \omega' \simeq \omega$

In the classical limit, Eq. (5.121) simplifies to the classical Thomson cross-section (which was used to measure α)

$$\boxed{\frac{d\sigma^{\gamma e \rightarrow \gamma e}}{d\Omega_L} = \frac{\alpha^2}{2m^2} [1 + \cos^2 \Theta_L]},$$

yielding the total cross-section

$$\boxed{\sigma^{\gamma e \rightarrow \gamma e} = \frac{\alpha^2}{2m^2} \frac{16\pi}{3}}.$$

- *Asymptotic limit:* $s \gg m^2 \Rightarrow \omega \gg m$

In this case, the so-called leading log approximation holds:

$$\sigma^{\gamma e \rightarrow \gamma e} = \frac{2\pi\alpha^2}{m^2} \frac{m^2}{s} \left[\ln \frac{s}{m^2} + \frac{1}{2} + \mathcal{O}\left(\frac{m^2}{s}\right) \right] \simeq \frac{2\pi\alpha^2}{s} \ln \frac{s}{m^2}.$$

- *In general* we can conclude that

$$\sigma^{\gamma e \rightarrow \gamma e} \sim \frac{\alpha^2}{m^2} \simeq 10^{-25} \text{ cm}^2$$

from which one can infer the “classical electron radius”

$$r_e^{\text{classical}} \sim \sqrt{\sigma_{\text{Thomson}}} \sim \frac{\alpha}{m} = 2.8 \cdot 10^{-13} \text{ cm}.$$

5.12 QED as a gauge theory

Recall the QED Lagrangian

$$\begin{aligned} \mathcal{L}^{\text{QED}} &= \bar{\psi}(i\gamma^\mu \partial_\mu - m)\psi - eq_e \bar{\psi}\gamma^\mu \psi A_\mu - \frac{1}{4} F_{\mu\nu} F^{\mu\nu} \\ &= \mathcal{L}_0^{\text{Dirac}} + \mathcal{L}' + \mathcal{L}_0^{\text{photon}} \end{aligned}$$

introduced in Sect. 5.8 which includes the following observables:

- *Fermions:* components of $\bar{\psi}\gamma^\mu\psi = j^\mu$
- *Photons:* components of $F^{\mu\nu}$: \vec{E} and \vec{B} field.

Neither ψ nor A_μ as such are observables. In particular, the phase of ψ cannot be observed. This means that QED must be invariant under phase transformations of ψ :

$$\psi(x) \rightarrow \psi'(x) = e^{ieq_e\chi(x)}\psi(x)$$

which is a unitary one-dimensional i. e. $U(1)$ transformation. Observe first the action on the Dirac Lagrangian:

$$\begin{aligned} \mathcal{L}_0^{\text{Dirac}} &\rightarrow \bar{\psi}'(i\gamma^\mu \partial_\mu - m)\psi' \\ &= \bar{\psi} e^{-ieq_e\chi(x)} e^{ieq_e\chi(x)} (i\cancel{\partial} - m)\psi - \bar{\psi}\gamma^\mu (\partial_\mu eq_e\chi(x))\psi \\ &= \mathcal{L}_0^{\text{Dirac}} - eq_e \bar{\psi}\gamma^\mu \psi (\partial_\mu \chi(x)). \end{aligned}$$

Therefore, the free Dirac field Lagrangian alone is not invariant under this transformation. In order for the extra term to vanish, A_μ has to be transformed, too:

$$A_\mu \rightarrow A'_\mu = A_\mu - \partial_\mu \chi(x)$$

| | | |
|------------------|--------------|---------|
| QED | photon | $U(1)$ |
| Weak interaction | W^\pm, Z^0 | $SU(2)$ |
| QCD | gluon | $SU(3)$ |

Table 5.3: Summary of gauge theories.

such that $F^{\mu\nu} = F'^{\mu\nu}$ since $F^{\mu\nu} = \partial^\mu A^\nu - \partial^\nu A^\mu$. This means that we are dealing with the gauge transformation known from classical electrodynamics. Because we have

$$-eq_e \bar{\psi} \gamma^\mu \psi A_\mu \rightarrow -eq_e \bar{\psi} \gamma^\mu \psi A_\mu + eq_e \bar{\psi} \gamma^\mu \psi (\partial_\mu \chi)$$

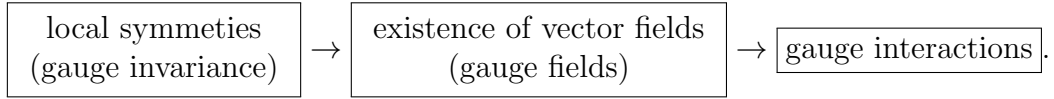
the complete Lagrangian \mathcal{L}^{QED} is invariant under $U(1)$ gauge transformations. This motivates the definition of the gauge covariant derivative

$$D_\mu = \partial_\mu + ieq_e A_\mu$$

which contains the photon-electron interaction.

In summary, the requirement of gauge invariance uniquely determines the photon-electron interaction and QED is a $U(1)$ gauge theory.

This suggests a new approach on theory building: start from symmetries instead of finding them in the final Lagrangian:



A summary of gauge theories with the corresponding gauge fields and gauge groups is given in Tab. 5.3.

Chapter 6

Tests of QED

In the previous chapter elements of the quantum electrodynamics theory are discussed. We now turn to precision tests of the theory which usually consist in the measurement of the electromagnetic fine structure constant α in different systems. Experimental results are compared with theoretical predictions. The validation process requires very high precision in both measurements and theoretical calculations. QED is then confirmed to the extent that these measurements of α from different physical sources agree with each other. The most stringent test of QED is given by the measurement of the electron magnetic moment. However, several other experimental tests have been performed in different energy ranges and systems:

- Low energy range, accessible with small experiments;
- High energy range, accessible with particle colliders (e.g. e^+e^- colliders);
- Condensed matter systems (quantum Hall effect, Josephson effect).

As we will see, the achieved precision makes QED one of the most accurate physical theories constructed so far.

6.1 Measurement of the electron anomalous magnetic moment

6.1.1 Electron magnetic moment

A rotating electrically charged body creates a magnetic dipole. In classical analogy, this is also the case for the spinning electron. External magnetic fields exert a torque on the electron magnetic moment. Electrons have an *intrinsic magnetic moment* μ , related to

their spin s :

$$\mu = -g \frac{e}{2m} s = -\frac{g}{2} \frac{e}{2m} \quad (6.1)$$

where e is the unit charge and m the electron mass. In the case of electrons the magnetic moment is anti-parallel to the spin. The g -factor is equal to 2, as calculated from Dirac's equation:

$$a \equiv \frac{g-2}{2} = 0.$$

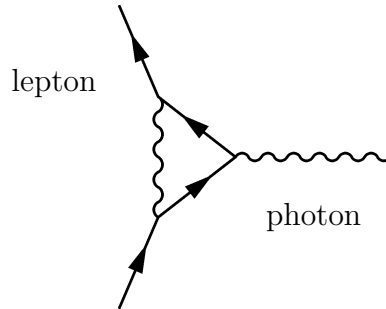
Corrections to the g -factor are given by higher order QED contributions as well as hadronic and weak interactions. There could be additional contributions from physics beyond the Standard Model (SM):

$$\frac{g}{2} = 1 + a_{\text{QED}}(\alpha) + a_{\text{hadronic}} + a_{\text{weak}} + a_{\text{new}}.$$

When adding the corrections we usually talk of the *anomalous magnetic moment* of the electron.

6.1.2 QED: higher order corrections

The one-loop corrections to the magnetic moment are due to vacuum fluctuation and polarization effects. A corresponding diagram is for example



The textbook calculation of the one-loop corrections gives corrections $\sim 10^{-3}$ (see [14, pp. 189]):

$$a = \frac{\alpha}{2\pi} \approx 0.0011614.$$

Hadronic and weak interactions are calculated (within the SM) to be very small and negligible, respectively.

As we will see, the precision achieved by experimental results needs QED predictions with α^4 precision.

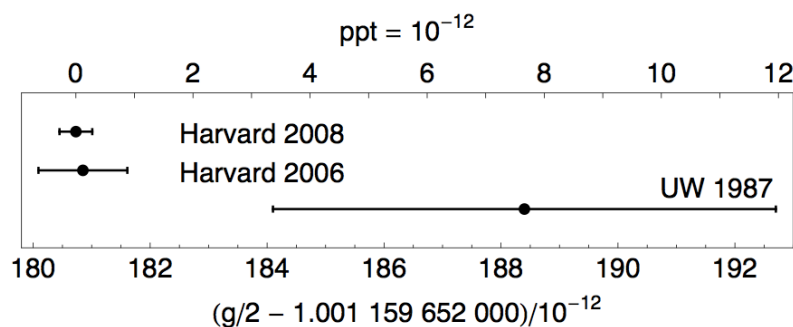


Figure 6.1: *Most accurate measurements of the electron $g/2$.* Source: [16, p. 177].

6.1.3 $g/2$ measurements

Nowadays the precision of the $g/2$ measurements is below 10^{-12} as is shown in Fig. 6.1. The latest measurements are 15 times more precise than the previous result which stood for about 20 years. As one can see in Fig. 6.1, the latest value is shifted by 1.7 standard deviations with respect to the previous result from 1987.

So, how did we get to this astonishing precision?

6.1.3.1 Experiment

The main ingredients of the experiment are:

- *Single-electron quantum cyclotron*
A Penning trap suspends and confines the electron in an atom-like state.
- *Fully resolved cyclotron and spin energy levels*
Accurate measurements of the resonant frequencies of driven transitions between the energy levels of this homemade atom—an electron bound to the trap—reveals the electron magnetic moment in units of Bohr magnetons, $g/2$.
- *Detection sensitivity sufficient to detect one quantum transitions*
Frequency detection sensitivity in the radio and microwave region.

The Penning trap confines electrons by using a strong vertical magnetic field B for radial confinement and a quadrupole electric field for axial confinement (see Fig. 6.2(a)). The magnetic field is produced by a solenoid while the electric field is produced by three electrodes: one ring and two endcaps. A sketch of the electron trajectory is shown in Fig. 6.2(b). The trajectory in the radial plane is characterized by two frequencies: The magneton frequency ω_- and the modified cyclotron frequency ω_+ . The cyclotron frequency is then $\omega = \omega_+ + \omega_-$. Since there is also a low-frequency oscillation in the z -direction, the overall trajectory has the shown form.

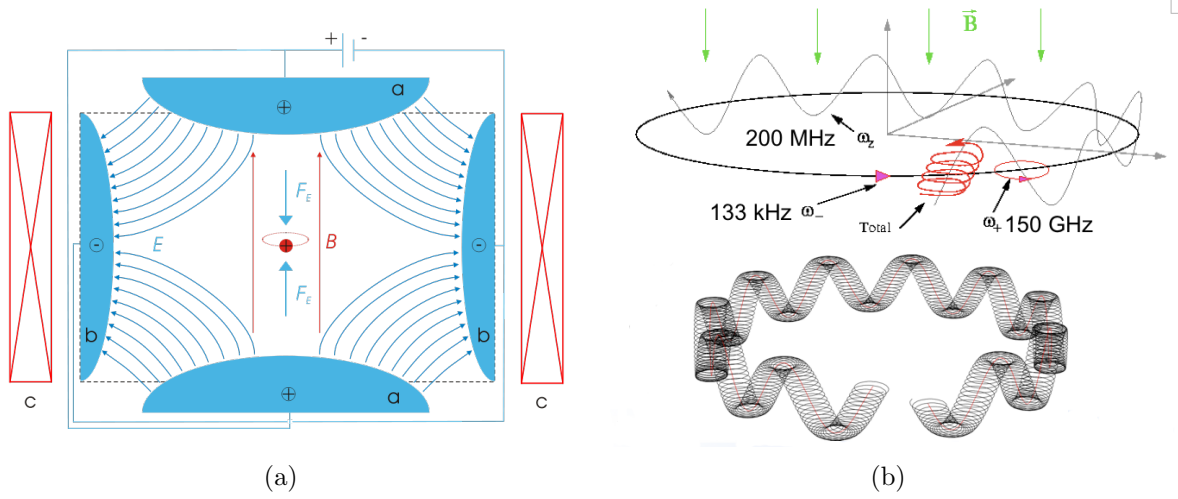


Figure 6.2: *Sketch of the fields and the electron trajectory in a Penning trap.* Confinement is achieved by a vertical magnetic field and a quadrupole electric field. Source: [17]. (a) The magneton frequency ω_- and the modified cyclotron frequency ω_+ contribute to the electron trajectory as well as a low-frequency oscillation in z -direction. (b)

A non-relativistic electron in a magnetic field has the following energy levels:¹

$$E(n, m_s) = \frac{g}{2} h \nu_c m_s + \left(n + \frac{1}{2} \right) h \nu_c \quad (6.2)$$

depending on the cyclotron frequency

$$\nu_c = \frac{eB}{2\pi m} \quad (6.3)$$

and on the spin frequency

$$\nu_s = \frac{g}{2} \nu_c = \frac{g}{2} \frac{eB}{2\pi m}. \quad (6.4)$$

Here n is the principal quantum number and m_s the spin quantum number. Eq. (6.4) yields

$$\frac{g}{2} = \frac{\nu_s}{\nu_c} = 1 + \frac{\nu_s - \nu_c}{\nu_c} \equiv 1 + \frac{\nu_a}{\nu_c}.$$

Since ν_s and ν_c differ only by one part per 10^3 , measuring ν_a and ν_c to a precision of one part per 10^{10} gives $g/2$ to one part per 10^{13} .

This technique of measuring $g/2$ has two main advantages:

¹See e. g. [18, § 112].

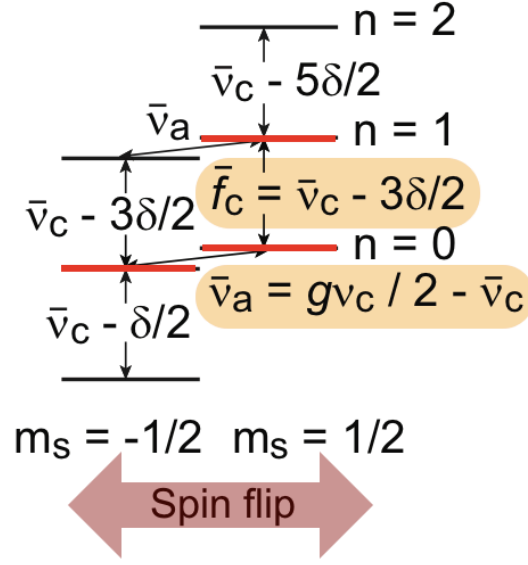


Figure 6.3: *Lowest cyclotron and spin levels of an electron in a Penning trap.* Source: [16, p. 180, modified].

1. One can measure the ratio of two frequencies to very high precision.
2. Since the B field appears in both numerator and denominator (see Eq. (6.4)), the dependence on the magnetic field cancels in the ratio.

Including the relativistic corrections, Eq. (6.2) is modified and the energy levels are given by:

$$E(n, m_s) = \frac{g}{2} h \nu_c m_s + \left(n + \frac{1}{2} \right) h \bar{\nu}_c - \underbrace{\frac{1}{2} h \delta \left(n + \frac{1}{2} + m_s \right)^2}_{\text{relativistic correction term}}$$

where $\bar{\nu}_c$ denotes the cyclotron frequency, shifted due to the Penning trap. Higher states are excited via microwave radiation. The experiment measures the following transition frequencies (see Fig. 6.3):

$$\begin{aligned} \bar{f}_c &\equiv \bar{\nu}_c - \frac{3}{2} \delta, \text{ corresponding to } (n, m_s) = (1, 1/2) \rightarrow (0, 1/2) \text{ and} \\ \bar{\nu}_a &\equiv \frac{g}{2} \nu_c - \bar{\nu}_c, \text{ corresponding to } (0, 1/2) \rightarrow (0, -1/2) \end{aligned}$$

with the cyclotron frequency $\nu_c \sim 150$ GHz.

A sketch of the experimental setup is shown in Fig. 6.4(a) and 6.4(b). A Penning trap is used to artificially bind the electron in an orbital state. For confinement, a high voltage

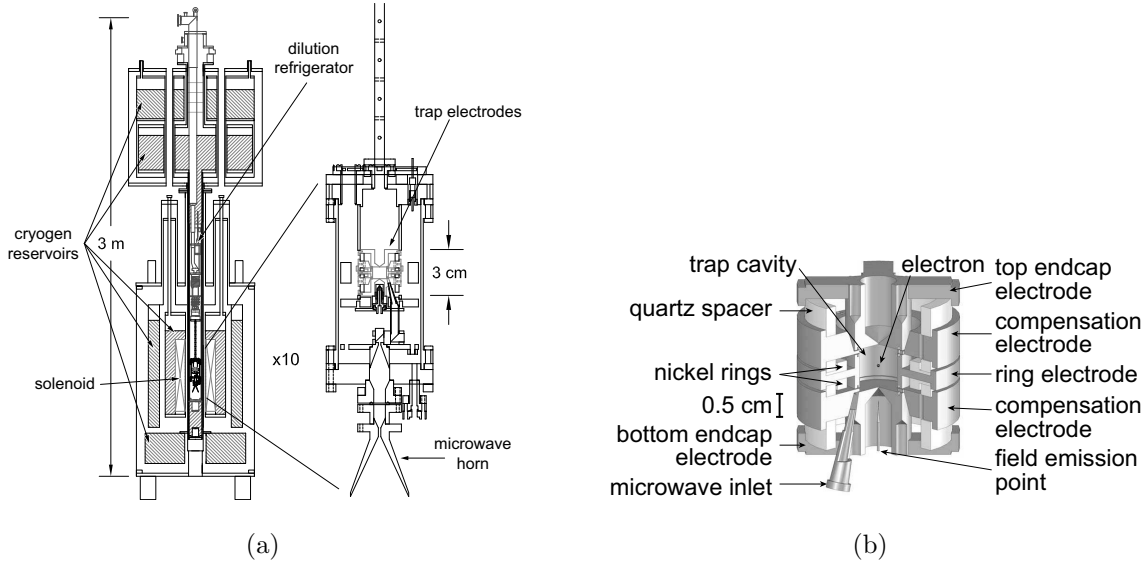


Figure 6.4: *Sketch of the experimental setup.* Overview of experimental apparatus. Source: [16, p. 185]. (a) The Penning trap cavity is used to confine a single electron and to inhibit spontaneous emission. Source: [16, p. 182]. (b)

(100 V) is applied between the cylindric and endcap contacts. Since $\nu_c \propto B$ (see Eq. (6.3)), a high magnetic field (5 T) is necessary to increase the spacing between the cyclotron energy levels. And finally, because the probability to occupy the orbital ground state is proportional to the Boltzmann factor,

$$\exp\left(-\frac{h\bar{\nu}_c}{k_B T}\right),$$

very low temperatures (100 mK) are needed.

In analyzing the results of Penning trap measurements, one has to correct for the frequency shifts due to the cavity. This can be done by measuring at various frequencies (see Fig. 6.5(a)). The result for $g/2$ given in [16] is

$$g/2 = 1.001\,159\,652\,180\,73\,(28) \quad [0.28 \text{ ppt}]. \quad (6.5)$$

6.1.3.2 Theoretical predictions

The QED calculations provide the prediction for $g/2$ up to the fifth power of α :

$$\frac{g}{2} = 1 + C_2 \left(\frac{\alpha}{\pi}\right) + C_4 \left(\frac{\alpha}{\pi}\right)^2 + C_6 \left(\frac{\alpha}{\pi}\right)^3 + C_8 \left(\frac{\alpha}{\pi}\right)^4 + C_{10} \left(\frac{\alpha}{\pi}\right)^5 + \cdots + a_{\text{hadronic}} + a_{\text{weak}} \quad (6.6)$$

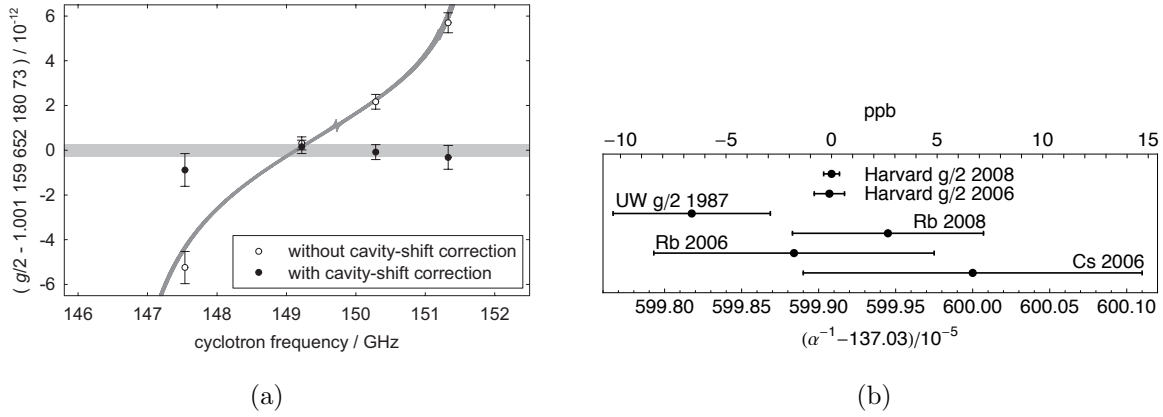


Figure 6.5: $g/2$ and fine structure constant. Four measurements of $g/2$ without (open) and with (filled) cavity-shift corrections. The light gray uncertainty band shows the average of the corrected data. The dark gray band indicates the expected location of the uncorrected data given the result in Eq. (6.5) and including only the cavity-shift uncertainty. Source: [16, p. 201]. (a) The most precise determinations of α . Source: [19, p. 264]. (b)

where

$$\begin{aligned}
 C_2 &= 0.500\,000\,000\,000\,00 \text{ (exact)} \\
 C_4 &= -0.328\,478\,444\,002\,90 \text{ (60)} \\
 C_6 &= 1.181\,234\,016\,827 \text{ (19)} \\
 C_8 &= -1.914\,4 \text{ (35)} \\
 C_{10} &= 0.0 \text{ (4.6)} \\
 a_{\text{hadronic}} &= 1.682(20) \cdot 10^{-12}.
 \end{aligned}$$

From Eq. (6.6) and the theoretical predictions we can on the one hand measure the coupling constant α (see Fig. 6.5(b)):

$$\begin{aligned}
 \alpha^{-1} &= 137.035\,999\,084 \text{ (33) (39)} \quad [0.24 \text{ ppb}][0.28 \text{ ppb}] \\
 &= 137.035\,999\,084 \text{ (51)} \quad [0.37 \text{ ppb}]
 \end{aligned}$$

and on the other hand, we can compare the measured $g/2$ with the expectation using α from other measurements

$$\begin{aligned}
 g/2 &= 1.001\,159\,652\,180\,73 \text{ (28)} \quad [0.28 \text{ ppt}] \text{ (measured)} \\
 g(\alpha)/2 &= 1.001\,159\,652\,177\,60 \text{ (520)} \quad [5.2 \text{ ppt}] \text{ (predicted)}.
 \end{aligned}$$

6.2 High energy tests

6.2.1 e^+e^- colliders

In addition to the low-energy experiments, QED has been tested also in high energy e^+e^- collisions [20, 21, 22].

We discuss here the following reactions:

- Bhabha scattering : $e^+e^- \rightarrow e^+e^-$
- Lepton pair production : $e^+e^- \rightarrow \mu^+\mu^-, \tau^+\tau^-$
- Hadronic processes : $e^+e^- \rightarrow q\bar{q} \rightarrow \text{hadrons}$

The energy range $12 \text{ GeV} \leq \sqrt{s} \leq 47 \text{ GeV}$ was investigated with the PETRA accelerator at DESY (Hamburg). High energy ranges ($90 \text{ GeV} \leq \sqrt{s} \leq 200 \text{ GeV}$) were covered by the LEP collider at CERN (Geneva). However, electroweak contributions to the cross-sections, like the one shown in Fig. 6.6, become considerable at these energies. Intermediate energies were covered by TRISTAN and SLC. Table 6.1 gives an overview of the e^+e^- colliders.

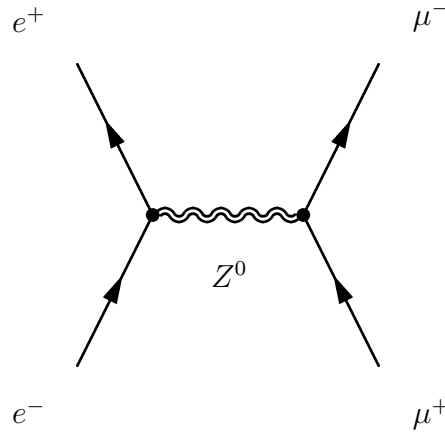


Figure 6.6: Electroweak contribution to $\mathcal{M}_{fi}(e^+e^- \rightarrow \mu^+\mu^-)$ at high energies.

The PETRA collider is shown in Fig. 6.7 as an example.

As an example for a typical detector we take a look at JADE (Figs. 6.8 and 6.9), using the same numbering as in the figure.

1. *Beam pipes counters.*
2. *End plug lead glass counters.*
3. *Pressure tank.*

| Accelerator | Experiment(s) | \sqrt{s} [GeV] | \mathcal{L}_{int} [pb $^{-1}$] |
|-------------|--------------------------------------|------------------|--|
| SPEAR | SPEAR | 2-8 | - |
| PEP | ASP, DELCO, HRS, MARK II, MAC | 0-29 | 300 |
| PETRA | JADE, MARK J, PLUTO, TASSO, CELLO | 12-47 | 20 |
| TRISTAN | TRISTAN | 50-60 | 20 |
| SLC | MARK II, SLD | 90 | 25 |
| LEP | ALEPH, DELPHI, OPAL, L3 | 90-200 | 200 |
| | | | 700 |

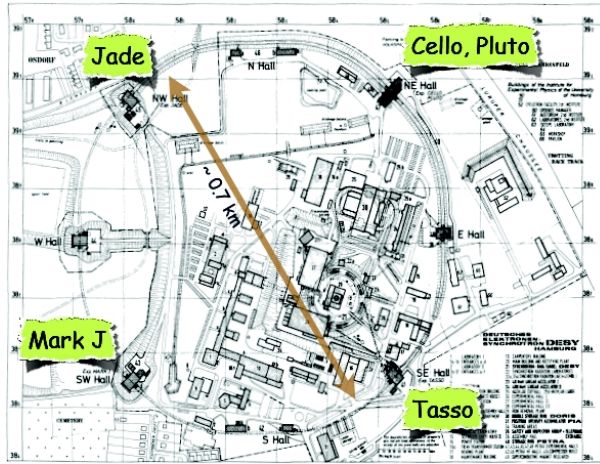
Table 6.1: Table of e^+e^- colliders

Figure 6.7: PETRA storage ring

4. *Muon chambers.* Detect muons.
5. *Jet chambers.* Records the trajectories of the produced particles.
6. *Time of flight counters.* Measure the time necessary for the particle to get from the collision center and thus its velocity.
7. *Coil.* Produces a magnetic field of 0.5 [T] parallel to the beam in the central region to measure the momentum of the particles by providing the curvature of their trajectories.
8. *Central lead glass counters.*
9. *Magnet yoke.*
10. *Muon filter.*
11. *Removable end plug.*

12. *Beam pipe.*
13. *Tagging counter.*
14. *Mini beta quadrupole.* Focus the beam to increase the luminosity of the beam in the experiment.
15. *Moving devices.*

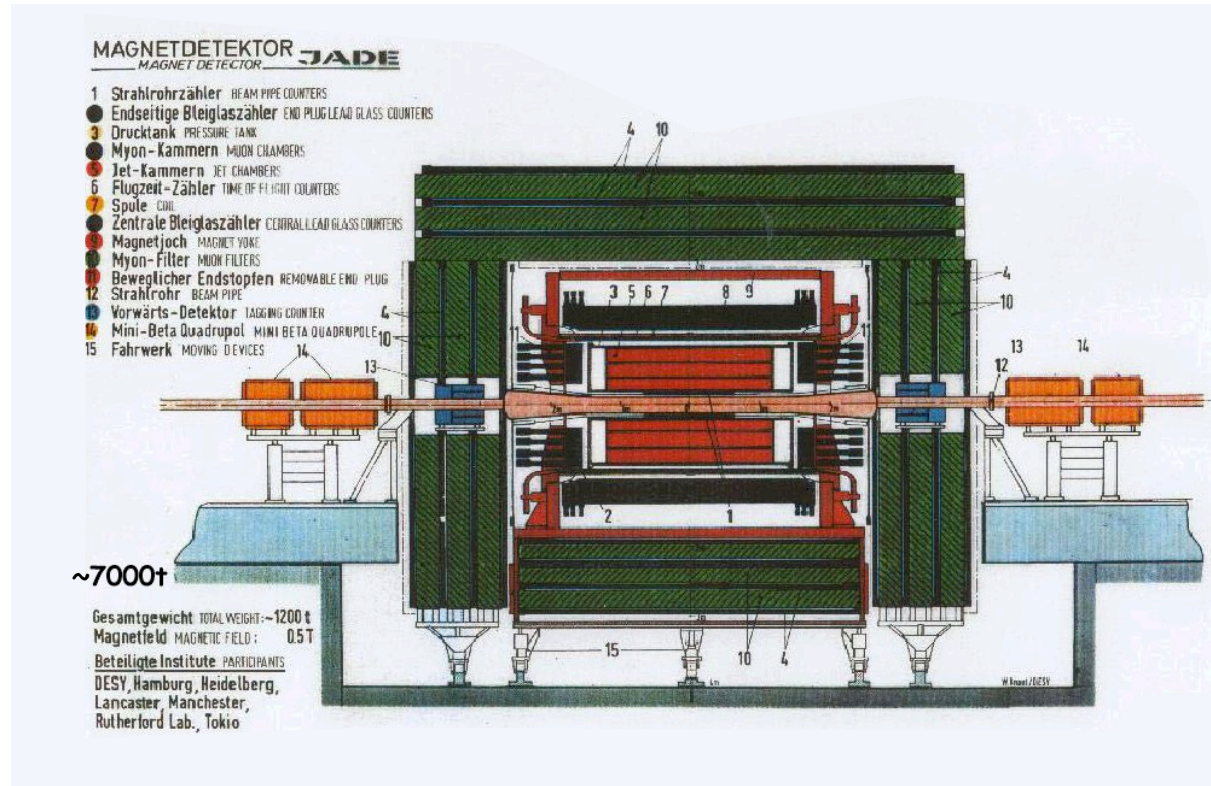


Figure 6.8: JADE detector : schematics

6.2.2 Detector elements

In order to help identify the particles produced in a collision (or their decay product) we can determine their charge and invariant mass using the methods presented in chapter 4. This measurement proceeds mostly in the inner part of the detector, see Fig. 4.15, by means of drift chambers or silicon trackers. If some of the produced particles are long living (i.e. are stable or decay weakly), this setup gives also the possibility to detect a decay vertex.

Further away from the beam axis are the **calorimeters**, whose function is to stop the particles and measure the energy they deposit. There are mostly two types of calorimeters:

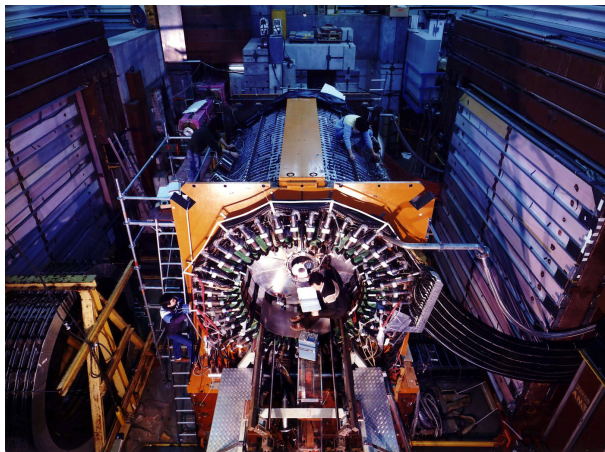


Figure 6.9: JADE detector

electromagnetic and hadronic. The angular resolution is limited by the size of each detector cell. Calorimeters are also able to measure neutral particles while the tracking devices described above can only detect charged particles.

Electromagnetic calorimeters stop and measure the energy of electrons, positrons and photons. All electromagnetically interacting particles leave at least a part of their energy in this detector part.

Hadronic calorimeters stop and measure the energy of hadrons, e.g. protons, neutrons and pions. Muons and antimuons are not stopped but leave some energy. Most modern experiments are also surrounded by **muon detectors** in order to distinguish the energy deposit of low energetic hadrons from the one of muons. Since it is practically impossible to stop muons, this last detector records the direction of passage of muons and, eventually, their momentum.

Fig. 6.10 shows the schematic view of the different signal hits for different types of particles. The energy deposit is usually depicted by a histogram.

- *Electron signature.* Electrons leave a curved trace in the inner tracking detector and deposit all their energy in the electromagnetic calorimeter, where they are completely stopped. There is hence no signal stemming from electrons in detectors further away from the collision point.
- *Hadron signature.* Charged hadrons leave a trace in the inner detector (curved by the magnetic field), – whereas uncharged hadrons do not –, deposit a part of their energy in the electromagnetic calorimeter and the rest of their energy in the hadronic calorimeter.

- *Muon signature.* Muons leave a curved trace in the inner detector and deposit some energy in the electromagnetic and hadronic calorimeters without being stopped, and then leave a signal in the muon detector.
- *Photon signature.* Photons do not leave a trace in the inner detector and are stopped in the electromagnetic calorimeter.

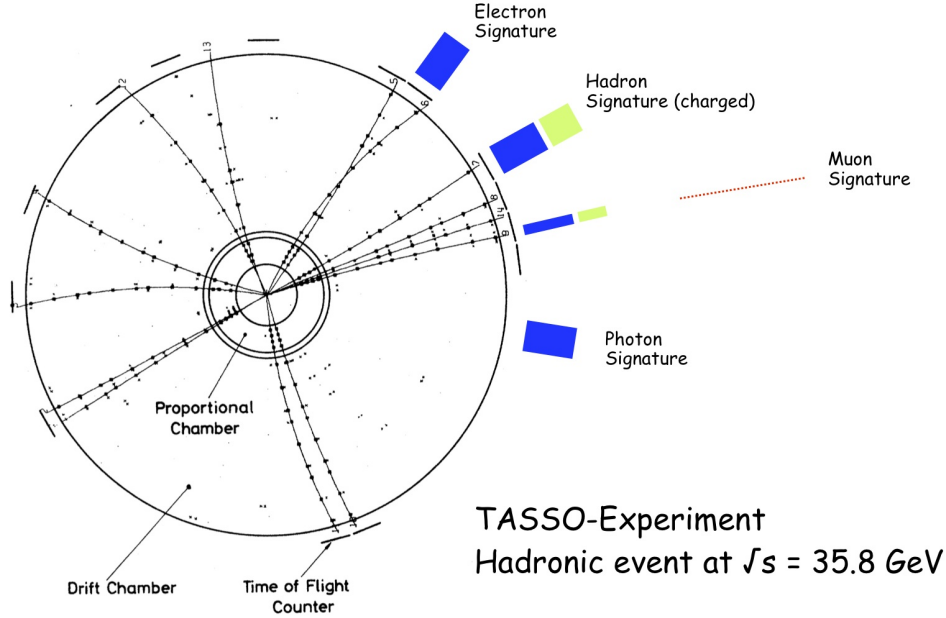


Figure 6.10: Event reconstruction principle

6.2.3 Cross section measurement

To measure a cross section we divide the measured number of events N by the integrated luminosity at that energy $\mathcal{L}(s)$,

$$\sigma(s) = \frac{N}{\mathcal{L}(s)}. \quad (6.7)$$

The last one is measured by counting the events occurring at small scattering angles and using the relation,

$$\sigma_{ee,\gamma\gamma}^{\text{theo}} = \frac{N(1-b)}{(\varepsilon A) \cdot \mathcal{L}}, \quad (6.8)$$

where A and b depend on the detector geometry, while ε is the efficiency (the probability to measure a particle, if it hits the detector).

Fig. 6.11 shows a typical integrated luminosity spectrum over the energy range 0–47 GeV.

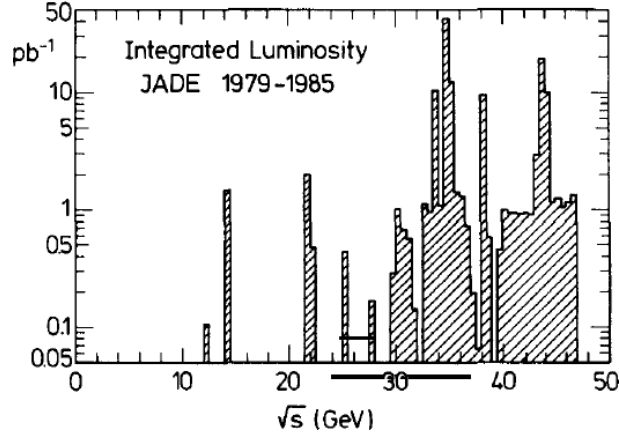


Figure 6.11: Integrated luminosity for the JADE experiment at PETRA

Reminder : e^+e^- kinematics One can write the differential cross section as,

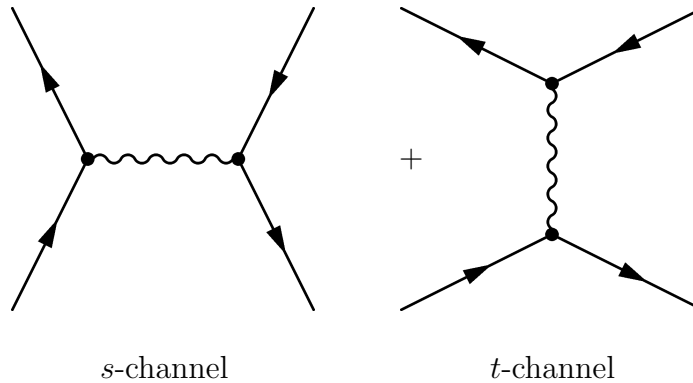
$$\frac{d\sigma_{\text{QED}}}{d\Omega} = \frac{d\sigma_0}{d\Omega} (1 + \delta_{\text{rad}}), \quad (6.9)$$

where δ_{rad} stands for the radiative corrections, i.e. terms coming from diagrams with more vertices (proportional to α in the case of QED). These include emission of further low energy exchange bosons and loop corrections.

6.2.4 Bhabha scattering

Leading order We first treat the leading order term, the one yielding $d\sigma_0/d\Omega$.

The following two diagrams contribute to the invariant amplitude :



Using Eq. (3.32) and the trace theorems of section 5.9, we get,

$$\begin{aligned} \frac{d\sigma_0}{d\Omega} &= \frac{\alpha^2}{4s} \left(\underbrace{\frac{t^2 + s^2}{u^2}}_{t\text{-channel}} + \underbrace{\frac{2t^2}{us}}_{\text{interference}} + \underbrace{\frac{t^2 + u^2}{s^2}}_{s\text{-channel}} \right) \\ &= \frac{\alpha^2}{4s} \left(\frac{3 + \cos^2 \vartheta}{1 - \cos \vartheta} \right)^2. \end{aligned} \quad (6.10)$$

Note that it is divergent for $\vartheta \rightarrow 0$. Fig.6.12 shows the $\cos \vartheta$ -dependence of each component in Eq. (6.10). We remark that the differential cross section is dominated by the t -channel component at all angles, and that the s -channel is almost constant, when compared to the last. The interference term is always negative. It is small in magnitude for large scattering angles ($\vartheta \sim \pi \Leftrightarrow \cos \vartheta \sim -1$) and diverges in the case of forward scattering ($\vartheta = 0 \Leftrightarrow \cos \vartheta = 1$).

Fig. 6.13 shows the typical trace left in the electronic calorimeter by a scattered e^+e^- -pair. Fig. 6.14 shows $\sigma^{e^+e^- \rightarrow e^+e^-}$ measured as a function of $\cos \vartheta$ for different center of mass

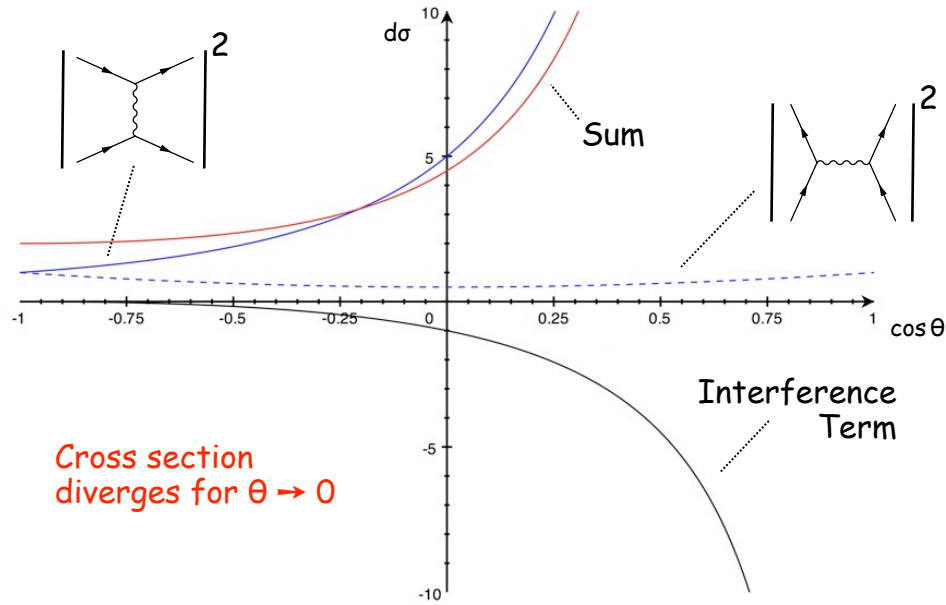


Figure 6.12: Relative magnitude of the different terms in $d\sigma_0/d\Omega$.

energies. It decreases following a $1/s$ -dependence.

Radiative corrections The diagrams contributing to the cross section and proportional to higher powers of α (or e) are shown in Table 6.2.

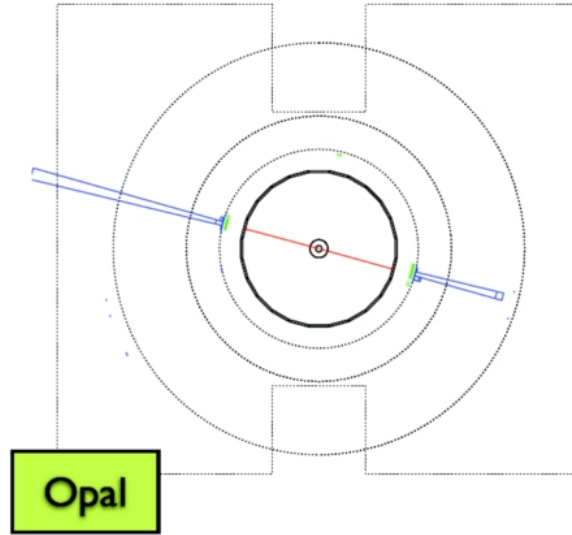


Figure 6.13: Typical event display of a Bhabha scattering event recorded by the Opal experiment. The length of the blue histogram corresponds to the amount of energy deposited in the electromagnetic calorimeter.

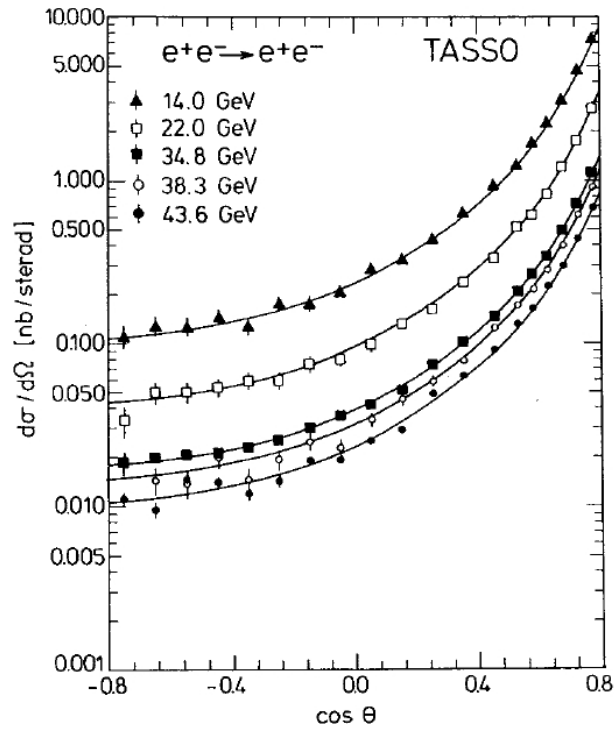
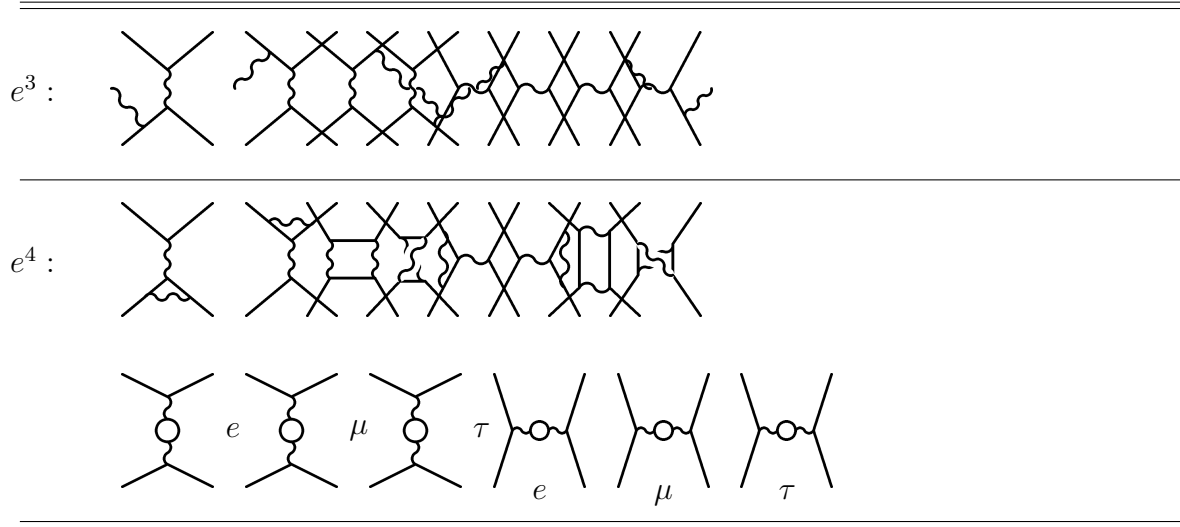


Figure 6.14: Energy and angle dependence of the cross section measured at TASSO and compared to leading order calculations.

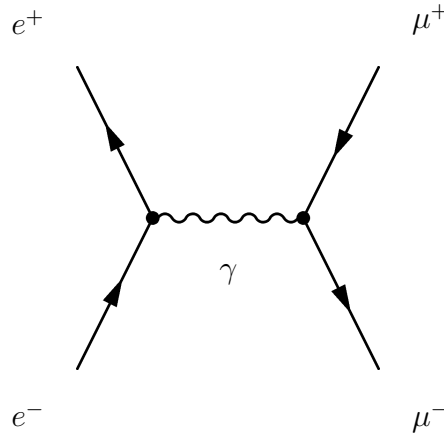
Table 6.2: Diagrams of radiative and loop corrections up to e^4

Because of momentum conservation, the diagrams of the e^3 -order imply that the electron-positron pair is no longer back-to-back after the collision. This effect is called **acollinearity**. The acollinearity angle is the angle $\xi = \pi - \phi$, where ϕ is the angle between the direction of the scattered electron and the scattered positron; for a back-to-back flight there is no acollinearity, thus $\xi = 0$. This angle has been measured at the JADE experiment and confirms higher order QED corrections in a very impressive way (see Fig. 6.15).

6.2.5 Lepton pair production

Muon pair production Looking at different final states gives also different results. We illustrate this by looking at the process $e^+e^- \rightarrow \mu^+\mu^-$. This is the simplest process of QED and is often used to normalize cross sections of other processes.

There is only one leading order Feynman diagram, namely,



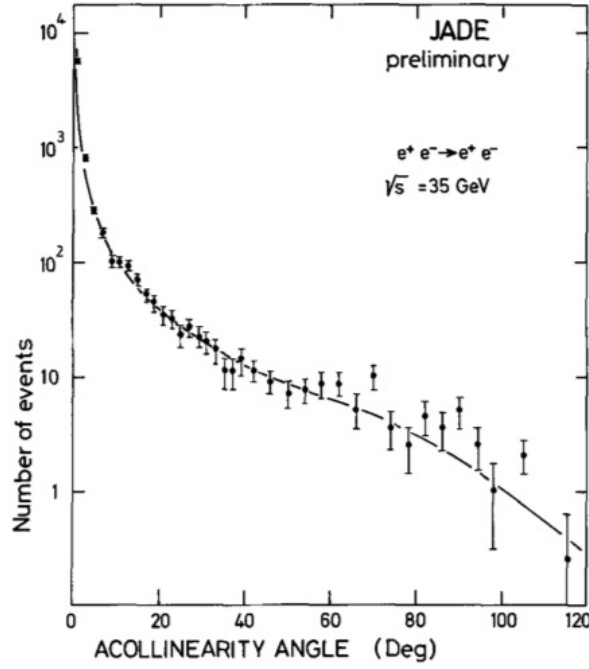


Figure 6.15: Comparison of measured acollinearity at JADE with the QED prediction.

and the leading order differential cross section is,

$$\frac{d\sigma_0}{d\Omega} = \frac{\alpha^2}{4s} \left(\frac{t^2 + u^2}{s^2} \right) = \frac{\alpha^2}{4s} (1 + \cos^2 \vartheta), \quad (6.11)$$

which is shown in Fig. 5.9.

Fig. 6.16 shows an event candidate: low energy deposits in the electromagnetic calorimeter and hits in the muon chambers.

Muon pair production : Z^0 exchange Since only s -channel contributes to the muon pair production, the diagram containing a Z^0 boson instead of a photon²,

²This contribution is also present in the case of Bhabha scattering, yet since the t -channel dominates over the s -channel, the effect is virtually invisible.

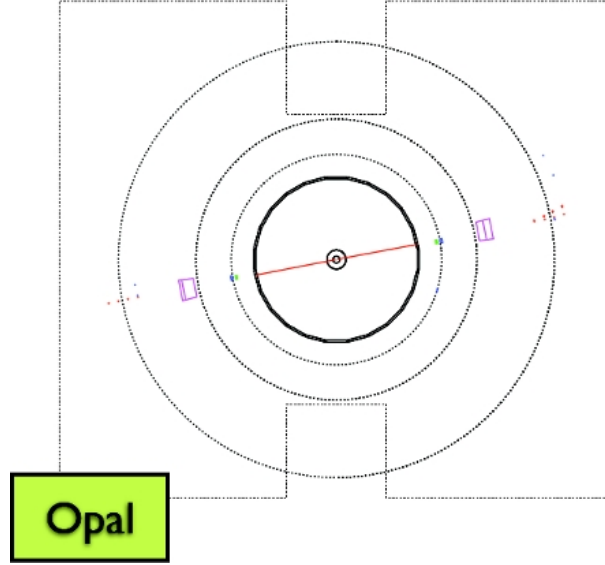
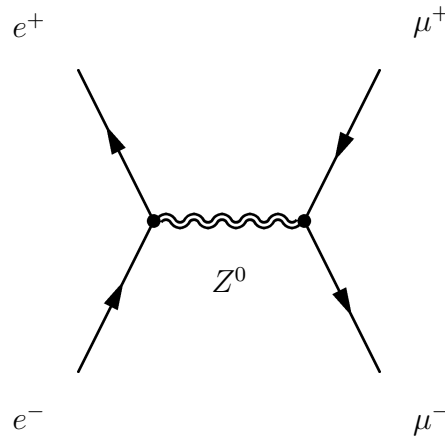


Figure 6.16: Typical event display of a muon pair production event recorded by the Opal experiment.



becomes comparable with the photon term (approx. 10%), even at leading order. This leads to a the modified cross section,

$$\frac{d\sigma_0^{\text{EW}}}{d\Omega} = \frac{\alpha^2}{4s}(1 + \cos^2 \vartheta + A \cos \vartheta). \quad (6.12)$$

This is illustrated in Fig. 6.17 comparing the QED and electroweak predictions to the data.

As an easy integration of Eq. (6.12) shows, the *total* cross section is not sensitive to the effects of electroweak interaction and we have a very good agreement with the QED value (Fig. 6.18).

For the \sqrt{s} -range measured at PETRA, electroweak corrections are small. In the case of LEP they are instead quite important, especially in the range around the Z^0 resonance,

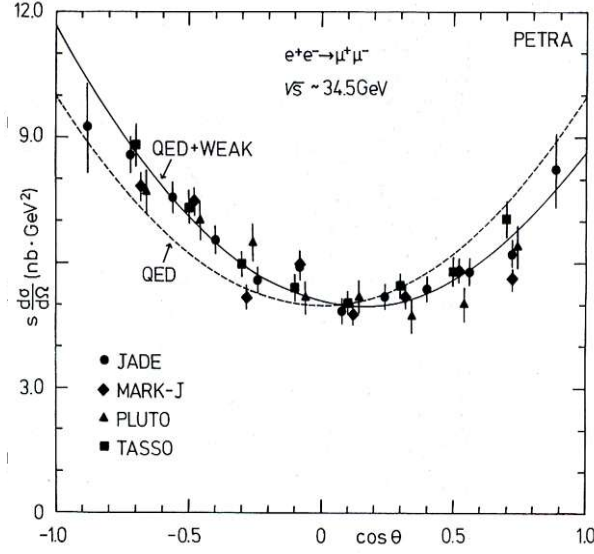


Figure 6.17: Comparison of $e^+e^- \rightarrow \mu^+\mu^-$ differential cross section measured at PETRA with the QED and electroweak predictions.

$$\sqrt{s} \sim m_Z \approx 90 \text{ [GeV]}.$$

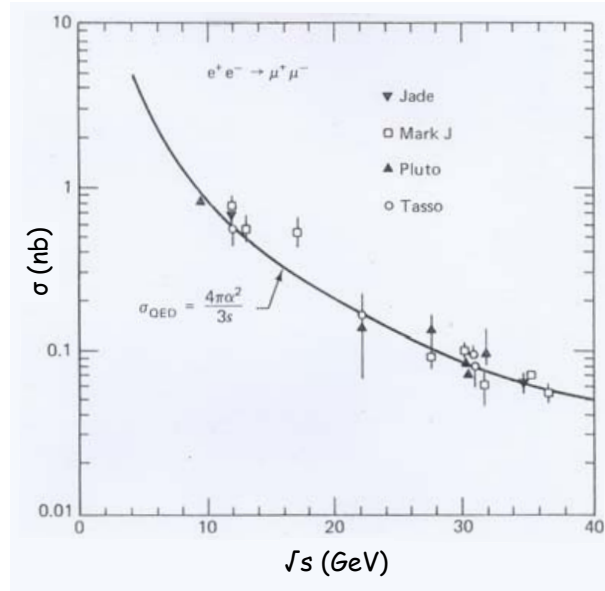
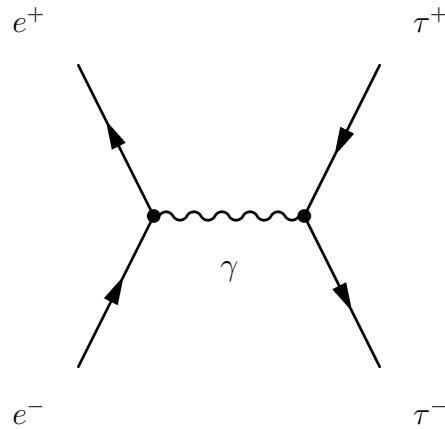


Figure 6.18: Comparison of measured total cross section at PETRA with the QED prediction.

Tau pair production At high enough energy ($\sqrt{s} \geq 2m_\tau \approx 3.6 \text{ [GeV]}$) the production of $\tau^+\tau^-$ -pair – which is very similar to the case of muon pair production – is possible:



The final state of a tau pair production event observed in the detector can contain hadrons, since the lifetime of τ is very short ($\tau_\tau = 2.9 \cdot 10^{-13}$ [s]) and it is the only lepton with sufficiently high mass to produce $q\bar{q}$ -pairs.

Fig. 6.19 shows an event where one of the two tau survived long enough, e.g. because of a large energy and thus a longer lifetime $\gamma\tau_\tau$ in the laboratory frame, to hit the electromagnetic calorimeter, while the other one decayed in three pions which then left traces in the electromagnetic and hadronic calorimeters.

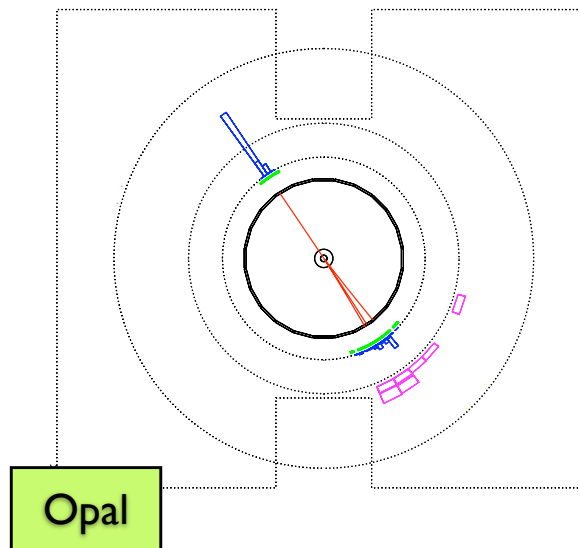


Figure 6.19: Typical event display of a tau pair production event recorded by the Opal experiment.

6.2.6 Hadronic processes

The production of quark-antiquark $q\bar{q}$ pair is another possible final state in e^+e^- annihilation.

When a bound $q\bar{q}$ state is produced, we speak of a **resonance** because the e^+e^- cross section looks like the amplification curve of a periodic system such as a pendulum or an RLC circuit near the resonant frequency. A famous resonance is the J/ψ resonance corresponding to a bound state of $c\bar{c}$.

Away from the resonances, there is in general no visible bound state, and the produced quarks hadronize in **jets** due to the confinement of the strong interaction : quarks cannot be seen as free particles.

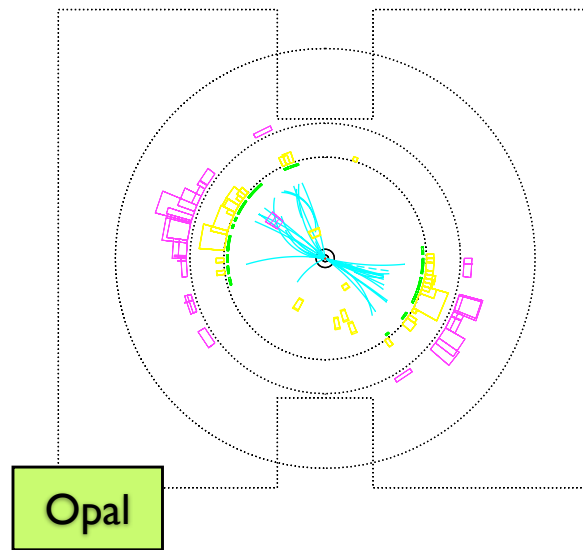
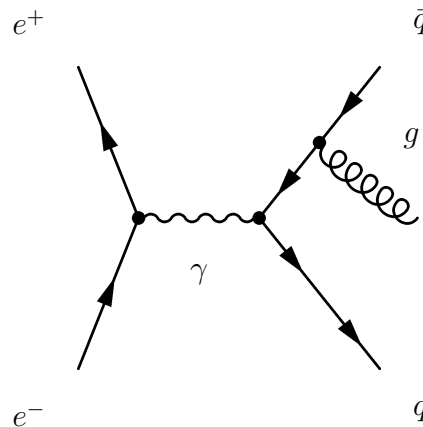


Figure 6.20: Typical display of jet production event recorded by the Opal experiment.

Due to the strength of strong interaction at low energy, the radiative effects (this time the radiated bosons are gluons),



take a much more dramatic form than in QED : Since gluons also have a color charge, they hadronize and for each emitted gluon one observes one more jet (Fig. 6.21).

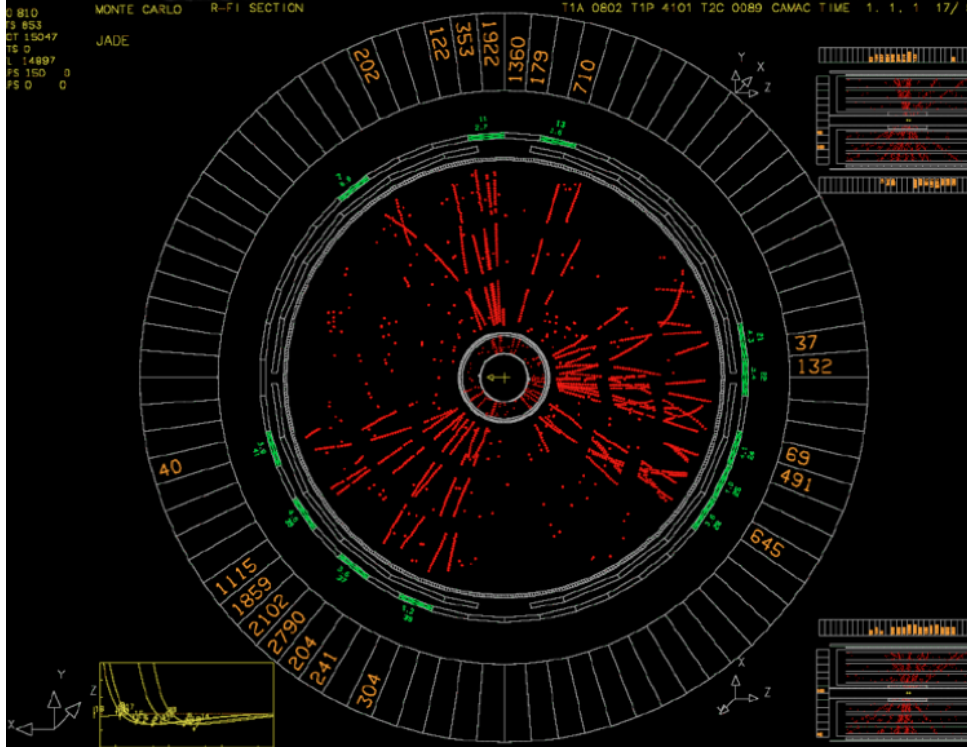


Figure 6.21: Typical event display of a 3-jets production.

6.2.7 Limits of QED

In this section, one addresses the question : what do we expect if QED is not the only theoretical model involved in the scattering processes discussed so far?

Suppose there is an energy scale Λ (equivalent to a length scale Λ^{-1}) at which QED does not describe the data anymore.

We would have changes of the various quantities, for instance, the potential, photon propagator and total cross section would be modified as follows :

$$\begin{aligned} \frac{1}{r} &\rightarrow \frac{1}{r} (1 - e^{-\Lambda r}) && \text{(potential)} \\ -\frac{1}{q^2} &\rightarrow -\frac{1}{q^2} \left(1 + \frac{q^2}{\Lambda^2}\right) && \text{(propagator)} \\ \sigma^{e^+e^- \rightarrow \mu^+\mu^-} &\rightarrow \frac{4\pi\alpha^2}{3s} \left(1 \pm \frac{s}{\Lambda^2 - s}\right)^2 && \text{(cross section).} \end{aligned}$$

The form of the potential is typical of a Yukawa coupling of a fermion with a massive spin 0 field. Since this particle is imagined as heavy – the energy available is smaller or similar to the production threshold Λ – we can treat this particle as spinless since spin effects are only significant in the relativistic case. This type of ansatz is thus standard in the sense that any new heavy particle that can be produced from an e^+e^- -annihilation will have the same effect on the potential, regardless of it being a scalar or a vector particle. The other quantities are then directly related to the change in the potential.

We have seen the electroweak effects to the QED cross section at the end of the previous subsection. This corresponds to $\Lambda \approx m_{Z^0}$ (Fig. 6.22).

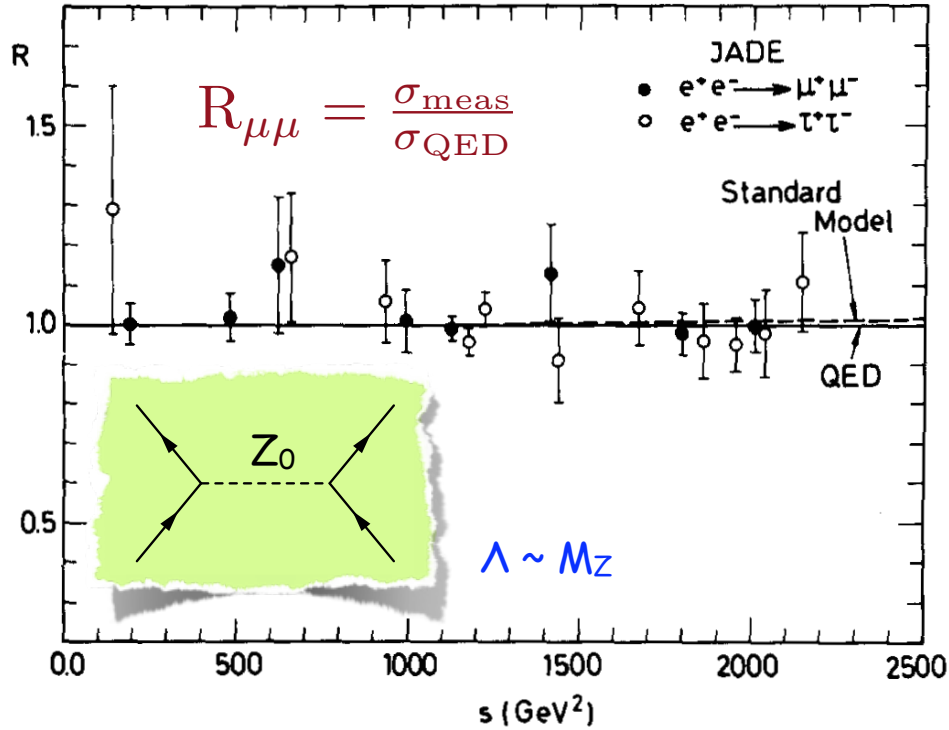


Figure 6.22: Comparison of measured total cross section at PETRA with the QED prediction for muon and tau pair production.

Fig. 6.23 shows the ratio,

$$R_{\mu\mu} = \frac{\sigma_{\text{meas}}^{e^+e^- \rightarrow \mu^+\mu^-}}{\sigma_{\text{QED}}^{e^+e^- \rightarrow \mu^+\mu^-}},$$

as measured at PETRA and TRISTAN. By comparing data and theory and varying Λ within the experimental error one can infer that – if any – new physics can only be brought in with a mass scale $\Lambda \geq 200 [\text{GeV}]$.

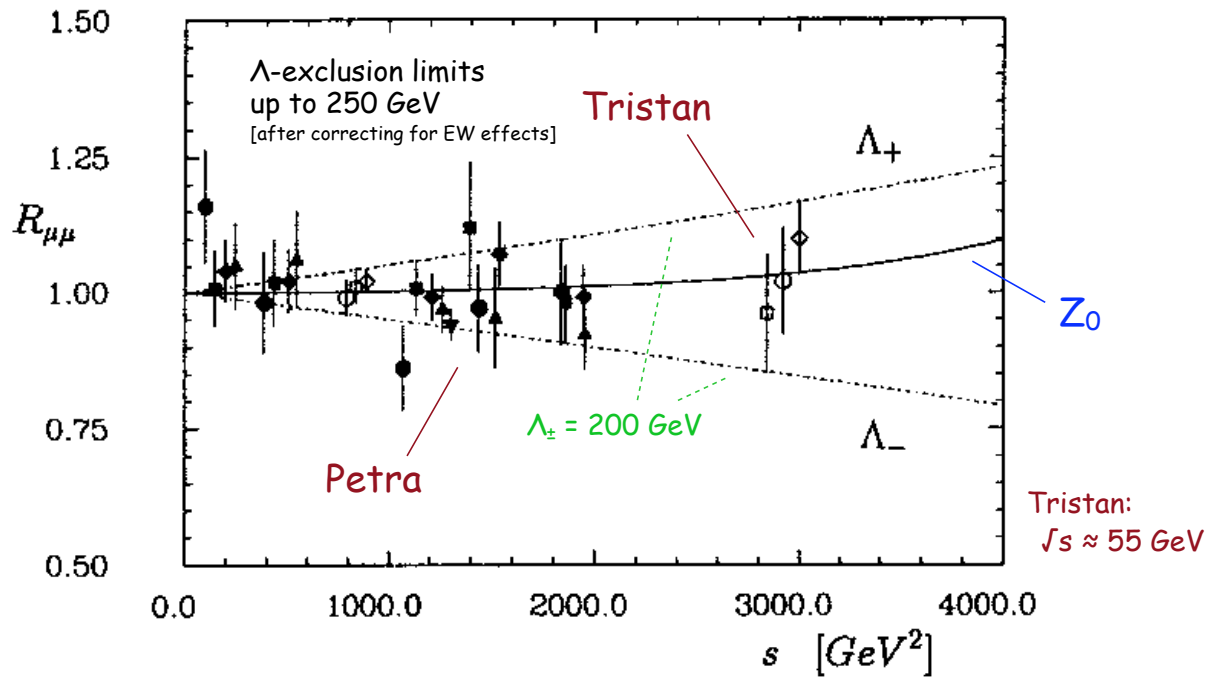


Figure 6.23: Comparison of measured total cross section at PETRA and TRISTAN with the QED prediction for muon pair production.

Chapter 7

Unitary symmetries and QCD as a gauge theory

Literature:

- Lipkin [23] (group theory concepts from a physicist's point of view)
- Lee [24], chapter 20 (extensive treatment of Lie groups and Lie algebras in the context of differential geometry)

Interactions between particles should respect some observed symmetry. Often, the procedure of postulating a specific symmetry leads to a unique theory. This way of approach is the one of **gauge theories**. The usual example of a gauge theory is QED, which corresponds to a local $U(1)$ -symmetry of the Lagrangian :

$$\psi \rightarrow \psi' = e^{ieq_e\chi(x)}\psi, \quad (7.1)$$

$$A_\mu \rightarrow A'_\mu = A_\mu - \partial_\mu\chi(x). \quad (7.2)$$

We can code this complicated transformation behavior by replacing in the QED Lagrangian ∂_μ by the **covariant derivative** $D_\mu = \partial_\mu + ieq_eA_\mu$.

7.1 Isospin $SU(2)$

For this section we consider only the strong interaction and ignore the electromagnetic and weak interactions. In this regard, isobaric nuclei (with the same mass number A) are very similar. Heisenberg proposed to interpret protons and neutrons as two states of the same object : the **nucleon**:

$$\begin{aligned} |p\rangle &= \psi(x) \begin{pmatrix} 1 \\ 0 \end{pmatrix}, \\ |n\rangle &= \psi(x) \begin{pmatrix} 0 \\ 1 \end{pmatrix}. \end{aligned}$$

We note the analogy to the spin formalism of nonrelativistic quantum mechanics, which originated the name *isospin*.

In isospin-space, $|p\rangle$ and $|n\rangle$ can be represented as a two-component spinor with $I = \frac{1}{2}$. $|p\rangle$ has then $I_3 = +\frac{1}{2}$ and $|n\rangle$ has $I_3 = -\frac{1}{2}$.

Since the strong interaction is blind to other charges (electromagnetic charge, weak hypercharge), the (strong) physics must be the same for any linear combinations of $|p\rangle$ and $|n\rangle$. In other words, for,

$$\begin{aligned} |p\rangle &\rightarrow |p'\rangle = \alpha |p\rangle + \beta |n\rangle, \\ |n\rangle &\rightarrow |n'\rangle = \gamma |p\rangle + \delta |n\rangle, \end{aligned}$$

for some $\alpha, \beta, \gamma, \delta \in \mathbb{C}$, or,

$$|N\rangle = \begin{pmatrix} \psi_p \\ \psi_n \end{pmatrix} \rightarrow |N'\rangle = U |N\rangle, \quad (7.3)$$

for some 2×2 matrix U with complex entries, the (strong) physics does not change if we switch from $|N\rangle$ to $|N'\rangle$ to describe the system.

We remark at this point that this symmetry is only an *approximate* symmetry since it is violated by the other interactions, and is hence *not* a symmetry of nature.

First we require the conservation of the norm $\langle N|N\rangle$ which we interpret as the number of particles like in quantum mechanics. This yields,

$$\begin{aligned} \langle N|N\rangle &\rightarrow \langle N'|N'\rangle = \langle N|U^\dagger U|N\rangle \stackrel{!}{=} \langle N|N\rangle \\ &\Rightarrow U^\dagger U = U U^\dagger = \mathbb{1} \Rightarrow U \in U(2). \end{aligned} \quad (7.4)$$

A general unitary matrix has 4 real parameters. Since the effect of U and $e^{i\varphi}U$ are the same, we fix one more parameter by imposing,

$$\det U \stackrel{!}{=} 1 \Rightarrow U \in SU(2), \quad (7.5)$$

the special unitary group in 2 dimensions. This group is a **Lie group** (a group which is at the same time a manifold). We use the representation,

$$U = e^{i\alpha_j \hat{I}_j}, \quad (7.6)$$

where the α_j 's are arbitrary group parameters (constant, or depending on the spacetime coordinate x), and the \hat{I}_j 's are the generators of the Lie group.

We concentrate on infinitesimal transformations, for which $\alpha_j \ll 1$. In this approximation we can write

$$U \approx \mathbb{1} + i\alpha_j \hat{I}_j. \quad (7.7)$$

The two defining conditions of $SU(2)$, Eq. (7.4) and (7.5), imply then for the generators,

$$\hat{I}_j^\dagger = \hat{I}_j \quad (\text{hermitian}), \quad (7.8)$$

$$\text{Tr } \hat{I}_j = 0 \quad (\text{traceless}). \quad (7.9)$$

In order for the exponentiation procedure to converge for noninfinitesimal α_j 's, the generators must satisfy a commutation relation, thus defining the **Lie algebra** $\mathfrak{su}(2)$ of the group $SU(2)$.

Quite in general, the commutator of two generators must be expressible as a linear combination of the other generators¹. In the case of $\mathfrak{su}(2)$ we have,

$$[\hat{I}_i, \hat{I}_j] = i\varepsilon_{ijk}\hat{I}_k, \quad (7.10)$$

where ε_{ijk} is the totally antisymmetric tensor with $\varepsilon_{123} = +1$. They are characteristic of the (universal covering group of the) Lie group (but independent of the chosen representation) and called structure constants of the Lie group.

The representations can be characterized according to their total isospin. Consider now $I = 1/2$, where the generators are given by

$$\hat{I}_i = \frac{1}{2}\tau_i$$

with $\tau_i = \sigma_i$ the Pauli spin matrices (this notation is chosen to prevent confusion with ordinary spin):

$$\tau_1 = \begin{pmatrix} 0 & 1 \\ 1 & 0 \end{pmatrix} \quad \tau_2 = \begin{pmatrix} 0 & -i \\ i & 0 \end{pmatrix} \quad \tau_3 = \begin{pmatrix} 1 & 0 \\ 0 & -1 \end{pmatrix}$$

which fulfill $[\sigma_i, \sigma_j] = 2i\varepsilon_{ijk}\sigma_k$. The action of the matrices of the representation (see Eq. (7.6)) is a non-abelian phase transformation:

$$|N'\rangle = e^{i\vec{\alpha} \cdot \frac{\vec{\tau}}{2}} |N\rangle.$$

For $SU(2)$, there exists only one diagonal matrix (τ_3). In general, for $SU(N)$, the following holds true:

- *Rank* $r = N - 1$: There are r simultaneously diagonal operators.
- *Dimension* of the Lie algebra $o = N^2 - 1$: There are o generators of the group and therefore o group parameters. E. g. in the case of $SU(2)/\{\pm 1\} \cong SO(3)$ this means that there are three rotations/generators and three angles as parameters.

¹Since we are working in a matrix representation of $SU(2)$ this statement makes sense. The difference between the abstract group and its matrix representation is often neglected.

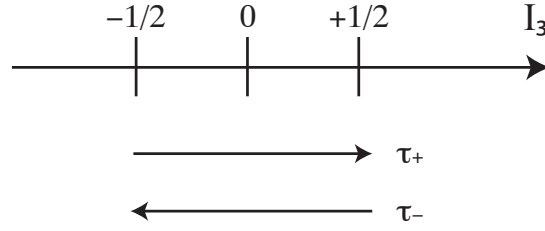


Figure 7.1: The nucleons $|n\rangle$ and $|p\rangle$ form an isospin doublet.

Isospin particle multiplets (representations) can be characterized by their quantum numbers I and I_3 : There are $2I + 1$ states. Consider for example once again the case $I = 1/2$. There are two states, characterized by their I_3 quantum number:

$$\left(\begin{array}{l} |I = \frac{1}{2}, I_3 = +\frac{1}{2}\rangle \\ |I = \frac{1}{2}, I_3 = -\frac{1}{2}\rangle \end{array} \right) = \left(\begin{array}{l} |p\rangle \\ |n\rangle \end{array} \right).$$

This is visualized in Fig. 7.1, along with the action of the operators $\tau_{\pm} = 1/2(\tau_1 \pm i\tau_2)$:

$$\begin{aligned} \tau_- |p\rangle &= \begin{pmatrix} 0 & 0 \\ 1 & 0 \end{pmatrix} \begin{pmatrix} 1 \\ 0 \end{pmatrix} = \begin{pmatrix} 0 \\ 1 \end{pmatrix} = |n\rangle \\ \tau_+ |n\rangle &= |p\rangle \\ \tau_- |n\rangle &= \tau_+ |p\rangle = 0. \end{aligned}$$

This is the smallest non-trivial representation of $SU(2)$ and therefore its fundamental representation.

Further examples for isospin multiplets are

| I | multiplets | | | I_3 |
|---------------|--|---|---|--|
| $\frac{1}{2}$ | $\begin{pmatrix} p \\ n \end{pmatrix}$ | $\begin{pmatrix} K^+ \\ K^0 \end{pmatrix}$ | $\begin{pmatrix} {}^3_2\text{He} \\ {}^3_1\text{H} \end{pmatrix}$ | $+\frac{1}{2}$ $-\frac{1}{2}$ |
| 1 | | $\begin{pmatrix} \pi^+ \\ \pi^0 \\ \pi^- \end{pmatrix}$ | | +1 0 -1 |
| $\frac{3}{2}$ | | $\begin{pmatrix} \Delta^{++} \\ \Delta^+ \\ \Delta^0 \\ \Delta^- \end{pmatrix}$ | | $+\frac{3}{2}$ $+\frac{1}{2}$ $-\frac{1}{2}$ $-\frac{3}{2}$ |

where $m_{\Delta} \approx 1232 \text{ MeV}$ and $m_{p,n} \approx 938 \text{ MeV}$.

All $I \geq 1$ representations can be obtained from direct products out of the fundamental $I = 1/2$ representation $\underline{2}$ where “2” denotes the number of states. In analogy to the addition of two electron spins where the Clebsch-Gordan decomposition reads $\text{rep}_{1/2} \otimes$

$\text{rep}_{1/2} = \text{rep}_0 \oplus \text{rep}_1$ and where there are two states for the spin-1/2 representation, one state for the spin-0 representation, and three states for the spin-1 representation, we have

$$\underbrace{2 \otimes 2}_{I=|\frac{1}{2} \pm \frac{1}{2}|=0,1} = \underbrace{1}_{\text{isosinglet}, I=0} \oplus \underbrace{3}_{\text{isotriplet}, I=1}. \quad (7.11)$$

However, there is an important difference between isospin and spin multiplets. In the latter case, we are considering a bound system and the constituents carrying the spin have the same mass. On the other hand, pions are not simple bound states. Their structure will be described by the quark model.

7.1.1 Isospin invariant interactions

Isospin invariant interactions can be constructed by choosing $SU(2)$ invariant interaction terms \mathcal{L}' . For instance, consider the Yukawa model, describing nucleon-pion coupling, where

$$\mathcal{L}'_{\pi N} = ig \bar{N} \vec{\tau} N \cdot \vec{\pi} = ig \bar{N}' \vec{\tau} N' \cdot \vec{\pi}' \quad (7.12)$$

which is an isovector and where the second identity is due to $SU(2)$ invariance. Infinitesimally, the transformation looks as follows:

$$N' = U N \quad U = \mathbb{1} + \frac{i}{2} \vec{\alpha} \cdot \vec{\tau} \quad (7.13)$$

$$\bar{N}' = \bar{N} U^\dagger \quad U^\dagger = \mathbb{1} - \frac{i}{2} \vec{\alpha} \cdot \vec{\tau} = U^{-1} \quad (7.14)$$

$$\vec{\pi}' = V \vec{\pi} \quad V = \mathbb{1} + i \vec{\alpha} \cdot \vec{t}. \quad (7.15)$$

The parameters \vec{t} can be determined from the isospin invariance condition in Eq. (7.12):

$$\bar{N} \tau_j N \pi_j = \bar{N} U^{-1} \tau_i U N V_{ij} \pi_j.$$

With $V_{ij} = \delta_{ij} + i\alpha_k (t_k)_{ij}$ (cp. Eq. (7.15)) and inserting the expressions for U and U^\dagger , this yields

$$\begin{aligned} \tau_j &= \underbrace{\left(\mathbb{1} - \frac{i}{2} \alpha_k \tau_k \right) \tau_i \left(\mathbb{1} + \frac{i}{2} \alpha_k \tau_k \right)}_{\substack{= \tau_i + \frac{i}{2} \alpha_k [\tau_i, \tau_k] + \mathcal{O}(\alpha_k^2) \\ = \tau_i + \frac{i}{2} \alpha_k 2i \varepsilon_{ikl} \tau_l + \mathcal{O}(\alpha_k^2)}} \left(\delta_{ij} + i\alpha_k (t_k)_{ij} \right) \\ &= \tau_j + i\alpha_k \{ i\varepsilon_{jkl} \tau_l + \tau_i (t_k)_{ij} \} \\ &= \tau_j + i\alpha_k \tau_i \underbrace{\{ i\varepsilon_{jki} + (t_k)_{ij} \}}_{\stackrel{!}{=} 0} \\ &\Rightarrow (t_k)_{ij} = -i\varepsilon_{kij}. \end{aligned}$$

This means that the 3×3 matrices t_k , $k = 1, 2, 3$, are given by the structure constants (see Eq. (7.10)). For the commutator we therefore have

$$[t_k, t_l]_{ij} = -\varepsilon_{kim}\varepsilon_{lmj} + \varepsilon_{lim}\varepsilon_{kmj} = \varepsilon_{klm}\varepsilon_{mij} = i\varepsilon_{klm}(-i\varepsilon_{mij}) = i\varepsilon_{klm}(t_m)_{ij} \quad (7.16)$$

where the second identity follows using the Jacobi identity. This means that the matrices t_k fulfill the Lie algebra

$$[t_k, t_l] = i\varepsilon_{klm}t_m.$$

The t_k s form the adjoint representation of $SU(2)$.

7.2 Quark model of hadrons

It is experimentally well established that the proton and the neutron have inner structure. The evidence is:

- Finite electromagnetic charge radius

$$\langle r_{p,n} \rangle = 0.8 \cdot 10^{-15} \text{ m}$$

(The neutron is to be thought of as a neutral cloud of electromagnetically interacting constituents.)

- Anomalous magnetic moment

$$\vec{\mu} = g \frac{q}{2m} \vec{s} \quad g_p = 5.59 \quad g_n = -3.83$$

- Proliferation of strongly interacting hadronic states (particle zoo)

$$p, n, \Lambda, \Delta^-, \Xi, \Sigma, \Omega, \dots$$

The explanation for these phenomena is that protons and neutrons (and the other hadrons) are bound states of quarks:

$$\left. \begin{array}{l} |p\rangle = |ud\rangle \\ |n\rangle = |dd\rangle \end{array} \right\} \text{ 3 quark states.}$$

The up quark and the down quark have the following properties

$$\begin{aligned} |u\rangle : & \quad q = +\frac{2}{3}, \quad I = \frac{1}{2}, \quad I_3 = +\frac{1}{2}, \quad S = \frac{1}{2}; \\ |d\rangle : & \quad q = -\frac{1}{3}, \quad I = \frac{1}{2}, \quad I_3 = -\frac{1}{2}, \quad S = \frac{1}{2}. \end{aligned}$$

| Quarks | | | Charge | Baryon number |
|---------------------|--------------------|--------------------|--------|---------------|
| Up 1.5 – 3 MeV | Charm 1270 MeV | Top 171 000 MeV | +2/3 e | 1/3 |
| Down 3.5 – 6 MeV | Strange 105 MeV | Bottom 4200 MeV | −1/3 e | 1/3 |
| Leptons | | | Charge | Lepton number |
| e^- | μ^- | τ^- | − e | 1 |
| ν_e | ν_μ | ν_τ | 0 | 1 |

Table 7.1: Quarks and leptons.

Thus, $|u\rangle$ and $|d\rangle$ form an isospin doublet and combining them yields the correct quantum numbers for $|p\rangle$ and $|n\rangle$. There are also quark-antiquark bound states: The pions form an isospin triplet while the $|\eta\rangle$ is the corresponding singlet state (see Eq. (7.11)):

$$\left. \begin{aligned} |\pi^+\rangle &= |u\bar{d}\rangle \\ |\pi^0\rangle &= \frac{1}{\sqrt{2}} (|u\bar{u}\rangle - |d\bar{d}\rangle) \\ |\pi^-\rangle &= |d\bar{u}\rangle \end{aligned} \right\} \text{triplet states, } I = 1$$

$$|\eta\rangle = \frac{1}{\sqrt{2}} (|u\bar{u}\rangle + |d\bar{d}\rangle) \left. \right\} \text{singlet state, } I = 0.$$

There are in total three known quark doublets:

$$\underbrace{\begin{pmatrix} |u\rangle \\ |d\rangle \end{pmatrix}}_{\text{up/down}} \quad \underbrace{\begin{pmatrix} |c\rangle \\ |s\rangle \end{pmatrix}}_{\text{charm/strange}} \quad \underbrace{\begin{pmatrix} |t\rangle \\ |b\rangle \end{pmatrix}}_{\text{top/bottom}} \quad \left(\begin{aligned} q &= +\frac{2}{3}, & I_3 &= +\frac{1}{2} \\ q &= -\frac{1}{3}, & I_3 &= -\frac{1}{2} \end{aligned} \right).$$

These quarks can be combined to give states like, e. g., $|\Lambda\rangle = |uds\rangle$.

7.3 Hadron spectroscopy

7.3.1 Quarks and leptons

Experimental evidence shows that, in addition to the three quark isospin doublets, there are also three families of leptons, the second type of elementary fermions (see Tab. 7.1). The lepton families are built out of an electron (or μ or τ) and the corresponding neutrino. The summary also shows the large mass differences between the six known quarks. All of the listed particles have a corresponding antiparticle, carrying opposite charge and baryon or lepton number, respectively.

Stable matter is built out of quarks and leptons listed in the first column of the family table. Until now, there is no evidence for quark substructure and they are therefore considered to be elementary. Hadrons, on the other hand, are composite particles. They are divided in two main categories as shown in the following table:

| Quarks | Flavor | Other numbers |
|----------|----------|---------------------|
| Up, Down | — | $S = C = B = T = 0$ |
| Charm | $C = +1$ | $S = B = T = 0$ |
| Strange | $S = -1$ | $C = B = T = 0$ |
| Top | $T = +1$ | $S = C = B = 0$ |
| Bottom | $B = -1$ | $S = C = T = 0$ |

Table 7.2: Additional quantum numbers for the characterization of unstable hadronic matter. Antiquarks have opposite values for these quantum numbers.

| Type | Matter | Antimatter |
|---------|------------|-------------------------|
| Baryons | qqq | $\bar{q}\bar{q}\bar{q}$ |
| Mesons | $q\bar{q}$ | |

Bound states such as $|qq\rangle$ or $|qq\bar{q}\rangle$ are excluded by the theory of quantum chromodynamics (see Sect. 7.4).

Unstable hadronic matter is characterized by the following additional flavor quantum numbers: Charm (C), Strangeness (S), Beauty (B), and Topness (T) (see Tab. 7.2). It is important to remember that in strong and electromagnetic interactions both baryon and flavor quantum numbers are conserved while in weak interactions only baryon quantum numbers are conserved. Therefore, weak interactions allow heavy quarks to decay into the stable quark family. The quark decay channels are shown in the following table:

| Quark \rightarrow | Decay products |
|---------------------|----------------|
| u, d | stable |
| s | uW^- |
| c | sW^+ |
| b | cW^- |
| t | bW^+ |

As we have seen, protons and neutrons are prominent examples of baryons. Their general properties can be summarized as follows:

| | Proton | Neutron |
|------------------------|---|---|
| Quarks | $ uud\rangle$ | $ udd\rangle$ |
| Mass | 0.9383 GeV | 0.9396 GeV |
| Spin | 1/2 | 1/2 |
| Charge | $e = 1.6 \cdot 10^{-19} \text{ C}$ | 0 C |
| Baryon number | 1 | 1 |
| Lifetime | stable: $\tau \geq 10^{32}$ years | unstable: $\tau_{n \rightarrow pe^- \bar{\nu}_e} = 887 \pm 2 \text{ s}$ |
| Production | gaseous hydrogen: ionization through electric field | under 1 MeV: nuclear reactors; 1 – 10 MeV: nuclear reactions |
| Target for experiments | liquid hydrogen | liquid deuterium |

The respective antiparticles can be produced in high-energy collisions, e. g.

$$\begin{aligned} pp &\rightarrow pp\bar{p}p \quad \text{with } |\bar{p}\rangle = |\bar{u}\bar{u}\bar{d}\rangle \quad \text{or} \\ pp &\rightarrow pp\bar{n}n \quad \text{with } |\bar{n}\rangle = |\bar{u}\bar{d}\bar{d}\rangle. \end{aligned}$$

Recall that in Sect. 4.1 we calculate the energy threshold for the reaction $pp \rightarrow pp\bar{p}p$ and find that a proton beam colliding against a proton target must have at least $|\vec{p}| = 6.5 \text{ GeV}$ for the reaction to take place.

7.3.2 Strangeness

We now take a more detailed look at the strangeness quantum number. In 1947, a new neutral particle, K^0 , was discovered from interactions of cosmic rays:

$$\pi^- p \xrightarrow{s} K^0 \Lambda, \quad \text{with consequent decays: } K^0 \xrightarrow{w} \pi^+ \pi^-, \quad \Lambda \xrightarrow{w} \pi^- p. \quad (7.17)$$

This discovery was later confirmed in accelerator experiments. The processes in Eq. (7.17) is puzzling because the *production* cross section is characterized by the strong interaction while the long lifetime ($\tau \sim 90 \text{ ps}$) indicates a weak *decay*. In this seemingly paradoxical situation, a new quantum number called “strangeness” is introduced. A sketch of production and decay of the K^0 is shown in Fig. 7.2. As stated before, the strong interaction conserves flavor which requires for the production $\Delta S = 0$. The decay, on the other hand, proceeds through the weak interaction: The s quark decays via $s \rightarrow uW^-$.

Baryons containing one or more strange quarks are called hyperons. With three constituting quarks we can have, depending on the spin alignment, spin-1/2 ($|\uparrow\downarrow\uparrow\rangle$) or spin-3/2 ($|\uparrow\uparrow\uparrow\rangle$) baryons (see Tab. 7.3).² There are 8 spin-1/2 baryons (octet) and 10 spin-3/2 baryons (decuplet). Octet and decuplet are part of the $SU(3)$ multiplet structure (see Sect. 7.4).³ All hyperons in the octet decay weakly (except for the Σ^0). They therefore have a long lifetime of about 10^{-10} s and decay with $|\Delta S| = 1$, e. g.

$$\begin{aligned} \Sigma^+ &\rightarrow p\pi^0, \quad n\pi^+ \\ \Xi^0 &\rightarrow \Lambda\pi^0. \end{aligned}$$

The members of the decuplet, on the other hand, all decay strongly (except for the Ω^-) with $|\Delta S| = 0$. They therefore have short lifetimes of about 10^{-24} s , e. g.

$$\begin{aligned} \Delta^{++}(1230) &\rightarrow \pi^+ p \\ \Sigma^+(1383) &\rightarrow \Lambda\pi^+. \end{aligned}$$

²The problem that putting three fermions into one symmetric state violates the Pauli exclusion principle is discussed in Sect. 7.4.

³However, this “flavor $SU(3)$ ” is only a sorting symmetry and has nothing to do with “color $SU(3)$ ” discussed in Sect. 7.4.

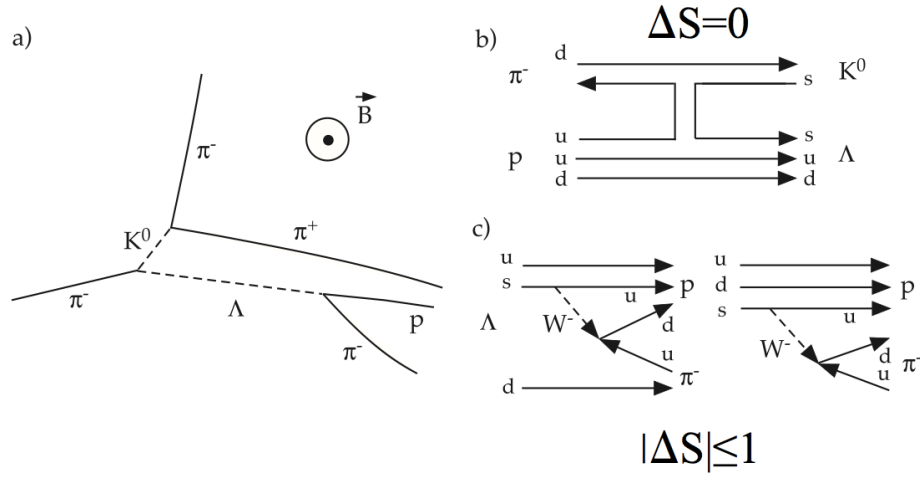


Figure 7.2: Sketch of the reaction $\pi^- p \rightarrow K^0 \Lambda$ and the decays of the neutral K^0 and Λ . Tracks detected in a bubble chamber (a). Feynman diagrams for the production and the Λ decay (b). Notice that $S(K^0) = 1$, $|K^0\rangle = |d\bar{s}\rangle$ and $S(\Lambda) = -1$, $|\Lambda\rangle = |uds\rangle$. Source: [8, p. 140].

| Spin-1/2: Octet | | | Spin-3/2: Decuplet | | |
|------------------|----------------------|-------------|---------------------|---------------|-------------|
| Baryon | State | Strangeness | Baryon | State | Strangeness |
| $p(938)$ | $ uud\rangle$ | 0 | $\Delta^{++}(1230)$ | $ uuu\rangle$ | 0 |
| $n(940)$ | $ udd\rangle$ | 0 | $\Delta^+(1231)$ | $ uud\rangle$ | 0 |
| $\Lambda(1115)$ | $ (ud - du)s\rangle$ | -1 | $\Delta^0(1232)$ | $ udd\rangle$ | 0 |
| $\Sigma^+(1189)$ | $ uus\rangle$ | -1 | $\Delta^-(1233)$ | $ ddd\rangle$ | 0 |
| $\Sigma^0(1192)$ | $ (ud + du)s\rangle$ | -1 | $\Sigma^+(1383)$ | $ uus\rangle$ | -1 |
| $\Sigma^-(1197)$ | $ dds\rangle$ | -1 | $\Sigma^0(1384)$ | $ uds\rangle$ | -1 |
| $\Xi^0(1315)$ | $ uss\rangle$ | -2 | $\Sigma^-(1387)$ | $ dds\rangle$ | -1 |
| $\Xi^-(1321)$ | $ dss\rangle$ | -2 | $\Xi^0(1532)$ | $ uss\rangle$ | -2 |
| | | | $\Xi^-(1535)$ | $ dss\rangle$ | -2 |
| | | | $\Omega^-(1672)$ | $ sss\rangle$ | -3 |

Table 7.3: Summary of the baryon octet and decuplet.

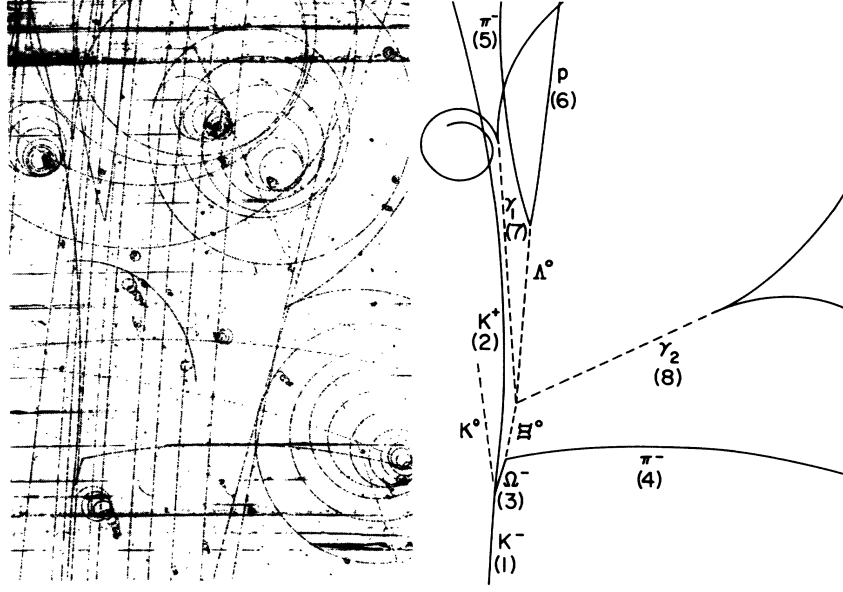


Figure 7.3: *Bubble chamber photograph (LHS) and line diagram (RHS) of an event showing the production and decay of Ω^- . Source: [25, p. 205].*

The quark model, as outlined so far, predicts the hyperon $|\Omega^- \rangle = |sss \rangle$ as a member of the spin-3/2 decuplet. Therefore, the observation of the production,

$$K^- p \rightarrow \Omega^- K^+ K^0,$$

and decay,

$$\Omega^- \rightarrow \Xi^0 \pi^-, \quad \Xi^0 \rightarrow \Lambda \pi^0, \quad \Lambda \rightarrow p \pi^-,$$

of the Ω^- at Brookhaven in 1964 is a remarkable success for the quark model. A sketch of the processes is given in Fig. 7.3. Note that the production occurs via a strong process, $\Delta S = 0$, while the decay is weak: $|\Delta S| = 1$.

7.3.3 Strong vs. weak decays

Generally speaking, strong processes yield considerably shorter lifetimes than weak processes. Consider, for instance, the following two decays,

$$\Delta^+ \rightarrow p + \pi^0$$

$$\tau_{\Delta} = 6 \cdot 10^{-24} \text{ s}$$

$$|uud \rangle \rightarrow |uud \rangle + \frac{1}{\sqrt{2}} (|u\bar{u} \rangle + |d\bar{d} \rangle)$$

(strong)

$$\Sigma^+ \rightarrow p + \pi^0$$

$$\tau_{\Sigma} = 8 \cdot 10^{-11} \text{ s}$$

$$|uus \rangle \rightarrow |uud \rangle + \frac{1}{\sqrt{2}} (|u\bar{u} \rangle - |d\bar{d} \rangle)$$

(weak).

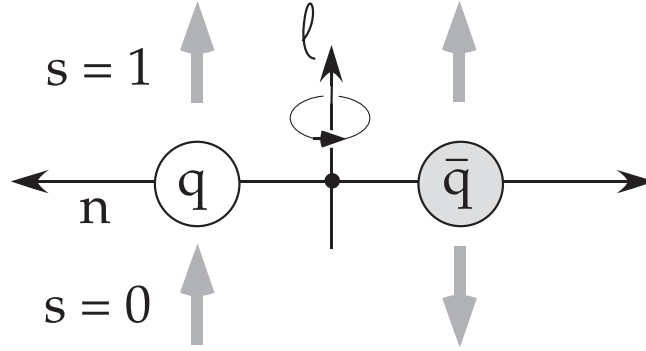


Figure 7.4: Sketch of the possible spin configurations for quark-antiquark bound states. The $q\bar{q}$ pair is characterized by orbital excitations l (rotation) and radial excitations n (vibration). Source: [8, p. 141].

The final state is identical in both decays but the lifetime is much longer for the weak process. Since the final state is equal, this difference in lifetime must come from a difference in the coupling constants. For $\tau \sim 1/\alpha^2$ where α is a coupling constant:

$$\frac{\alpha_{\text{weak}}}{\alpha_{\text{strong}}} \sim \sqrt{\frac{\tau_{\Delta}}{\tau_{\Sigma}}} = 2.7 \cdot 10^{-7}.$$

7.3.4 Mesons

Mesons are quark-antiquark bound states: $|q\bar{q}\rangle$. In analogy to the spin states of a two-electron system (and not to be confused with the isospin multiplets discussed on p. 128), the $|q\bar{q}\rangle$ bound state can have either spin 0 (singlet) or spin 1 (triplet) (see Fig. 7.4). Radial vibrations are characterized by the quantum number n while orbital angular momentum is characterized by the quantum number l . The states are represented in spectroscopic notation:

$$n^{2s+1}l_J$$

where $l = 0$ is labeled by S , $l = 1$ by P and so on. A summary of the $n = 1$, $l = 0$ meson states is shown in Tab. 7.4. A summary of the states with $l \leq 2$ can be found in Fig. 7.5.

7.3.5 Gell-Mann-Nishijima formula

Isospin is introduced in Sect. 7.1. The hadron isospin multiplets for $n = 1$, $l = 0$ are shown in Fig. 7.6. This summary leads to the conclusion that the charge Q of an hadron with baryon number B and strangeness S is given by

$$Q = I_3 + \frac{B + S}{2}$$

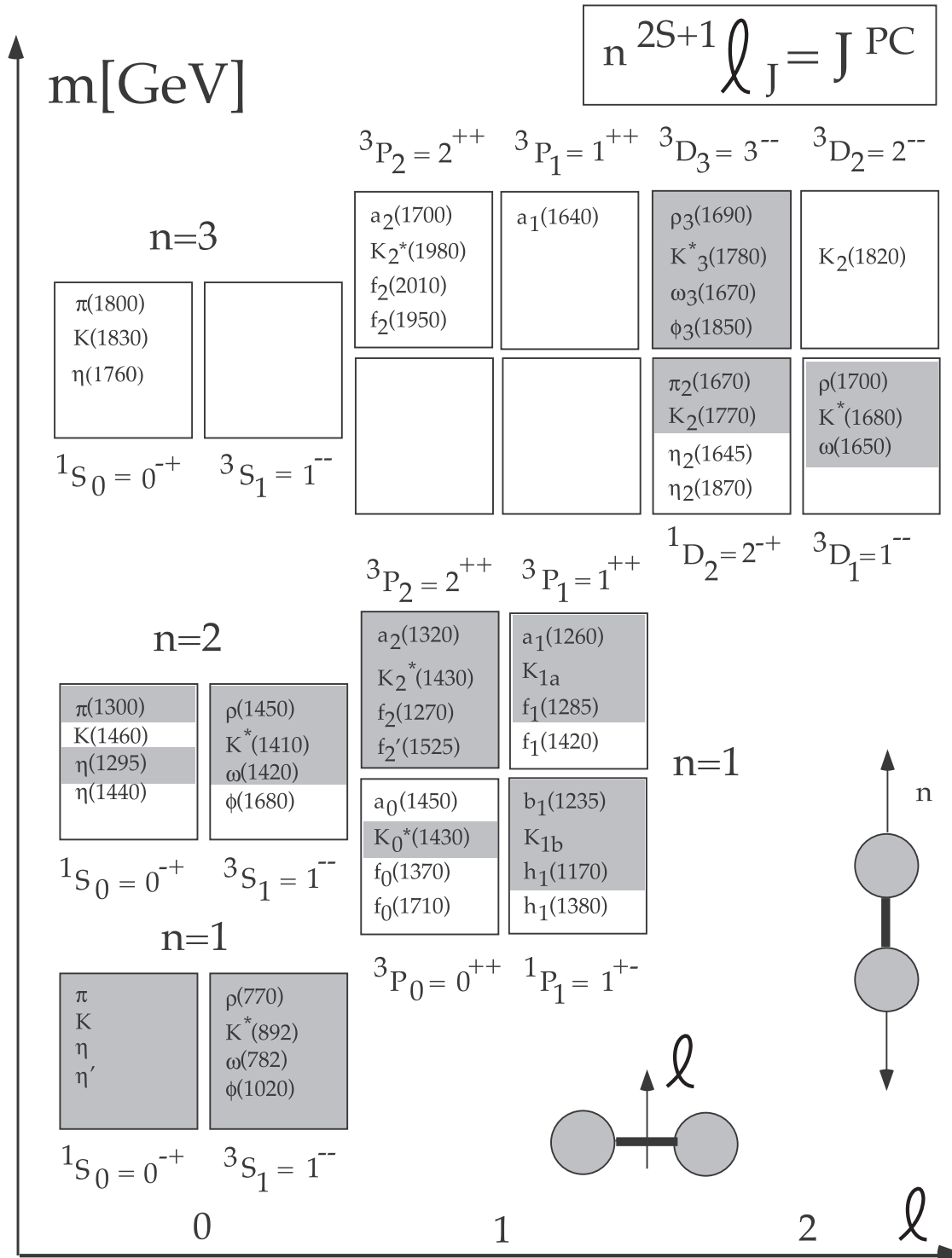


Figure 7.5: Summary of mesons from u, d, s quarks for $\ell \leq 2$. Cells shaded in grey are well established states. Source: [8, p. 143].

| Mesons ($n = 1, l = 0$) | | | | | |
|----------------------------------|-------------------|---|------------------------|--------------|-------------------------------|
| 1^1S_0 (spin 0) | | | 1^3S_1 (spin 1) | | |
| $\pi^+(140)$ | | $ ud\rangle$ | $\rho^+(770)$ | | $ ud\rangle$ |
| $\pi^-(140)$ | | $ \bar{u}d\rangle$ | $\rho^-(770)$ | | $ \bar{u}d\rangle$ |
| $\pi^0(135)$ | $1/\sqrt{2}$ | $ d\bar{d} - u\bar{u}\rangle$ | $\rho^0(770)$ | $1/\sqrt{2}$ | $ d\bar{d} - u\bar{u}\rangle$ |
| $K^+(494)$ | | $ u\bar{s}\rangle$ | $K^{*+}(892)$ | | $ u\bar{s}\rangle$ |
| $K^-(494)$ | | $ \bar{u}s\rangle$ | $K^{*-}(892)$ | | $ \bar{u}s\rangle$ |
| $K^0(498)$ | | $ d\bar{s}\rangle$ | $K^{*0}(896)$ | | $ d\bar{s}\rangle$ |
| $\bar{K}^0(498)$ | | $ \bar{d}s\rangle$ | $\bar{K}^{*0}(896)$ | | $ \bar{d}s\rangle$ |
| $\eta(547)$ | $\sim 1/\sqrt{6}$ | $ u\bar{u} + d\bar{d} - 2s\bar{s}\rangle$ | $\phi(1020) = \psi_1$ | | $- s\bar{s}\rangle$ |
| $\eta'(958)$ | $\sim 1/\sqrt{3}$ | $ u\bar{u} + d\bar{d} + s\bar{s}\rangle$ | $\omega(782) = \psi_2$ | $1/\sqrt{2}$ | $ u\bar{u} + d\bar{d}\rangle$ |

Table 7.4: Summary of $n = 1, l = 0$ meson states.

which is called Gell-Mann-Nishijima formula. As an example, consider the Ω^- hyperon where $0 + (1 - 3)/2 = -1$.

7.4 Quantum chromodynamics and color $SU(3)$

The quark model, as discussed so far, runs into a serious problem: Since the quarks have half-integer spin, they are fermions and therefore obey Fermi-Dirac statistics. This means that states like

$$\Delta^{++} = |u^\uparrow u^\uparrow u^\uparrow\rangle, \quad S = \frac{3}{2}$$

where three quarks are in a symmetric state (have identical quantum numbers) are forbidden by the Pauli exclusion principle.

The way out is to introduce a new quantum number that allows for one extra degree of freedom which enables us to antisymmetrize the wave function as required for fermions:

$$\Delta^{++} = \mathcal{N} \sum_{ijk} \varepsilon_{ijk} |u_i^\uparrow u_j^\uparrow u_k^\uparrow\rangle$$

where \mathcal{N} is some normalization constant and the quarks come in three different “colors”:⁴

$$|q\rangle \rightarrow |q_{1,2,3}\rangle = \begin{pmatrix} |q_1\rangle \\ |q_2\rangle \\ |q_3\rangle \end{pmatrix}.$$

Since color cannot be observed, there has to be a corresponding new symmetry in the Lagrangian due to the fact that the colors can be transformed without the observables

⁴The new charge is named “color” because of the similarities to optics: There are three fundamental colors, complementary colors and the usual combinations are perceived as white.

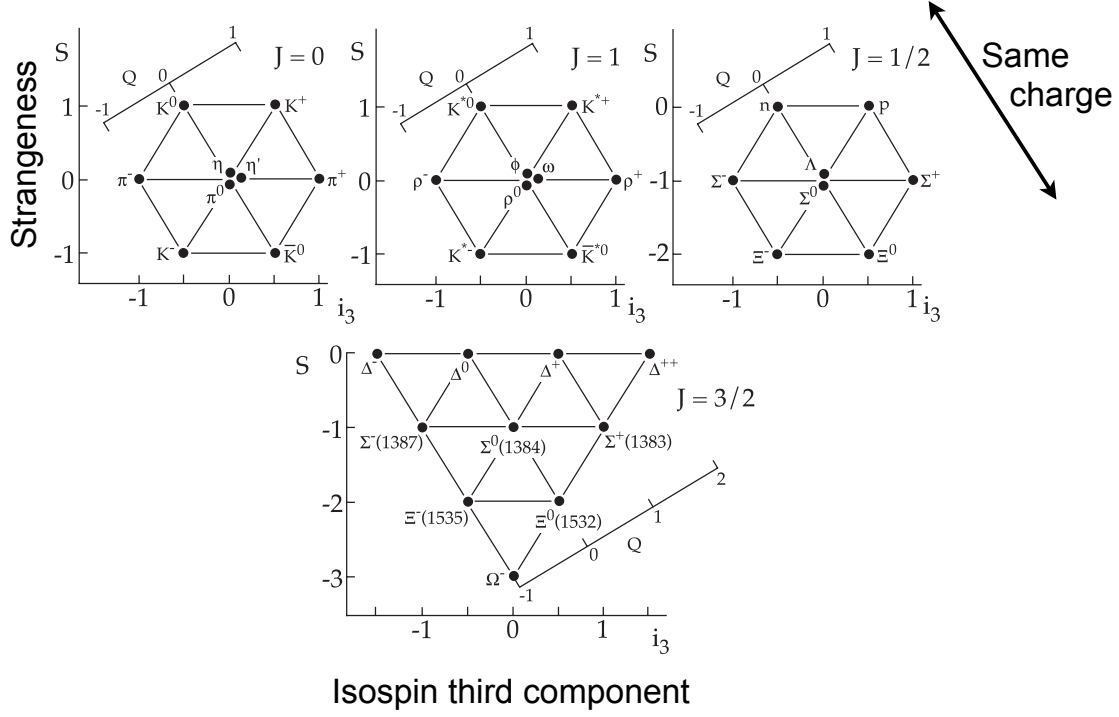


Figure 7.6: *Summary of hadron isospin multiplets.* $n = 1$, $l = 0$. Source: [8, p. 147].

being affected. In the case of our new charge in three colors the symmetry group is $SU(3)$, the group of the special unitary transformations in three dimensions. The Lie algebra of $SU(3)$ is

$$[T^a, T^b] = if^{abc}T^c$$

where, in analogy to Eq. (7.10), f^{abc} denotes the structure constants and where there are 8 generators T^a (recall that $o = N^2 - 1 = 8$, see p. 127) out of which $r = N - 1 = 2$ are diagonal.

The fundamental representation is given by the 3×3 matrices $T^a = \frac{1}{2}\lambda^a$ with the Gell-Mann matrices

$$\begin{aligned} \lambda_1 &= \begin{pmatrix} \overbrace{\begin{pmatrix} 0 & 1 \\ 1 & 0 \end{pmatrix}}^{\tau_1} & 0 \\ 0 & 0 \end{pmatrix} & \lambda_2 &= \begin{pmatrix} \overbrace{\begin{pmatrix} 0 & -i \\ i & 0 \end{pmatrix}}^{\tau_2} & 0 \\ 0 & 0 \end{pmatrix} & \lambda_3 &= \begin{pmatrix} \overbrace{\begin{pmatrix} 1 & 0 \\ 0 & -1 \end{pmatrix}}^{\tau_3} & 0 \\ 0 & 0 \end{pmatrix} & \lambda_4 &= \begin{pmatrix} 0 & 0 & 1 \\ 0 & 0 & 0 \\ 1 & 0 & 0 \end{pmatrix} \\ \lambda_5 &= \begin{pmatrix} 0 & 0 & -i \\ 0 & 0 & 0 \\ i & 0 & 0 \end{pmatrix} & \lambda_6 &= \begin{pmatrix} 0 & 0 & 0 \\ 0 & 0 & 1 \\ 0 & 1 & 0 \end{pmatrix} & \lambda_7 &= \begin{pmatrix} 0 & 0 & 0 \\ 0 & 0 & -i \\ 0 & i & 0 \end{pmatrix} & \lambda_8 &= \frac{1}{\sqrt{3}} \begin{pmatrix} 1 & 0 & 0 \\ 0 & 1 & 0 \\ 0 & 0 & -2 \end{pmatrix}. \end{aligned}$$

One can observe that these matrices are hermitian and traceless,

$$\lambda_a^\dagger = \lambda_a \quad \text{Tr } \lambda^a = 0.$$

Furthermore, one can show that

$$\text{Tr} (\lambda^a \lambda^b) = 2\delta^{ab}$$

and

$$\lambda_{ij}^a \lambda_{kl}^a = 2 \left(\delta_{il} \delta_{kj} - \frac{1}{3} \delta_{ij} \delta_{kl} \right) \quad (\text{Fierz identity}).$$

The structure constants of $SU(3)$ are given by

$$f_{abc} = \frac{1}{4i} \text{Tr} ([\lambda_a, \lambda_b] \lambda_c)$$

and are antisymmetric in a , b , and c . The numerical values are

$$\begin{aligned} f_{123} &= 1 \\ f_{458} &= f_{678} = \frac{\sqrt{3}}{2} \\ f_{147} &= f_{156} = f_{246} = f_{257} = f_{345} = f_{367} = \frac{1}{2} \\ f_{abc} &= 0 \quad \text{else.} \end{aligned}$$

As in the case of $SU(2)$, the adjoint representation is given by the structure constants which, in this case, are 8×8 matrices:

$$(t^a)_{bc} = -if_{abc}.$$

The multiplets (again built out of the fundamental representations) are given by the direct sums

$$\underline{3} \otimes \bar{\underline{3}} = \underline{1} \oplus \underline{8} \tag{7.18}$$

where the bar denotes antiparticle states and

$$\underline{3} \otimes \underline{3} \otimes \underline{3} = \underline{1} \oplus \underline{8} \oplus \underline{8} \oplus \underline{10}. \tag{7.19}$$

The singlet in Eq. (7.18) corresponds to the $|q\bar{q}\rangle$ states, the mesons (e.g. π), while the singlet in Eq. (7.19) is the $|qqq\rangle$ baryon (e.g. p , n). The other multiplets are colored and can thus not be observed. Working out the $SU(3)$ potential structure, one finds that an attractive QCD potential exists only for the singlet states, while the potential is repulsive for all other multiplets.

The development of QCD outlined so far can be summarized as follows: Starting from the observation that the nucleons have similar properties, we considered isospin and $SU(2)$ symmetry. We found that the nucleons n and p correspond to the fundamental representations of $SU(2)$ while the π is given by the adjoint representation. To satisfy the Pauli exclusion principle, we had to introduce a new quantum number and with it a new $SU(3)$ symmetry of the Lagrangian. This in turn led us to multiplet structures where the colorless singlet states correspond to mesons and baryons.

Construction of QCD Lagrangian We now take a closer look at this $SU(3)$ transformation of a color triplet,

$$|q\rangle = \begin{pmatrix} q_1 \\ q_2 \\ q_3 \end{pmatrix} \rightarrow |q'\rangle = \begin{pmatrix} q'_1 \\ q'_2 \\ q'_3 \end{pmatrix} = e^{ig_s \alpha_a T^a} \begin{pmatrix} q_1 \\ q_2 \\ q_3 \end{pmatrix} = U |q\rangle, \quad (7.20)$$

where $g_s \in \mathbb{R}$ is used as a rescaling (and will be used for the perturbative expansion) of the group parameter α introduced previously. The reason of introducing it becomes clear in the context of gauge theories.

In analogy to the QED current,

$$j_{\text{QED}}^\mu = eq_e \bar{q} \gamma^\mu q,$$

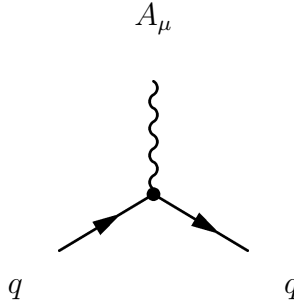
we introduce the **color current**⁵, which is the conserved current associated with the $SU(3)$ symmetry,

$$j_a^\mu = g_s \bar{q}_i \gamma^\mu T_{ij}^a q_j \quad a = 1 \cdots 8. \quad (7.21)$$

In the same spirit, by looking at the QED interaction,

$$\mathcal{L}_{\text{QED}}^{\text{int}} = -j_{\text{QED}}^\mu A_\mu = eq_e \bar{q} \gamma^\mu q A_\mu,$$

yielding the vertex,

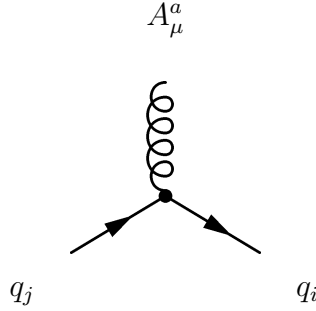


where we can see the photon – the electrically uncharged $U(1)$ gauge boson of QED –, we postulate an interaction part of the QCD Lagrangian of the form,

$$\mathcal{L}_{\text{QCD}}^{\text{int}} = -j_a^\mu A_\mu^a = g_s \bar{q}_i \gamma^\mu T_{ij}^a q_j A_\mu^a, \quad (7.22)$$

which translates in the vertex (which is not the only one of QCD as we shall see),

⁵The Einstein summation convention still applies, even if the color index i and j are not in an upper and lower position. This exception extends also to the color indices a, b, \dots of the gauge fields to be introduced. There is no standard convention in the literature, and since there is no metric tensor involved, the position of a color index, is merely an esthetic/readability problem.



Now there are 8 $SU(3)$ gauge bosons A_μ^a for QCD : one for each possible value of a . They are called **gluons** and are themselves colored.

Continuing with our analogy, we define the **covariant derivative of QCD**⁶,

$$D_\mu = \partial_\mu \mathbb{1} + ig_s T^a A_\mu^a, \quad (7.23)$$

and state that the QCD Lagrangian should have a term of the form,

$$\tilde{\mathcal{L}}_{\text{QCD}} = \bar{q}(i\not{D} - m)q. \quad (7.24)$$

Up to this point, both QED and QCD look nearly identical. Their differences become crucial when we look at local gauge symmetries. Such a transformation can be written,

$$|q(x)\rangle \rightarrow |q'(x)\rangle = e^{ig_s \alpha_a(x) T^a} |q(x)\rangle, \quad (7.25)$$

and we impose as before that the Lagrangian must be invariant under any such transformation. This is equivalent of imposing,

$$\begin{aligned} D'_\mu |q'(x)\rangle &\stackrel{!}{=} e^{ig_s \alpha_a(x) T^a} D_\mu |q(x)\rangle \\ &\Leftrightarrow \langle \bar{q}'(x) | i\not{D}' | q'(x) \rangle = \langle \bar{q}(x) | i\not{D} | q(x) \rangle. \end{aligned}$$

For $\alpha_a(x) \ll 1$, we can expand the exponential and keep only the first order term,

$$\begin{aligned} D'_\mu |q'(x)\rangle &= (\partial_\mu + ig_s T^c A_\mu^c) (\mathbb{1} + ig_s \alpha_a(x) T^a) |q(x)\rangle \\ &\stackrel{!}{=} (\mathbb{1} + ig_s \alpha_a(x) T^a) \underbrace{(\partial_\mu + ig_s T^c A_\mu^c)}_{D_\mu} |q(x)\rangle. \end{aligned}$$

Making the ansatz $A_\mu^c = A_\mu^c + \delta A_\mu^c$ where $|\delta A_\mu^c| \ll |A_\mu^c|$ and expanding the former equation to first order in δA_μ^c (the term proportional to $\alpha_a(x) \delta A_\mu^c$ has also been ignored), we get,

$$\begin{aligned} ig_s T^c \delta A_\mu^c + ig_s (\partial_\mu \alpha_a(x)) T^a + i^2 g_s^2 T^c A_\mu^c \alpha_a(x) T^a &\stackrel{!}{=} i^2 g_s^2 \alpha_a(x) T^a T^c A_\mu^c \\ \Rightarrow T^c \delta A_\mu^c &\stackrel{!}{=} -(\partial_\mu \alpha_a(x)) T^a + ig_s [T^a, T^c] \alpha_a(x) A_\mu^c, \end{aligned}$$

⁶Note that D_μ acts on color triplet and gives back a color triplet; ∂_μ does not mix the colors, whereas the other summand does (T^a is a 3×3 matrix).

or, renaming the dummy indices and using the Lie algebra $su(3)$,

$$\begin{aligned} T^a \delta A_\mu^a &= -(\partial_\mu \alpha_a(x)) T^a - g_s f_{abc} T^a \alpha_b(x) A_\mu^c & \forall T^a \\ \Rightarrow A_\mu'^a &= A_\mu^a - \underbrace{\partial_\mu \alpha_a(x)}_{\text{like in QED}} - \underbrace{g_s f_{abc} \alpha_b(x) A_\mu^c}_{\text{non-abelian part}}. \end{aligned} \quad (7.26)$$

Eq. (7.26) describes the (infinitesimal) gauge transformation of the gluon field.

In order for the gluon field to become physical, we need to include a kinematical term (depending on the derivatives of the field). Remember the photon term of QED,

$$\mathcal{L}_{\text{QED}}^{\text{photon}} = -\frac{1}{4} F_{\mu\nu} F^{\mu\nu} \quad F_{\mu\nu} = \partial_\mu A_\nu - \partial_\nu A_\mu,$$

where the last is gauge invariant. As we might expect from Eq. (7.26), the non-abelian part will get us into trouble. Let's look at,

$$\begin{aligned} \delta(\partial_\mu A_\nu^c - \partial_\nu A_\mu^c) &= -\partial_\mu \partial_\nu \alpha_a + \partial_\nu \partial_\mu \alpha_a - g_s f_{abc} \alpha_b (\partial_\mu A_\nu^c - \partial_\nu A_\mu^c) \\ &\quad - g_s f_{abc} ((\partial_\mu \alpha_b) A_\nu^c - (\partial_\nu \alpha_b) A_\mu^c). \end{aligned}$$

We remark that the two first summands cancel each other and that the third looks like the $SU(3)$ transformation under the adjoint representation.

We recall that,

$$\begin{aligned} q_i &\rightarrow q'_i = (\delta_{ij} + i g_s \alpha_a T_{ij}^a) q_j & \text{(fundamental representation)} \\ B_a &\rightarrow B'_a = (\delta_{ac} + i g_s \alpha_b t_{ac}^b) B_c & \text{(adjoint representation)} \end{aligned}$$

respectively, where,

$$t_{ac}^b = -i f_{bac} = i f_{abc}.$$

Hence, if $F_{\mu\nu}^a$ transforms in the adjoint representation of $SU(3)$, we should have,

$$\delta F_{\mu\nu}^a \stackrel{!}{=} -g_s f_{abc} \alpha_b F_{\mu\nu}^c.$$

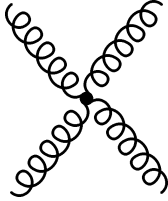
We now make the ansatz,

$$F_{\mu\nu}^a = \partial_\mu A_\nu^a - \partial_\nu A_\mu^a - g_s f_{abc} A_\mu^b A_\nu^c, \quad (7.27)$$

and prove that it fulfills the above constraint.

$$\begin{aligned} \delta F_{\mu\nu}^a &= \delta(\partial_\mu A_\nu^a - \partial_\nu A_\mu^a) - g_s f_{abc} \delta(A_\mu^b A_\nu^c) \\ &= -g_s f_{abc} \alpha_b (\partial_\mu A_\nu^c - \partial_\nu A_\mu^c) - g_s f_{abc} ((\partial_\mu \alpha_b) A_\nu^c - (\partial_\nu \alpha_b) A_\mu^c) \\ &\quad - g_s f_{abc} (-(\partial_\mu \alpha_b) A_\nu^c + (\partial_\nu \alpha_b) A_\mu^c) - g_s f_{abc} (-g_s f_{bde} \alpha_d A_\mu^e A_\nu^c - g_s f_{cde} \alpha_d A_\mu^b A_\nu^e), \end{aligned}$$

Finally we have also a 4-gluon term $(-g_s f_{abc} A_\mu^b A_\nu^c) (-g_s f_{ade} A_d^\mu A_e^\nu)$ yielding the **4-gluon vertex**

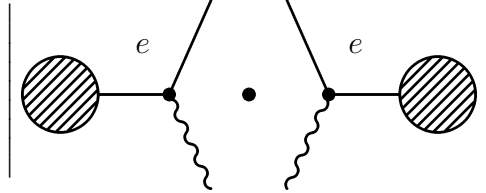



$$= -ig_s^2 [f_{abe}f_{cde}(g_{\mu\lambda}g_{\nu\rho} - g_{\mu\rho}g_{\nu\lambda}) + f_{ade}f_{bce}(g_{\mu\nu}g_{\lambda\rho} - g_{\mu\lambda}g_{\nu\rho}) + f_{ace}f_{bde}(g_{\mu\rho}g_{\nu\lambda} - g_{\mu\nu}g_{\rho\lambda})] \quad (7.31)$$

Unlike in QED, gluons are able to interact with themselves. This comes from the fact that the theory is non-abelian. As a consequence, there is no superposition principle for QCD: the field of a system of strongly interacting particles is *not* the sum of the individual fields. Thence, there is no plane wave solution to QCD problems, and we cannot make use of the usual machinery of Green's functions and Fourier decomposition. Up to now there is no known solution.

7.4.1 Strength of QCD interaction

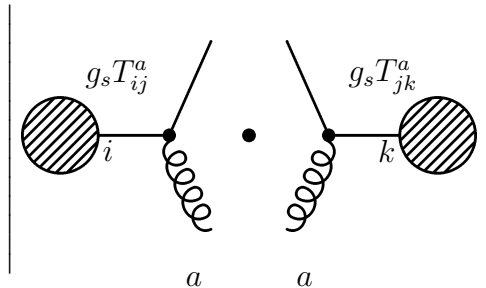
In QED, when we take a term of the form,



where the  denotes some other part of the Feynman diagram, the expression is proportional to $e^2 = 4\pi\alpha$.

In the case of QCD, we have a few more possibilities. We look at the general $SU(n)$ case. The QCD result can be found by setting $n = 3$.

First, for the analogous process to the one cited above :



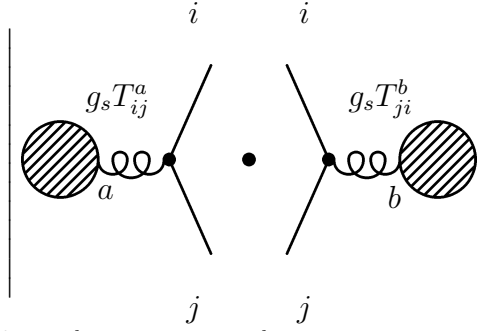
which is proportional to $g_s^2 T_{ij}^a T_{jk}^a = 4\pi\alpha_s C_F \delta_{ik}$, where

$$C_F = \frac{n^2 - 1}{2n}, \quad (7.32)$$

is the color factor, the Casimir operator of $SU(n)$. To find it, we used one of the Fierz identities (see exercises), namely,

$$\begin{aligned} T_{ij}^a T_{jk}^a &= \frac{1}{2} \left(\delta_{ik} \delta_{jj} - \frac{1}{n} \delta_{ij} \delta_{jk} \right) \\ &= \frac{1}{2} \left(n \delta_{ik} - \frac{1}{n} \delta_{ik} \right) = \frac{n^2 - 1}{2n} \delta_{ik}. \end{aligned}$$

Next we look at,



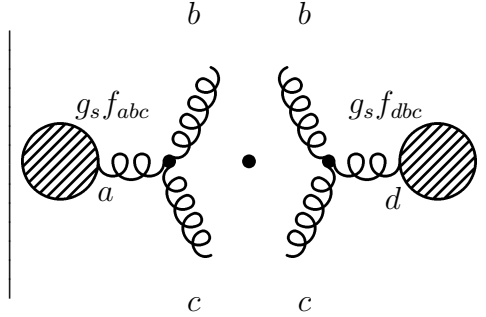
which is proportional to $g_s^2 T_{ij}^a T_{ji}^b = 4\pi\alpha_s T_F \delta^{ab}$, where

$$T_F = \frac{1}{2}. \quad (7.33)$$

To find it, we used the fact that,

$$\text{Tr} (T^a T^b) = \frac{1}{2} \delta^{ab}.$$

Finally we investigate the case where,



which is proportional to $g_s^2 f_{abc} f_{dbc} = 4\pi\alpha_s C_A \delta^{ad}$, where

$$C_A = n. \quad (7.34)$$

To find it, we used the relation,

$$f_{abc} = -2i \text{Tr} \left([T^a, T^b] T^c \right),$$

that we have shown in the beginning of this section.

In the case of QCD, $C_F = \frac{4}{3}$, $T_F = \frac{1}{2}$, $C_A = 3$. From the discussion above, we can heuristically draw the conclusion that gluons tend to couple more to other gluons, than to quarks.

At this stage, we note two features specific to the strong interaction, which we are going to handle in more detail in a moment :

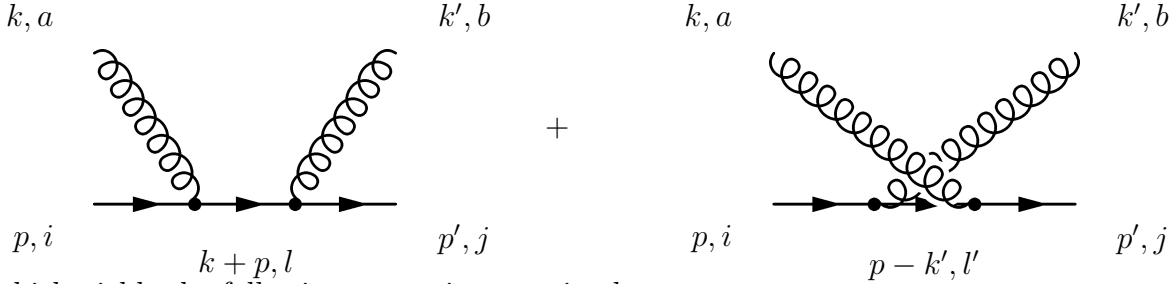
- **Confinement** : At low energies (large distances), the coupling becomes very large, so that the perturbative treatment is no longer valid, and the process of hadronization becomes important. This is the reason why we cannot observe color directly.
- **Asymptotic freedom** : At high energies (small distances) the coupling becomes negligible, and the quarks and gluons can move almost freely.

As an example, of typical QCD calculation, we sketch the calculation of the

Gluon Compton scattering

$$g(k) + q(p) \rightarrow g(k') + q(p').$$

There are at first sight two Feynman diagrams coming into the calculation,



which yields the following scattering matrix element,

$$\begin{aligned} -i\mathcal{M}_{fi} = & -ig_s^2 \left[\bar{u}(p') \not{\epsilon}^*(k') \frac{1}{\not{p} + \not{k} - m} \not{\epsilon}(k) u(p) T_{jl}^b T_{li}^a \right. \\ & \left. + \bar{u}(p') \not{\epsilon}(k) \frac{1}{\not{p} - \not{k}' - m} \not{\epsilon}^*(k') u(p) T_{jl'}^a T_{li}^b \right]. \end{aligned} \quad (7.35)$$

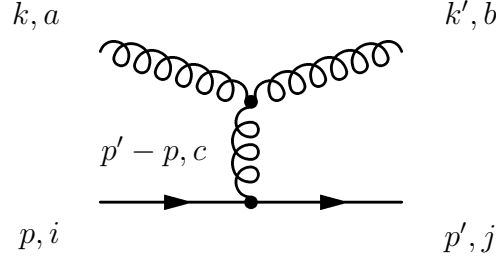
We start by checking the gauge invariance (\mathcal{M}_{fi} must vanish under the substitution $\varepsilon_\mu(k) \rightarrow k_\mu$):

$$-i\mathcal{M}'_{fi} = -ig_s^2 \bar{u}(p') \not{\epsilon}^*(k') u(p) (T_{ji}^b T_{li}^a - T_{jl'}^a T_{li}^b),$$

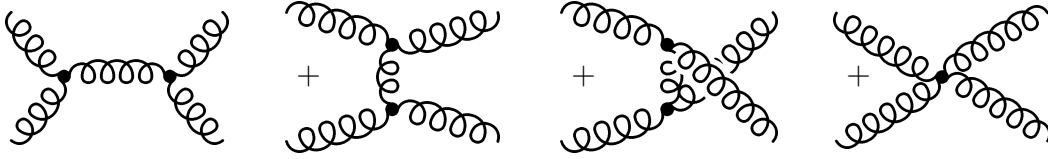
where

$$T_{ji}^b T_{li}^a - T_{j'l'}^a T_{l'i}^b = [T^b, T^a]_{ji} = if_{bac} T_{ji}^c \neq 0!$$

So we need another term, which turns out to be the one corresponding to the Feynman diagram,

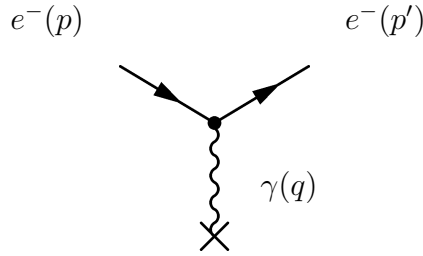


The calculation of the gluon-gluon scattering goes analogously. We need to consider the graphs,



7.4.2 QCD coupling constant

To leading order, a typical QED scattering process takes the form,

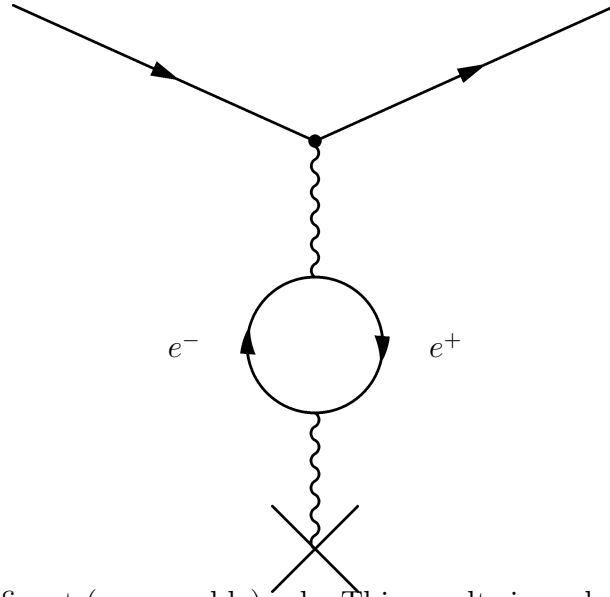


with $q^2 = (p' - p)^2 \leq 0$.

In the Coulomb limit (long distance, low momentum transfer), the potential takes the form,

$$V(R) = -\frac{\alpha}{R} \quad R \gtrsim \frac{1}{m_e} \approx 10^{-11} [\text{cm}]. \quad (7.36)$$

When $R \leq m_e^{-1}$, quantum effects become important (loop corrections, also known as vacuum polarization), since the next to leading order (NLO) diagram,



starts to play a significant (measurable) role. This results in a change of the potential to,

$$V(R) = -\frac{\alpha}{R} \left[1 + \frac{2\alpha}{3\pi} \ln \frac{1}{m_e R} + \mathcal{O}(\alpha^2) \right] = -\frac{\bar{\alpha}(R)}{R}, \quad (7.37)$$

where $\bar{\alpha}(R)$ is called the effective coupling.

We can understand the effective coupling in analogy to a solid state physics example : in an insulator, an excess of charge gets screened by the polarization of the nearby atoms. Here we create e^+e^- pairs out of the vacuum, hence the name **vacuum polarization**.

As we can see from Eq. (7.37), the smaller the distance $R \leq m_e^{-1}$, the bigger the observed “charge” $\bar{\alpha}(R)$. What we call the electron charge e (or the fine structure constant α) is the limiting value for very large distances or low momentum transfer as shown in Fig. 7.4.2.

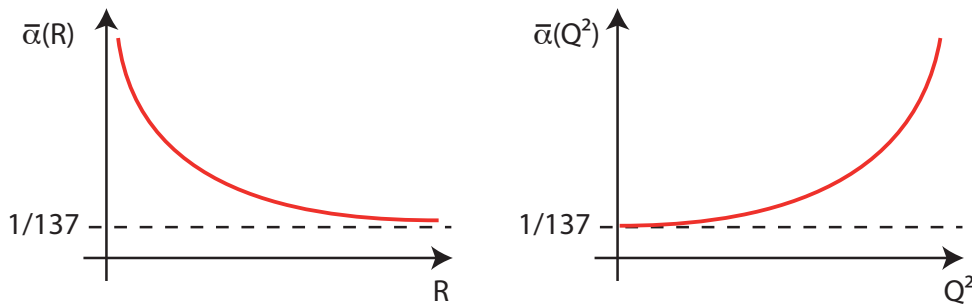
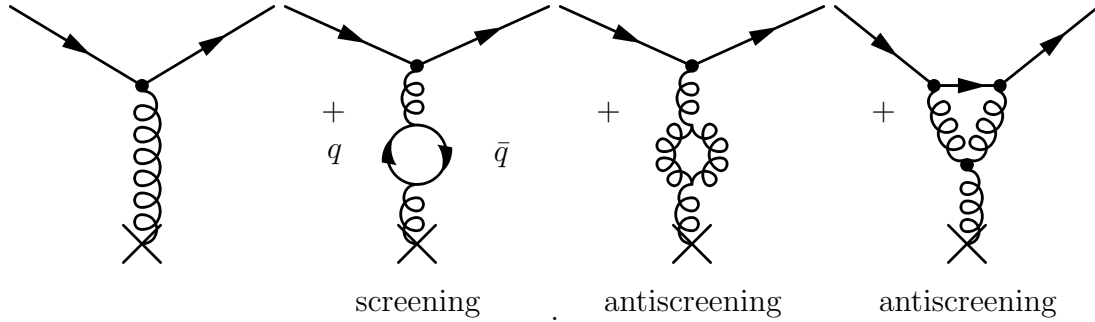


Figure 7.7: Evolution of the effective electromagnetic coupling with distance and energy ($Q^2 = -q^2$).

For example the measurements done at LEP show that, $\bar{\alpha}(Q^2 = m_Z^2) \approx \frac{1}{128} > \alpha$.

In the case of QCD, we have at NLO, the following diagrams,



We can picture the screening/antiscreening phenomenon as follows,

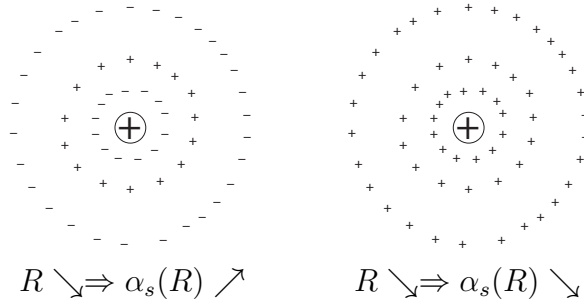


Figure 7.8: Screening and antiscreening.

For QCD, the smaller the distance R (or the bigger the energy Q^2), the smaller the observed coupling $\bar{\alpha}_s(R)$. At large distances, $\bar{\alpha}_s(R)$ becomes comparable with unity, and the perturbative approach breaks down as we can see in Fig. 7.4.2. The region concerning confinement and asymptotic freedom are also shown.

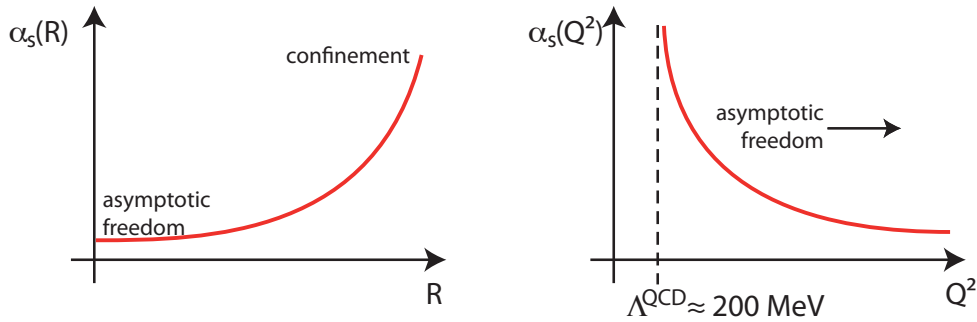


Figure 7.9: Evolution of the effective strong coupling with distance and energy ($Q^2 = -q^2$).

The β -function of QCD In the renormalization procedure of QCD, we get a differential equation for $\alpha_s(\mu^2)$ where μ is the renormalization scale,

$$\mu^2 \frac{\partial \alpha_s}{\partial(\mu^2)} = \beta(\alpha_s) \quad (7.38)$$

$$\beta(\alpha_s) = -\alpha_s \left[\beta_0 \frac{\alpha_s}{4\pi} + \beta_1 \left(\frac{\alpha_s}{4\pi} \right)^2 + \beta_2 \left(\frac{\alpha_s}{4\pi} \right)^3 + \cdots \right], \quad (7.39)$$

with

$$\beta_0 = \frac{11}{3}n_c - \frac{2}{3}n_f = 11 - \frac{2}{3}n_f \quad (\text{NLO}) \quad (7.40)$$

$$\beta_1 = \frac{17}{12}n_c^2 - \frac{5}{12}n_c n_f - \frac{1}{4} \left(\frac{n_c^2 - 1}{2n_c} \right) n_f, \quad (\text{NNLO}) \quad (7.41)$$

where n_c is the number of colors and n_f is the number of quark flavors. These two numbers enter into the calculation through gluon respectively quark loop corrections to the propagators.

We remark at this stage that unless⁷ $n_f \geq 17$, we have $\beta_0 > 0$, whereas in the case of QED, we get,

$$\beta_0^{\text{QED}} = -\frac{4}{3} < 0. \quad (7.42)$$

This fact explains the completely different behavior of the effective couplings of QCD and QED.

To end this chapter, we will solve Eq. (7.38) retaining only the first term of the power expansion of β .

$$\begin{aligned} \mu^2 \frac{\partial \alpha_s}{\partial(\mu^2)} &= -\frac{\beta_0}{4\pi} \alpha_s^2 \\ \frac{\partial \alpha_s}{\alpha_s^2} &= -\frac{\beta_0}{4\pi} \partial(\ln \mu^2) \\ \int_{\alpha_s(Q_0^2)}^{\alpha_s(Q^2)} \frac{d\alpha_s}{\alpha_s^2} &= -\frac{\beta_0}{4\pi} \int_{\ln Q_0^2}^{\ln Q^2} d(\ln \mu^2), \end{aligned}$$

and hence,

$$\boxed{\frac{1}{\alpha_s(Q^2)} = \frac{1}{\alpha_s(Q_0^2)} + \frac{\beta_0}{4\pi} \ln \frac{Q^2}{Q_0^2}}. \quad (7.43)$$

⁷As of 2009, only 6 quark flavors are known and there is experimental evidence (decay width of the Z^0 boson) that there are no more than 3 generations with light neutrinos.

We thus have a relation between $\alpha_s(Q^2)$ and $\alpha_s(Q_0^2)$, giving the evolution of the effective coupling.

A mass scale is also generated, if we set,

$$\frac{1}{\alpha_s(Q^2 = \Lambda^2)} = 0 \Rightarrow \alpha_s(\Lambda^2) = \infty.$$

Choosing $\Lambda = Q_0$, we can rewrite Eq. (7.43) as,

$$\boxed{\alpha_s(Q^2) = \frac{4\pi}{\beta_0 \ln \frac{Q^2}{\Lambda^2}}}. \quad (7.44)$$

Chapter 8

QCD in e^+e^- annihilations

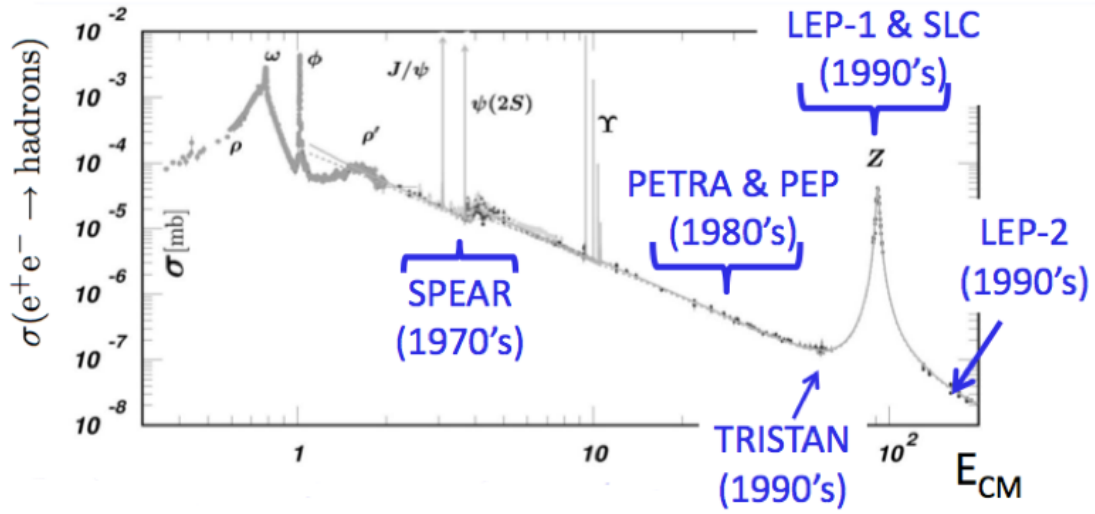
Literature:

- Dissertori/Knowles/Schmelling [27]
- Ellis/Stirling/Webber [28]
- Bethke [29, 30]
- Particle Data Group [26]
- JADE, Durham, and Cambridge jet algorithms [31, 32, 33, 34]
- FastJet Package, Fast k_T , SIScone [35, 36, 37]

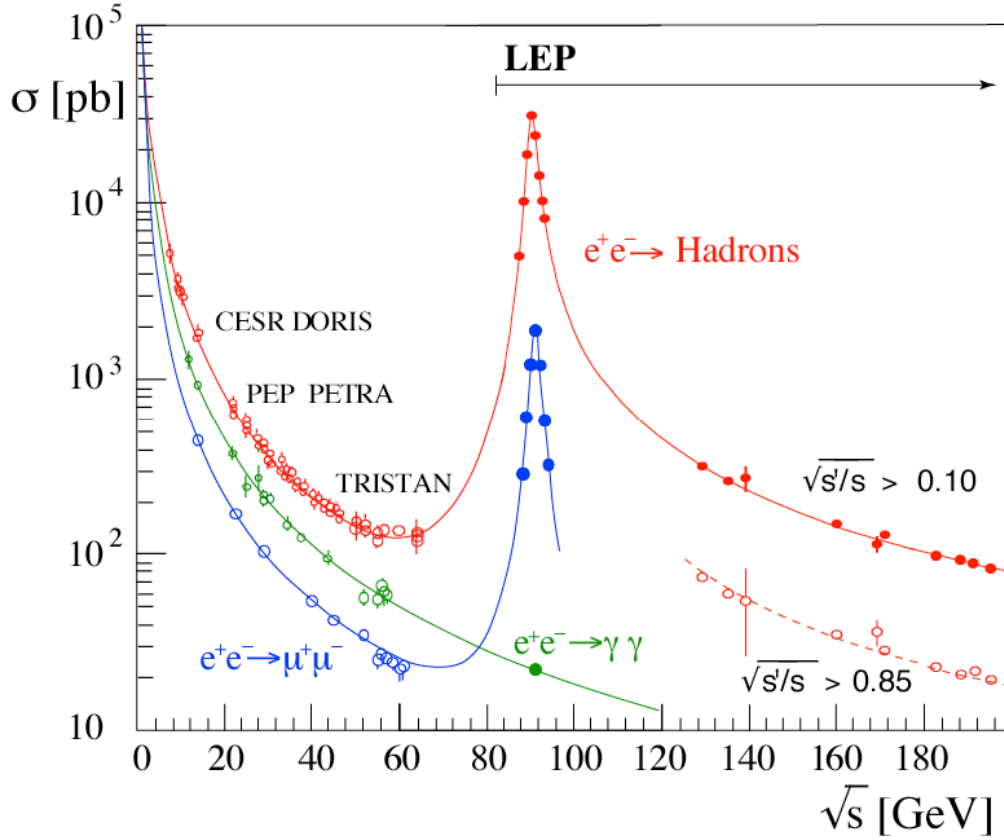
In Chap. 7, QCD is introduced as an $SU(3)$ gauge theory. Here we continue this discussion and consider QCD processes following e^+e^- annihilations. The main focus is on the definition and application of observables linking theoretical predictions with measurable quantities: Jets and event shapes are discussed; the applications include measurements of the parton spins, the strong coupling constant, and the QCD color factors. The chapter is concluded by an outlook to hadronization and non-perturbative QCD.

Some examples of e^+e^- colliders and their energies are given in Tab. 6.1. Fig. 8.1(a) maps the corresponding eras onto the available center of mass energies. A half-logarithmic plot comparing $\sigma^{e^+e^- \rightarrow \text{hadrons}}$ to $\sigma^{e^+e^- \rightarrow \mu^-\mu^+}$ is given in Fig. 8.1(b). Experimental milestones include:

- *SPEAR (SLAC)*: Discovery of quark jets.
- *PETRA (DESY) & PEP (SLAC)*: First high energy (> 10 GeV) jets; discovery of gluon jets (at the PETRA collider, see Fig. 8.2); many pioneering QCD studies.



(a)



(b)

Figure 8.1: *Cross sections in e^+e^- annihilations.* (a) Cross section for $e^+e^- \rightarrow \text{hadrons}$ as a function of the center of mass energy. The E_{CM} dependence is linear because the plot is double-logarithmic. Source: [38]. (b) Comparison of cross sections for $e^+e^- \rightarrow \text{hadrons}$ and for $e^+e^- \rightarrow \mu^-\mu^+$. Both cross sections show the same $1/s$ dependence on the center of mass energy squared, except at the Z resonance.

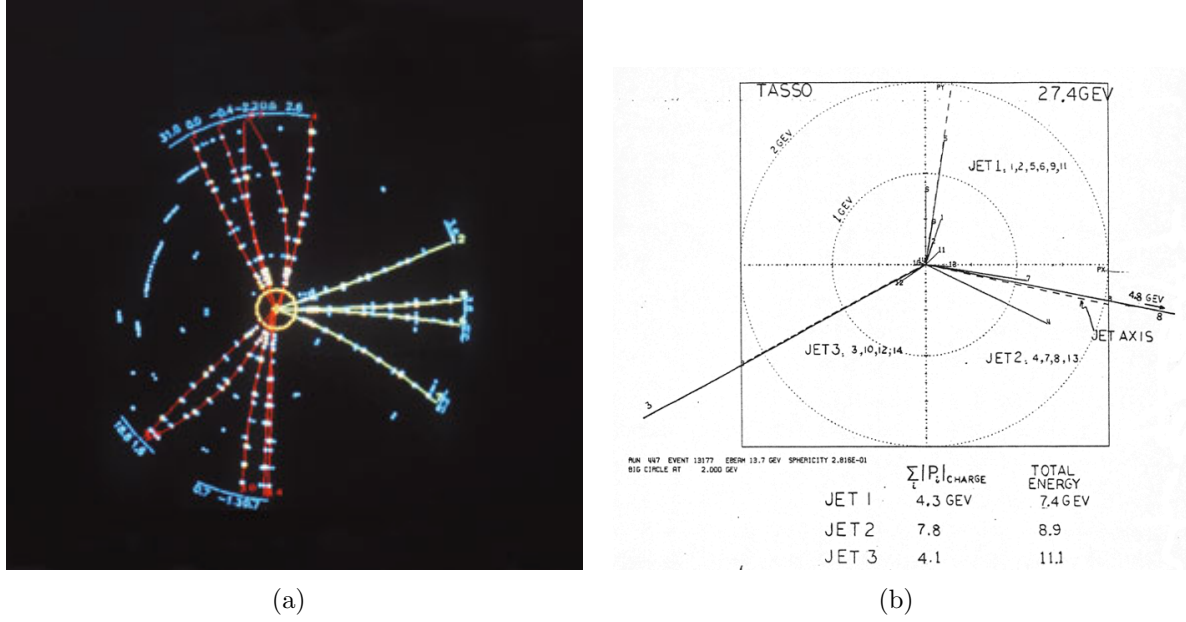


Figure 8.2: *Gluon discovery at the PETRA collider at DESY, Hamburg. Event display (a) and reconstruction (b).*

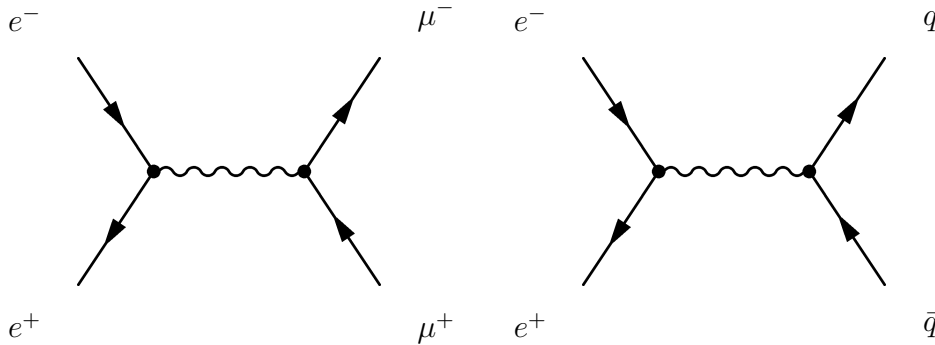
- *LEP (CERN) & SLC (SLAC)*: Large energies (small α_s , see later) mean more reliable calculations and smaller hadronization uncertainties. Large data samples are collected: $\sim 3 \cdot 10^6$ hadronic Z decays per experiment. This allows for precision tests of QCD.

8.1 The basic process: $e^+e^- \rightarrow q\bar{q}$

In Sect. 5.10 we calculated the cross section for $e^+e^- \rightarrow \mu^+\mu^-$ and found

$$\sigma_{e^+e^- \rightarrow \mu^+\mu^-} = \frac{4\pi\alpha_{\text{em}}^2}{3s} = \frac{86.9 \text{ nbGeV}^2}{s} \quad (8.1)$$

where the finite electron and muon masses have been neglected. Here, we consider the basic process $e^+e^- \rightarrow q\bar{q}$. In principle, the same Feynman diagram contributes:



The only differences are the fractional electric charges of the quarks and the fact that the quarks appear in $N_c = 3$ different colors which cannot be distinguished by measurement. Therefore, the cross section is increased by a factor N_c . For the quark-antiquark case one thus finds (for $m_q = 0$)

$$\sigma_0^{e^+e^- \rightarrow q\bar{q}} = \frac{4\pi\alpha_{\text{em}}^2}{3s} e_q^2 N_c = \frac{86.9 \text{ nb GeV}^2}{s} e_q^2 N_c. \quad (8.2)$$

We assume $\sum_q \sigma^{e^+e^- \rightarrow q\bar{q}} = \sigma^{e^+e^- \rightarrow \text{hadrons}}$, i.e. the produced quark-antiquark pair will always hadronize.

With Eq. (8.1) and (8.2), neglecting mass effects and gluon as well as photon radiation, we find the following ratio:

$$R = \frac{\sigma^{e^+e^- \rightarrow \text{hadrons}}}{\sigma^{e^+e^- \rightarrow \mu^+\mu^-}} = N_c \sum_q e_q^2. \quad (8.3)$$

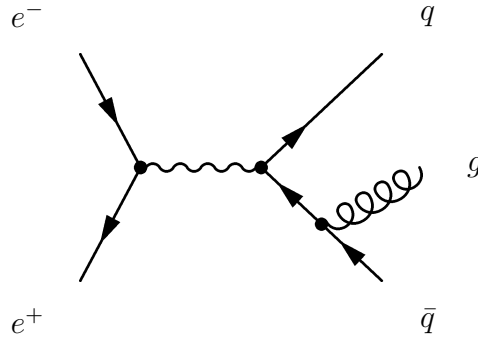
The sum runs over all flavors that can be produced at the available energy. For E_{CM} below the Z peak and above the Υ resonance (see Fig. 8.3), we expect¹

$$R = N_c \sum_q e_q^2 = N_c \left[\underbrace{\left(\frac{2}{3}\right)^2}_u + \underbrace{\left(-\frac{1}{3}\right)^2}_d + \underbrace{\left(-\frac{1}{3}\right)^2}_s + \underbrace{\left(\frac{2}{3}\right)^2}_c + \underbrace{\left(-\frac{1}{3}\right)^2}_b \right] = N_c \frac{11}{9}.$$

This is in good agreement with the data for $N_c = 3$ which confirms that there are three colors. At the Z peak one also has to include coupling to the Z boson which can be created from the e^+e^- pair instead of a photon. The small remaining difference visible in the plot is because of QCD corrections for gluon radiation (see later).

8.1.1 Singularities

In order to achieve a better prediction, we have to go beyond the basic QED prediction by including QCD dynamics: Consider the production of a quark-antiquark pair along with a gluon:



¹Recall that the top quark mass is $m_t \approx 171 \text{ GeV}$.

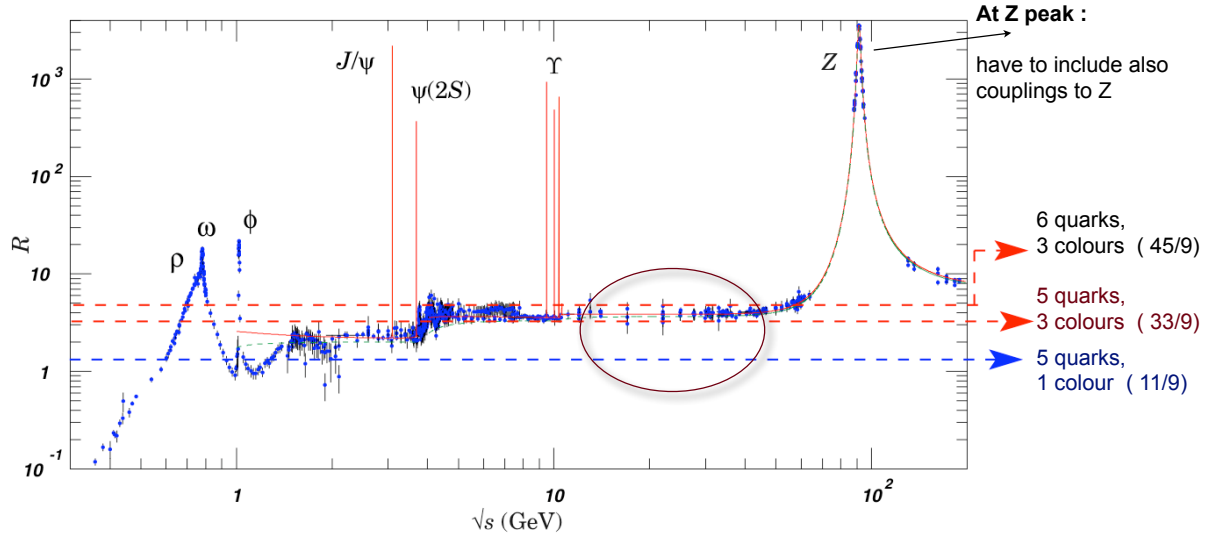


Figure 8.3: Ratio $R = \sigma^{e^+e^- \rightarrow \text{hadrons}} / \sigma^{e^+e^- \rightarrow \mu^+\mu^-}$ as a function of the center of mass energy. As expected by Eq. (8.3), there is roughly no energy dependence besides various resonances. The data confirm that there are three quark colors.

We define the kinematic variables

$$x_i = 2 \frac{p_i \cdot Q}{Q^2} = \frac{E_i^*}{E_{\text{beam}}} \quad (8.4)$$

where $Q = p_{e^+} + p_{e^-} = p_{\gamma/Z}$ and $Q^2 = s$. Energy-momentum conservation ($\sum_i p_i = Q$) requires that, in this case,

$$x_q + x_{\bar{q}} + x_g = 2 \quad (8.5)$$

$$x_i \leq 1. \quad (8.6)$$

One can calculate the differential cross section

$$\frac{d^2\sigma}{dx_q dx_{\bar{q}}} = \sigma_0 \frac{\alpha_s}{2\pi} C_F \frac{x_q^2 + x_{\bar{q}}^2}{(1 - x_{\bar{q}})(1 - x_q)} \quad (8.7)$$

where $C_F = 4/3$ is the color factor of the fundamental representation. Note that this expression is singular for

- $x_q \rightarrow 1$, e. g. $\bar{q} \parallel g$,
- $x_{\bar{q}} \rightarrow 1$, e. g. $q \parallel g$, and for
- $(x_q, x_{\bar{q}}) \rightarrow (1, 1)$, e. g. $x_g \rightarrow 0$.

Because of the kinematic constraints imposed by energy-momentum conservation (Eq. (8.5) and (8.6)), the allowed region (part of which we have to integrate Eq. (8.7) over to find a cross section) for a $\gamma^* \rightarrow q\bar{q}g$ event is of the form shown in Fig. 8.4.

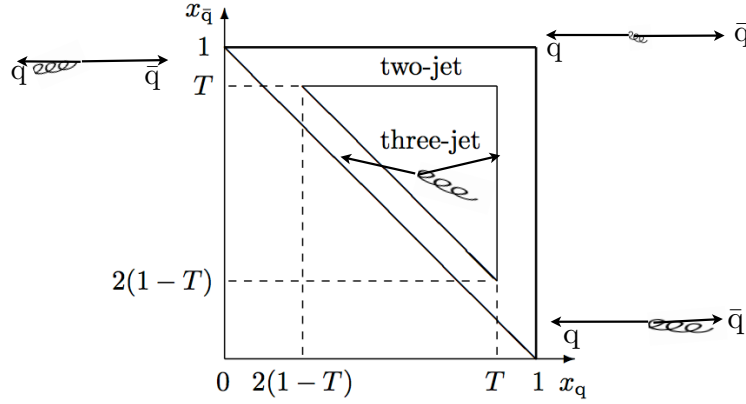


Figure 8.4: A Dalitz plot showing the allowed region of the x_q - $x_{\bar{q}}$ plane for a $\gamma^* \rightarrow q\bar{q}g$ event with massless partons. The thick lines indicate the singularities where $x_q = 1$ and $x_{\bar{q}} = 1$. Their intersection marks the position of the soft gluon singularity: $x_g = 0$. The concept of jets will be introduced later, but it is clear that there has to be at least a certain angle between the gluon and the quarks if the jet in gluon direction is to be detected separately. Source: [27, p. 74].

So, how does one deal with these singularities to find a meaningful expression for the cross section to first order? Consider first the two-jet cross section. Two jets are detected when the gluon is either very soft or almost parallel to the quarks such that only two energy flows back-to-back can be measured. Including interference terms, the cross section in the case of an unresolved gluon is given by (integration over two-jet region, see Fig. 8.4)

$$\begin{aligned}
 \sigma_{\text{two-jet}}(T) &= \underbrace{\left| \text{tree} \right|^2}_{\mathcal{O}(\alpha_s^0)} + \underbrace{\left| \text{tree} + \text{gluon} \right|^2}_{\mathcal{O}(\alpha_s^1)} \\
 &\quad + 2\text{Re} \left(\underbrace{\text{tree} \cdot \text{gluon}}_{\mathcal{O}(\alpha_s^1)} \right) + \mathcal{O}(\alpha_s^2) \\
 &= \sigma_0 (1 + \alpha_s f(T) + \mathcal{O}(\alpha_s^2))
 \end{aligned}$$

where T stems from the criterion separating the two- and three-jet regions of the Dalitz plot: $\max\{x_q, x_{\bar{q}}, x_g\} < T$. The singularities of the second and third term cancel and the result is a function of the parameter T . However, our problem is not yet resolved, since $\lim_{T \rightarrow 1} f(T) = -\infty$.

If the gluon can be resolved, a three-jet event is detected and the integration is over the

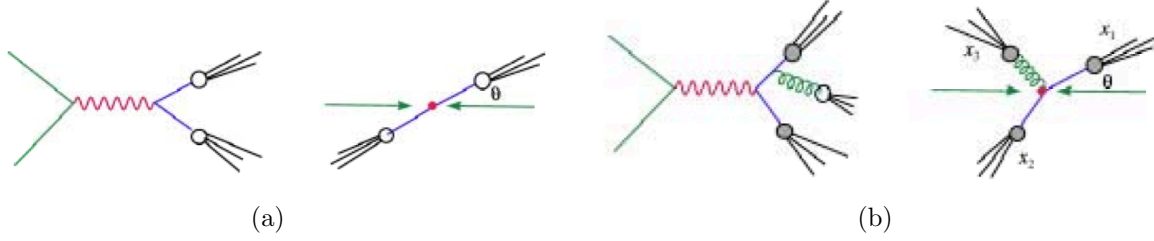


Figure 8.5: *Hadronization of quarks and gluons*. Diagrams of the processes $e^+e^- \rightarrow q\bar{q} \rightarrow$ hadrons (a) and $e^+e^- \rightarrow q\bar{q}g \rightarrow$ hadrons (b). The RHS shows the situation in the center of mass frame. Source: [39, p. 5 and 6].

three-jet region of Fig. 8.4:

$$\sigma_{\text{three-jet}}(T) = \left| \text{Diagram} \right|^2 + \mathcal{O}(\alpha_s^2) = \sigma_0 \alpha_s g(T) + \mathcal{O}(\alpha_s^2)$$

where $\lim_{T \rightarrow 1} g(T) = +\infty$. Combining the two-jet and three-jet cross sections, one finds that the dependence on T cancels yielding a finite result for the total cross section:

$$\begin{aligned} \sigma_{\text{tot}} &= \sigma_{\text{two-jet}} + \sigma_{\text{three-jet}} + \dots = \sigma_0 \left(1 + \alpha_s [f(T) + g(T)] + \mathcal{O}(\alpha_s^2) \right) \\ &= \boxed{\sigma_0 \left(1 + \frac{3}{4} C_F \frac{\alpha_s}{\pi} + \mathcal{O}(\alpha_s^2) \right)}. \end{aligned}$$

8.2 Jets and other observables

We now focus on entities actually observable in experiment. We do not observe free quarks but only colorless hadrons produced by the “hadronization/fragmentation” of quarks and gluons. For instance, the processes discussed so far can be visualized as in Fig. 8.5.

The anatomy of the process $e^+e^- \rightarrow Z \rightarrow$ hadrons is sketched in Fig. 8.6. The things that we can do based on such a process include

- Measure α_s ,
- Measure the masses of (heavy) quarks,
- Measure gluon self-coupling,
- Study hadronization and particle correlations, and
- Study the transition between the non-perturbative and perturbative regime and the properties of quark or gluon jets.

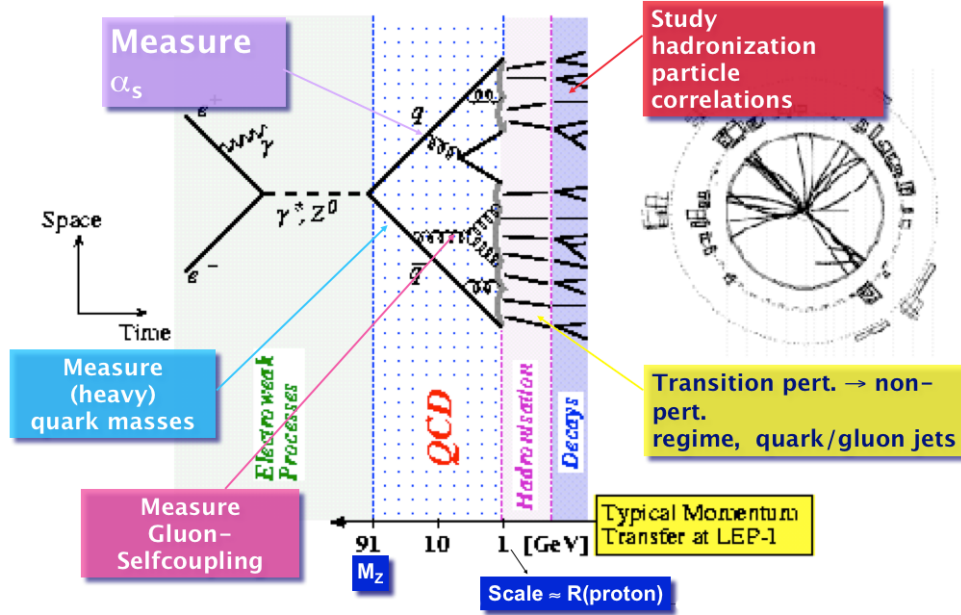


Figure 8.6: *The anatomy of the process $e^+e^- \rightarrow \gamma^*, Z^0 \rightarrow \text{hadrons}$.* Source: [40, p. 13, modified].

8.2.1 Jet algorithms

Let us turn to the question: What is a jet?

Fig. 8.7 shows a multi-jet event recorded by the ALEPH detector. A possible verbal definition of “jet” would be “cluster/spray of particles (tracks, calorimeter deposits) or flow of energy in a restricted angular region”. Jets are the connection between the quarks and gluons of QCD and the signals actually measured in the detectors. If we are to extract this information from the data, we clearly need some kind of algorithmic definition of this concept: In the “final state” of many interesting interactions there are quarks and gluons. These are the fundamental particles of QCD. Confinement (see p. 148) means that in the detector we see hadrons (together with leptons and photons), but not single quarks or gluons. At energies much larger than $\Lambda^{\text{QCD}} (\sim 1 \text{ GeV})$ these hadrons appear confined into jets. Our aim is to compare the predictions based on partons (quarks and gluons) with the measurements on hadrons. Therefore, we need an algorithmic definition of a jet which

1. can be applied both to data *and* predictions and
2. gives a close relationship between partons and jets of hadrons.

The basic requirement for such an algorithm is applicability at all relevant levels of theory and experiment: partons, stable particles, measured objects (calorimeter objects, tracks, etc.) while always finding the same jet. Furthermore, the algorithm has to be independent of the very details of the detector, e.g. the granularity of the calorimeter, the energy

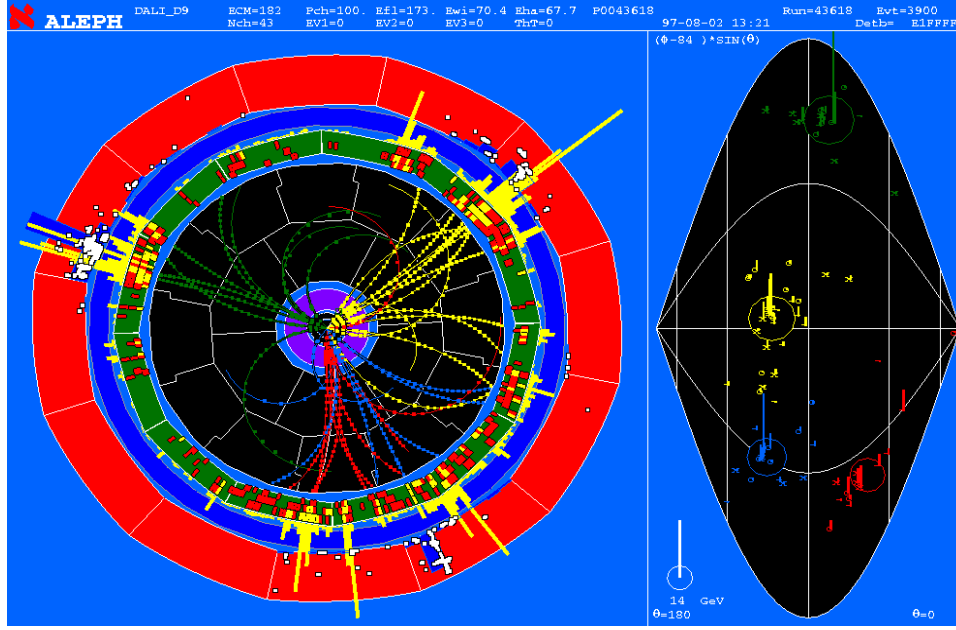


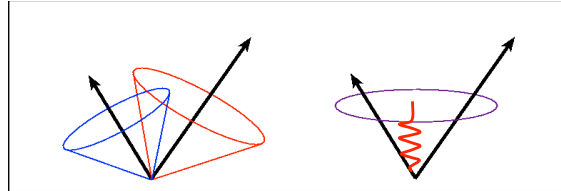
Figure 8.7: *Multi-jet event in the ALEPH detector.*

response, etc. Finally, it should also be easy to implement. In order that we can test QCD predictions, there has to be a close correspondence between the jet momentum (i. e. energy, momentum, and angle) at the parton level and at the hadron level.

NB: Other requirements might strongly depend on the specific application/measurement being performed: For a precision test of QCD there may be requirements which for an analysis of W decays or searches for new physics might not be necessary (e. g. infrared safety).

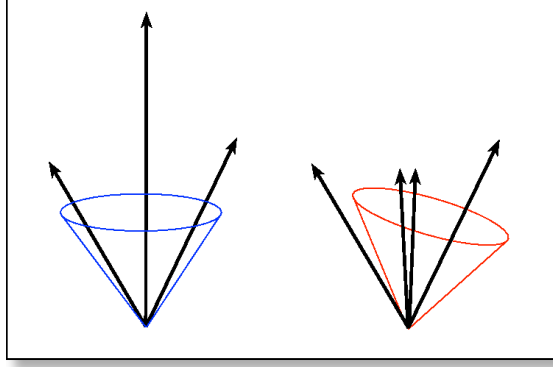
Further requirements come from QCD: We want to compare perturbative calculations with the data. Therefore, the algorithm has to be insensitive to “soft physics” which requires infrared safety and collinear safety.

Infrared safety requires that the configuration must not change when adding a further soft particle. This would be violated by the following behavior²:



Collinear safety means that the configuration does not change when substituting one particle with two collinear particles. The problem is visualized in this figure:

²Source: [41, pp. 4].



Infrared and collinear safety yield algorithms with the required insensitivity to soft physics: They guarantee the cancellation (between real and virtual emission diagrams) of the infrared and collinear divergencies in *every order* of perturbation theory.

8.2.1.1 Examples of jet algorithms

There are two classes of jet algorithms in use. Algorithms of the class “JADE” are used mainly for e^+e^- annihilations (i.e. for the analysis of events with purely leptonic initial states), but more recently, this class of jet algorithms is also used at hadron colliders. We will concentrate on this class here. The second class of jet algorithms is called “CONE” and is mainly used at hadron colliders with some applications also at e^+e^- colliders.

JADE class algorithms are characterized by

- a “metric” y_{ij} (measure of distance in momentum space),
- a criterion of resolution y_{cut} , and a
- procedure of recombination.

The original definition of the metric from the JADE experiment at PETRA reads

$$y_{ij} = \frac{2E_i E_j (1 - \cos \theta_{ij})}{E_{CM}^2} \approx \frac{m_{ij}^2}{E_{CM}^2} \quad (8.8)$$

where m_{ij} is the invariant mass of the particle pair (i, j) , see Fig. 8.8(a) Given this metric and a pre-defined resolution y_{cut} , the algorithm is:

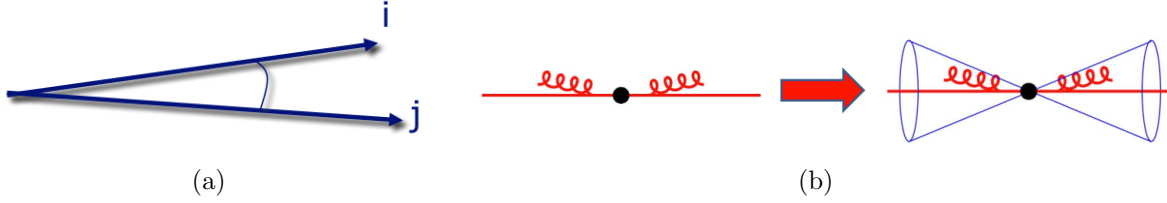
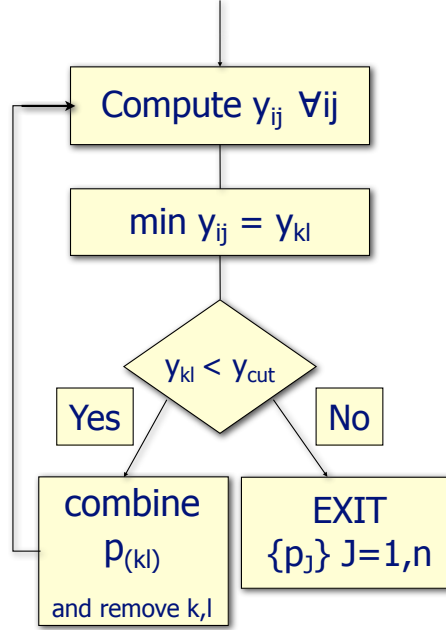


Figure 8.8: Particle pair (a) and recombination of close particles (b).



First, all distances y_{ij} between pairs (i, j) are calculated. Then we search for the smallest invariant mass: $\min_{(i,j)} y_{ij} = y_{kl}$. The fact that y_{kl} is the smallest distance in momentum space of all pairs (of particles or, in the subsequent steps, also pseudo-particles) means that the pair (k, l) is either nearly parallel, $\theta_{kl} = 0$, or one or both of the particles are very soft, see Fig. 8.8(b). If the distance cannot be resolved, $y_{kl} < y_{cut}$, the two particles (k, l) are combined (clustered) into one new pseudo-particle with the combined momentum $p_{(kl)} = p_k + p_l$ (i. e. momentum is conserved), see Fig. 8.9(a). This is the so-called E scheme. Applying this algorithm will reduce complex events until there is a certain number of jets left, as is sketched in Fig. 8.9(b).

The proposed algorithm has some very useful characteristics:

- Infrared safety,

$$y_{ij} \rightarrow 0 \text{ for } E_i \text{ or } E_j \rightarrow 0,$$

and collinear safety,

$$y_{ij} \rightarrow 0 \text{ for } \theta_{ij} \rightarrow 0,$$

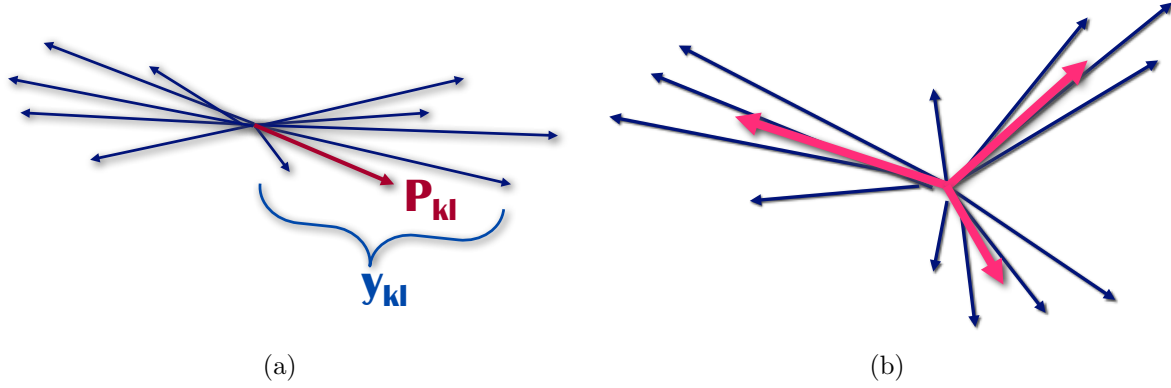


Figure 8.9: *Recombination of particle pair with small invariant mass (a) and reduction of particle pattern to jets (b).*

(in every order of perturbation theory, see p. 161 and Eq. (8.8)).

- All particles are assigned to one and only one jet.
- The algorithm's sequence does not depend on y_{cut} .
- The number of found jets is a monotonic function of y_{cut} .

For the discussed algorithm there is no need to stick to the JADE metric of Eq (8.8); alternative metrics can be introduced. For instance, the DURHAM metric is

$$y_{ij} = \frac{2 \min(E_i^2, E_j^2) (1 - \cos \theta_{ij})}{E_{CM}^2} \approx \frac{k_\perp^2}{E_{CM}^2} \quad (8.9)$$

where k_\perp is the transverse momentum of the less energetic particle with respect to the more energetic one. The introduction of this metric was motivated by perturbative QCD calculations: It allows for the resummation of large logarithms of the type $\ln^m(y_{\text{cut}})$ in all orders of perturbation theory (see e. g. [27, pp. 139]). These logarithms appear order-by-order in the expressions for jet cross sections, jet rates, etc.

Now is a good time to recall the Dalitz plot of Fig. 8.4 where we separated a two-jet and a three-jet region. The algorithmic jet definition we have developed enables us to define the three-jet region: Apply the jet algorithm until three jets are left. If the distance between the jets can be resolved, $\min_{(i,j)}(y_{ij}) > y_{\text{cut}}$, there are three jets, else it is a two-jet event. The shape of the found three-jet region is somewhat different, since y_{ij} also depends on the angle θ_{ij} , see Fig. 8.10.

In order to compare the analyzed data to the predictions of QCD, we need perturbative predictions for jet rates. For the reaction $e^+e^- \rightarrow \text{hadrons}$ the leading order predictions are as follows. For the JADE algorithm we have

$$\sigma_{\text{three-jet}}^{LO}(y_{\text{cut}}) = \sigma_0 C_F \frac{\alpha_s}{2\pi} \left[2 \ln^2 y_{\text{cut}} + 3 \ln y_{\text{cut}} - \frac{\pi^2}{3} + \frac{5}{2} - f(y_{\text{cut}}) \right] \quad (8.10)$$

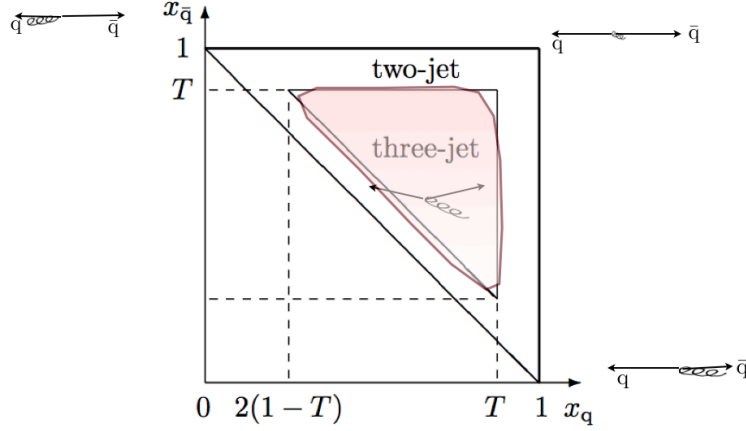


Figure 8.10: A Dalitz plot showing the allowed region of the x_q - $x_{\bar{q}}$ plane for a $\gamma^* \rightarrow q\bar{q}g$ event with massless partons. The three-jet region is determined using an algorithmic jet definition.

where $f(y_{\text{cut}}) \rightarrow 0$ for $y_{\text{cut}} \rightarrow 0$. The prediction for the DURHAM algorithm is the same, except for the factor “2” in front of “ $\ln^2 y_{\text{cut}}$ ”. In simple terms, the logarithm terms arise because the vertex where the gluon is radiated off contributes a factor proportional to $\alpha_s/E_{\text{gluon}}$ to the integrand which upon integration yields $\int_{y_{\text{cut}}} dE/E$.

Resummation³ with the DURHAM algorithm looks as follows. First, let

$$R_2(y_{\text{cut}}) = \frac{\sigma_{\text{two-jet}}}{\sigma_{\text{tot}}}.$$

One can show that

$$\begin{aligned} R_2 &= \exp \left\{ - \int_{sy_{\text{cut}}}^s \frac{dq^2}{q^2} \frac{C_F \alpha_s(q^2)}{2\pi} \left[\ln \frac{s}{q^2} - \frac{3}{2} \right] \right\} \\ &\approx 1 - \int_{sy_{\text{cut}}}^s \frac{dq^2}{q^2} \frac{C_F \alpha_s(q^2)}{2\pi} \ln \dots + \dots \approx 1 - \frac{C_F \alpha_s}{2\pi} \ln^2 y_{\text{cut}} + \dots \end{aligned}$$

where $R_2(y_{\text{cut}} \rightarrow 0) = 0$. This is an example of the characteristics an algorithm has to have if you want to perform “high-precision” perturbative QCD calculations. Now there also exists an algorithm of the k_t (DURHAM) type for hadron colliders, see later.

To conclude this section, we turn to the comparison of jet algorithms. There is no such thing as the best “benchmark” variable which allows to compare algorithms in a general manner. The suitability and performance of an algorithm depends very strongly on the performed analysis. Usually we would like to have a good resolution of energies and angles

³Resummation in QCD is analogous to the treatment of infrared divergencies in QED, see e.g. [14, pp. 202]

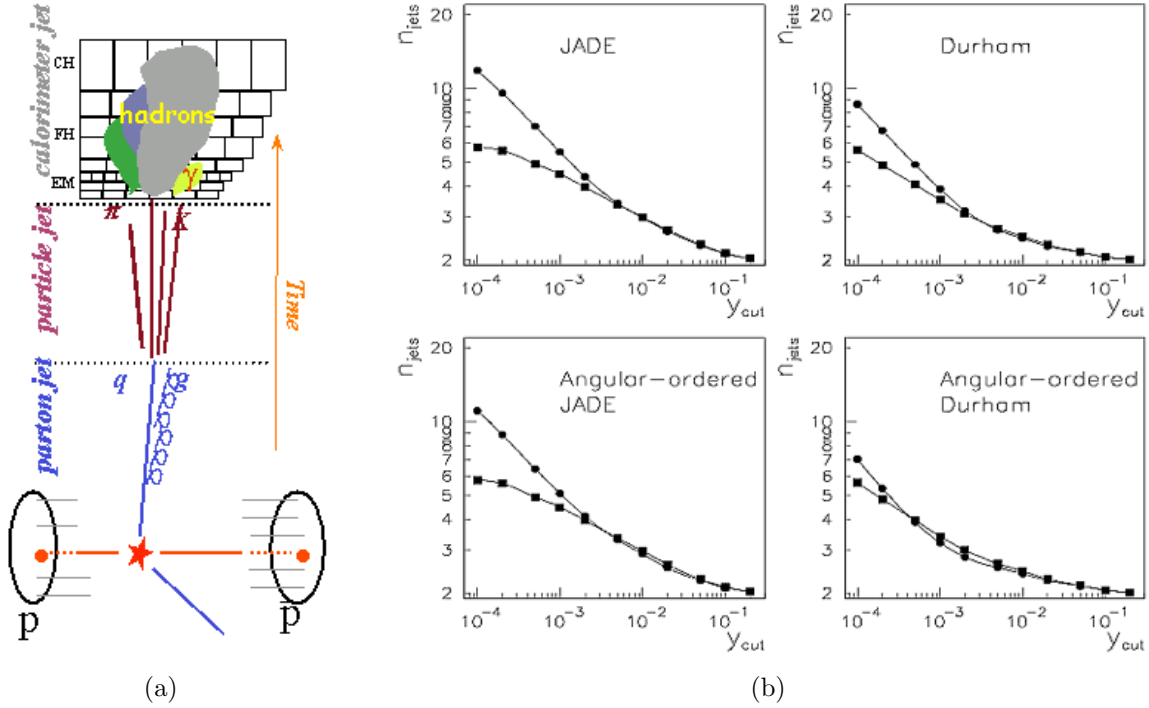


Figure 8.11: Visualization of levels at which the algorithms have to deliver good resolution (a) and comparison of jet algorithms (b). The mean number of jets is displayed as a function of y_{cut} . The parton level is denoted by squares and the hadron level by circles. The results were obtained by HERWIG Monte Carlo simulation at $E_{CM} = M_Z$. Source: [34, p. 28]. For details compare [34, pp. 7].

of the jets at the parton, hadron, and detector levels (see Fig. 8.11(a) for a visualization), as well as a good efficiency and purity to find a certain number of jets at a certain level. For some jet algorithms, the mean number of jets as a function of y_{cut} at the hadron and parton levels, as obtained by HERWIG (Hadron Emission Reactions With Interfering Gluons) Monte Carlo simulation at $E_{CM} = M_Z$, is compared in Fig. 8.11(b). Another comparison⁴ is shown in Fig. 8.12. The fraction of events with 2 jets which have 2, 3, 4, and 5 sub-jets is given as a function of y_{cut} or r^2 , the radius fraction squared, respectively. The data stem from HERWIG Monte Carlo simulations at $E_{CM} = 1.8 \text{ TeV}$ with $75 \text{ GeV} < E_t(\text{jet } 2) < 100 \text{ GeV}$. Data from a k_t algorithm are shown in Fig. 8.12(a) while the results in Fig. 8.12(b) come from a CONE algorithm with radius $R = 0.7$.

8.2.2 Event shape variables

The introduced jet algorithms can be used as a starting point to define more refined observables that capture the event topologies.

⁴More on k_t and CONE algorithms can be found in [41].

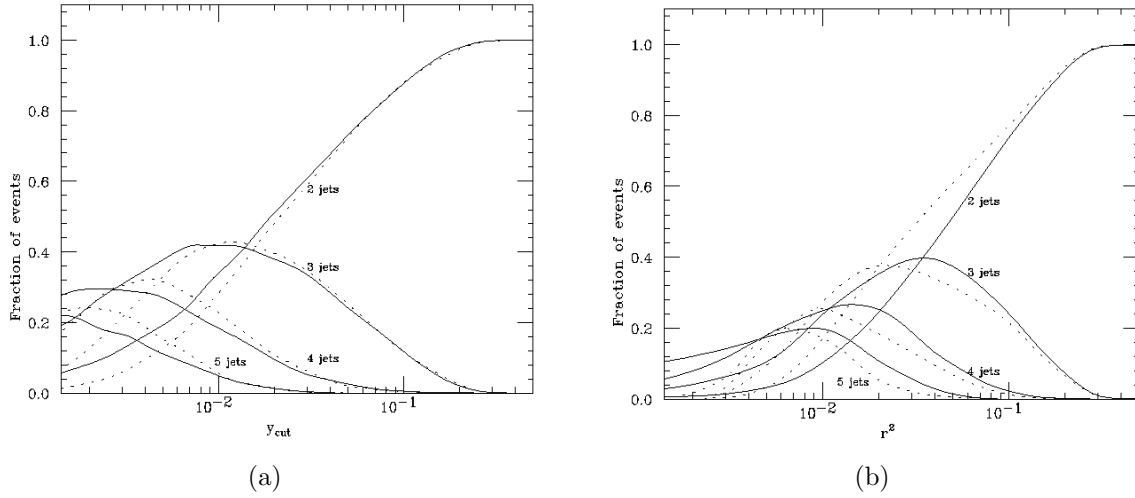


Figure 8.12: *Comparison of k_t (a) and CONE (b) algorithms.* Legend: —parton level, \cdots calorimeter level. The fraction of two-jet events with 2, 3, 4, and 5 sub-jets is given as a function of y_{cut} or r^2 . The data is generated by HERWIG Monte Carlo simulations at $E_{CM} = 1.8 \text{ TeV}$ with $75 \text{ GeV} < E_t(\text{jet } 2) < 100 \text{ GeV}$.

An example for an event shape variable is the *differential two-jet rate*. The definition goes as follows: Apply the DURHAM algorithm until exactly three jets are left (in contrast to the possibility to run the algorithm until a certain resolution is reached). Then take the minimal distance y_{ij} of all pairs (i, j) and call it y_{23} (or y_3): $\min_{(i,j)} y_{ij} = y_{23} = y_3$. This gives one value for each event. The distribution of these values for all events is an “event-shape distribution”. Therefore, one can plot the differential cross section as in Fig. 8.13. There is one histogram entry for each event. The data come from hadronic Z decays at LEP. Observe that two-jet events are more likely than three-jet events. The perturbative regime is limited to high gluon energies. Hadronization effects that have to be phenomenologically modeled spoil the perturbative calculations at low y_3 values.

As another example for an event-shape variable, let us consider *thrust*. It was invented around 1978 and first used at PETRA. The idea is to select the axis that maximizes the sum of the longitudinal momentum components:



The thrust of an event is then defined as

$$T = \max_{\vec{n}} \frac{\sum_i |\vec{p}_i \cdot \vec{n}|}{\sum_i |\vec{p}_i|}$$

where $|\vec{n}| = 1$ and the sum runs over the three-momenta of all final states. The thrust axis is defined by the vector \vec{n}_T for which the maximum is obtained. This definition means that for $T = 1$ the event is perfectly back-to-back while for $T = 1/2$ the event is spherically symmetric:

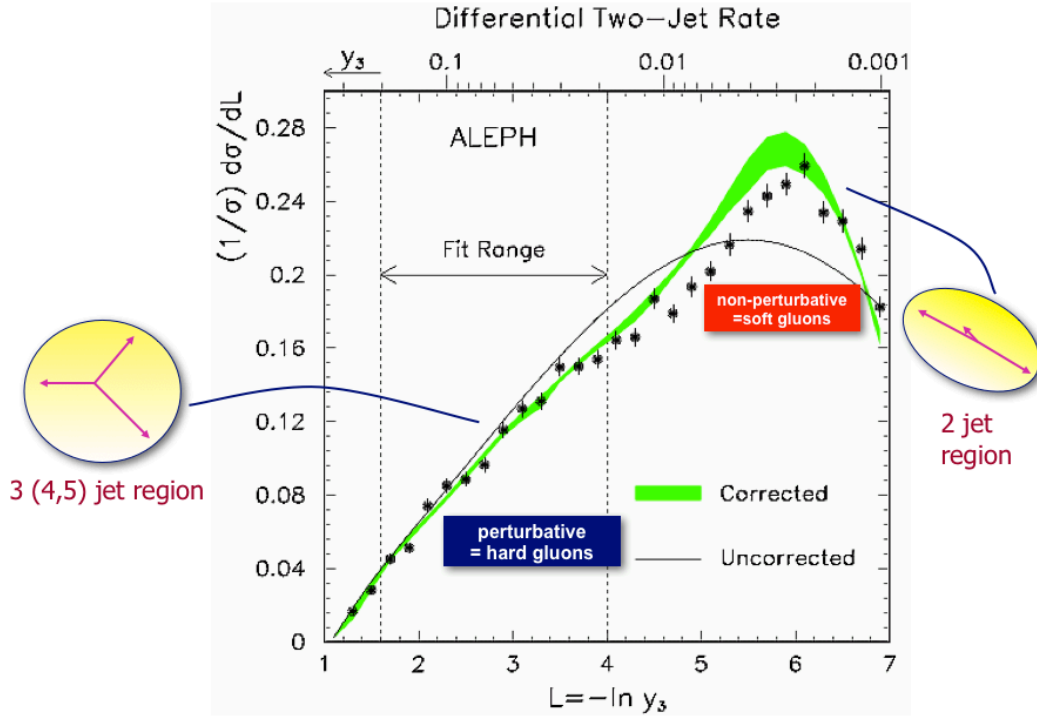


Figure 8.13: Differential two-jet rate for hadronic Z decays at LEP.



This point is also illustrated with ALEPH data of Z decays in Fig. 8.14 where Fig. 8.14(a) corresponds to $T \rightarrow 1$ and Fig. 8.14(b) to $T \rightarrow 1/2$. The corresponding event-shape distribution is shown in Fig. 8.15 (compare also the differential two-jet rate event-shape distribution in Fig. 8.13).

There are further event-shape variables suitable for different purposes. Some examples are given in the following.

- *Thrust major* T_{major} : The thrust major vector \vec{n}_{Ma} is defined in the same way as the thrust vector \vec{n}_T , but with the additional condition that \vec{n}_{Ma} must lie in the plane perpendicular to \vec{n}_T :

$$T_{\text{major}} = \max_{\vec{n}_{\text{Ma}} \perp \vec{n}_T} \frac{\sum_i |\vec{p}_i \cdot \vec{n}_{\text{Ma}}|}{\sum_i |\vec{p}_i|}.$$

- *Thrust minor* T_{minor} : The minor axis is perpendicular to both the thrust axis and

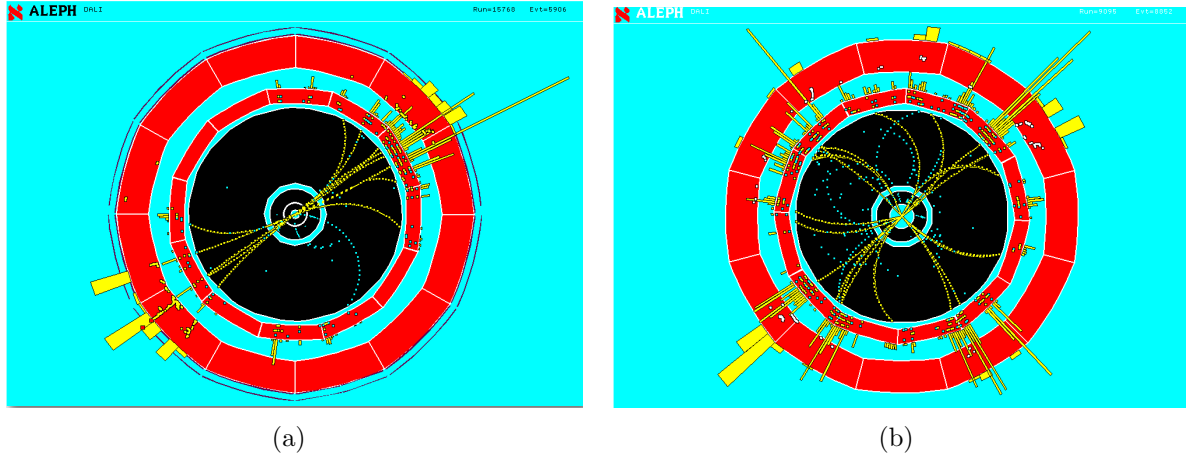


Figure 8.14: *Event displays of Z decays recorded at ALEPH. The thrust is nearly 1 for (a) and close to $1/2$ for (b).*

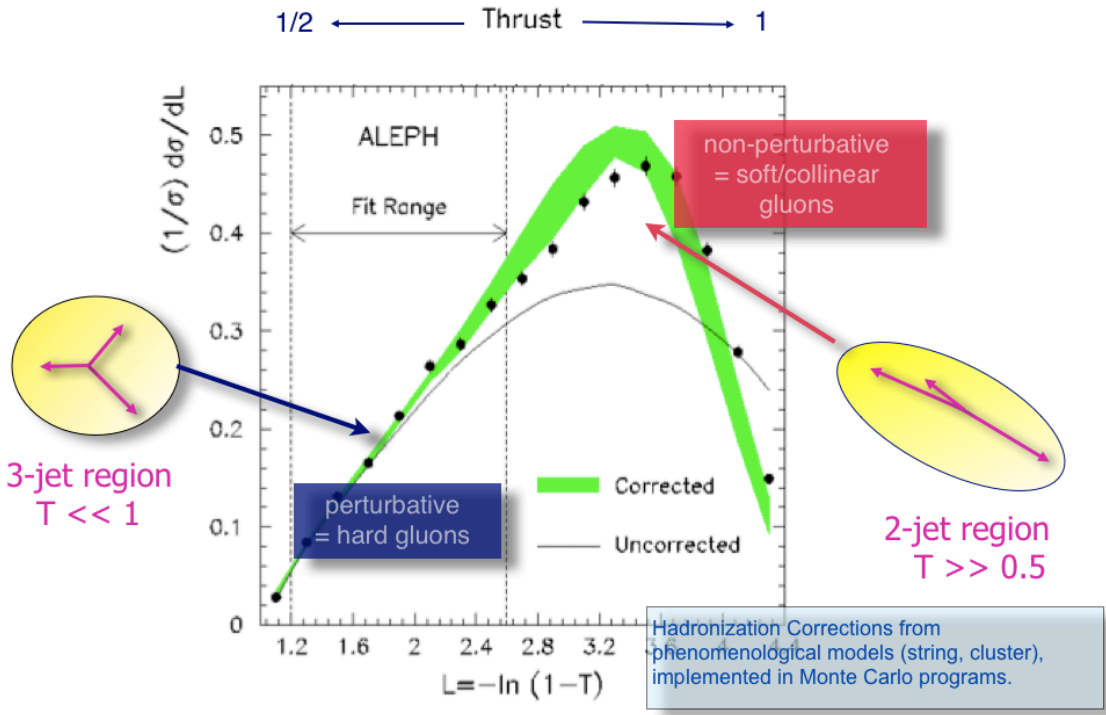


Figure 8.15: *Thrust for hadronic Z decays at LEP. Observe that the two- and three-jet events are indicated by thrust values close to 1 and $1/2$, respectively. Again, in the non-perturbative regime hadronization corrections from phenomenological models are needed.*

the major axis: $\vec{n}_{\text{Mi}} = \vec{n}_T \times \vec{n}_{Ma}$. The value of the thrust minor is given by

$$T_{\text{minor}} = \frac{\sum_i |\vec{p}_i \cdot \vec{n}_{\text{Mi}}|}{\sum_i |\vec{p}_i|}.$$

- *Oblateness* O : The oblateness is defined as the difference between thrust major and thrust minor:

$$O = T_{\text{major}} - T_{\text{minor}}.$$

- *Sphericity* S : The sphericity is calculated from the ordered eigenvalues $\lambda_{i=1,2,3}$ of the quadratic momentum tensor:

$$\begin{aligned} M^{\alpha\beta} &= \frac{\sum_i p_i^\alpha p_i^\beta}{\sum_i |\vec{p}_i|^2}, \quad \alpha, \beta = 1, 2, 3 \\ \lambda_1 &\geq \lambda_2 \geq \lambda_3, \quad \lambda_1 + \lambda_2 + \lambda_3 = 1 \\ S &= \frac{3}{2}(\lambda_2 + \lambda_3). \end{aligned}$$

The sphericity axis \vec{n}_S is defined along the direction of the eigenvector associated to λ_1 , the semi-major axis \vec{n}_{sMa} is along the eigenvector associated to λ_2 .

- *Aplanarity* A : The aplanarity is calculated from the third eigenvalue of the quadratic momentum tensor:

$$A = \frac{3}{2}\lambda_3.$$

- *Planarity* P : The planarity is a linear combination of the second and third eigenvalue of the quadratic momentum tensor:

$$P = \lambda_2 - \lambda_3.$$

- *Heavy jet mass* ρ : A plane through the origin and perpendicular to \vec{n}_T divides the event into two hemispheres, H_1 and H_2 from which the corresponding normalized hemisphere invariant masses are obtained:

$$M_i^2 = \frac{1}{E_{CM}^2} \left(\sum_{k \in H_i} p_k \right)^2, \quad i = 1, 2.$$

The larger of the two hemisphere masses is called the heavy jet mass,

$$\rho = \max(M_1^2, M_2^2),$$

and the smaller is the light jet mass M_L ,

$$M_L = \min(M_1^2, M_2^2).$$

- *Jet mass difference* M_D : The difference between ρ and M_L is called the jet mass difference:

$$M_D = \rho - M_L.$$

- *Wide jet broadening* B_W : A measure of the broadening of particles in transverse momentum with respect to the thrust axis can be calculated for each hemisphere H_i using the relation

$$B_i = \frac{\sum_{k \in H_i} |\vec{p}_k \times \vec{n}_T|}{2 \sum_j |\vec{p}_j|}, \quad i = 1, 2$$

where j runs over all particles in the event. The wide jet broadening is the larger of the two hemisphere broadenings,

$$B_W = \max(B_1, B_2),$$

and the smaller is called the narrow jet broadening B_N ,

$$B_N = \min(B_1, B_2).$$

- *Total jet broadening* B_T : The total jet broadening is the sum of the wide and the narrow jet broadenings:

$$B_T = B_W + B_N.$$

- *C-parameter* C : The C-parameter is derived from the eigenvalues of the linearized momentum tensor $\Theta^{\alpha\beta}$:

$$\Theta^{\alpha\beta} = \frac{1}{\sum_i |\vec{p}_i|} \sum_i \frac{p_i^\alpha p_i^\beta}{|\vec{p}_i|}, \quad \alpha, \beta = 1, 2, 3.$$

The eigenvalues λ_j of this tensor define C by

$$C = 3(\lambda_1 \lambda_2 + \lambda_2 \lambda_3 + \lambda_3 \lambda_1).$$

The discussed event-shape variables have been extensively used to analyze LEP data. Examples are given in Fig. 8.16: Fig. 8.16(a) shows thrust predictions and measurements; predictions and data for thrust, heavy jet mass, total jet broadening, wide jet broadening, and the C-parameter are shown in Fig. 8.16(b).

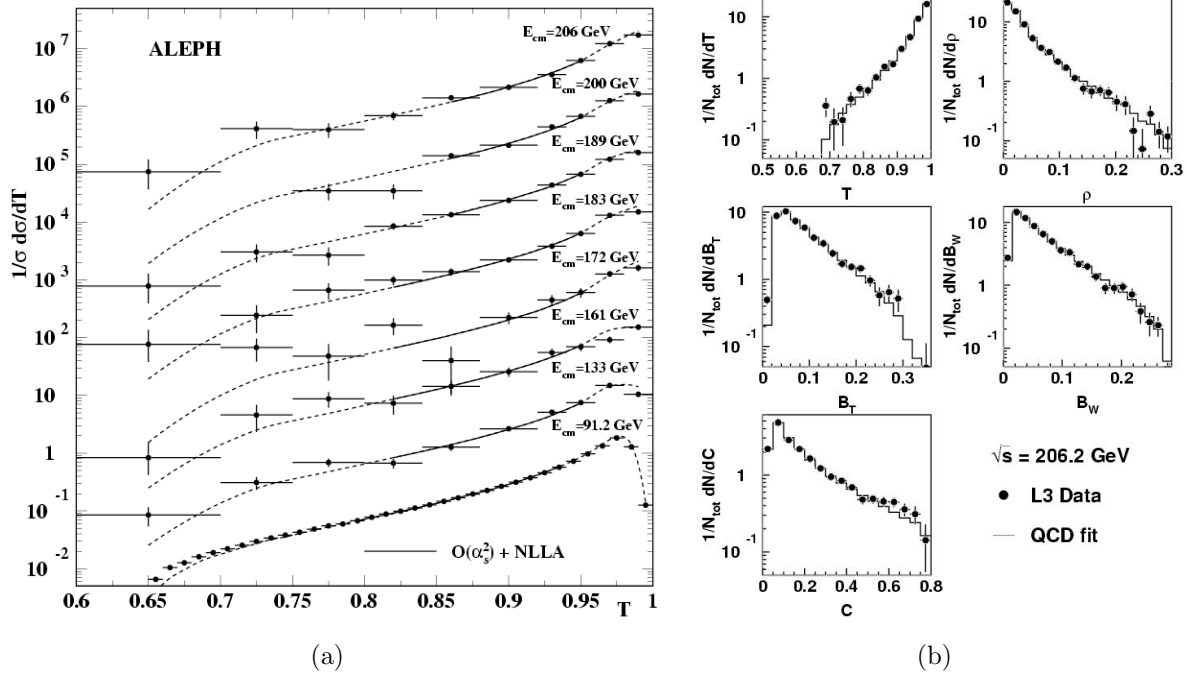


Figure 8.16: Comparison of predictions and LEP data for some event-shape variables. Thrust data are shown for several center of mass energies (a). The other analyses deal with heavy jet mass, total jet broadening, wide jet broadening, and the C-parameter (b).

8.2.3 Applications

Examples for applications of the observables discussed above in this section are measurements of the strong coupling constant α_s (see later, Sect. 8.3), the discovery of quark and gluon jets, measurements of the quark and gluon spin, the triple-gluon vertex, and jet rates or the analysis of differences between quark and gluon jets.

Quark jets were discovered at the SPEAR storage ring (SLAC) [42]. The data are shown in Fig. 8.17. For higher energies particles cluster around an axis and the Monte Carlo simulation based on a jet model fits the data better than the simulation based on an isotropic phase-space model. This is the first observation of a jet structure.

Gluon jets were discovered at PETRA (DESY) [43, 44, 45, 46]. Here, the relevant observable is oblateness (see p. 170). The first three-jet event seen by TASSO is shown in Fig. 8.18(a). In Fig. 8.18(b) one can observe that events at $E_{CM} \sim 30$ GeV exhibit larger oblateness (planar structure) than predicted by models without hard gluon radiation.

When it comes to parton spins the question is: How do you measure the spin of unobservable particles? For spin-1/2 fermions annihilating into a vector boson, conservation of angular momentum predicts a distribution

$$\frac{d\sigma}{d\cos\Theta^*} \sim 1 + \cos^2\Theta^*$$

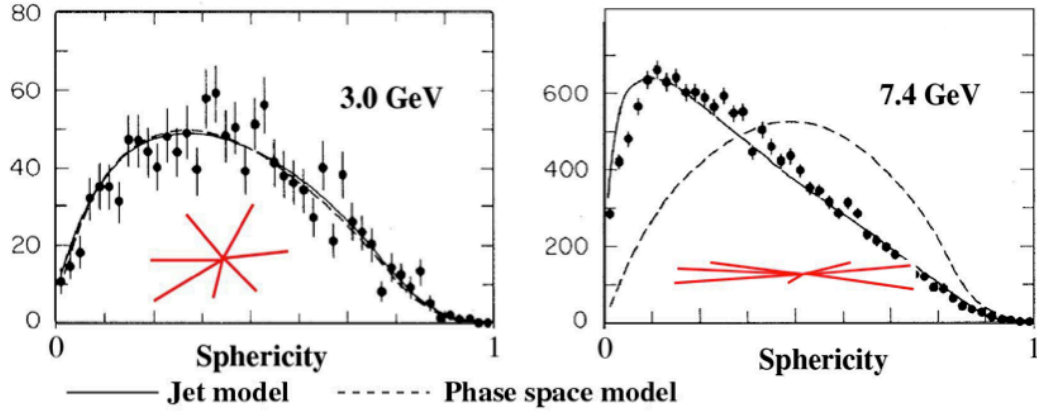


Figure 8.17: *Discovery of quark jets at SPEAR (SLAC)*. Observed sphericity (see p. 170) distributions for data, jet model (solid curves) and phase-space model (dashed curves) for $E_{CM} = 3 \text{ GeV}$ (LHS) and 7.4 GeV (RHS). Source: [42, 38, p. 1611].

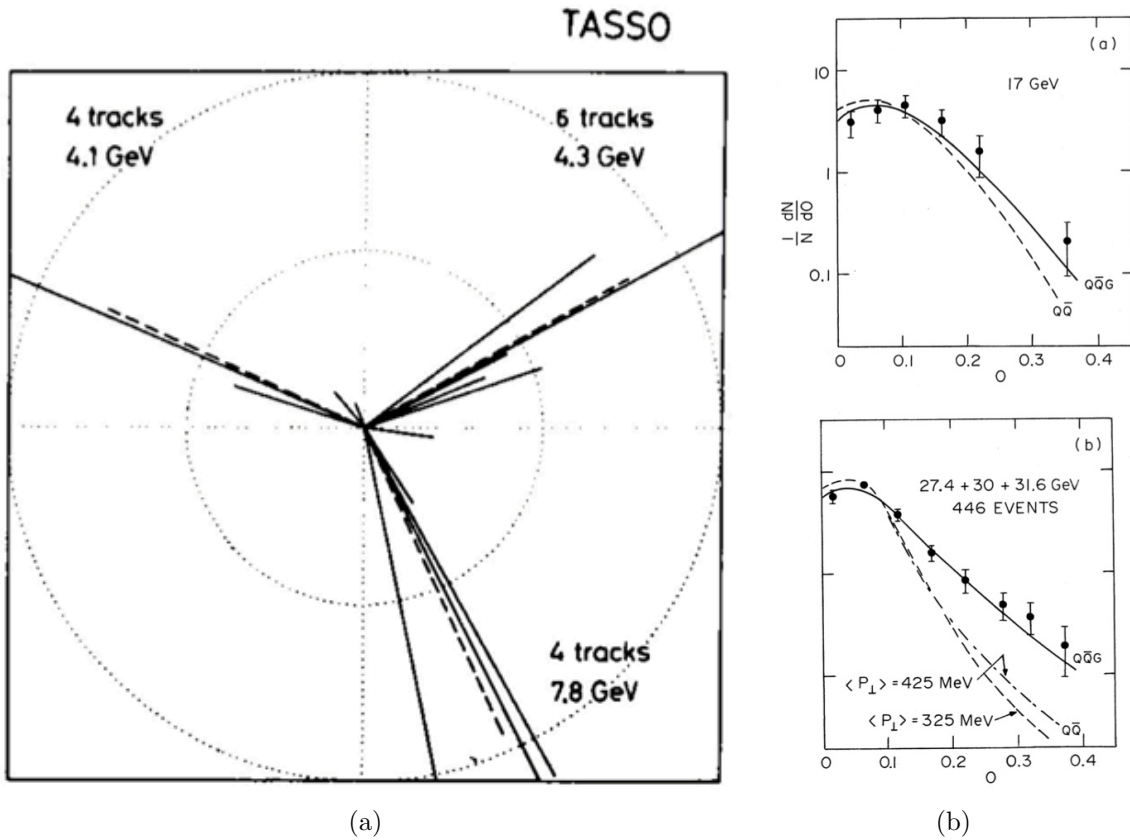


Figure 8.18: *The first three-jet event seen by TASSO (a) and the distribution $N^{-1} dN/dO$ as a function of oblateness, measured at MARK-J (b)*. In both figures of (b) the solid curves are the predictions based on the $q\bar{q}g$ model and the dashed curve is based on the standard $q\bar{q}$ model. Source: [44, p. 832].

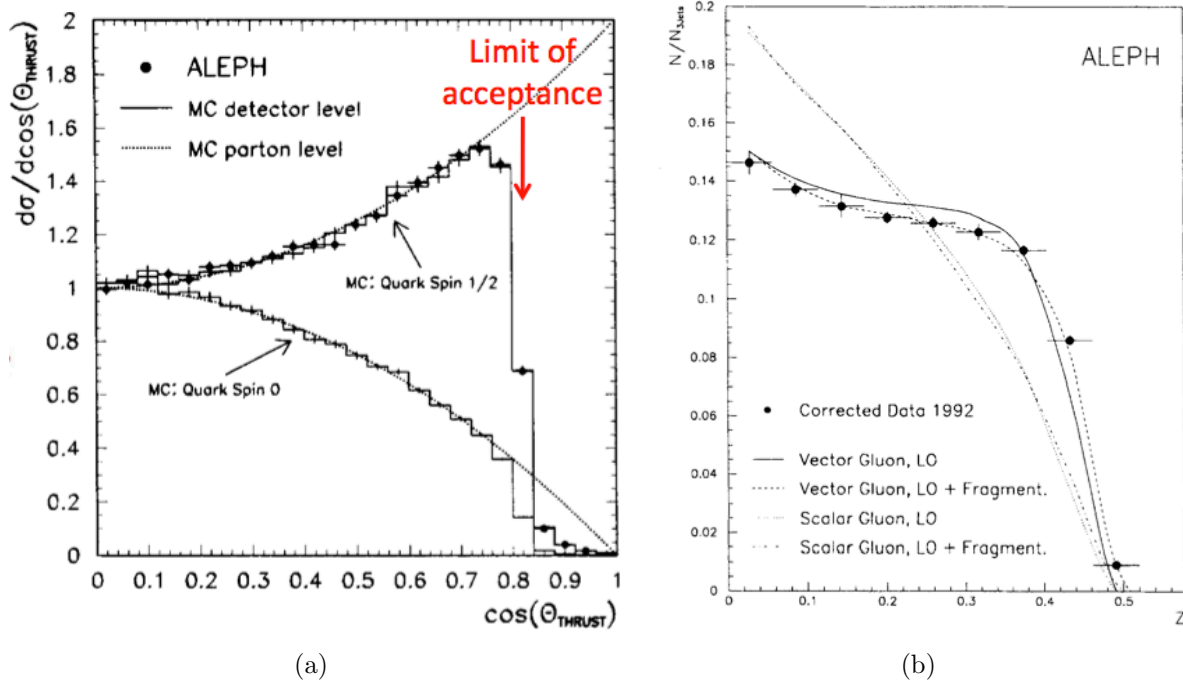


Figure 8.19: Measurements of quark (a) and gluon (b) spin by ALEPH. Source: [47].

if the final state particles have spin 1/2 and

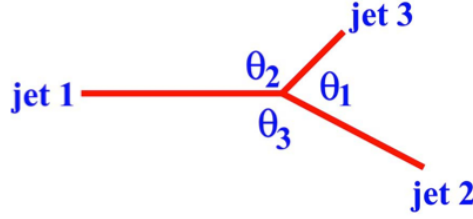
$$\frac{d\sigma}{d\cos\Theta^*} \sim 1 - \cos^2\Theta^* = \sin^2\Theta^*$$

for spin-0 particles in the final state. Therefore, the quark direction has to be measured to measure the quark spin. At LEP energies the thrust axis in two-jet events to a very good approximation aligns with the direction of the primary quarks. Thus, one can take the thrust direction in two-jet events. The exact expression for the spin-1/2 case reads

$$\frac{d\sigma}{d\cos\Theta^*} = \frac{\alpha_{\text{em}}^2 e_q^2 \pi N_c}{2s} (2 - \beta_q^{*2} + \beta_q^{*2} \cos^2\Theta^*) \beta_q^*$$

where $\beta_q^* = \sqrt{1 - 4m_q^2/s} \rightarrow 1$ for $m_q = 0$. The resulting angular distribution found by ALEPH [47] is shown in Fig. 8.19(a). The experimental data are compared to a Monte Carlo simulation. The data are in perfect agreement with the spin-1/2 assignment for the quarks while a spin-0 assignment is clearly excluded. The sharp drop in the distribution around $\cos\Theta^* \sim 0.8$ is due to the finite detector acceptance.

Let us turn to the gluon spin. Hard gluon radiation leads to three-jet events. So, after applying a jet algorithm to select the three-jet events, how do we know which one is the gluon jet? Recall that the probability to radiate off a soft gluon is larger than to radiate off a hard gluon. Therefore, for three jets



with energies

$$E_i = E_{CM} \frac{\sin \theta_i}{\sum_j \sin \theta_j},$$

if ordered by energy, $E_1 > E_2 > E_3$, jet 3 is the gluon jet in 75% of the events. Defining the variable

$$Z = \frac{1}{\sqrt{3}}(x_2 - x_3)$$

(recall $x_i = 2E_i/E_{CM}$), the Dalitz plot looks like in Fig. 8.20. The arrow length is proportional to the jet energy. The following cases have to be compared: In the spin-1 case (“vector gluon”) the prediction reads

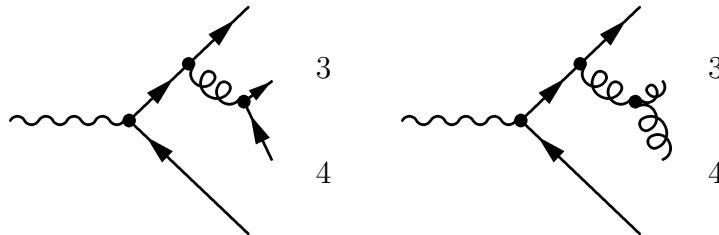
$$\frac{d^2\sigma^v}{dx_1 dx_2} \propto \left[\frac{x_1^2 + x_2^2}{(1-x_1)(1-x_2)} + \text{permutations } (1, 2, 3) \right]$$

while for spin-0 (“scalar gluon”)

$$\frac{d^2\sigma^s}{dx_1 dx_2} \propto \left[\frac{x_3^2}{(1-x_1)(1-x_2)} + \text{permutations } (1, 2, 3) - 10 \frac{\sum a_q^2}{\sum a_q^2 + v_q^2} \right]$$

where a_q and v_q are the axial-vector and vector couplings of the quarks to the intermediate photon or Z boson and the sums run over all contributing quark flavors. For e^+e^- annihilation via a photon only the vector coupling contributes, on the Z resonance both terms have to be taken into account. The ALEPH data shown in Fig. 8.19(b) clearly indicate that gluons have spin 1.

As we have seen before (see p. 144), the kinematic term of the QCD ($SU(3)$, non-abelian, gluon) Lagrangian contains a three-gluon term yielding a three-gluon vertex, a feature not present in QED ($U(1)$, abelian, photon). The splitting of a radiated gluon into two gluons will lead to a four-jet event, just like the splitting into a quark-antiquark pair:



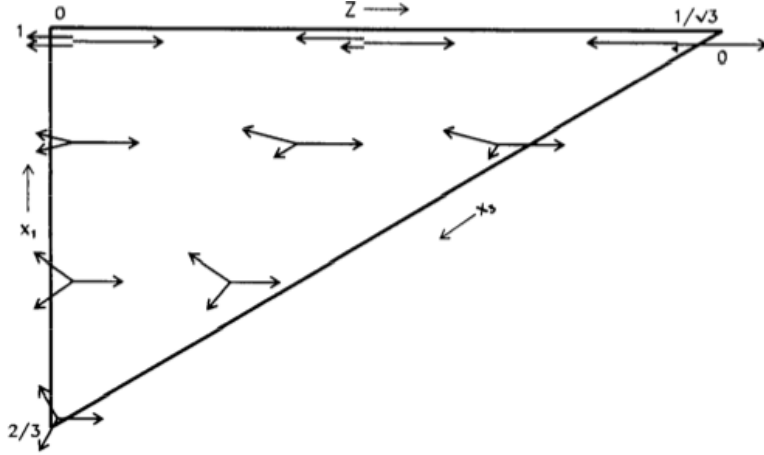


Figure 8.20: Phase space as function of x_1 and Z for energy-ordered jet configurations, $x_1 > x_2 > x_3$. The arrow length is proportional to the energy. Source: [47].

For gluon radiation off quarks one finds that the gluon is preferentially polarized in the plane of the splitting process. On the other hand, for a gluon splitting into two gluons there is a positive correlation between the plane spanned by the two new gluons and the polarization of the branching one. Finally, in case a gluon splits into two quarks, the plane defined by the momenta of the two quarks is anticorrelated with the polarization of the splitting gluon. So we conclude that for four-jet events induced by a gluon splitting into a $q\bar{q}$ pair, the distribution of the angle between the plane defined by the two primary quarks and the plane defined by the two secondary quarks should be enhanced around 90° (see Fig. 8.21). However, in a non-abelian theory we have contributions also from the triple-gluon interaction, and in this case the favored angle between the two planes spanned by the primary and secondary partons is rather small. Therefore, the shape of the distribution of this angle is sensitive to the color factors (see Sect. 7.4.1). Like in the three-jet case, it is difficult to distinguish between jets induced by the primary and the secondary partons. However, because of the $1/E$ characteristic of radiated gluons we expect the two secondary particles to be less energetic than the two primary quarks: If the jets are ordered by energy, $E_1 > E_2 > E_3 > E_4$, jets 3 and 4 are more likely to come from the radiated particles. So we arrive at the definition of the angular correlation variable called Bengtsson-Zerwas angle

$$\chi_{\text{BZ}} = \angle[(\vec{p}_1 \times \vec{p}_2), (\vec{p}_3 \times \vec{p}_4)] = \frac{(\vec{p}_1 \times \vec{p}_2) \cdot (\vec{p}_3 \times \vec{p}_4)}{|(\vec{p}_1 \times \vec{p}_2)| |(\vec{p}_3 \times \vec{p}_4)|}$$

where \vec{p}_i , $i = 1, \dots, 4$ are the energy-ordered momenta of the four partons (jets). In Fig. 8.21 LEP measurements of χ_{BZ} are compared with the predictions by QCD on the one hand and an abelian model with three quark colors but no three-gluon coupling on the other. The data agree with QCD being an $SU(3)$ gauge theory rather than an abelian gauge theory.

At the end of our discussion of jet algorithms Fig. 8.12(a) is shown. It displays the fraction

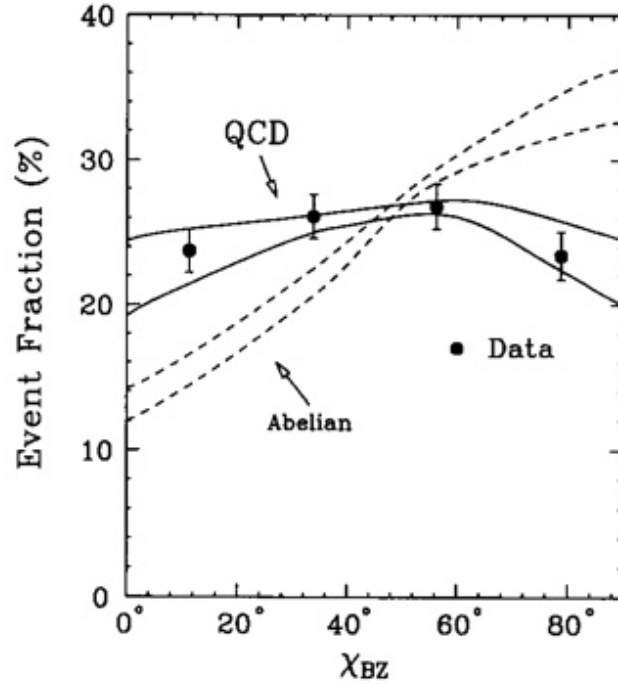


Figure 8.21: *Distribution of χ_{BZ} measured by L3.* The predictions for QCD and the abelian model are shown as bands indicating the theoretical uncertainties. Source: [48, p. 233].

of 2-jet events with 2, 3, 4, and 5 sub-jets as a function of y_{cut} . These predictions can be tested comparing measurements at highest LEP energies to Monte Carlo simulations which incorporate leading-order matrix elements for two-jet and three-jet production, plus approximations for multiple soft or collinear gluon radiation. Fig. 8.22 shows the n -jet rate according to the DURHAM (k_t) algorithm as a function of y_{cut} .

We conclude this section with a discussion of the differences between quark and gluon jets. Quark and gluon jets have different coupling strengths to emit gluons (see Sect. 7.4.1 and Fig. 8.23). Therefore, from couplings alone one expects a larger multiplicity in gluon jets of the order $C_A/C_F = 9/4$, and a softening of the momentum distributions for particles coming from the gluon jet. Thus gluon jets are more “soft” and “fat” than quark jets (see Fig. 8.24). Also the scaling violations, i.e. change of multiplicities with energy and momentum scale are different. In Fig. 8.24(d) the CONE algorithm is applied to data of OPAL (LEP) and compared to CDF data. The variable r denotes the radius of the considered cone fraction when R is the radius parameter of the cone algorithm:

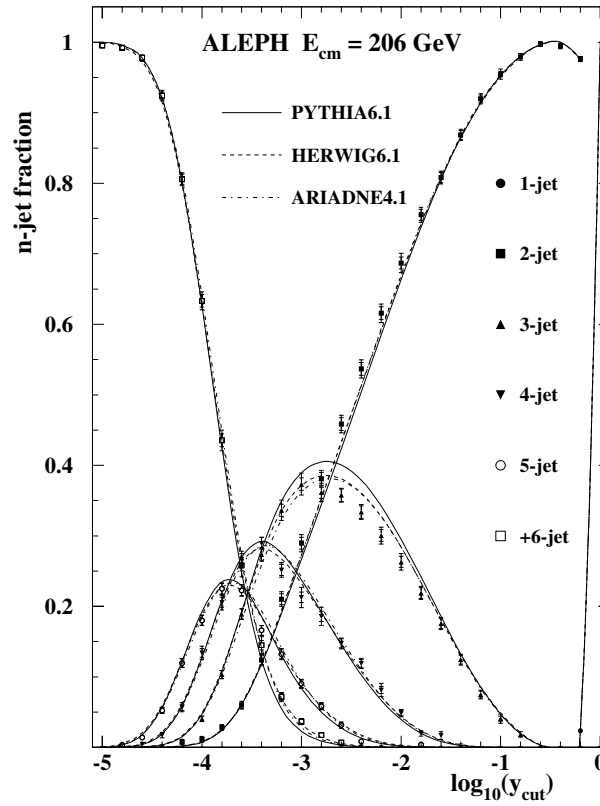


Figure 8.22: ALEPH measurements of the n -jet rate (DURHAM) as a function of y_{cut} .

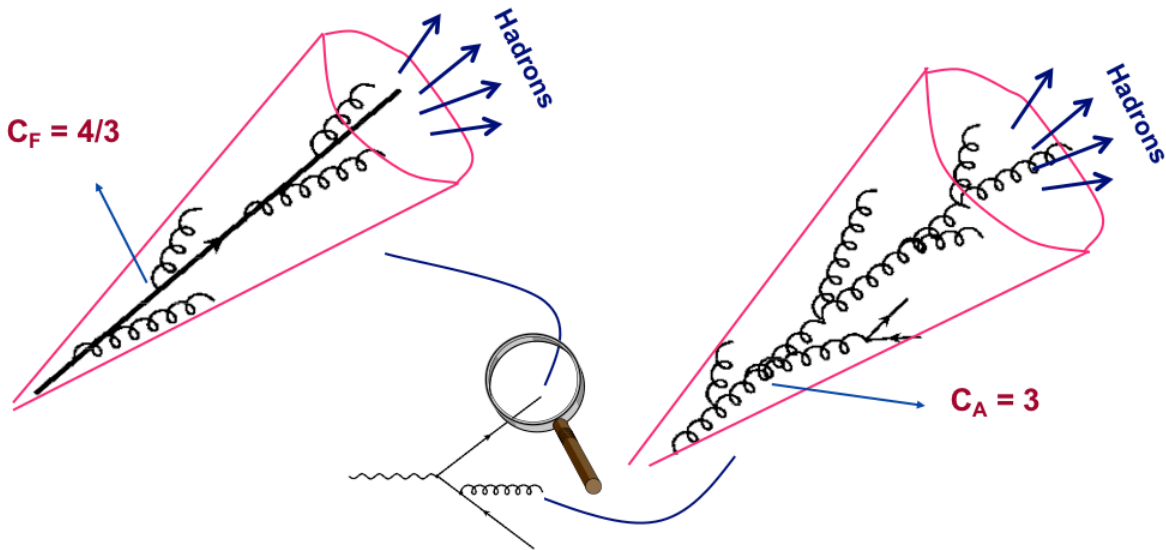
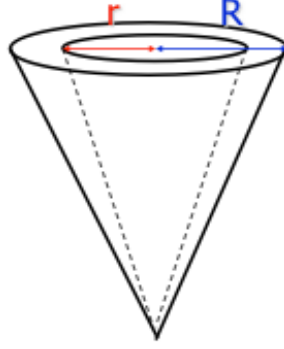


Figure 8.23: Comparison of quark and gluon jets. For a discussion of the difference in coupling strength see Sect. 7.4.1.



$\Psi(r)$ denotes the energy in a fraction of the cone and $\Phi(r)$ is defined by $\Phi(r) = d/dr \Psi(r)$.

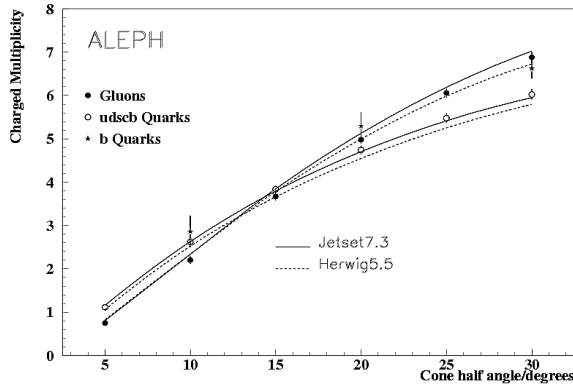
8.3 Measurements of the strong coupling constant

The QCD Lagrangian is introduced in Sect. 7.4:

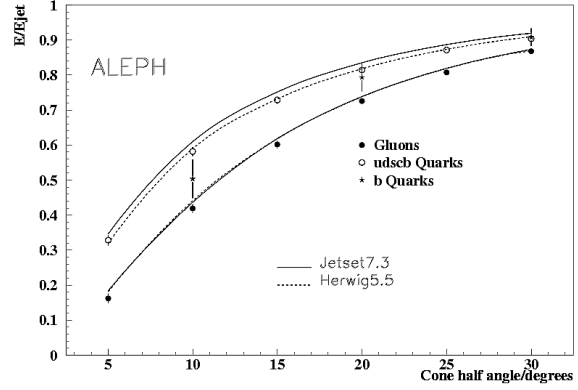
$$\begin{aligned}
 \mathbf{L}_{\text{QCD}} = & \left[\begin{array}{c} a \quad b \\ \text{---} \quad \text{---} \\ \delta_{ab} \end{array} + \begin{array}{c} b \\ \text{---} \quad \text{---} \\ a \quad c \end{array} + \begin{array}{c} a \quad b \\ \text{---} \quad \text{---} \\ c \quad d \end{array} \right] \\
 & \qquad \qquad \qquad g_s f^{abc} \qquad \qquad \qquad g_s^2 f^{abefcde} \\
 & + \sum_{\text{flavours}} \left[\begin{array}{c} i \quad j \\ \text{---} \quad \text{---} \\ \delta_{ij} \end{array} + \begin{array}{c} j \\ \text{---} \quad \text{---} \\ i \quad a \end{array} \right] \\
 & \qquad \qquad \qquad g_s T_{ij}^a
 \end{aligned}$$

Except for the quark masses, there is only one free parameter in it: the strong coupling constant α_s which is discussed in Sect. 7.4.2. Recall that the differential equation for the strong coupling constant depending on the renormalization scale μ , $\alpha_s(\mu^2)$, is

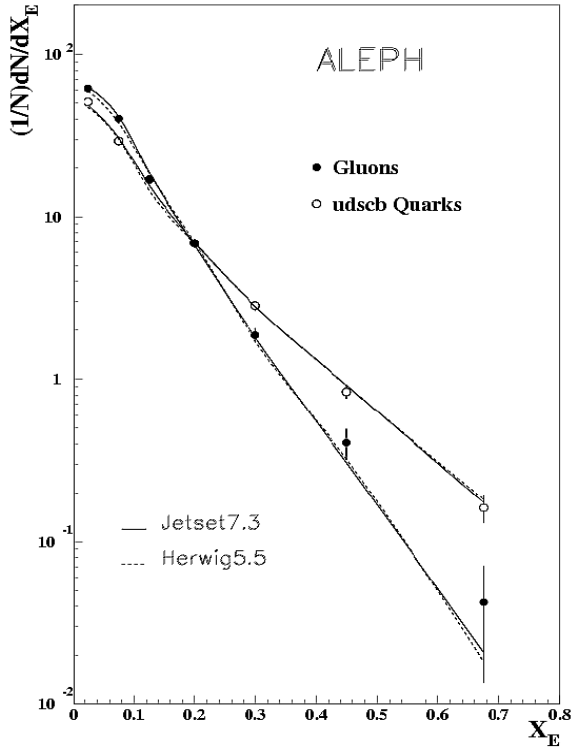
$$\mu^2 \frac{\partial \alpha_s^2(\mu^2)}{\partial \mu^2} = \beta(\alpha_s(\mu^2))$$



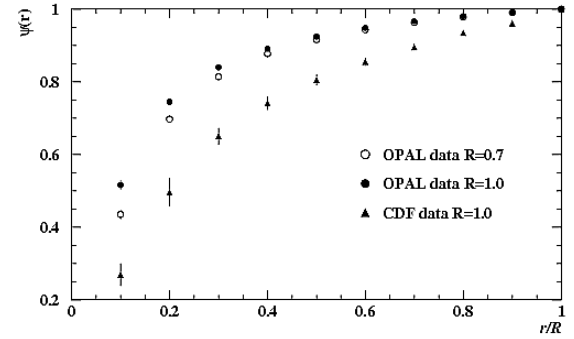
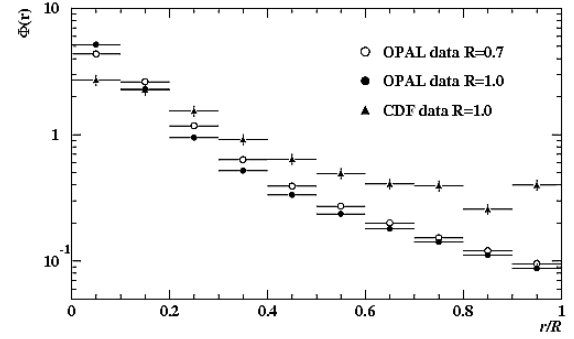
(a)



(b)



(c)



(d)

Figure 8.24: *Comparison of quark and gluon jets.* Note that gluon jets are more “soft” and “fat” than quark jets. The variable x_E is the energy fraction of the particles with respect to the jet energy (c). The variable r in (d) denotes the considered fraction of the cone.

which, retaining only the first term of the power expansion for β and absorbing the factor of 4π into the coefficient β_0 , yields

$$\alpha_s(Q^2) \equiv \frac{g_s^2(Q^2)}{4\pi} = \frac{1}{\beta_0 \ln(Q^2/\Lambda_{\text{QCD}}^2)}.$$

At that point we also stressed that

$$\beta_0 = \frac{1}{4\pi} \left(11 - \frac{2}{3}n_f \right) > 0 \text{ for (the likely case of) } n_f < 17$$

which makes the effective coupling constant behave like shown in Fig. 7.4.2. The following expansion holds for $\alpha_s(\mu^2)$ (see Eq. (7.43)):

$$\boxed{\alpha_s(\mu^2) \approx \alpha_s(Q^2) \left[1 - \alpha_s(Q^2)\beta_0 \ln \frac{\mu^2}{Q^2} + \alpha_s^2(Q^2)\beta_0^2 \ln^2 \frac{\mu^2}{Q^2} + \mathcal{O}(\alpha_s^3) \right]}. \quad (8.11)$$

To measure the coupling strength one uses as many methods as possible in order to demonstrate that QCD really is the correct theory of strong interactions by showing that one universal coupling constant describes all strong interactions phenomena. Consider the perturbative expansion of the cross section for some QCD process:

$$\sigma^{\text{pert}} = \alpha_s(\mu^2)A + \alpha_s^2(\mu^2) \left[B + \beta_0 A \ln \frac{\mu^2}{Q^2} \right] + \mathcal{O}(\alpha_s^3) \quad (8.12)$$

where the coefficients A and B depend on the specific process. So, if only the leading order (LO) expansion is known, the following holds:

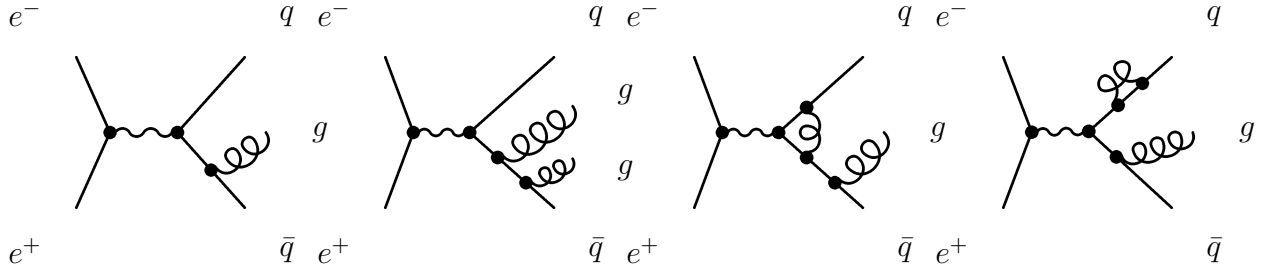
$$\sigma_{\text{LO}}^{\text{pert}} = \alpha_s(\mu^2)A = \alpha_s(Q^2)A - \alpha_s^2(Q^2)\beta_0 A \ln \frac{\mu^2}{Q^2} + \mathcal{O}(\alpha_s^2)$$

where in the second step we inserted the expansion from Eq. (8.11). This means that the result depends strongly on the choice of the renormalization scale μ . Since the corrections to the cross section can be relatively large, it is possible to find significantly different values for the measured effective coupling constant $\alpha_s^{\text{meas,eff}}$ for two different processes: Consider two processes, where the LO calculations predict

$$\begin{aligned} \sigma_{\text{LO};1}^{\text{pert}} &= \alpha_s A_1 \\ \sigma_{\text{LO};2}^{\text{pert}} &= \alpha_s A_2. \end{aligned}$$

The predictions are compared to the cross sections σ_1^{exp} and σ_2^{exp} from experiment. Finally, because of the said strong scale dependence, the result may be $\alpha_{s;1}^{\text{meas,eff}} \neq \alpha_{s;1}^{\text{meas,eff}}$.

To solve the problem of the correction depending on the renormalization scale being too large, one has to take the calculation to next-to-leading order (NLO) to reduce the scale dependence of the prediction. For our example reaction $e^+e^- \rightarrow q\bar{q}g$ this means

Figure 8.25: *Feynman diagrams for $e^+e^- \rightarrow q\bar{q}g$ to NLO.*

considering the diagrams shown in Fig. 8.25. The NLO expression is again obtained from the expansion in Eq. (8.12):

$$\begin{aligned}\sigma_{\text{NLO}}^{\text{pert}} &= \alpha_s(\mu^2)A + \alpha_s^2(\mu^2) \left[B + \beta_0 A \ln \frac{\mu^2}{Q^2} \right] + \mathcal{O}(\alpha_s^3) \\ &= \alpha_s(Q^2)A + \alpha_s^2(Q^2)B + \alpha_s^3(Q^2)\beta_0^2 A^2 \ln^2 \frac{\mu^2}{Q^2} + \mathcal{O}(\alpha_s^4)\end{aligned}$$

where in the second line we inserted for $\alpha_s(\mu^2)$ the expansion from Eq. (8.11) and the dependence on $\ln(\mu^2/Q^2)$ cancels. Thus, the scale dependence of the prediction is much smaller than in the LO case. The scale dependence cancels completely at fully calculated order.

By comparing the NLO prediction for the cross section to experiment, one can extract $\alpha_s(Q^2)$, e. g. $\alpha_s(M_Z^2)$. This information can in turn be used to predict other process cross sections at NLO. Furthermore, by varying the scale μ^2 one can estimate the size of the NNLO contributions.

This procedure extends analogously to NNLO. Diagrams that have to be included at NNLO are shown in Fig. 8.26. The prediction reads

$$\sigma_{\text{NNLO}}^{\text{pert}} = \alpha_s(Q^2)A + \alpha_s^2(Q^2)B + \alpha_s^3(Q^2)C + \mathcal{O}\left(\alpha_s^4, \ln^3 \frac{\mu^2}{Q^2}\right)$$

where the scale dependence is reduced even further. NNLO is the lowest order at which scale variations at NLO can be tested.

As an example for the scale dependence of the extracted strong coupling constant, see Fig. 8.27 where $\alpha_s(M_Z^2)$ from jet rates at LEP is shown as a function of $\ln(\mu^2/Q^2)$. Note that the scale dependence is reduced by the extension to NLO, as mentioned before. The theoretical error is taken to be the range of values covered by the projection of the bands over $-1 < \ln(\mu^2/Q^2) < 1$ on the abscissa. The right figure shows how the central values and errors obtained this way for three different shape variables converge with improvements in the theory.

There has been an enormous progress in the measurements of the strong coupling during the last 20 years. This is due to major improvements on the theoretical and also the

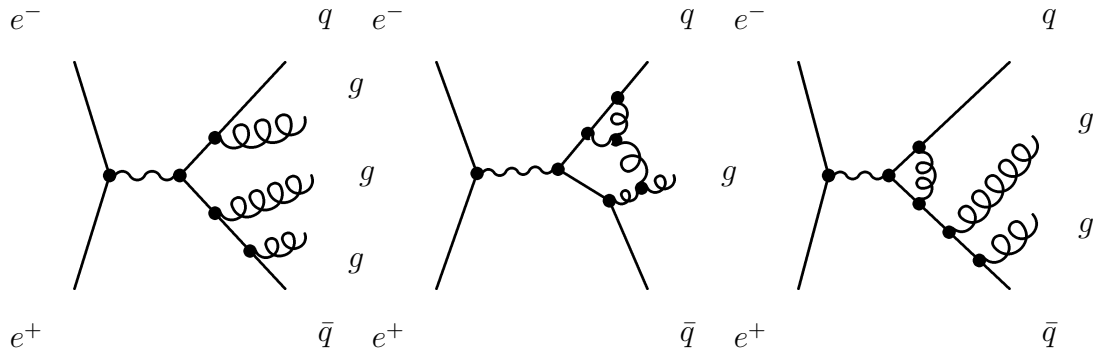
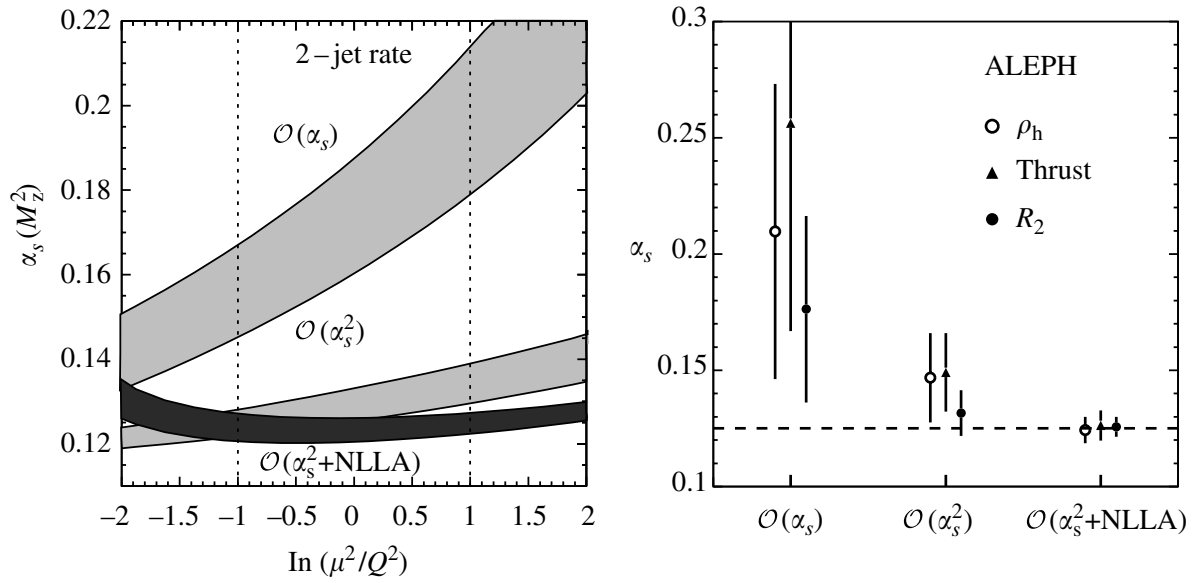
Figure 8.26: *Feynman diagrams for $e^+e^- \rightarrow q\bar{q}g$ at NNLO.*

Figure 8.27: *Estimate of theoretical uncertainties for a measurement of the strong coupling constant from event shape variables. NLLA refers to resummation of logarithms. Source: [27, p. 307].*

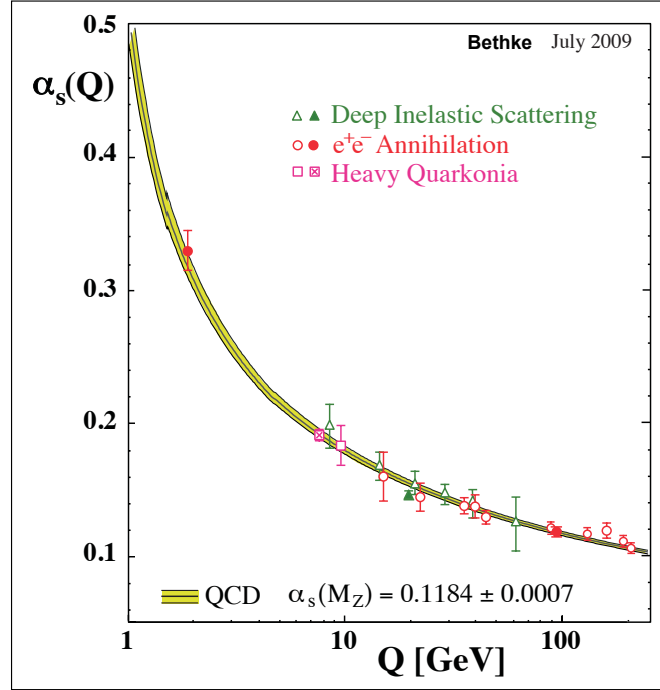


Figure 8.28: Summary of measurements of α_s as a function of the respective energy scale Q . The curves are QCD predictions. Source: [30, p. 12].

experimental side. A summary of measurements of α_s as a function of the respective energy scale Q is shown in Fig. 8.28.

In general, observables can be classified according to the influence the structure of the final state has on their value.

Inclusive observables do not look at the structure of the final state. Examples are total cross sections and ratios of cross sections (see e.g. Eq. (8.3)). Advantages of inclusive observables are that they do not (or only weakly) depend on non-perturbative corrections (hadronization) and that the perturbative series is now known to NNNLO. The disadvantage lies in the low sensitivity in some cases.

Non-inclusive (exclusive) observables, on the other hand, look at some structure in the final state depending on the momenta of the final state particles. Examples are jet rates and event shape distributions. Advantages of non-inclusive observables are high sensitivity and that the perturbative series is now known to NNLO (and resummation, see later). Disadvantages are that in some cases even the NNNLO corrections might be relevant and that hadronization (non-perturbative) corrections are needed.

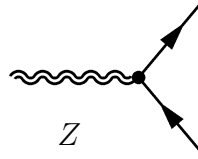
As an example for the usage of inclusive observables, consider the determination of α_s from inclusive Z or τ decays. In general, the prediction of the cross section ratio R reads

$$R = \frac{\sigma_{Z,\tau \rightarrow \text{hadrons}}}{\sigma_{Z,\tau \rightarrow \text{leptons}}} = R_{\text{EW}}(1 + \delta_{\text{QCD}} + \delta_{\text{mass}} + \delta_{\text{np}})$$

where the overall factor R_{EW} depends on the electroweak couplings of the quarks.⁵ The corrections are dominated by the perturbative QCD correction δ_{QCD} . The other terms take into account the finite quark masses and the non-perturbative corrections. The perturbative QCD correction term is given by

$$\delta_{QCD} = c_1 \frac{\alpha_s}{\pi} + c_2 \left(\frac{\alpha_s}{\pi} \right)^2 + c_3 \left(\frac{\alpha_s}{\pi} \right)^3 + \dots$$

Diagrammatically speaking, the factor R_{EW} arises from



while the perturbative QCD corrections come from diagrams like in Fig. 8.25 and 8.26. For the case of

$$R_Z = \frac{\sigma^{Z \rightarrow \text{hadrons}}}{\sigma^{Z \rightarrow \text{leptons}}}$$

the prediction reads $R_{EW} = 19.934$, $c_1 = 1.045$, $c_2 = 0.94$, and $c_3 = -15$. The corresponding measurement is visualized in Fig. 8.29: Divide the number of hadronic decays by the number of leptonic decays to find $R_Z = 20.767 \pm 0.025$. From this ratio the following value of the strong coupling at the Z resonance can be extracted:

$$\begin{aligned} \alpha_s(M_Z) &= 0.1226 \pm \underbrace{0.0038}_{\text{exp., mostly statistical}} \pm \underbrace{0.0002}_{M_t: \pm 5 \text{ GeV}} \pm \underbrace{0.0002}_{\text{renormalization schemes}} \\ &= 0.1226 \begin{matrix} +0.0058 \\ -0.0038 \end{matrix} . \end{aligned}$$

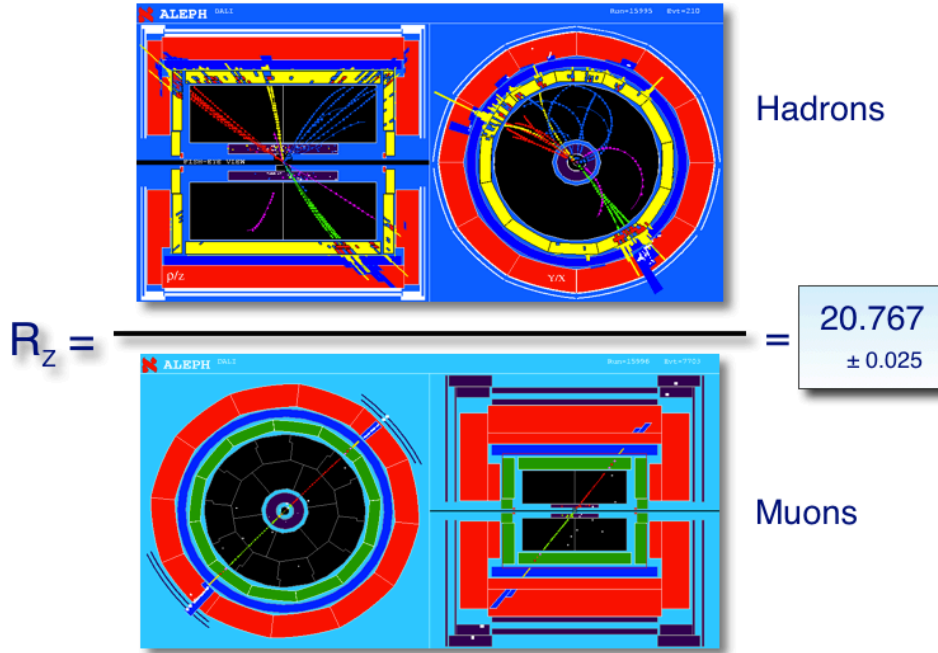
Finally, we state a new result from 2009, obtained using NNNLO predictions:

$$\alpha_s(M_Z) = 0.1193 \begin{matrix} +0.0028 \\ -0.0027 \end{matrix} \pm 0.0005.$$

We now turn to non-inclusive observables such as event-shapes and jet rates. We have already seen perturbative predictions for some examples of non-inclusive quantities in Sect. 8.2. There it is stated that the log terms in the predictions are because of the $\int dE/E$ integration arising from

$$\frac{d\sigma^{q \rightarrow qg}}{dE_{\text{gluon}}} \propto \sigma_0 \frac{\alpha_s}{2\pi} \frac{1}{E_{\text{gluon}}}$$

⁵ R_{EW} is a modified version of the ratio $R = N_c 11/9$ of Sect. 8.1.

Figure 8.29: Visualization of R_Z measurement.

where σ_0 is the Born cross section for $Z \rightarrow q\bar{q}$ (see Sect. 8.1). Recall that the perturbative prediction is given by:

$$\frac{1}{\sigma_0} \frac{d\sigma}{dx} = \alpha_s(\mu^2) A(x) + \alpha_s^2(\mu^2) \left[B(x) + \beta_0 A(x) \ln \frac{\mu^2}{Q^2} \right] + \mathcal{O}(\alpha_s^3)$$

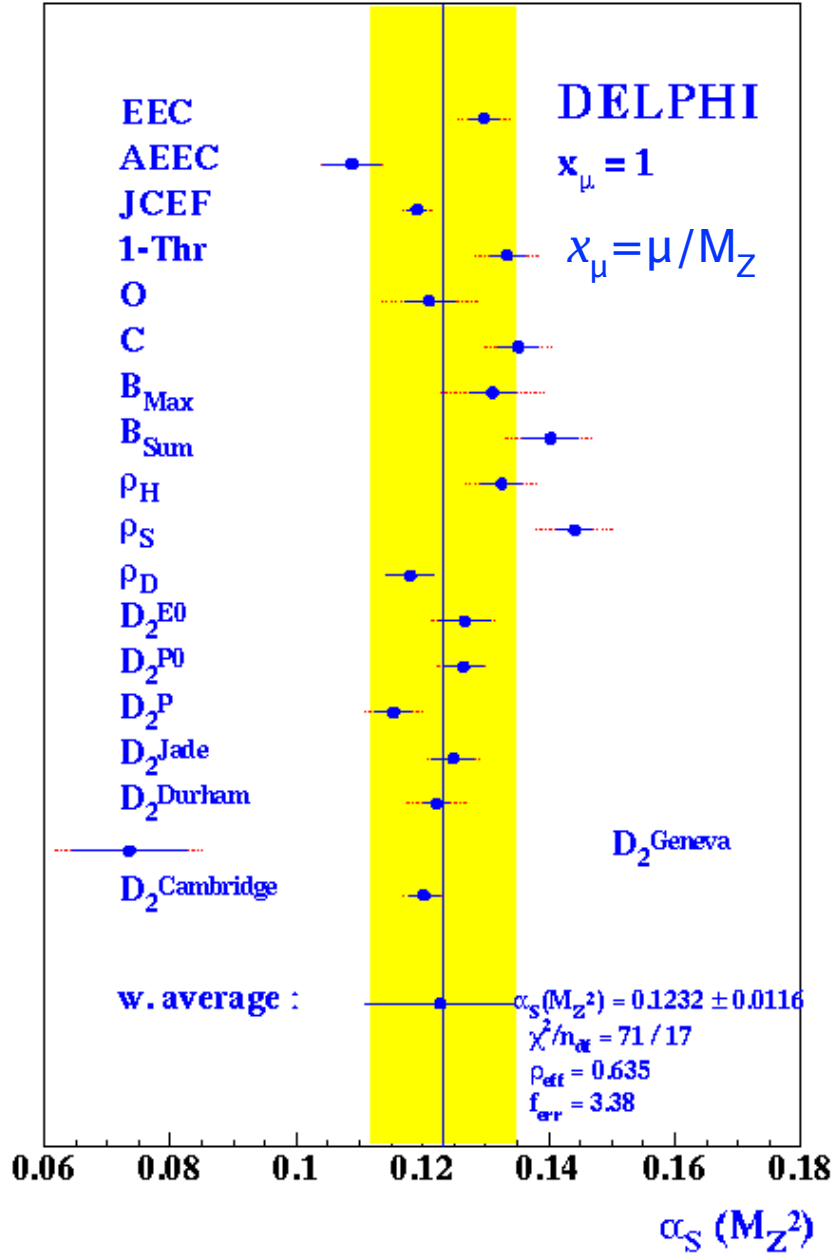
where the coefficients A and B are calculable for the class of observables x which are infrared and collinear safe, i.e. infrared singularities from real and virtual radiative corrections cancel (thrust, jet rates, C-parameter, etc.). To recall the important example of thrust, see Fig. 8.15.

Let us take a look at the results obtained by NLO fits. First measurements gave indications that the missing higher order terms are large: The coupling constant should be the same for all variables, but the results vary too much (see Fig. 8.30) which indicates that the expansion to NLO does not suffice. Typical results obtained by NLO fits are

$$\alpha_s(M_Z) = 0.120 \pm 0.010.$$

As we have seen before, to obtain perturbative corrections, we have to do integrals of the type $\int_{y_{\text{cut}}}^s dE_{\text{gluon}}/E_{\text{gluon}}$ which gives rise to the logarithm terms in $\sigma_{\text{three-jet}}^{LO}$ (see Eq. (8.10)):

$$\sigma_{\text{three-jet}}^{LO} = \sigma_0 C_F \frac{\alpha_s}{2\pi} [\ln^2 y_{\text{cut}} + \dots]$$

Figure 8.30: *NLO results for $\alpha_s(M_Z)$.* Source: [40, p. 29, modified].

where the color factor $C_F = 4/3$ —the problem being that for $y_{\text{cut}} \rightarrow 0$ the series does not converge.⁶ The resummation procedure mentioned earlier (see p. 165) also works for the three-jet rate:

$$\begin{aligned} R_3 &= \frac{C_F \alpha_s}{2\pi} \ln^2 y_{\text{cut}} - \frac{C_F^2 \alpha_s^2}{8\pi^2} \ln^4 y_{\text{cut}} + \dots \\ &= 1 - \exp \left\{ - \int_{sy_{\text{cut}}}^s \frac{dq^2}{q^2} \frac{C_F \alpha_s(q^2)}{2\pi} \left[\ln \frac{s}{q^2} - \frac{3}{2} \right] \right\}. \end{aligned}$$

Combined (to avoid double counting of logarithmic terms in resummed expressions and in full fixed order prediction) with full NLO calculations this gives theoretically much improved predictions. Typical results are:

$$\alpha_s(M_Z) = 0.120 \pm 0.005.$$

There are different sources of the remaining uncertainties. *Experimental uncertainties* include

- track reconstruction,
- event selection,
- detector corrections (via cut variations or different Monte Carlo generators),
- background subtraction (LEP2), and
- ISR corrections (LEP2).

They amount to about 1% uncertainty. Furthermore, there are *hadronization uncertainties* arising from the differences in behavior of various models for hadronization such as PYTHIA (string fragmentation), HERWIG (cluster fragmentation), or ARIADNE (dipole model and string fragmentation). These uncertainties are typically about 0.7 to 1.5%. Finally, there are also *theoretical uncertainties*, for instance

- renormalization scale variation,
- matching of NLO with resummed calculation, and
- quark mass effects.

⁶Recall that y_{cut} is the resolution parameter deciding if two particles are distinguished or seen as one pseudo-particle.

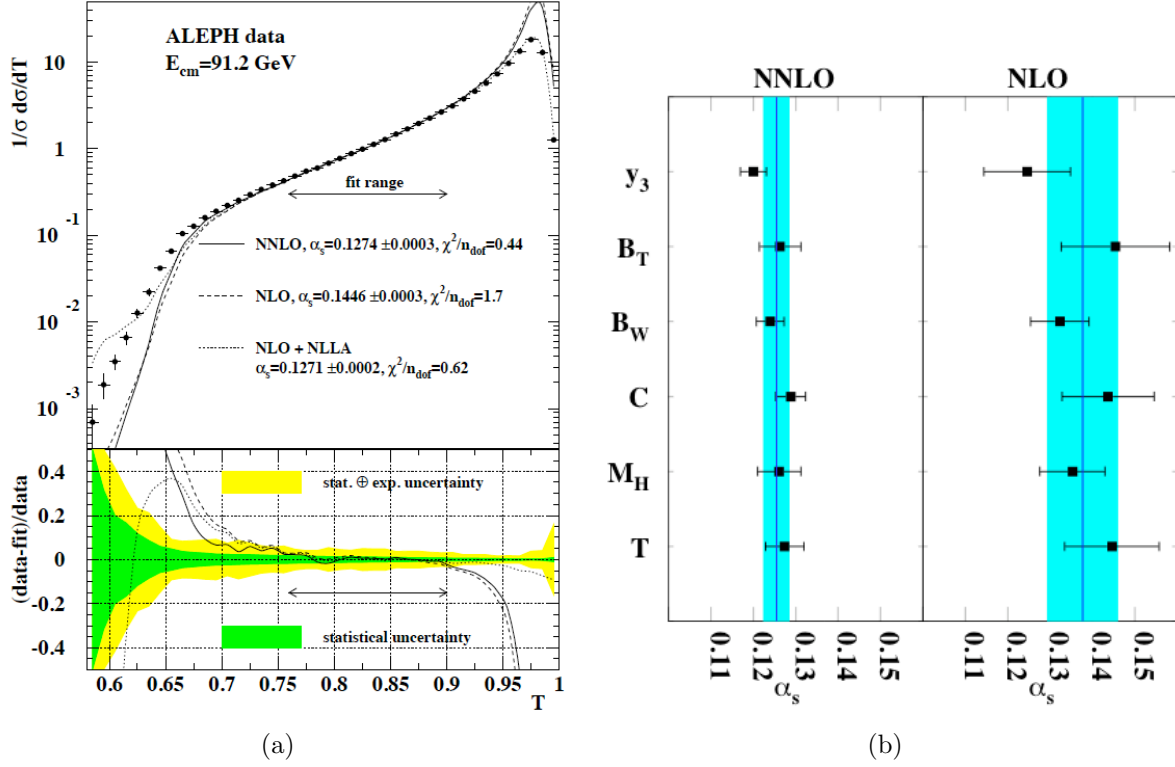


Figure 8.31: NNLO fit to ALEPH thrust data (a) and visualization of improvement in NNLO over NLO (b). Source: [50, p. 11 and 17].

The corresponding uncertainty is typically 3.5 to 5 %.

As we have seen, the perturbative predictions have to be to sufficiently high order if we are to accurately determine the strong coupling constant: Now a NNLO prediction is available. Bearing in mind the foregoing, it has to be of the form

$$\frac{1}{\sigma_0} \frac{d\sigma}{dy}(y, Q, \mu) = \alpha_s(\mu)A(y) + \alpha_s^2(\mu)B(y, x_\mu) + \alpha_s^3(\mu)C(y, x_\mu) + \mathcal{O}(\alpha_s^4)$$

where y denotes an event shape variable and $x_\mu = \mu/Q$. At this level of precision, one has to take care of additional issues, such as quark mass effects and electro-weak effects which typically contribute around or below the per-cent range.

The first determination of $\alpha_s(M_Z)$ based on NNLO (and NLLA) calculations of event shape distributions [49, 50] yields

$$\alpha_s(M_Z) = 0.1224 \pm 0.0009 \text{ (stat)} \pm 0.0009 \text{ (exp)} \pm 0.0012 \text{ (hadr)} \pm 0.0035 \text{ (theo)}.$$

The fit to ALEPH thrust data is shown in Fig.8.31(a). The largely reduced scatter of values for different variables at NNLO is visualized in Fig.8.31(b). Note that the reduced perturbative uncertainty is 0.003.

The most precise determination of the strong coupling constant is obtained from jet observables at LEP. Precision at the 2% level is achieved from the three-jet rate [51]:

$$\alpha_s(M_Z) = 0.1175 \pm 0.0020 \text{ (exp)} \pm 0.0015 \text{ (theo)}.$$

The three-jet rate is known to have small non-perturbative corrections and to be very stable under scale variations (for a certain range of the jet resolution parameter). For a comparison of LO, NLO, and NNLO predictions to the corresponding ALEPH data, see Fig. 8.32(a).

The LEP results concerning the determination of the strong coupling constant (see Fig. 8.32(b)) can be summarized as follows (combination by S. Bethke, a couple of years ago).

- Tau decays (NNLO)

$$\alpha_s(M_Z) = 0.1181 \pm 0.0030$$

- R_Z (NNLO)

$$\alpha_s(M_Z) = 0.1226^{+0.0058}_{-0.0038}$$

- Event shapes (NLO + NNLO)

$$\alpha_s(M_Z) = 0.1202 \pm 0.0050$$

- All (not including recent NNNLO results)

$$\alpha_s(M_Z) = 0.1195 \pm 0.0035$$

- Latest world average (S. Bethke, 2009 [30])

$$\boxed{\alpha_s(M_Z) = 0.1184 \pm 0.0007}$$

8.4 Measurements of the QCD color factors

Because they determine the gauge structure of strong interactions, the color factors are the most important numbers in QCD, besides α_s . Discussing the triple-gluon vertex we concluded that our observables also allow to test the gauge structure of QCD. We have already learned that the color factors (for $SU(3)$) $C_F = 4/3$, $C_A = 3$, and $T_F = 1/2$ measure the relative probabilities of gluon radiation ($q \rightarrow qg$), triple gluon vertex ($g \rightarrow gg$), and gluon splitting ($g \rightarrow q\bar{q}$).

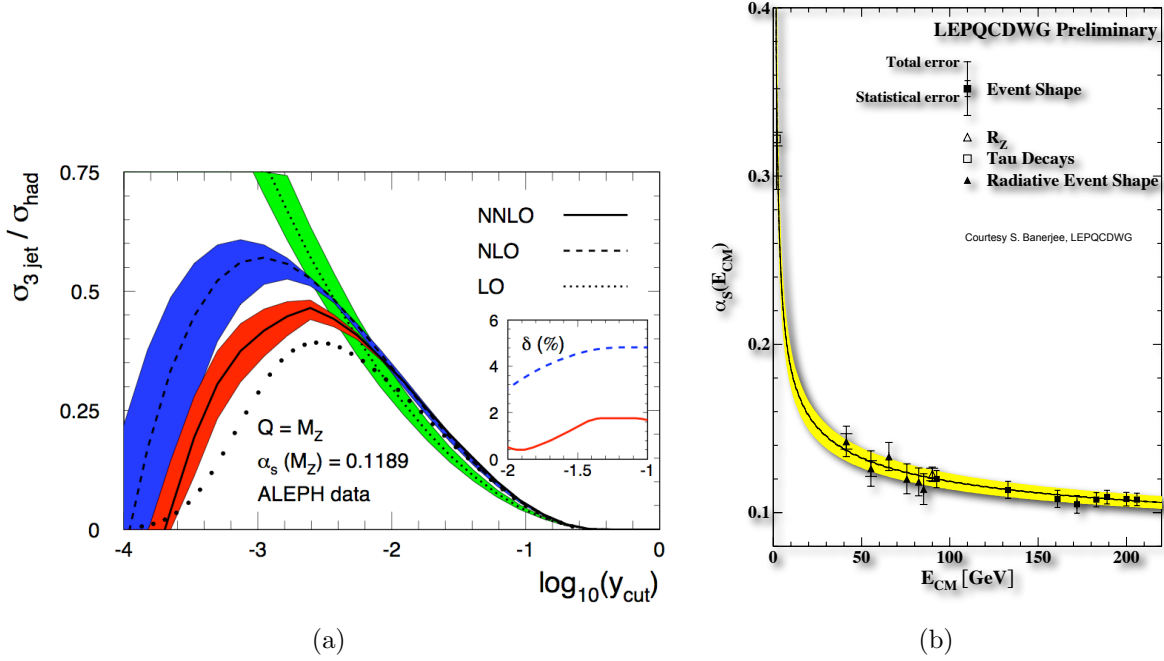


Figure 8.32: NNLO, NLO, and LO fits to ALEPH data for the three-jet rate (a) and summary of LEP results for α_s (b).

The cross section prediction for four-jet events at order α_s^2 can be shown to be

$$\frac{1}{\sigma_0} \frac{d\sigma_{\text{four-jet}}}{dy} = \frac{\alpha_s^2 C_F^2}{\pi^2} \left[\sigma_A(y) + \left(1 - \frac{1}{2} \frac{C_A}{C_F} \right) \sigma_B(y) + \left(\frac{C_A}{C_F} \right) \sigma_C(y) + \left(\frac{T_F}{C_F} n_f \right) \sigma_D(y) + \left(1 - \frac{1}{2} \frac{C_A}{C_F} \right) \sigma_E(y) \right]$$

where σ_i , $i = A, \dots, E$ are kinematic factors independent of the gauge group of QCD.

The combined measurements of the QCD color factors are summarized in Fig. 8.33: Four-jet and event shape results have been combined accounting for correlations between the measurements. In addition, constraints on C_A/C_F from differences between quark and gluon jets (see p. 177) are included. This yields

$$C_A = 2.89 \pm 0.21$$

$$C_F = 1.30 \pm 0.09$$

which is precise to 7% and agrees with the $SU(3)$ values of $C_A = 3$ and $C_F = 1.33$.

8.5 Hadronization

The trouble with hadronization is that perturbative calculations are no longer useful since α_s ceases to be comparatively small at length scales of about the proton radius.

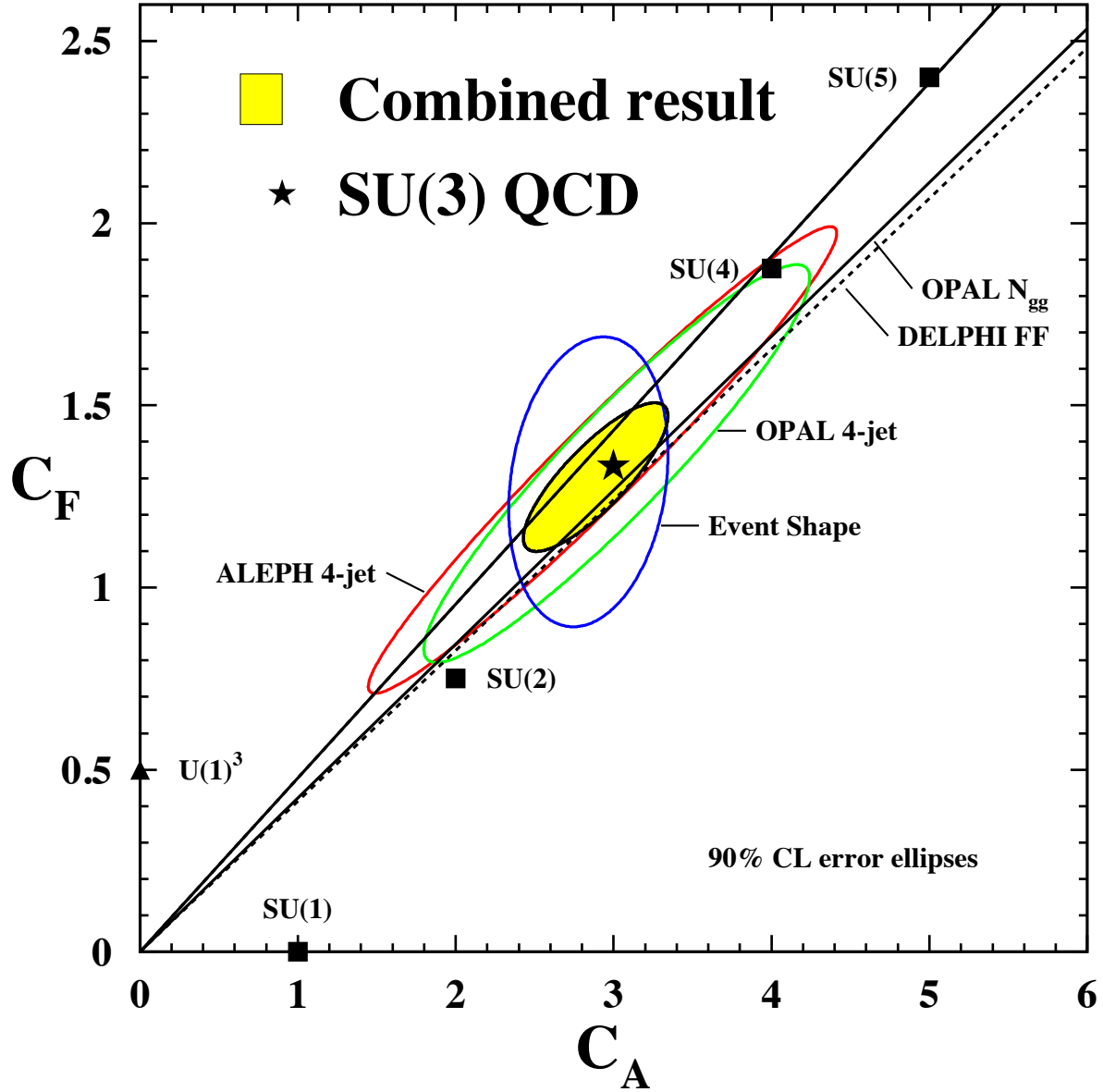


Figure 8.33: Combined measurements of the color factors C_A and C_F . The ellipses show the correlated measurements using four-jet events or event shape distributions while the lines represent the results of determinations of C_A/C_F from DELPHI (dashed) and OPAL (solid). Source: [52, p. 82].

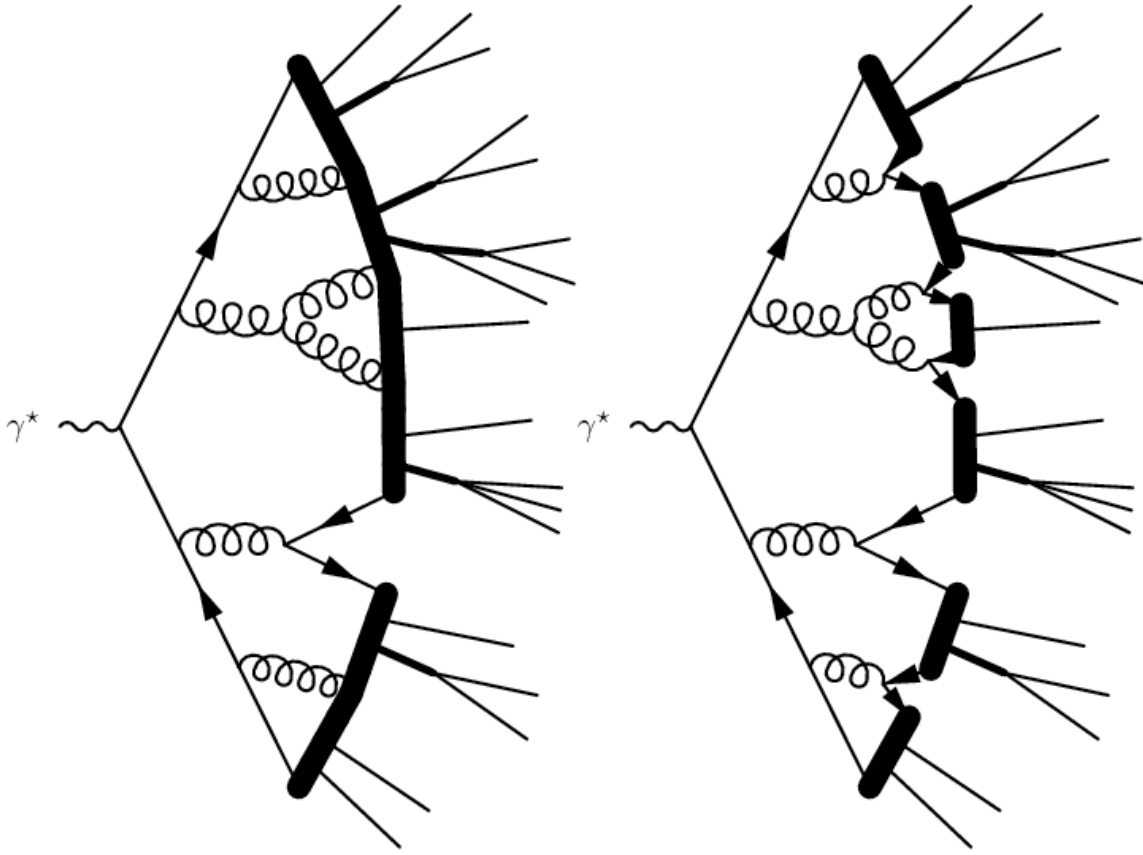
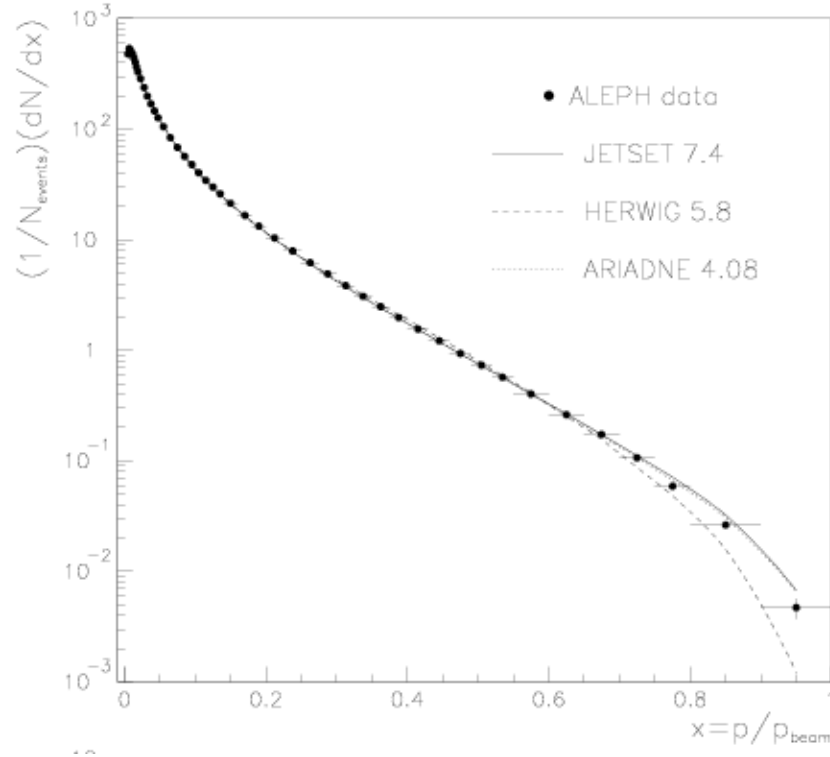


Figure 8.34: *Visualization of phenomenological models of hadronization.* (LHS) string fragmentation: JETSET/PYTHIA; (RHS) Cluster fragmentation: HERWIG. Source: [27, p. 164]

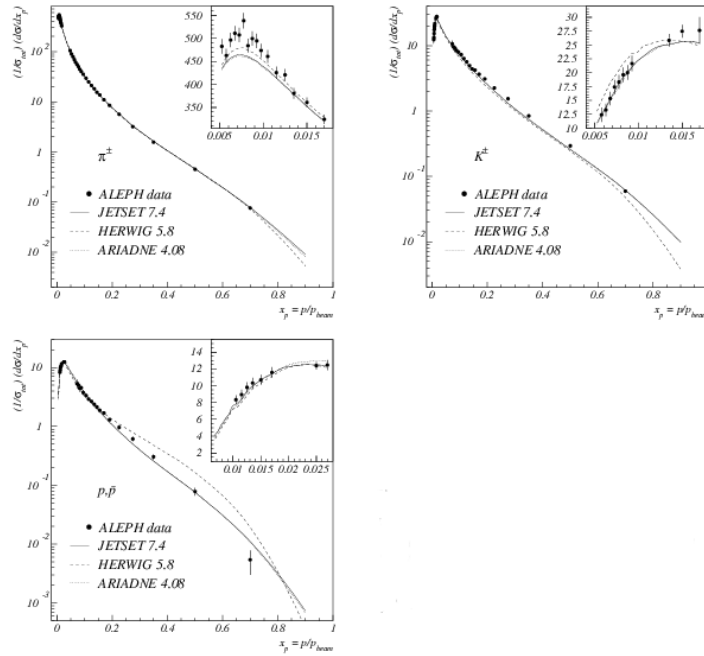
Perturbative QCD is applicable to the transition from the primary partons to a set of final state partons. This is pictured as a cascading process that is dominated by the collinear and soft emissions of gluons and mainly light quark-antiquark pairs. By contrast, phenomenological models are used to describe the non-perturbative transition from these final state partons to hadrons which then may decay according to further models (recall Fig. 8.6).

The parameters determining the behavior of the numerical models have to be adjusted using experimental data. Hadronization can be modeled by string fragmentation (JETSET/PYTHIA) or cluster fragmentation (HERWIG). For a visualization of this difference, see Fig. 8.34.

Fig. 8.35 shows comparisons of simulations to ALEPH data for hadron momentum distributions of the final state: Fig. 8.35(a) shows simulation and data for an inclusive variable and Fig. 8.35(b) deals with pions, kaons, and protons, respectively.



(a)



(b)

Figure 8.35: *Hadron momentum distributions, ALEPH data and simulation.* Inclusive measurement (a) and differential cross section for pions, kaons, and protons (b) compared with the predictions of JETSET, HERWIG, and ARIADNE. All observables are shown as functions of $x = p_{\text{hadron}}/p_{\text{beam}}$.

Bibliography

- [1] F. Halzen and A. Martin. *Quarks & Leptons*. Wiley, 1984.
- [2] I. Aitchison and A. Hey. *Gauge Theories in Particle Physics*. Taylor & Francis, 2002.
- [3] A. Seiden. *Particle Physics*. Addison Wesley, 2004.
- [4] O. Nachtmann. *Phänomene und Konzepte der Elementarteilchenphysik*. Vieweg, 1986.
- [5] R. Hagedorn. *Relativistic Kinematics*. W. A. Benjamin, 1963.
- [6] E. Byckling and K. Kajantie. *Particle Kinematics*. Wiley, 1973.
- [7] F. Hinterberger. *Physik der Teilchenbeschleuniger und Ionenoptik*. Springer, 2008.
- [8] C. Amsler. *Kern- und Teilchenphysik*. UTB, 2007.
- [9] <http://pdg.lbl.gov/2006/hadronic-xsections/hadron.html>.
- [10] <http://www-cdf.fnal.gov/physics/new/qcd/run2/ue/chgjet/etaphi.html>.
- [11] <http://en.wikipedia.org/wiki/Pseudorapidity>.
- [12] <http://www.phys.ufl.edu/~rfield/cdf/chgjet/dijet.eps>.
- [13] G. Arnison et al. *Physics Letters B*, Jan 1983.
- [14] M. E. Peskin and D. V. Schroeder. *An Introduction to Quantum Field Theory*. Westview, 1995.
- [15] E. Freitag and R. Busam. *Complex analysis*. Springer, 2005.
- [16] G. Gabrielse. Measurements of the electron magnetic moment. In B. L. Roberts and W. J. Marciano, editors, *Lepton Dipole Moments: The Search for Physics Beyond the Standard Model*, volume 20 of *Advanced Series on Directions in High Energy Physics*. World Scientific, 2009.
- [17] http://upload.wikimedia.org/wikipedia/commons/thumb/b/b6/penning_trap.svg/800px-penning_trap.svg.png.

- [18] L. D. Landau and E. M. Lifschitz. *Quantenmechanik*. Harri Deutsch, 1986.
- [19] G. Gabrielse. Determining the fine structure constant. In B. L. Roberts and W. J. Marciano, editors, *Lepton Dipole Moments: The Search for Physics Beyond the Standard Model*, volume 20 of *Advanced Series on Directions in High Energy Physics*. World Scientific, 2009.
- [20] R.P. Feynman. *QED: The strange theory of light and matter*. Princeton University Press, 1988.
- [21] A. Ali and P. Soeding. *High energy electron positron physics*. World Scientific, 1988.
- [22] P. Dittmann and V. Hepp. *Particles and Fields*, 10, 1981.
- [23] H. Lipkin. *Lie groups for pedestrians*. Dover, 2002.
- [24] J. M. Lee. *Introduction to smooth manifolds*. Springer, 2006.
- [25] V. Barnes et al. *Physical Review Letters*, Jan 1964.
- [26] Particle data group. <http://pdg.lbl.gov/>.
- [27] G. Dissertori, I. K. Knowles, and M. Schmelling. *Quantum Chromodynamics: High Energy Experiments and Theory*. Oxford University Press, 2nd edition, 2009.
- [28] R. K. Ellis, W. J. Stirling, and B. R. Webber. *QCD and Collider Physics*. Cambridge University Press, 1996.
- [29] S. Bethke. *arXiv:hep-ex/0606035*, 2007.
- [30] S. Bethke. *arXiv:0908:1135*, 2009.
- [31] JADE collaboration. *Phys. Lett. B*, 123:460, 1983.
- [32] Yu. L. Dokshitzer. *J. Phys. G*, 17:1537, 1991.
- [33] N. Brown and W. J. Stirling. *Phys. Lett. B*, 252:657, 1990.
- [34] Yu. L. Dokshitzer et al. *JHEP*, 9708:1, 1997.
- [35] M. Cacciari and G. P. Salam. *arXiv:0707.1378*, 2007.
- [36] G. P. Salam and G. Soyez. *JHEP*, 05:86, 2007.
- [37] M. Cacciari and G. P. Salam. *Phys. Lett. B*, 641:57, 2006.
- [38] B. Gary. CTEQ Summer School, Madison WI, June 26, 2009. <http://www.phys.psu.edu/~cteq/schools/summer09/talks/gary-cteq-madison-2009-talk.pdf>.

- [39] Wu-Ki Tung. Perturbative QCD and the parton structure of the nucleon. 2001.
- [40] S. Bethke. Eleven years of QCD at LEP. *EPJ direct*, 2002.
- [41] G. C. Blazey et al. Run II jet physics: Proceedings of the run II QCD and weak boson physics workshop. *arXiv:hep-ex/0005012*, 2000.
- [42] G. Hanson et al. SLAC-LBL Collaboration. *Phys. Rev. Lett.*, 35:1609, 1975.
- [43] TASSO Collaboration. *Phys. Lett. B*, 86(2):243, 1979.
- [44] MARK-J Collaboration. *Phys. Rev. Lett.*, 43(12):830, 1979.
- [45] PLUTO Collaboration. *Phys. Lett. B*, 86:418, 1979.
- [46] JADE collaboration. *Phys. Lett. B*, 91:142, 1980.
- [47] ALEPH Collaboration. *Phys. Rept.*, 294:1, 1998.
- [48] L3 Collaboration. *Phys. Lett. B*, 248:227, 1990.
- [49] G. Dissertori, A. Gehrmann-De Ridder, T. Gehrmann, E.W.N. Glover, G. Heinrich, and H. Stenzel. *arXiv:0712.0327*, 2008.
- [50] G. Dissertori, A. Gehrmann-De Ridder, T. Gehrmann, E.W.N. Glover, G. Heinrich, G. Luisoni, and H. Stenzel. *arXiv:0906.3436*, 2009.
- [51] G. Dissertori, A. Gehrmann-De Ridder, T. Gehrmann, E.W.N. Glover, G. Heinrich, and H. Stenzel. *arXiv:0806.4601*, 2008.
- [52] S. Kluth. *arXiv:hep-ex/0603011*, 2006.

Index

- acceleration
 - method, 33
- accelerator
 - circular, 33, 34
 - history, 34
 - linear, 34
 - motivation, 29
 - use, 29
- acollinearity, 116
- adjoint
 - Dirac, 59
 - hermitian, 59
- annihilation operator, 65
- anti-commutation relations
 - Dirac field operator, 65
 - ladder operators, 66
- antiparticle, 15, 60, 131
- antiscreening, 150
- asymptotic freedom, 147, 150
- baryon, 131, 140
 - number, 131
 - conservation, 32
- beam
 - energy, 29
 - Gaussian shaped, 40
 - of secondary particles, 31
- Bhabha scattering, 17, 85, 113
- Boltzmann factor, 106
- Breit system, 10
- calorimeter, 110
 - electromagnetic, 111
 - hadron, 111
- center of mass
 - energy, 32
 - frame, 10
- centripetal force, 34
- CERN, 38
- chirality
 - γ_5 , 62
 - $m = 0$, 62
 - basis, 62
 - eigenstates, 62
 - projectors $P_{R,L}$, 63
 - vs. helicity, 63
- Clifford algebra, 58
- CMS, 44
- collider
 - experiment, 29
- colliding beam, 31
 - vs. fixed target, 32
- collinear safety, 161
- color, 138
 - current, 141
 - factor, 146
 - measurements of color factors, 190
 - number of colors, 156
- completeness relation
 - photon, 72
- Compton scattering, 85
 - cross-section, 94
 - gluon, 147
 - unpolarized cross-section, 96
- CONE algorithm, 162
- confinement, 121, 147, 150
- continuity equation, 56
- contraction of operators, 80
- contravariant, 7
- correspondence principle, 55
- cosmic rays, 29
- coupling constant, 81
- covariant, 7

- derivative
 - QCD, 142
 - QED, 125
- creation operator, 65
- cross section, 23, 40
 - differential, 26
 - $e^+e^- \rightarrow \mu^+\mu^-$, 93
 - elastic, 26
 - invariant, 26
 - singularities, 156
 - $e^+e^- \rightarrow q\bar{q}$, 155
 - measurement, 112
 - pp , 40
 - $p\bar{p}$, 40
 - total, 40
- crossing symmetry, 14
- current-field interaction Lagrangian, 81
- cyclotron, 34
 - frequency, 36
 - isochronous, 36
- Dalitz plot, 16, 53
 - $\gamma \rightarrow q\bar{q}g$, 157
- de Broglie equation, 29
- decay, 8
 - three body, 53
 - two-particle, 9
- DESY, 108
- detector, 43
 - colliding beams, 43
 - elements, 110
 - fixed target, 43
- Dirac
 - equation, 58
 - free particle, 60
 - solution, 59
 - u and v , 60
- field, 65
 - field operator, 65
 - Lagrangian, 81
 - momentum operator, 66
- propagator, 68
- DURHAM algorithm, 164
- $e^+e^- \rightarrow \mu^+\mu^-$, 92
- elastic scattering
 - scattering angle, 12
- electrodynamics
 - classical, 99
- electron
 - e^+e^- annihilation, 49, 85
 - anomalous magnetic moment, 4, 101
- electron volt, 3
- elementary
 - interactions, 4
 - particle, 1
- ermeticity, 43
- event shape variable, 166
 - aplanarity, 170
 - applications, 171
 - Bengtsson-Zerwas angle, 176
 - C-parameter, 171
 - differential two-jet rate, 167
 - event shape distribution, 168
 - heavy jet mass, 170
 - jet mass difference, 171
 - light jet mass, 170
 - oblateness, 170
 - planarity, 170
 - sphericity, 170
 - thrust, 167
 - thrust major, 168
 - thrust minor, 168
 - total jet broadening, 171
 - wide jet broadening, 171
- experiment
 - accelerator-based, 29
 - fixed target, 31
 - non-accelerator-based, 29
- Fermi
 - golden rule, 21
- Feynman
 - propagator, 69
 - rules, 87
 - application, 88
 - momentum space, 93
 - position space, 82

- field
 - conservative, 34
 - electrostatic, 34
 - magnetic, 34
- Fierz identity, 140
- fine structure constant, 4
 - determination, 106
- fixed target
 - vs. colliding beam, 32
- four-current, 15
- four-momentum, 8
- four-vector, 7
 - time-like, 8
- four-velocity, 7
- frame
 - center of mass, 13
 - laboratory, 13
- frequency
 - positive/negative frequency part, 79
- fundamental constant, 2
- g -factor, 102
 - higher order corrections, 102
 - QED prediction, 106
- gamma matrices, 56
 - Dirac-Pauli representation, 58
 - γ_5 , 62
- gauge
 - field, 99
 - group, 99
 - theory, 99, 125
 - QCD, 138
 - QED, 125
 - transformation, 95
- Gell-Mann matrices, 139
- Gell-Mann-Nishijima formula, 138
- gluon, 5, 142
 - gauge field, 99
 - soft, 158
 - spin, 172
- gravitation, 4
- Green's function, 68
- hadron
 - nomenclature, 131
 - spectroscopy, 131
- hadronization, 121, 191
 - string/cluster fragmentation, 193
- handedness, 61, 62
- helicity, 61
 - $m \neq 0$, 63
 - vs. chirality, 63
- high energy limit, 12
- hyperon, 133
- $+i\epsilon$ convention, 69
- infrared
 - safety, 161
- interaction, 1
 - electromagnetic, 4
 - strong, 5
 - weak, 5, 99
 - chirality, 64
- invariant
 - amplitude, 88
- isospin, 126
 - doublet, 128, 131
 - invariant interactions, 129
 - isovector, 129
 - multiplets, 128
 - singlet, 131
 - triplet, 131
- JADE (PETRA), 162
- JADE algorithms, 162
- jet, 121
 - algorithm, 160
 - comparison, 165
 - CONE, 162
 - DURHAM, 164
 - examples, 162
 - JADE, 162
 - definition, 160
 - gluon, 172
 - jet rates, 164
 - quark, 172
 - quark vs. gluon jets, 177
 - three-jet event, 49, 158

- two-jet event, 47, 158
- Källén function, 11
- kinematical region, 16
- kinematics
 - relativistic, 7
- Klein-Gordon equation, 56
- Klein-Nishima formula, 97
- Kronecker product, 58
- laboratory frame, 10
- ladder operators, 65
- LEP, 49
- lepton
 - families, 131
 - number, 131
 - pair production, 116
- LHC, 38, 40
- Lie algebra, 127
- lifetime, 22
 - strong vs. weak processes, 135
- luminosity, 40
 - integrated, 42, 112
- \mathcal{M}_{fi} , 88
- magnet
 - dipole, 37
 - quadrupole, 37
- Mandelstam variables, 10
- mass
 - invariant, 51
 - mass-shell condition, 8
 - missing, 49
 - rest mass, 51
- Maxwell's equations
 - Lagrangian, 81
- meson, 131, 136, 140
- metric (jet algorithms), 162
- metric tensor, 7
- Møller
 - flux factor, 13
 - scattering, 17, 85, 87
- momentum
 - longitudinal, 46
 - measurement, 44
 - transverse, 46
- Monte Carlo, 191
 - HERWIG, 166
- Neumann series
 - time evolution operator, 76
- neutrino
 - detection, 49
 - oscillations, 29
 - signature, 50
- neutron
 - charge radius, 130
 - general properties, 132
 - inner structure, 130
- new physics, 102
- Newton, 8
- normal ordering, 67, 79
 - vs. time ordering, 79
- normalization (state), 67
- nucleon, 125
- number operator, 66
- Ω^- , 135
- optical theorem, 27
- particle
 - relativistic, 8
 - zoo, 130
- parton
 - spin, 172
- Pauli
 - exclusion principle, 65
 - in QCD, 138
 - matrices, 58, 127
- Penning trap, 103
- phase space, 24
 - $2 \rightarrow 2$, 24
- photon
 - field operator, 72
 - gauge field, 99
- pion
 - π^0 , 52
 - π^+ , 8

- polarization
 - sum, 64
 - vector, 72
- $P_{R,L}$, 63
- probability density, 56
- propagator
 - fermion, 70
 - corrections, 85
 - Feynman, 69
 - photon, 73
 - corrections, 85
- proper time, 7
- proton
 - antiproton production, 32
 - charge radius, 130
 - general properties, 132
 - inner structure, 130
- pseudorapidity, 46
- PSI, 34, 38
- QCD, 5, 99, 125, 153
 - 3-gluon vertex, 144, 175
 - 4-gluon vertex, 145
 - β -function, 150, 181
 - covariant derivative, 142
 - current, 141
 - effective coupling, 151
 - experiments overview, 153
 - gauge group, 176
 - gluon propagator, 144
 - in e^+e^- annihilations, 153
 - Lagrangian, 142, 144, 179
 - observables, 159
 - inclusive, 184
 - non-inclusive, 184
 - perturbative regime, 191
 - strong coupling constant, 179
 - NNLO prediction, 189
 - results for $\alpha_s(M_Z)$, 190
 - scale dependence, 182
- QED, 4, 55, 101
 - \mathcal{S} -matrix, 78
 - $2 \rightarrow 2$, 79
 - first order, $\mathcal{S}^{(1)}$, 82
 - integral representation, 78
 - second order, $\mathcal{S}^{(2)}$, 83
 - effective coupling, 149
 - gauge theory, 98
 - interaction
 - Hamiltonian, 81
 - Lagrangian, 81
 - timescale, 78
 - Lagrangian, 80, 99
 - limits, 122
 - observables, 98
 - potential
 - Coulomb limit, 148
 - tests, 101
 - high energy, 108
- quantum mechanics, 55
- quark, 5, 130
 - decay, 132
 - doublets, 131
 - families, 131
 - mass effects, 156
 - model, 130
 - spin, 172
- radiative corrections, 114
- reaction channel
 - s -channel, 15
 - t -channel, 15
- relative velocity, 13
- renormalization scale, 181
- representation
 - Dirac, 74
 - Heisenberg, 74
 - Schrödinger, 74
- resolution, 31
- resonance, 121
- resummation, 164, 165
- ρ , 51
- \mathcal{S} -operator, 20
 - unitarity, 26
- scalar propagator, 68
- scattering
 - $2 \rightarrow 2$, 24

- angle, 12
 - $2 \rightarrow 2$, 12
- elastic, 9, 12
 - angular distribution, 13
- Schrödinger equation, 55
- Σ^\pm , 53
- singularities, 156
- slash notation, 59
- special relativity
 - notation, 7
- spectroscopic notation, 136
- spin, 61
 - summation, 90
- spinor, 58
 - space
 - Hamiltonian, 61
 - operator, 61
- strangeness, 132, 133
- strong interaction, 125
- structure constants, 127
- $SU(2)$, 126
 - adjoint representation, 130
 - fundamental representation, 128
 - isospin, 125
- $SU(3)$
 - adjoint representation, 140
 - color and flavor, 133
 - fundamental representation, 139
 - Lie algebra, 139
- $SU(N)$, 126
 - dimension of $su(N)$, 127
 - rank, 127
- Super-Kamiokande, 29
- superposition
 - principle, 145
- Swiss Light Source, 38
- symmetry
 - approximate, 126
 - crossing, 14
 - gauge
 - QED, 98
 - internal
 - isospin, 125
 - unitary, 125
- synchrotron, 37
 - momentum, 38
 - radiation, 38
 - radius, 37
- Tevatron, 40
 - luminosity, 42
- time evolution operator
 - interaction picture, 75
 - perturbation series, 77
 - properties, 75
- time ordering, 71, 76
 - time ordered exponential, 77
 - vs. normal ordering, 79
- total
 - decay width, 22
- trace theorems, 90
- $U(1)$, 98
- unit, 2
 - Heaviside-Lorentz, 4
 - natural, 3
- unitarity, 27
- vacuum
 - polarization, 148
 - state, 67
- vacuum polarization, 149
- W boson
 - decay, 50
 - discovery, 50
 - gauge field, 99
 - production, 50
- Wick's theorem, 80
- Yang-Mills theory, 144
- Yukawa theory, 5
 - \mathcal{L}' , 129
- Z boson, 52
 - gauge field, 99